PhD degree in Molecular Medicine, curriculum in Molecular Oncology,

PhD degree in Molecular Medicine

European School of Molecular Medicine (SEMM),

University of Milan and University of Naples "Federico II"

Faculty of Medicine, MED/04

ONCOGENE-INDUCED ALTERED DNA REPLICATION DYNAMICS

Aurora Cerutti

IFOM-IEO Campus, Milan

Matricola n. R08403

Supervisor: Dr. Fabrizio d'Adda di Fagagna

IFOM, Milan

Internal co-supervisor: Prof. Marco Foiani

IFOM, Milan

External co-supervisor: Dr. Philippe Pasero

IGH, Montpellier

Anno accademico 2012-2013

TABLE OF CONTENTS

LIST OF ABBREVIATIONS

53BP1	p53 binding protein 1
AKT	akt murine thymoma viral oncogene homolog 1
ALT	alternative lengthening of telomere
ARF	alternate reading frame
AT	ataxia-teleangectasia
ATM	ataxia telangiectasia mutated
ATR	ataxia telangiectasia and Rad3-related
ATRIP	ATR-interacting protein
B2M	Beta-2-microglobulin
BER	base excision repair
BLM	Bloom
BMI1	BMI1 polycomb ring finger oncogene
BRAF	v-raf murine sarcoma viral oncogene homolog B
BRCA1	breast cancer 1
BrdU	bromodeoxyuridine
CBX7	chromobox homolog 7
CDC6	cell division cycle 6
CDK	cyclin-dependent kinase
CDKN2a	cyclin-dependent kinase inhibitor 2A
CDS	coding DNA sequence
CDT1	chromatin licensing and DNA replication factor 1
CFS	Common Fragile Site
CHK1	Checkpoint 1
CHK2	Checkpoint 2
CldU	Clorodeoxyuridine
CLIP	cross-linking immunoprecipitation
CS	cockaine syndrome
DAPI	4',6-diamidino-2-phenylindole
DBR	double-strand break repair
DDR	DNA damage response
DNA-PKcs	DNA-PK catalytic subunit
dNTP	deoxyribonucleotide
DSB	double-strand break
EED	embryonic ectoderm development
EGF	Epidermal Growth Factor
ER	estrogen receptor
ERFS	Early Replicating Fragile Site
EZH2	enhancer of zeste homolog 2
GLB1	Galactosidase beta 1
GPx	glutathione peroxidase
H3K27me3	Histone 3 lysine 27 trimethylation
H3K9	histone 3 lysine 9
HDM2	Human double minute 2
HNPCC	Hereditary nonpolyposis colorectal cancer
HP1	heterochromatin protein-1
HR	homologous recombination
HRAS	Harvey rat sarcoma viral oncogene homolog
hTERT	Telomerase reverse transcriptase
HU	Hydroxyurea

IdU	Iododeoxyuridine
IOD	inter origin distance
IR	Ionizing radiation
KO	Knock out
KRAS	Kirsten rat sarcoma viral oncogene homolog
LIGIV	Ligase IV
MAPK1	mitogen-activated protein kinase 1
MCM	Mini Chromosome Maintenance
MDC1	mediator of DNA damage checkpoint 1
MDM2	mouse double minute 2
MEF	mouse embryonic fibroblast
MMR	mismatch repair
MOS	Moloney sarcoma oncogene
MRN	Mre11-Rad50-Nbs1
mRNA	messenger RNA
MSI	Microsatellite instability
NAC	N-acetyl-cysteine
NBS	Nijmegen breakage syndrome
NER	nucleotide excision repair
NHEJ	non-homologous end joining
NOX	NADPH-dependent oxidase
OIS	oncogene-induced senescence
ORC	origin recognition complex
ORI	DNA replication origin
Pc	Polycomb
PcG	Polycomb group proteins
PCNA	Proliferating cell nuclear antigen
PFA	paraformaldehyde
Ph	Polyhomeotic
PIK3	phosphatidylinositol-4,5-bisphosphate 3-kinase
PNA	Peptide Nucleic Acid
PRC	Polycomb Repressive Complex
pre-miRNA	precursor microRNA
pre-RC	pre-Replication Complex
PSC	Posterior Sex Comb
PTEN	phosphatase and tensin homolog
RAC1	ras-related C3 botulinum toxin substrate 1
Rb	retinoblastoma protein
RIDDLE	Radiosensitivity, Immunodeficiency, Dysmorphic features and learning difficulties
RING1	ring finger protein 1
ROS	reactive oxygen species
RPA	replication protein A
RTK	Receptor Tyrosine kinase
SA-β-gal	senescence-associated-β-galactosidase
SAHF	senescence-associated heterochromatin foci
SASP	senescent-associated secretory phenotype
SDF	senescence-associated DNA-damage foci
SDS	sodium dodecyl sulphate
Sem	standard error of the mean

shRNA	short hairpin RNA
SISP	stress-induced premature senescence
SLCC	Squamous Lung Cell Carcinoma
SMC1	structural chromosome maintenance 1
SOD	superoxide dismutase
SSB	Single-strand break
ssDNA	single-stranded DNA
SUZ12	suppressor of zeste 12 homolog
TER	DNA replication termination
TIF	telomere induced focus
TLS	translesion synthesis
TopBP1	topoisomerase II binding protein 1
TRF1	telomeric-repeat-binding factor 1
TrxG	Trithorax Group proteins
TS	template-switching
TTD	trychothiodystrophy
UV	ultraviolet
WRN	Werner
XP	xeroderma pigmentosum
XRCC4	X-Ray Repair Cross-Complementing Protein

LIST OF FIGURES

Notes about the figures

Figures 18, 19, 20, 21, 22, 23 describe my original work that has been published, so they are considered as adapted from (Suram et al EMBO Journal, 2012).

FIgures 71, 72, 73, 74, 75 describe my original work that has been included in a manuscript under revision, so they are considered as adapted from (Piunti, et al, under revision, 2013).

ABSTRACT

Oncogene activation is a key step of cellular transformation. However normal cells have developed a tumor suppressive barrier to restrain the oncogene-induced uncontrolled cellular proliferation. This barrier consists in a permanent cell cycle arrest - known as Oncogene Induced Senescence (OIS) - that is triggered as a consequence of a robust DNA damage response (DDR) activation due to oncogene-induced hyper-replication and the consequent accumulation of DNA damage (Bartkova et al., 2006; Di Micco et al., 2006). However the molecular mechanisms underlying the complex interplay between oncogene activation, DNA replication and DDR activation are still poorly understood. Thus in this thesis I tried to unveil the impact that oncogene activation has on DNA replication dynamics and DDR activation.

Previous studies from my laboratory demonstrated that oncogene activation leads to DNA replication stress that affects mainly fragile sites, as seen by Loss Of Heterozygosity (LOH) occurring preferentially at fragile sites (Di Micco et al., 2006). Since it has been recently demonstrated that telomeres resemble fragile sites (Sfeir et al., 2009), I attempted to understand the impact that oncogene activation could have on telomere structure and function. In this thesis I have shown that oncogenic Ras expression impairs telomere replication, as seen by an increase in telomeric fork stalling. This is also accompanied by the appearance of fragile telomeres together with stochastic telomeric attrition. Furthermore, both *in vitro* - human fibroblast - and *in vivo* - human nevi preneoplastic lesions - oncogene activation results in the accumulation of persistent telomeric DDR. These results revealed a novel and unprecedented link between oncogene activation and telomere dysfunction, refining the model underlying the establishment of oncogene-induced senescence.

After this site-specific study, I proceeded with whole genome analyses of the dynamics underlying oncogene-induced altered DNA replication. Previous studies in literature showed that oncogene activation leads to increased fork stalling and increased replication initiation (Bartkova et al., 2006; Di Micco et al., 2006; Jones et al., 2013).

However these studies were conducted in DDR deficient cells (Di Micco et al., 2006) or tumor cell lines (Bartkova et al., 2006; Jones et al., 2013) without following the impact of oncogene activation over time. Thus to better understand the kinetics of oncogene-induced altered DNA replication, here I performed a whole genome study of DNA replication dynamics and DDR activation upon oncogene activation over time, from the initial hyperproliferative burst to OIS establishment. I discovered that oncogene activation has an immediate effect on DNA replication dynamics. Indeed from the very initial phase oncogene activation results in high fork speed and low frequency of initiation, together with high levels of unidirectional forks. This is accompanied by a prompt and robust DDR activation. As time passes frequency of initiation increases, the level of unidirectional forks and fork speed decreases, as cells approach senescence.

Oncogene activation results also in increased level of Reactive Oxygen Species (ROS). Beyond their toxic effects, ROS are essential intracellular second messengers for several cytokines and growth factors (Lee et al., 1999) mediating mitogenic signalling (Irani et al., 1997). However the mechanism underlying oncogene-induced ROS production are not completely understood. The data presented in this thesis revealed that oncogene-induced ROS production is mediated by the NADPH oxidase NOX4. Upon oncogene activation, pharmacological inhibition of NOX4 enzymatic activity blocked ROS production. The absence of ROS restrains the oncogene-induced hyperproliferation and DDR activation, preventing OIS establishment. Furthermore NOX4 inhibition leads to fork speed reduction together with differential regulation of local origin initiation. Overall this data revealed the fundamental role of NOX4 - and consequently of ROS - in mediating oncogene-induced hyperproliferation. ROS appears to be the fuel of Ras-induced hyperproliferation and it seems to directly affect DNA replication dynamics.

Polycomb repressive complexes (PRCs) are mainly known for their role in establishing and maintaining cell identity during development as well as in adult organisms. PRCs exert these functions by repressing a large set of genes involved in

development, proliferation and differentiation via trimethylation of H3K27, catalysed mainly by EZH2. PRCs have been found highly overexpressed in various cancers and their role in promoting cancer progression has been ascribed to their repressive function on the INK4a-ARF locus. However recent independent studies revealed a more direct role of PRCs on S phase progression and on the regulation of DNA replication(Francis et al., 2009; Hansen et al., 2008; Pasini et al., 2004). Indeed EZH2 has been shown to colocalized with sites of ongoing DNA replication (Hansen et al., 2008). I therefore attempted to better characterise the role of PRCs on DNA replication. EZH2 knock out (KO) lead to impairment of cell cycle progression, with cells blocked at G1/S transition. Furthermore absence of proficient PRCs - obtained by EZH2 KO - impairs DNA replication dynamics leading to reduced fork speed, increased frequency of initiation and increased fork stalling, demonstrating that PRCs deficiency leads to replication stress. Overall the data presented in this thesis unveil a novel and unprecedented function of PcG proteins in the regulation of cellular proliferation through a direct role in DNA replication dynamics underlying novel mechanisms of proliferation control that opens new perspective in the field.

INTRODUCTION

CHAPTER 1. DNA damage and DNA damage response

1.1 Different types of DNA damage

Nuclear DNA is the most important component of a cell. It retains all the information that defines any single aspect of the cell and thus plays a central role in essential cellular functions. Being the most precious component of a cell, DNA must be safeguarded from alteration and damage in order to maintain its integrity.

DNA is daily subjected to exogenous and endogenous sources of DNA damage. It is regularly exposed to environmental DNA damaging agents such us UV light, IR, chemical compounds. Furthermore, during normal DNA and cellular metabolism, DNA lesions are introduced as a consequence of errors in DNA replication, or by the action of nucleases, as well as of the action of by-products of oxygen metabolism deriving from normal respiration and also as a part of inflammatory response (Altieri et al., 2008; Jackson and Bartek, 2009).

The lesions occurring at DNA include base modifications, replication errors, DNA inter-strand and intra-stand crosslinks, DNA-protein crosslinks, single-strand breaks (SSBs) and double-strand breaks (DSBs).

Base modifications comprise DNA depurination and deamination, generated by spontaneous hydrolytic reactions, and base oxidation (Cadet et al., 2003), caused by oxygen free radicals derived from cellular respiration by-products.

Errors during DNA replication can alter DNA by introducing mismatches, small insertions or deletions. Moreover abortive topoisomerase I and II activity can lead to generation of SSBs and DSBs.

DNA crosslinks, either inter- or intra-strand or DNA-protein crosslinks, are produced by alkylating agents, such as *cis*-platin and psoralen, as well as by exposure to UV and IR. These kinds of damages alter the structure of the DNA double helix and this situation can

become problematic when a DNA replication fork is approaching these lesions. Indeed replication forks encountering a structural block stall, exposing DNA single strand nicks that can easily turn into DNA DSBs by the action of nucleases.

Other sources of SSBs and DSBs are oxygen free radicals deriving from cellular oxygen metabolism or by exposure to IR. Indeed the energy released by free oxygen radicals can break the phosphodiester bonds in the backbone of the DNA helix generating a single-strand DNA break; when two of these breaks are close to each other on opposite DNA strands a DSB is generated (Altieri et al., 2008).

1.2 The DNA Damage Response (DDR)

Any kind of damage that introduces discontinuities in the nuclear DNA elicits a rapid cellular response, known as DNA Damage Response (DDR). This pathway first detects the presence of damage by DNA damage sensors. Once the damage is sensed, a signalling cascade starts transducing to downstream kinases the presence of DNA damage. The final outcome of DDR activation is the induction of proper DNA repair pathways, together with the block of cell cycle. Indeed the DDR pathway plays two fundamental roles in the response to DNA damage: it triggers the appropriate repair pathway while it also acts as a checkpoint, inducing cell cycle to arrest to give cells the time to repair the damage. Thus DDR pathway avoids the propagation of corrupted DNA to daughter cells maintaining genome integrity by the coordination of the cell cycle arrest and cellular attempts to repair DNA damage (Figure 1, (Sulli et al., 2012)).

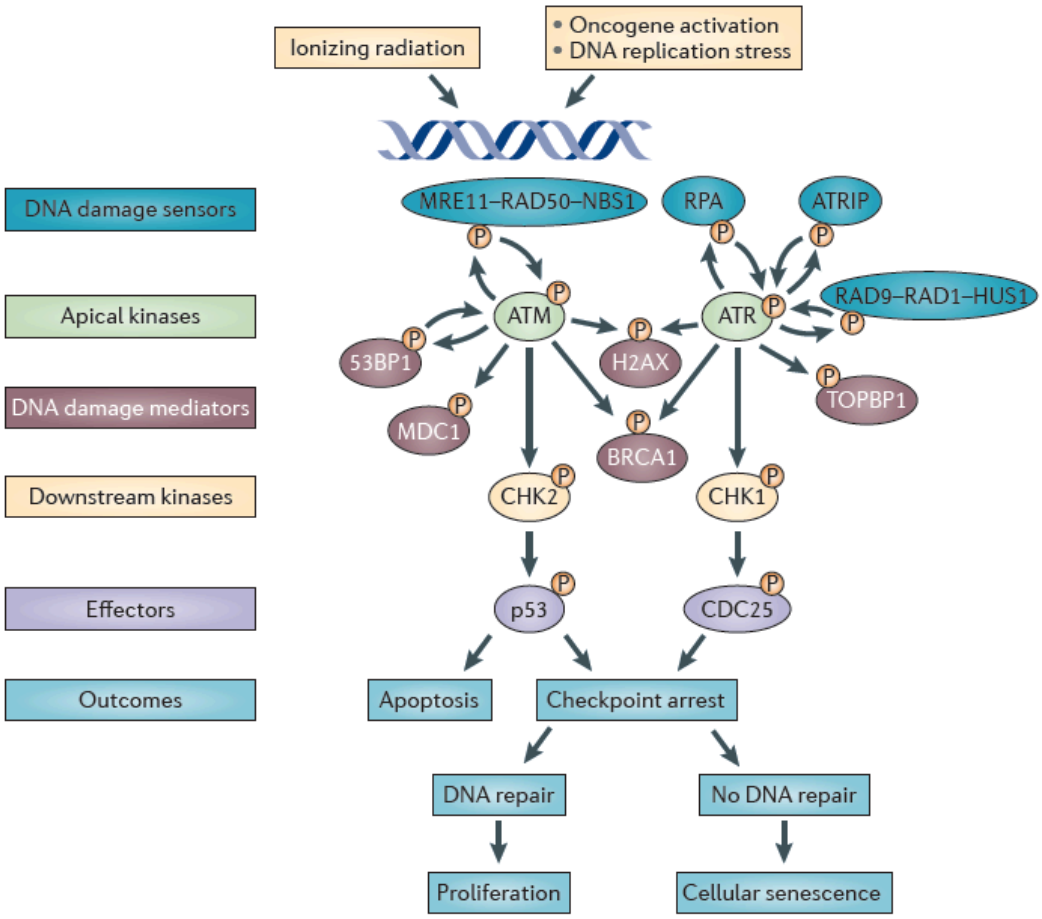

adapted from Sulli et al 2012

Figure 1. The DNA damage checkpoint response cascade.
The DDR pathway presents two main DNA damage sensors: the MRE11-RAD50-NBS1 (MRN) complex recognizes DSBs, while Replication Protein A (RPA) and the RAD9–RAD1–HUS1 (9-1-1) complex detects regions of single-stranded DNA. Once the damage is sensed, the apical kinases ATM - and ATR, which is bound by ATRIP, are recruited to the site of damage through the MRN complex or RPA and 9-1-1 complex respectively. These apical kinases in turn phosphorylate (P) the histone variant H2AX on Ser139 (known as γH2AX) to recruit other components of the DDR cascade such as MDC1, 53BP1, BRCA1. The diffusible downstream kinases CHK1 (mainly phosphorylated by ATR) CHK2 (mainly phosphorylated by ATM) spread the signal to downstream effectors such as CDC25 and p53. The activation of DDR pathway can result in three different outcomes: transient cell-cycle arrest, when cell cycle is transiently blocked to allow DNA damage to be repaired before cycling is resumed; apoptosis, programmed cell death; or cellular senescence, a permanent cell cycle arrest. Adapted from (Sulli et al., 2012).

1.2.1 Different types of DNA repair pathways.

The choice of the proper repair system depends on the type of lesion and on the cell cycle phase in which the damage occurred. We can distinguish four main DNA repair pathways: base excision repair (BER) and nucleotide excision repair (NER); mismatch repair (MMR); double strand break repair (DBR), which includes homologous recombination (HR) and non-homologous end joining (NHEJ) pathways.

BER allows for the recognition and excision of a damage base, by the action of specific DNA-glycosylases, and it is active throughout the cell cycle (Fortini and Dogliotti, 2007; Hitomi et al., 2007).

NER detects DNA damage by the presence of structural abnormalities in the double helix, proceeding then with their excision and replacement. It acts mainly during G1 phase by removing bulky lesions, such as those caused by exposure to UV radiation or to polycyclic aromatic hydrocarbons produced by cigarette smoke, and the distorting intrastrand DNA produced by chemotherapeutic agents, such as cisplatin (Batty and Wood, 2000).

MMR is the repair system devoted to fix errors introduced during replication, such as base mismatches, small insertion or deletion loops. In case these mismatches are not solved, they will give rise to permanent mutations in the genome during the next round of replication. Thus MMR plays an essential role in maintaining the stability of the genome during replication (Jiricny, 2006).

BER, NER and MMR share a similar repair mechanism that comprises lesion recognition and excision, followed by DNA synthesis of the removed nucleotides and ligation to the single strand nick. Excision consists of an incision in the strand containing the lesion and the removal of 1-2 nucleotides in BER or 12-30 nucleotides as in NER or hundreds in MMR.

If left unrepaired during G1 phase, bulky DNA lesions can hinder the progression of DNA polymerases. Cells have developed two main mechanisms to deal with this kind of damage occurring during S phase, known as DNA damage tolerance pathways. In one case DNA replication may continue by using a translesion synthesis (TLS) polymerases, which replicate across the damage, in an error-prone manner. The other DNA damage tolerance pathway consists of template-switching (TS), an error-free process that repairs gaps in newly replicated DNA using the newly synthesized sister chromatid as a template (Branzei and Foiani, 2007; Lehmann et al., 2007).

1.2.1.1 Double-Stranded Break (DSB) repair pathways

There are two main pathways ascribed to the repair of DSBs: Homologous Recombination (HR) and Non Homologous End Joining (NHEJ). NHEJ repairs predominantly DSBs that occur during G1 phase, whereas HR is mainly devoted to repair of DSBs that are formed during S and G2 phases.

HR is an accurate repair mechanism that uses the undamaged sister chromatid as repair template. Hence it mainly works during late S/G2 phases. The first step in HR pathway is the resection of the DSB end in 5'- to 3' direction by a nuclease activity that is modulated by MRE11/RAD50/NBS1 (MRN) complex. This complex presents various biochemical properties such as 3' to 5' exonuclease activity, single strand endonuclease activity and DNA unwinding activity, that together with a 5'- to 3' exonuclease allows the resection of the DSB and create a 3'-ended single stranded DNA (ssDNA) necessary to initiate strand invasion. After resection, RAD51, with the help of BRCA2, binds to ssDNA creating a nucleoprotein filament that invades sister chromatid and pairs at the undamaged complementary sequence. DNA heteroduplex is formed. The annealed 3'-terminus of the damage molecule is extended by a DNA polymerase and DNA ligation takes place. DNA crossovers formed at the border between homo- and heteroduplex, known as Holliday junctions, are solved to yield two intact DNA molecules by RecQ helicases, such as the Bloom protein (BLM), a 3'-5' helicase, or the Werner protein (WRN), that has 3' → 5' helicase and exonuclease activity (Sung et al., 2003).

Differently, NHEJ does not require an undamaged template molecule and it essentially re-joins any compatible broken DNA ends. The first step in NHEJ consists in the binding of the two extremities of a DSB by the heterodimeric DNA end-binding protein Ku (ku70-

ku80). This complex then recruits the DNA-dependent protein kinase catalytic subunit (DNA-PKcs). Once bound to DNA ends, DNA-PKcs undergoes autophosphorylation and it phosphorylates other targets such as replication protein A (RPA), Werner protein (WRN) and Artemis. At this point the DNA ends can be ligated by the DNA ligase IV in association with its binding partners, XRCC4 and XRCC4-like factor (XLF, also known as Cernunnos), completing the NHEJ (Ahnesorg et al., 2006). Artemis plays a fundamental role in processing DNA "dirty" ends derived from exposure to IR or alkylating agents, to make them suitable for the LIGIV-XRCC4 mediated ligation.

NHEJ allows for the ligation of DNA ends regardless of their genomic loci. Therefore translocations or deletions can occur, making NHEJ an error prone repair pathway.

1.2.2 The DNA damage checkpoint pathways

The break of the sugar-phosphate backbone leads to the exposure of single-stranded DNA and/or the generation of DSBs. Specialized complexes, after sensing these two kinds of lesions, recruit to the site of damage and activate two large protein kinases, ataxia telangiectasia and RAD3-related (ATR), or ataxia telangiectasia (ATM), respectively (Zou, 2007; Shiloh and Ziv, 2013). Upon recruitment of one of these apical kinases to the site of lesion, local phosphorylation *in cis* of the histone variant H2AX occurs. This local phosphorylation of H2AX is the key step in the nucleation of DDR (Celeste et al., 2002). Indeed γH2AX - the phosphorylated form of H2AX - recruits at the site of damage additional ATM complexes, resulting in a positive feedback loop that increases the local ATM activity and promotes the spreading of γH2AX along the chromatin.

In unperturbed conditions ATM is present as a homodimer in which internal domain conformation blocks the kinase domain. When a DSB occurs, this leads to a conformational change in the ATM protein that stimulates the kinase to phosphorylate serine 1981, thus inducing the homodimer to dissociate, releasing the activated ATM

monomer. In its activated form, ATM can phosphorylate its several targets, both at the site of damage, such as Nijmegen breakage syndrome (NBS1), breast cancer 1 (BRCA1), and structural chromosome maintenance (SMC1) and in the nucleoplasm such p53. The activated form of ATM phosphorylates also important DNA damage mediators that help in establishing a strong positive feedback loop that strengthens and supports the checkpoint cascade. Some of these mediators are p53 binding protein 1 (53BP1) and mediator of DNA damage checkpoint (MDC1). After the activation of apical kinases and DNA damage mediators, downstream kinases are also activated. In case of ATM activation the main downstream kinases is CHK2. When activated, CHK2 phosphorylates downstream effectors such as p53, stabilizing it and leading to its activation.

On the other hand, upon single-stranded DNA (ssDNA) exposure, the single-stranded DNA binding protein A (RPA) binds to the ssDNA and recruits ATR to the site of damage. This recruitment occurs via ATR-interacting protein (ATRIP), to which ATR is usually bound both in unperturbed and perturbed conditions (Cortez et al., 2001). Thus upon accumulation of RPA on ssDNA both ATR and ATRIP are recruited to the site of damage (Cimprich and Cortez, 2008). Independent recruitment to RPA-ssDNA of the heterotrimeric 911 complex (constituted by RAD9, RAD1 and HUS1) and of topoisomerase binding protein 1 (TOPBP1) induces further ATR recruitment to the site of damage and boosts ATR kinase activity. Indeed TOBP1 mediates ATR activation (Kumagai et al., 2006), which then phosphorylates several substrates including CHK1, a fundamental downstream kinase that controls cellular responses to DNA damage and replication stress acting on downstream effectors such as CDC25 phosphatases (Cimprich and Cortez, 2008).

Hence DSBs, such as those formed upon IR, mainly trigger ATM kinase, whereas single-stranded DNA coated with RPA, activates ATR. Although RPA-coated ssDNA it is mainly generated upon perturbed DNA replication, it can also result from resection of one DNA strand at DSBs in cells in the S and G2 phases of the cell cycle. Thus DSBs that are

processed by HR in S/G2 have the opportunity to involve both ATM and ATR kinase at the same DNA lesion, further boosting the checkpoint-signalling cascade (Jazayeri et al., 2006).

To engage DDR factors that are far from the damaged site, local ATM and ATR activity should reach a certain threshold (Buscemi et al., 2004). When DNA damage induces ATM to surpass this threshold, the downstream kinase CHK2 is activated by ATM phosphorylation. CHK2 then goes in the nucleoplasm, and further spreads DDR signalling by phosphorylating its targets (Lukas et al., 2003). CHK1 is also activated by phosphorylation, mainly by ATR, but to a lesser extent also by ATM. After activation, similarly to CHK2, CHK1 diffuses in the nucleoplasm, phosphorylating its substrates, further enforcing the checkpoint pathway cascade.

The checkpoint cascade is thus amplified in several, often redundant, signalling pathways (Cuadrado et al., 2006; Jazayeri et al., 2006) that ultimately act on key cellular effectors, such p53 and the CDC25 phosphatases.

Upon DNA damage, a rapid cell-cycle arrest is achieved by the inactivation of CDC25, essential phosphatases for cellular proliferation (Mailand et al., 2000). On the other hand, a stable cell-cycle arrest is accomplished by a slower p53 induction. The DDR kinases stabilise p53 by phosphorylating it, and then, once active, p53 triggers the transcription of p21, a cyclin dependent kinase (CDKs) inhibitor (Deng et al., 1995), which is then responsible for the establishment of a stable cell cycle arrest.

Upon DNA damage, γH2AX helps in the amplification of the signal by spreading γH2AX for hundreds of kilobases away from the DNA damage site. In this way γH2AX acts as a molecular ‘velcro’ recruiting and retaining numerous DDR factors at the site of damage (Downey and Durocher, 2006). Thus γH2AX becomes a cytologically detectable nuclear focus, which consists of several copies of the same proteins that are compacted on the chromatin close to the site of damage. DDR foci are formed at the site of damage by the

upstream factors of the DDR pathway that act in the proximity of the damaged site. On the other hand, downstream factors such as CHK2, CHK1, p53, CDC25 do not form DDR foci.

The formation of DDR foci at the site of damage requires mainly two steps. The first step consists of an initial recruitment to the site of damage of activated ATM and other DDR factors, and it is independent from H2AX. Once at the site of damage, ATM and other DDR factors induce a subsequent accumulation of DDR foci by phospho-specific protein-protein interactions. In this second step H2AX is fundamental for foci formation: without H2AX the formation of visible foci does not occur, mainly because most of the phospho-specific protein-protein interactions rely on the molecular velcro formed by γH2AX. This confirms the essential role played by γH2AX in DDR signalling amplification and activation (Celeste et al., 2003b).

DDR foci are stable sites at the damaged DNA at which DDR factors accumulate in a very dynamic manner, as shown by photobleaching experiments (Celeste et al., 2003b). To detect the DDR activation it is thus possible to exploit the high local concentration of DDR factors at damage sites. These DDR factors represent a robust and specific set of markers to detect DDR activation. Indeed by performing immunostainings with antibodies against γH2AX or other DDR factors that accumulate at the site of damage, a typical nuclear pattern of discrete bright foci becomes visible.

Once DNA is repaired, checkpoint recovery occurs. This process consists in the dismantling of DDR foci by the action of phosphatases dedicated to the dephosphorylation of γH2AX, as well as by chromatin remodelling complexes (Panier and Durocher, 2013). In this way DNA damage response is terminated and cells can re-enter cell cycle.

1.2.3 The DDR through the cell cycle

G1 checkpoint activation occurs whenever DNA damage accumulates during G1. It is able to induce a prolonged G1 arrest, brought about by the ATM (ATR) - CHK2 (CHK1) - p53/MDM2 - p21 pathway. The level of ATM and CHK2 are constant throughout cell cycle. On the contrary, ATR and CHK1 levels fluctuate during cell cycle. Early-to-mid G1 presents low levels of ATR and CHK1. In late G1, the expression of ATR and CHK1 increases as a consequence of E2F-dependent S-phase-promoting transcriptional programme activation. Under unperturbed conditions, in late G1 the expression of cyclins E and A are induced together with CDC25A phosphatase, the activator of cyclin E(A)/CDK2 kinase. Indeed CDC25A dephosphorylate CDKs leading to their activation (Pines, 1999): the active cyclin E(A)/CDK2 kinase complex promotes the entrance into S phase via the activation of a specific signalling cascade. In physiological conditions, ATR/CHK1 (but not ATM/CHK2) keeps CDC25A levels under control by phosphorylation of CD25A, inducing its ubiquitin-mediated proteosomal degradation (Zhang et al., 2003). Under genotoxic stresses, this physiological mechanism is further boosted by the increased activation of CHK1 and CHK2. This induces the downregulation of CDC25A and therefore cyclin E(A)/CDK2 complexes are inhibited, thus blocking the cells in G1 (Bartek and Lukas, 2003). ATM/ATR activation leads ultimately to the simultaneous phosphorylation of p53 and CDC25A, respectively. However these events act differently on cell cycle: the CDC25A-degradation cascade induced by ATR phosphorylation is faster since it does not necessitate transcription or newly synthetized proteins. By contrast p53 pathway that acts on transcription, affects cell cycle progression in a slower manner than the CDC25A-proteolysis. Thus, independently of p53, the CHK1/CHK2-CDC25A checkpoint is rapidly executed, and it postpones the G1/S transition only for a few hours. A prolonged block in G1 can then occur only with the sustained p53-dependent mechanism (Kastan and Bartek, 2004).

The p53 transcription factor is directly activated by ATM and ATR. These kinases phosphorylate p53 at its serine 15, within its amino-terminal transactivation domain. In the same domain, also threonine 18 and serine 20, together with probably some other p53 sequence(s), are also targeted by ATM and ATR or CHK1 and CHK2, respectively (Bartek et al., 2004; Craig et al., 2003; Shiloh, 2003).

Upon DNA damage, ATM and ATR further stabilize p53 by targeting MDM2, the ubiquitin ligase that normally binds p53 inducing a rapid p53 turnover via ubiquitin-mediated proteasomal degradation (Maya et al., 2001). This further contributes to the accumulation of functional p53 protein as well as to its increased activity as a transcription factor.

The main transcriptional target of p53 is the p21CIP1/WAF1 inhibitor of cyclin-dependent kinases (Wahl and Carr, 2001). p21 binds and inhibits the G1/S-promoting cyclin E/Cdk2 kinase, and therefore causes a G1 arrest. This leads to a sustained G1 blockade, due to the inability to initiate DNA synthesis, but also due to maintenance of the Rb/E2F pathway in its active, growth-suppressing mode. Thus, the G1 checkpoint response targets two crucial tumor suppressor pathways, governed by p53 and Rb (see paragraph *2.2 The p53 and Rb pathways*). These two pathways are most commonly deregulated in human cancer.

Intra-S-phase checkpoint is activated when DNA damage occurs during S phase. The aim of this checkpoint is to transiently block the firing of late replication origins, in order to avoid S phase progression into mitosis before that the damage is solved. Another important function of the intra-S-phase checkpoint is to protect the integrity stalled forks. This checkpoint brings about a slow down in DNA synthesis using two parallel pathways, both controlled by the ATM/ATR machinery. ATR phosphorylates CDC25A inactivating it. As a consequence CDK2 is inhibited and thus blocks the loading onto chromatin of CDC45, one of its downstream target. Since CDC45 is required for the recruitment of DNA polymerase alpha onto pre-replication complexes (pre-RC), the block of CDC45 via

CDK2 inhibition prevents the initiation of new origin firing (Bartek and Lukas, 2003). Also ATM acts in the intra-S-phase checkpoint pathway by phosphorylating NBS1 and the cohesin protein SMC1 (Kitagawa et al., 2004).

The G2/M checkpoint occurs when DNA damage occurs during G2, or when cells have reached G2 with some unrepaired damage that occurred in the previous S or G1 phase. The aim of the G2/M checkpoint is to prevent the cells with unrepaired DNA to enter mitosis. G2/M checkpoint targets the cyclin B/CDK1 kinase, which has a mitosis-promoting activity. ATM/ATR, CHK1/CHK2 and/or p38-kinase-mediated subcellular sequestration, mediate the inhibition of cyclin B/CDK1 kinase activity. CDK1 inhibition occurs also by of degradation and/or inhibition of the CDC25 family of phosphatases that normally activate CDK1 at the G2/M boundary (Bulavin et al., 2001; Donzelli and Draetta, 2003).

Equivalent to the role of the checkpoint mediators in the S-phase checkpoint, 53BP1 and BRCA1 are also involved in the regulation of the G2-checkpoint responses (DiTullio et al., 2002; Xu et al., 2001). G2 checkpoint probably partly depends on the transcriptional programmes regulated by BRCA1 and p53. In this way, cell cycle inhibitors such as CDK inhibitor p21 and GADD45a (growth arrest and DNA-damage-inducible 45 alpha) are upregulated, leading to cell cycle arrest (Taylor and Stark, 2001).

1.2.4 Defects in DNA repair and checkpoint processes

Given the essential function of DNA damage response pathway, defects in this signalling cascade, from DNA damage recognition to repair and recombination processes, have been linked to genomic instability, immunodeficiency, cancer predisposition and premature aging syndromes.

Mutations in the *Atm* gene are responsible for the development of Ataxia Telangiectasia (AT). Patients with AT show ataxia starting between the first and third year of life, as a result of progressive neuronal degeneration characterized by loss of Purkinje cells in the cerebellum. AT is further characterized by telangiectasia in the face, a humoral and cellular

immunodeficiency, an increased sensitivity towards IR, and a high predisposition to develop lymphomas and leukaemia (Shiloh and Kastan, 2001; Thompson and Schild, 2002). Indeed, loss of ATM predisposes human and mice to lymphoma development and to some other malignancies (Shiloh and Kastan, 2001).

The Nijmegen breakage syndrome (NBS) is similar to AT, and was formerly viewed as a variant form of AT. Distinction from AT was possible after the identification of the defective gene, *Nbs1* (Shiloh, 1997). NBS patients show no telangiectasia and, often exhibit microcephaly, café au lait macules, vitiligo, or altered eye pigmentations, and it often associated with mental retardation. In some patients with AT-like disorders (AT-LD), mutations in the MRE11 gene were identified (Stewart et al., 1999).

Disruption of both alleles of *Atr* causes embryonic lethality in mice (Brown and Baltimore, 2003). However hypomorphic mutations in *Atr* that lead to low levels of ATR expression, are associated with Seckel syndrome, a human disease characterized by growth retardation, dwarfism, microcephaly and mental retardation. Furthermore, *Atr* haploinsufficiency enhances tumorigenesis in mice that are defective for DNA-mismatch repair (O'Driscoll et al., 2003). Other mutations in additional components of these signalling pathways also lead to cancer predisposition.

In mice, the lack of H2AX (Bassing et al., 2003) or 53BP1 (Ward et al., 2003) results in cell-cycle checkpoint defects and cancer predisposition. The inability to recruit 53BP1 to sites of DNA DSBs has been recently ascribed to a human syndrome, called RIDDLE (Radiosensitivity, Immunodeficiency, Dysmorphic features and learning difficulties; (Stewart et al., 2007)). Even haploinsufficiency for *H2AX* provokes detectable genomic instability and enhanced tumor susceptibility in the absence of p53 (Bassing et al., 2003) (Celeste et al., 2003a).

Although MDC1 seems to be required for cell-cycle checkpoint function (Stucki and Jackson, 2004), mutations in the gene have not yet been linked to enhance tumor development in mice or humans.

Since the homozygous-deficient state of *Chk1* cannot be tested because of its lethality, *Chk1* heterozygosity was proved in various transgenic mouse models. *Chk1* heterozygosity moderately enhances the tumorigenic phenotype of *Wnt1* transgenic mice (Liu et al., 2000). This enhancement was explained as a haploinsufficient tumor suppressor mechanism. *Chk1* conditional disruption in mammary epithelial cells showed inappropriate S-phase entry, accumulation of DNA damage during replication and inappropriate mitotic entry (Lam et al., 2004). These observations support the idea that checkpoint defects associated with *Chk1* haploinsufficiency can contribute to tumorigenesis.

Even though *Chk2*-/- mice do not spontaneously develop tumours (Hirao et al., 2002), skin tumorigenesis induced by carcinogen exposure is enhanced in absence of *Chk2*. Moreover individuals with *Chk2* variants are predisposed to develop breast and prostate cancer (Bartek and Lukas, 2003). Thus all these observations indicate that *Chk2* acts as a tumor suppressor gene.

The incidence of breast and ovarian cancers in women is noticeably increased when a single mutated allele of either *Brca1* or *Brca2* is inherited (King et al., 2003). Moreover, since the tumours from these individuals always lose the second allele, both *Brca* genes present the feature of classic tumor suppressor genes (Venkitaraman, 2002).

Mutations in the enzymes involved in other DNA repair pathways, such as mismatch repair (MMS) or nucleotide excision repair (NER), lead to congenital syndromes, characterized by increased genomic instability and enhanced tumor formation. Inherited mutation in MMR genes results in three different diseases, characterized by increased genomic instability and high risk of tumor formation: Hereditary nonpolyposis colorectal cancer (HNPCC) syndrome, Muir-Torre syndrome and the Turcot syndrome. Microsatellite

instability (MSI) - the expansion or contraction of short nucleotide repeats - is a common feature of tumours developed in the MMR deficiency syndromes (Aaltonen et al., 2007).

Patient with defects in NER pathway develop rare autosomal recessive disorders, such as xeroderma pigmentosum (XP), trychothiodystrophy (TTD) and cockaine syndrome (CS). Beyond marked differences between these disorders these patients share some clinical features. They show complex neurological abnormalities like progressive neurological degeneration, developmental delay, progressive sensoneural deafness. These neurological problems derived from primary neuronal degeneration (XP) or as a consequence of reduced myelination in the brain (CS and TTD), due to DNA damage occurring in neuronal cells. Moreover XP patient are hypersensitive to UV light, with an increased risk of skin cancer (de Boer and Hoeijmakers, 2000).

To sum up, deficiencies in the DNA damage checkpoint pathway allows the survival and extended growth of cells with genomic abnormalities, thereby enhancing the probability of malignant transformation. On the other hand the response to DNA damage accumulation in checkpoint-proficient cells can lead to different cellular outcomes. In case DNA damage generated in proliferating cells is promptly and properly fixed, cells will rapidly resume normal proliferation. Otherwise, when DNA damage is particularly severe, cells may decide to undergo programmed cell death, or apoptosis, that allows to eliminate damaged cells from a cell population (Taylor et al., 2008). An additional outcome is also possible. Cells may enter an irreversible cell-cycle arrest induced by DDR signalling. This condition is known as cellular senescence and it will be described in Chapter 2.

CHAPTER 2. Cellular senescence

2.1 General features of cellular senescence

Cellular senescence was first described by Hayflick and Moorhead in 1961 (Hayflick and Moorhead, 1961). They discovered that after an initial robust proliferation, human lung foetal fibroblasts eventually irreversibly lose their ability to divide. They display a replicative limit of approximately 50 cell divisions when serially passaged in monolayer cultured in standard tissue conditions. Thus it was proposed that these normal cells have an intrinsic replicative potential limit, known as Hayflick's limit, in honour of Hayflick work. Most of the cells present in a human body are in a reversible growth arrested state, known as quiescent or G0-phase. Quiescent cells can re-enter cell cycle and proliferate again upon appropriate mitogenic stimuli and space. Therefore, quiescent state is different from senescence, since senescence cells are permanently arrested despite the presence of space and of nutrient and growth factors in the culture medium. Cellular senescence differs also from post-mitotic differentiated cells such as neurons or muscle cells. Indeed these cells have lost their ability to divide and they are irreversibly blocked from re-entering the cell cycle as a consequence of a programmed differentiation process, which has nothing to do with cellular senescence.

Senescent cells are characterized by a flattened and enlarged morphology. Even though they are not able to divide they are metabolically active. The typical DNA content of a senescent cell correspond to the G1-phase DNA content, even though some oncogenes induces a part of cells to arrest with a S- or G2 DNA content (Olsen et al., 2002).
Another feature of senescent cells is their resistance to apoptotic cell death. The apoptotic program is a cellular mechanism that is activated to avoid the proliferation of cells that have damaged DNA and works by inducing the so-called "programmed cell death".

The factors that determine the choice between senescence and apoptosis are still unclear. The nature of the damage, together with the duration and the intensity may play an important role in the choice between senescence and apoptosis. Also the cell type can influence such decision. For example damaged lymphocyte preferentially undergo apoptosis, while damaged human fibroblast tend to senescence. These differences can be ascribed to the physiological turnover of different cells type in the body (Lechel et al., 2005). Even though cellular senescence and apoptosis are mutually exclusive, they share common components, among which p53. Thus the resistance to apoptosis of senescence cells can result from the action of p53 that is preferentially activating genes responsible for proliferation arrest, rather than those involved in cell death (Jackson and Pereira-Smith, 2006).

Senescent cells have an altered gene expression profile, largely due to altered transcription (Mason et al., 2004). The main alteration in the gene expression profile lies on the gene encoding for cell cycle inhibitors or activators. Senescent cells often accumulate p21 and p16, two cyclin-dependent kinase inhibitors (CDKIs) that are part respectively of p53 and Rb tumor suppressive pathways. Moreover upon senescence, proliferative genes, such as cyclin A, cyclin B and PCNA, are stably repressed by the Rb-dependent inactivation of E2F transcription factors (Narita et al., 2003; Stein et al., 1991). Senescent cells have also a secretory phenotype: they release proteins that can modify the tissue microenviroment resulting in the enforcement of the senescence state (Acosta et al., 2008; Kuilman et al., 2008).

2.1.1 Senescence markers

At present markers that exclusively identify the senescent state have not been found. However it is possible to exploit some specific feature of senescent cells to distinguish them. Since senescent cells do not replicate DNA, it is possible to detect them with immunostaining for proliferation markers, such as PCNA and Ki-67, or with the

incorporation of 5-bromodeoxyuridine (BrdU) or 3H-thymidine. However these markers do not distinguish between senescent cells and quiescent or differentiated post-mitotic cells. To make sure that the absence of DNA replication is due to a senescent state, you need to couple it with other markers, such as the senescence associated β-galactosidase (SA-β-gal). SA-β-gal, is an enzyme active at pH 6.0 specifically in senescent cells and not found in pre-senescent, quiescent or immortal and transformed cells (Dimri et al., 1995). The function of SA-β-gal activity during senescence establishment remained unknown. Only recently it has been shown that SA-β-gal activity derives from the activity of the lysosomal-β-galactosidase (designated GLB1) that is normally active at acidic pH 4.5 (Lee et al., 2006). As cells enter senescence the level of lysosomal-β-galactosidase protein increases as a consequence of increased in their lysosomal content. In this way SA-β-gal activity reaches threshold levels becoming detectable by histochemical staining. However SA-β-gal is a marker for increased lysosomes number and activity that we can exploit to infer the senescent state.

Another marker often used to identify senescent cell is p16 (Krishnamurthy et al., 2004). p16 is indeed an key regulator of senescence state. However, not all senescent cell types expressed p16 (Beausejour et al., 2003), and in case of loss of Rb function, it can also be expressed in some tumor cells.

It is also possible to use some cytological markers to identify some senescent cells. These cytological markers are known as senescence associated-heterochromatin foci (SAHFs, (Narita et al., 2003) and senescence-associated DNA-damage foci (SDFs, (d'Adda di Fagagna et al., 2003)).

SAHFs are distinct heterochromatic nuclear structures, that can be detected by the preferential binding of the DNA dye 4',6-diamidino-2-phenylindole (DAPI), as compacted DNA foci. They are characterized by the presence of certain heterochromatin-associated histone modifications (such as, H3K9 trimethylation) as well as typical proteins found in heterochromatin (such as heterochromatin protein-1 (HP1)). p16-Rb pathway is

responsible for SAHFs formation at E2F genes, thus leading to transcriptional silencing of proliferation promoting genes of E2F family (Narita et al., 2003). However, SAHFs are formed in a cell type- and insult-dependent manner. Therefore SAHFs are not clearly detectable in all cell types undergoing senescence or in all types of senescence (Di Micco et al., 2011; Kosar et al., 2011).

SDFs are distinct bright nuclear foci present in senescent cells from mice and humans. They contain proteins involved in DNA damage checkpoint activation and DNA damage repair and are typical of senescent state (see paragraph 1.2. *The DNA damage response (DDR)*).

2.2 The p53 and Rb pathways

The main tumor suppressive pathways governing senescence are the p53 and p16-Rb pathways. Their activation is mainly induced by three different mechanisms: telomere shortening, DNA damage accumulation and the upregulation of CDKN2A locus (which encodes for INK4A and ARF) (Collado et al., 2007). Even though these pathways interact they can also act independently to induce cell cycle arrest. They share some common activators, but they can respond to different stimuli. The propensity to activate one or the other pathway, or both of them is cell-type-dependent and species-dependent. Here we discuss all these feature of p53 and Rb pathways.

Upon exposure to stimuli that activate DDR, like telomere dysfunction or IR, senescence is primarily induced through the p53 pathway. In unperturbed conditions, p53 protein levels are kept at a physiological range by the action of HDM2 (MDM2 in mice). Indeed HDM2 is an E3 ubiquitin-protein ligase that specifically facilitate p53 turnover through ubiquitin-mediated proteasomal degradation. Upon DNA damage accumulation, the DDR pathway stabilizes p53 levels by targeting HDM2 for degradation. Moreover DDR apical kinases directly phosphorylate p53, thus, activating it. In addition, the alternate-reading-frame

protein (ARF), often found upregulated in senescent cells, controls p53 by inhibiting HDM2 activity (Sherr and McCormick, 2002).

A key transcriptional target of p53 is p21, a CDK inhibitor crucial to the establishment of p53-dependent senescence (Brown et al., 1997). Indeed p21 is responsible for the inactivation of cyclin E/CDK2, thus inducing an arrest in G1. Experimental impairment of p53, p21 or DDR factors (for example ATM or CHK2) prevents telomere- or damage induced senescence (Brown et al., 1997; d'Adda di Fagagna et al., 2003; Gire et al., 2004; Won et al., 2006), demonstrating the fundamental role of these factors in the senescence establishment.

p16-Rb pathway can be induced independently of p53, even though p16-Rb activation usually occurs secondary to the induction of p53 pathway (Jacobs and de Lange, 2004). Differences in the activation of these pathways can be ascribed also to different cell type used. For example cultured epithelial cells are more prone than fibroblasts to induce p16 and arrest proliferation. There are also species-specific differences: upon experimental telomeres uncapping mouse cells primarily activate the p53 pathway, whereas human cells induce both the p53 and p16-pRb pathways in (Smogorzewska and de Lange, 2002).

Other senescence-causing stimuli can induce p16 expression. One possible mechanism is linked to the regulation of Polycomb INK4a repressors, like a reduced expression of BMI1 (Bracken et al., 2007; Itahana et al., 2003) or CBX7 (Gil et al., 2004). Consistent with this idea, BMI1 or CBX7 overexpression extends the replicative lifespan of human and mouse fibroblasts (Jacobs et al., 1999). I will discuss in detail the role of Polycomb in cellular senescence in the paragraph *4.3 Polycomb and cellular senescence.*

p16 is a CDK inhibitor that keeps Rb in an active, hypophosphorylated form. Also p21 can help in Rb activation. In this way the active form of Rb inhibits E2F from transcribing genes that are needed for proliferation, further enforcing cellular senescence (Sherr and McCormick, 2002; Sherr and Roberts, 1999).

However a recent study (Velimezi et al., 2013) revealed an additional regulatory interplay between the DDR apical kinase ATM and the downstream effector ARF. Indeed the authors demonstrated that ATM is suppressing ARF levels in a transcription independent manner by targeting ARF to ubiquitin-mediate proteosomal degradation. Furthermore in xenografts and tissue culture models, inhibition of ATM triggered the tumour-suppressive effects of ARF and loss of ATM expression correlated with increased ARF levels in human clinical samples. This study highlights the existence of a cross talk between ARF protein turnover and DDR signalling, and it reveals two pathways that lead to ARF induction: oncogene activation and ATM suppression. Thus, upon ATM suppression, the subsequent increased ARF activity results to be a secondary anti-tumor response that can start a positive feed back loop to boost the remaining active DDR signalling pathway ATR/Chk1 (Eymin et al., 2006; Velimezi et al., 2013).

2.3 Different types of cellular senescence

Cellular senescence occurs in response to different stimuli. According to this we can distinguish three main types of cellular senescence: replicative senescence; stress induced premature senescence (SIPS) including the subtypes culture shock-induced senescence and DNA damaging agents induced senescence; oncogene induced senescence (OIS).

Here we briefly discuss about the first types of cellular senescence, while we will dedicate an entire chapter to deeply discuss the feature of oncogene-induced senescence (OIS).

Replicative senescence results from exhaustion of cell proliferative capacity. Under optimal growth conditions, an intrinsic “clock” induces cell proliferation inevitably to stop. This "clock" is particularly sensitive to the number of DNA replication rounds performed. This can be ascribed to the so-called "end replication problem", whereby DNA polymerase cannot completely replicate DNA ends. Thus at each round of DNA replication, cells lose 50-200 base pairs of telomeric DNA. Given the correlation between telomere attrition and

proliferative exhaustion, telomere attrition was suggested as the cause of replicative senescence (Harley et al., 1990). Further studies demonstrated this hypothesis by introducing telomerase in normal human cells: this resulted in extended life-span and avoidance of senescence, at least *in vitro* (Bodnar et al., 1998).

Thus telomere shortening is the phenomenon that limits the proliferative lifespan of many human cell types. Cells undergo replicative senescence due to critically short telomeres. Senescence is determined by the generation of even one or few telomeres sufficiently short to induce the senescent signal (Hemann et al., 2001; Herbig et al., 2004). Progressive telomere shortening activates a strong DDR by direct recognition of few telomeres in the cell (d'Adda di Fagagna et al., 2003; Herbig et al., 2004). When telomere length goes below a certain threshold, telomeres are not anymore sensed as physiological chromosome termini but as DSBs. As a consequence, DDR is activated and DDR foci start to appear in the proximity to the telomeric DNA (d'Adda di Fagagna et al., 2003; Herbig et al., 2004).

DDR is necessary both in the establishment and maintenance of senescence. Indeed functional inactivation of components of DDR pathway, such as CHK2, p53 or p21 was sufficient to extend proliferation of cultured the human fibroblasts beyond their senescence limit (Bond et al., 1994; Brown et al., 1997; Gire et al., 2004).

In summary, progressive telomere shortening eventually causes chromosome ends to be recognized as DNA breaks, to activate a consequent DDR and to enforce senescence.

The concept of stress induced premature senescence (SIPS) derived from the observation that various cellular stresses could cause a premature senescence phenotype, is very similar to replicative senescence. Indeed SIPS and replicative senescence share molecular and cellular features. The main difference between these two phenomena is that replicative senescence is physiologically programmed and occurs when telomeres become critically short, while SIPS is not programmed and it occurs in response to external cellular stress. An important example of SIPS is the culture shock-induced senescence. When placed in

culture, explanted mouse embryonic fibroblasts (MEFs) stop proliferating after only 15-30 cell divisions. There is no evidence linking this proliferative block to telomere shortening below a critical length. Instead the loss of proliferative capacity seems to result from the non-physiological conditions that cell culture procedures include. Among them the disruption of cell-cell contacts, plating on plastic, lack of heterotypic interaction between different cell types, medium-to-cell ratio as well as hyperoxia. Oxygen sensitivity is the major determinant of culture shock-induced senescence and it shows critical differences between human and mouse cells. Mouse cells are more sensitive to oxygen tension than human cells. These differences can explain their differences in proliferation when placed in culture.

MEFs do not senescence under physiological (3%) oxygen conditions but do senescence in parallel cultures at 20% oxygen. The block in proliferation of MEFs at 20% oxygen has been ascribed to the activation of DDR (Di Micco et al., 2008). Even though human fibroblasts are less sensitive to oxygen tension, some human fibroblasts cell lines, when cultured at low oxygen tension, can achieve up to 20 population doublings more compared with counterparts grown at 20% oxygen.

Another example of SIPS is the DNA damaging agents-induced senescent. Treatment with IR creates DSBs that results in the activation of ATM-p53-p21 pathway within few hours from treatment, while p16 induction and SA-β-gal activity are observed only several days after IR treatment (Suzuki et al., 2006). Upon IR treatment distinct nuclear foci are formed at site of damage, also known as ionizing radiation-induced DNA damage foci (IRIF). They contains protein complexes devoted to DSBs recognition as well as mediator proteins, similarly to the ones observed in senescent cells with shortened and dysfunctional telomeres (d'Adda di Fagagna et al., 2003; Herbig et al., 2004). The main difference between replicative senescence and SIPS is that SIPS occurs without affecting telomeric shortening. Indeed IR does not seem to accelerate telomeric erosion. Moreover senescent induction is not prevented by expression of hTERT in different types of normal cells

undergoing SIPS (by IR or UV treatment or exposure to hydrogen peroxide). This reveals that DNA lesions can trigger senescence mediated by ATM-p53 pathway in a telomere-shortening-independent manner (Gorbunova et al., 2002). Furthermore it has recently been shown that IR-induced senescence is triggered by irreparable DNA damage at telomeres, independently of telomere shortening. Indeed this persistent telomeric DNA damage did not occur preferentially at critically short telomeres and the analyses were all made in quiescent cells - post-mitotic differentiated neuronal cells or contact inhibited cells – thus telomere length was not affected (Fumagalli et al., 2012).

The ability of DNA damaging agents, such as cisplatin and doxorubicin, to induce SIPS is exploited in various cancer treatments. SIPS is also triggered by the exposure to drugs inducing replication stress such as hydroxyurea, aphidicolin, or etoposide. Indeed, since replication stress induces replication fork to stall and some of the stalled forks can collapse, this leads to the generation of DSBs and the activation of the ATR/CHK1 pathway (Marusyk et al., 2007). The ability of several DNA damaging agents to induce *in vitro* a G1-restricted senescence in different cell types and in many cancer cell lines, indicates the existence of a basal senescence mechanism that is preserved, even though many cancer cell lines are known to carry severe genetic defects (Chang et al., 1999).

CHAPTER 3. Oncogene-induced senescence

3.1 General features of Oncogene-induced Senescence

Cellular senescence plays a central role in promoting a stable cell cycle arrest in response of various cellular stresses. Beyond the different types of senescence I discussed in the previous chapter, another type of senescence can result from the activation of an oncogene and is known as Oncogene-induced senescence (OIS). OIS was first observed *in vitro* in primary human and mouse cells, after the overexpression of oncogenic HRAS (HRASV12) (Serrano et al., 1997). Further studies revealed that the Raf-Mek pathway downstream of Ras is the most relevant in the induction of senescence (Lin et al., 1998; Zhu et al., 1998). These observations *in vitro* were then demonstrated *in vivo* using mouse models with inducible endogenous oncogenes (Collado et al., 2005).

The first compelling evidence for the occurrence of senescence *in vivo* was revealed in human nevi. Nevi are melanocytes that, due to the sustained $BRAF^{600}$ expression, underwent a permanent cell cycle arrest and display the typical features of senescence, such as induction of p16 and SA-β-gal activity (Michaloglou et al., 2005). Furthermore this was also the first demonstration of the association of cellular senescence with pre-malignant stages of tumorigenesis. Indeed human nevi are premalignant lesion that remain senescent for decades and hardly progress into malignant stages (melanoma) (Bennett, 2003; Chin et al., 1998; Robinson et al., 1998). This observation highlighted the fundamental role of oncogene-induced senescence as a tumor suppressive mechanism exploited by the cells to restrain the hyperproliferation induced by oncogene activation, ultimately leading to a permanent cell cycle arrest that blocks the progression towards cellular transformation and the consequent malignant stages. In this way OIS prevents the expansion of a pool of cells bearing an activated oncogene and prevents the formation of potential tumor.

The main players in this tumour-suppressive mechanism are DNA hyper-replication and DNA damage response (DDR). It is commonly thought that oncogene activation first induces DNA hyper-replication that then leads to the accumulation of DNA damage. This in turn triggers a robust DDR activation, which is responsible for the onset of senescence. In case of DDR deficient cells, senescence cannot be stably established and cells undergo uncontrolled proliferation leading to cellular transformation (Figure 2). Thus this model highlights a causative role of DNA replication in inducing DNA damage and DDR activation in cells undergoing OIS (Bartkova et al., 2006; Di Micco et al., 2006; Halazonetis et al., 2008).

In the following paragraphs, after the description of various oncogenes able to induce senescence, I will discuss in detail the molecular bases underlying OIS.

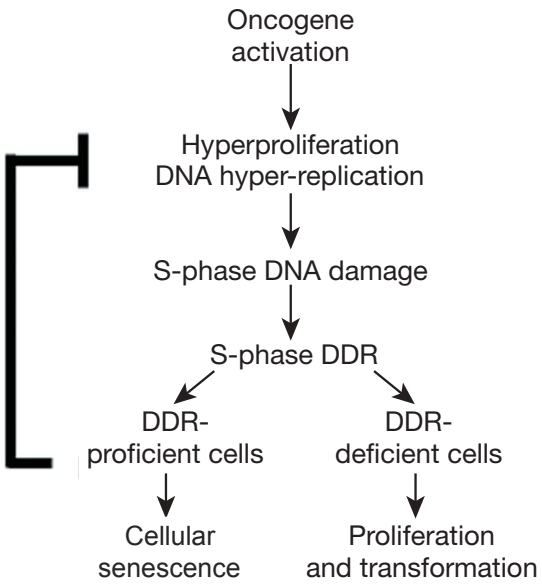

adapted from Di Micco et al 2006

Figure 2. Model of the events following oncogene activation.
Oncogene activation first induces cells to hyperproliferate by triggering DNA hyper-replication. This then leads to the generation of DNA damage. As the consequence of DNA damage, a robust DDR is activated, ultimately leading to senescence establishment. In case of DDR deficient cells, senescence cannot be stably established and cells undergo uncontrolled proliferation leading to cellular transformation. Adapted from (Di Micco et al., 2006).

3.2 Different oncogenes induce OIS

After the discovery of oncogenic Ras-induced cellular senescence, similar observations were obtained with other oncogenes, further confirming and extending the concept of OIS as a tumor suppressive mechanism (Evan and d'Adda di Fagagna, 2009).

Increased expression and/or activation of other members of the RAS mitogenic pathway, such as EGF receptor, RAC1, RAF, MOS and MEK can induce cellular senescence *in vitro*. (Bartkova et al., 2006; Debidda et al., 2006; Lin et al., 1998; Zhu et al., 1998). Furthermore, evidence for *in vivo* cellular senescence was demonstrated for some of these oncogenes (Collado et al., 2005; Collado and Serrano, 2010; Michaloglou et al., 2005).

On the other hand, loss of PTEN function, an inhibitor of RAS pathway, also leads to the establishment of cellular senescence. PTEN encodes for a dual protein and lipid phosphatase that antagonizes PI3K/AKT signalling, a downstream element in the RAS cascade that triggers responses important for tumor development. Furthermore, beyond induction of senescence *in vitro*, Pten deficient prostate cells undergo a p53-dependent senescence that limits tumorigenesis (Chen et al., 2005).

Coherent with the idea that RAS transduction pathways transmit their signals to the nucleus to control cellular proliferation, the triggering of a number of key nuclear-localized positive regulators of cell cycle progression has been shown to induce senescence: increased expression of E2F transcription factors, crucial regulators of G1/S cell-cycle transition, induces premature senescence (Johnson and Degregori, 2006).

Moreover CDC6, a DNA replication licensing factor, and CYCLIN E, a CDK modulator involved in DNA replication initiation, can both induce cellular senescence when ectopically expressed, with decline in BrdU incorporation rates and accumulation of SA-β-gal activity (Bartkova et al., 2006).

Consequently, the triggering of a cell-cycle progression stimulus, from extracellular signals down to DNA replication licensing, can result in a senescence outcome. It is

presently unclear whether these signals lie on a unique pathway or on separate converging ones.

3.3 Oncogene-induced DDR

The first evidence for a causative role of DDR activation in OIS establishment was demonstrated in two independent studies (Bartkova et al., 2006; Di Micco et al., 2006), revealing that the oncogene-induced DNA replication stress is a key effector of DDR activation. These discoveries were achieved by deeply characterising the effect of oncogenic RAS both *in vitro* in normal human fibroblast and *in vivo* in mouse models (Di Micco et al., 2006), or by analysing the effects of various oncogenes, such as Mos, Cdc6 and cyclin E *in vitro* and examining precancerous lesions for the presence of senescence cells - showing SA-β-gal activity - and DDR activation.

In normal human fibroblasts, oncogenic RAS activation leads to a first hyperproliferative burst, which is then followed by a slow down in the cells growth, due to the accumulation of DNA damage. This DNA damage in turn triggers a robust DNA Damage Response (DDR) activation, which is essential for the establishment and maintenance of a permanent cell cycle arrest known as Oncogene Induced Senescence (OIS; (Di Micco et al., 2006)). On the other hand, oncogenic Ras activation in DDR-deficient human fibroblasts - by the permanent CHK2 knock down (shCHK2) - does not lead to cellular senescence but induces cellular transformation. Indeed, when these cells are injected into nude mice, they induce tumor formation, which is not the case for DDR-proficient senescent cells (Di Micco et al., 2006). Similar results were obtained by knocking down ATM in a cell line carrying both endogenous copies of *ras* gene mutated and exhibiting constitutive activation of DDR and senescence (Bartkova et al., 2006). Furthermore the prevalence of senescence in preneoplastic rather than in neoplastic lesions (Bartkova et al., 2006) supports the idea of oncogene-induced senescence as a barrier to tumor progression.

These results revealed the importance of DDR activation in the establishment and maintenance of oncogene-induced senescence and the fundamental role of OIS as a tumor suppressive mechanism exploited by cells to avoid cellular transformation and progression into malignancy.

BOX1: DNA replication

Since DNA replication is one of the main aspects onto which oncogenic signalling converges, here I described the fundamental molecular steps that characterize and control normal DNA replication.

In all eukaryotes DNA replication is a tightly regulated process that guarantees proper duplication of genomic DNA ensuring chromosomal DNA being replicated only once per cell cycle (Vaziri et al., 2003). The origin recognition complex (ORC), a six-subunit complex, binds specifically to sites of DNA replication initiation, also known as DNA replication origins (ORI). During late mitosis and G1 phase, ORC tags the initiation sites for the recruitment of replication licensing factors, CDC6 and CDT1. Once at the initiation site, CDC6 and CDT1 coordinate the loading of the MCMs (Mini Chromosome Maintenance) complex with helicase activity on the origin. Once MCMs are loaded, a fully licensed pre-replication complex (pre-RC) exists. The Pre-RC is activated by recruitment of additional factors including MCM10, CDC45, SLD2-3, DPB11 and GINS complex. The initiation of DNA replication in S-phase additionally requires DBF4/CDC7 kinase and CDKs activity. Indeed CDKs stimulate DNA replication origin licensing by phosphorylating CDC6 and preventing its degradation and nuclear export at G1/S transition (Mailand and Diffley, 2005) and by recruiting CDC45, which in turn brings DNA polymerases to the origins. At this stage, DNA synthesis begins. Cells developed different mechanisms to ensure DNA being replicated only once per cell cycle. ORC, CDC6 and CDT1 are required for the loading of MCMs onto DNA. To avoid MCMs continued association on DNA, the downregulation of ORC, CDC6 and CDT1 at the end

of G1 phase effectively prevents re-licensing of DNA replication origins. Cyclin E and CDKs activity also limit the assembly of pre-RC complex to G1 phase by modulating the levels of key replication proteins. Furthermore, an inhibitor of the licensing system, GEMININ, binds tightly to CDT1, blocking its ability to bind MCMs. Failure of this mechanism leads to re-replication DNA damage accumulation. In mammals, variations in the expression of MCMs, CDC6, CDT1, GEMININ and CYCLIN E induces genomic instability and tumor development.

3.4 Oncogenes-induced DNA replication stress

DNA replication plays fundamental roles in OIS establishment. Indeed the DDR activation that is responsible for the induction of senescence is completely dependent on DNA replication: oncogene-expressing cells unable to undergo S phase - by aphidicolin treatment or contact inhibition - do not accumulate DDR (Di Micco et al., 2006).

Oncogenes act on a plethora of molecular pathways to promote uncontrolled cellular proliferation. Beyond the transcriptional activation of proliferative genes, c-Myc controls DNA replication by direct interaction with the pre-replicative complex, revealing a direct control of DNA replication dynamic (Dominguez-Sola et al., 2007). Oncogenic Ras up-regulates the expression of Cdc6 (Di Micco et al., 2006), a crucial positive regulator of DNA replication origin licencing. Indeed Cdc6, together with Cdt1, helps the loading of MCM (Mini Chromosome Maintenance) complex onto replication origin during G1, licencing the origin for firing in the subsequent S phase.

Therefore the upregulation of Cdc6 induces a specific phenomenon known as re-replication that consists in replication origins firing more than once per cell cycle (Takeda et al., 2005). This phenomenon leads to amplification of the genomic region close to the re-replicated origin and it can also induce DNA topological problems that can turn into DSBs, thus leading to genomic instability (Di Micco et al., 2006). Moreover also

overexpression of Cyclin E induces Cdc6, and overexpression of Cdc6 itself can induce cellular senescence (Bartkova et al., 2006), revealing that DNA replication dynamics are the central node onto which oncogenic signalling converges.

DNA combing experiments in DDR deficient cells (shCKH2) revealed that oncogenic Ras overexpression induces an increase in origin firing together with an increase asymmetric fork progression that stems from increased fork instability and fork pausing (Di Micco et al., 2006). In agreement with these results, also Cyclin E overexpression in U2OS leads to premature termination of DNA replication that can results in fork stalling or fork collapse and subsequent formation of DNA DSBs (Bartkova et al., 2006), and thus leading to genomic instability.

Further evidence that strengthens the link between oncogene-induced altered DNA replication and genomic instability derived from the analysis of single nucleotide polymorphism at common fragile sites upon oncogene activation. Fragile sites are genomic regions difficult to replicate, where replication forks slow down, especially upon limited nucleotide pools, and seem to be caused by the paucity of DNA replication origins inside fragile regions (Casper et al., 2002; Durkin and Glover, 2007; Letessier et al., 2011). The analyses revealed that upon oncogene activation Loss Of Heterozygosity (a measure of genomic instability LOH) is more likely to occur at fragile sites than in the rest of the genome (Bartkova et al., 2005; Di Micco et al., 2006).

Importantly, it was recently shown that mammalian telomeres present some of the typical features of fragile site. Fragile sites are genomic loci composed by repetitive sequences that challenge replication and display abnormal cytological patterns in metaphase chromosome upon replication stress. Therefore this discovery was achieved by metaphase spreads analysis and combing experiments in TRF1 knock out MEFs. Indeed most of chromatids of TRF1 KO showed irregular multiple telomeric patterns, often spatially detached from the chromatid end. These aberrant telomeres then correlate with increased

fork stalling and problems in telomere replication, further supporting the fragility of telomeres (Sfeir et al., 2009). Noteworthy, telomeres, when dysfunctional can promote cancer progression, most probably by inducing chromosomal instability (Chin et al., 2004; Rudolph et al., 2001). However the causative effect that makes telomeres dysfunctional in preneoplastic lesion - thus in presence of an active oncogene - have not been yet identified.

Taken together all these data indicate that oncogene activation is first causing a hyperproliferative burst that results in aberrant DNA hyper-replication and subsequent DDR accumulation.

However other studies revealed a much more complex interplay between altered DNA replication and DDR, where DNA damage itself is able to alter DNA replication dynamics. (Doksani et al., 2009; Ge et al., 2007; Petrini, 2009). Indeed upon DNA replication stress - induced by HU or aphidicolin treatment - dormant replication origins are activated to cope with the fork stalling and ensure S phase completion on time (Ge et al., 2007). In addition, DSB can activate DNA replication events. Indeed the induction of a single DSB in the entire yeast genome is able to induce the firing of DNA replication origins in the immediate vicinity of the break (Doksani et al., 2009; Petrini, 2009). Even though the signal that produced the effect of origin firing has not been discovered yet, these findings further highlight the complexity of the dynamics interconnecting oncogene activation, DNA replication, and DNA damage.

3.5 Possible mechanisms underlying oncogene-induced DNA replication stress

Growing evidence for the complexity of the molecular processes involved in oncogene-induced DNA replication stress is demonstrated by recent studies that are trying to dissect the mechanisms by which oncogene-induced replication stress is inducing DNA damage, leading to genomic instability.

Recent reports suggest that dNTP pools play a fundamental role in oncogene-induced

replication stress. Indeed it has been proposed that cyclin E overexpression leads to depletion of the dNTP pools that results in replication stress and increased fork stalling. The dNTP pool depletion is due to increased active replication origins: the consumption of dNTPs is faster than their biosynthesis, thus as cells run out of dNTPs, replication fork stall more easily due to the lack of the right complementary dNTP to be incorporated in the DNA. Moreover upon dNTP pool depletion the chances to induce mutation due to the incorporation in the DNA of the wrong dNTP is higher, thus further leading to genomic instability (Bester et al., 2011). The importance of dNTP pools in oncogene-induced replication stress has been also demonstrated in a recent report showing that oncogenic Ras expression downregulates RRM2 - a key enzyme involved in the dNTP pool biosynthesis - already after 24 hour from oncogenic Ras infection. Furthermore RRM2 downregulation itself is sufficient to induced replication stress and subsequent OIS establishment (Aird et al., 2013). Thus dNTP pools depletion occurring upon oncogene activation depends both on increased consumption due to increased DNA replication as well as on the lack of *de novo* biosynthesis. However the oncogene-mediated downregulation of dNTP biosynthesis is a bit counterintuitive: if the oncogene is inducing cells to replicate more, why should it block the synthesis of dNTPs, essential compounds for replication? Further studies are needed to elucidate this novel and unprecedented aspect.

Other studies revealed that oncogene-induced replication stress lies on an increased topological stress that results in unusual replication intermediates entering mitosis, thus leading to genotoxic stress (Neelsen et al., 2013).

Collision of replication and transcription machinery is another possible mechanism underlying the oncogene-induced replication stress, and there is growing evidence supporting this hypothesis. As shown in (Jones et al., 2013) cyclin E overexpression leads to an increase in replication initiation that results in higher frequency of collision of replication-transcription machinery. The collision leads to fork breakage and increase DNA damage that is mainly resolved by homologous recombination. Furthermore the

replication stress resulted to be dependent on transcription: indeed transcription inhibition was sufficient to prevent DNA damage caused by oncogene-induced replication stress (Jones et al., 2013). These data are in line with the results presented in (Barlow et al., 2013), where DNA replication stress is shown to affect mainly early replicating and actively transcribed gene clusters. The approach used allowed the mapping of the DNA regions that were coupled with DNA damage upon replication stress, induced both by HU treatment as well as by oncogene activation. Interestingly, both replication stresses induced DNA damage at the same DNA regions, which were characterized by gene clusters actively transcribed and early replicating. The authors propose a new concept of fragile sites, differing from common fragile sites (CFS): early replication fragile sites (ERFS). ERFS are sites located in actively transcribed regions, thus with an open chromatin configuration. They are early replicating regions, showing high density of DNA replication origins, together with a high G-C content (Barlow et al., 2013). CFS consist in very large genes characterized by a condensed chromatin configuration. They are late replicating regions, with low density of replication origins, with a high A-T content. Moreover their sequences are prone to form secondary structures, thus impeding proper fork progression through the locus (Ozeri-Galai et al., 2012). Common to both ERFS and CFS is the fact that they are protected by ATR kinase activity, and their DNA lesions are mainly repaired by homologous recombination (Barlow et al., 2013). Furthermore, they are both subjected to oncogene-induced replication stress. The reason for the replication stress-induced instability of CFS lies on the oncogene-induced increase in origin firing and the resulting reduced fork speed: this would hamper replication completion in those regions, such as CFS, with few replication origins and challenging sequences to replicate. Instead at ERFS, the increase in active origins in actively transcribed regions would increase replication-transcription collision thus inducing fork stalling and ERFS instability (Barlow et al., 2013; Mortusewicz et al., 2013).

The complex mechanisms underlying oncogene-induced replication stress highlight the

importance of the coordination between DNA replication and transcription, in order to prevent genomic instability. Cells exploit various mechanisms to coordinate DNA replication and transcription to avoid their collision. For example Sen1/Senataxin helicase allows efficient progression of the DNA replication machinery through transcribed genes by removing RNA/DNA structures (Alzu et al., 2012). Furthermore topoisomerase I was previously found to be critical for preventing the formation of RNA-DNA hybrids and maintaining efficient replication fork speed through transcribed genes (Tuduri et al., 2009).

3.6 Oncogene-induced Reactive Oxygen Species production

Reactive oxygen species are highly reactive compounds that are formed upon incomplete reduction of oxygen. They include superoxide anion (O_2^-), hydrogen peroxide (H_2O_2) and the hydroxyl radical (HO·). O_2^- is produced by NADPH as a by-product of respiration. H_2O_2 exert its toxicity by its reduction to (HO·) by metal-catalysed Fenton chemistry. ROS are highly toxic to cells, since they induce lipid peroxidation, DNA and amino acid oxidation. Cells developed homeostatic pathways to keep these compounds at physiological levels. These pathways lead to the activation of specific enzymes, like superoxide dismutase (SOD), glutathione peroxidase (GPx), and catalase, devoted to the clearance of unbalanced ROS levels. However, the imbalance between the production of ROS and the capacity of cells to counteract them induces oxidative stress (D'Autreaux and Toledano, 2007).

Beyond their toxicity there is growing evidence demonstrating that ROS are also essential intracellular second messengers. Indeed the existence of motifs sensitive to the redox status - such as metal co-factors and cysteine residues in phosphatases and kinases - in many cell cycle regulatory proteins suggests that oscillations in intracellular redox state could have a crucial role in regulating progression from G0/G1 to S- to G2- and M- cell cycle phases (Menon and Goswami, 2007). Moreover ROS help in activating the mitogenic and growth

factor signalling required for progression through the cell cycle by various mechanisms. For example H2O2 production results in tyrosine phosphorylation and activation of EGF receptor (Gamou and Shimizu, 1995). $O2^-$ activates PKC enzyme inducing disulphide bond formation (Knapp and Klann, 2000). Furthermore, the control of signal transduction by oxygen species through reversible phosphotyrosine phosphatase inhibition is a widespread and conserved component of the biochemical machinery that is activated by RTKs (Chiarugi and Cirri, 2003).

Oxidizing agents can also impact on tumor suppressors: cysteine redox modifications regulate p53 DNA binding activity (Rainwater et al., 1995) and H_2O_2 exposure leads to reversible formation of ARF oligomers involving three critical cysteines (Menendez et al., 2003). Similarly, expression and phosphorylation of Rb protein is redox regulated in human natural killer cells and fibroblasts treated with thiol antioxidants (Menon et al., 2003). Moreover H_2O_2 exposure can directly induce disulfide bond formation between two ATM monomers, leading to ATM activation also in absence of DNA DSBs and MRN complex (Guo et al., 2010).

Furthermore transformed cells produce elevated levels of ROS, including hydrogen peroxide. The use of antioxidant can inhibit tumor cell proliferation, pointing to a crucial role of ROS in mediating loss of growth control, highlighting ROS functions as mitogenic signalling compounds (Behrend et al., 2003). Interestingly, various independent studies demonstrated the presence of a direct link between oncogene activation and an increased production of ROS. Indeed it has been reported that the expression of MYC in human fibroblasts increases levels of intracellular ROS (Vafa et al., 2002). In addition, it has been demonstrated that RAS activation induces the production of ROS and that Ras-induced ROS play mitogenic functions crucial for cellular transformation. Treatment with the ROS scavenger N-acetyl-cysteine (NAC) completely inhibited the mitogenic activity of oncogenic Ras-expressing cells, further supporting the role of ROS as mitogenic signalling molecules that fuel Ras-induced hyperproliferation (Irani et al., 1997). There is some

evidence that at least in some cells, ROS production by oncogenic RAS proceeds through a PI3K and RAC-dependent pathway (Cho et al., 2002; Sundaresan et al., 1996) and the subsequent regulation of a cytosolic NADPH-dependent oxidase (NOX). However little is known about the pathway that Ras regulates to induce ROS production and further studies need to be undertaken to unveil the mechanisms exploited by ROS to promote proliferation.

Furthermore the mechanisms that underlie ROS-induced DNA damage upon oncogene activation are not yet clear. ROS-induced DNA damage could be a consequence of ROS toxicity that induces spurious DNA damage, or it could depend on ROS acting like mitogenic molecules thus mediating oncogene-induced replication stress.

CHAPTER 4. Role of Polycomb in cancer and senescence

4.1 Polycomb group protein: epigenetic control of cell identity and cellular proliferation

Polycomb group proteins (PcG) were first discovered in *Drosophila melanogaster* for their ability to induce, when mutated, homeotic transformations (Kennison, 1995; Orlando and Paro, 1995; Schwartz and Pirrotta, 2008; Simon, 1995; Simon and Kingston, 2009). Indeed mutations in Polycomb group genes are able to induce spatial-temporal deregulation of homeotic genes expression, leading to developmental defects (Simon and Kingston, 2009). A second class of developmental regulators that counteract the effects of PcG mutations is Trithorax Group proteins (TrxG). PcG and TrxG proteins act on common regulatory pathways and play a crucial role in maintaining a pre-set active (TrxG) or repressed (PcG) transcriptional state during development (Kennison, 1995; Orlando and Paro, 1995; Simon, 1995). PcG and TrxG proteins are chromatin-modifying factors that play essential roles in regulating the cellular epigenetic status, modifying the chromatin surrounding their association sites (Morey and Helin, 2010; Sparmann and van Lohuizen, 2006). TrxG act as global inducers of epigenetically active states, which is balanced by an antagonistic repressed state mediated by PcG proteins.

PcG proteins are highly conserved in evolution and consist in two biochemically distinct multiprotein complexes known as Polycomb Repressive Complex (PRC) 1 and 2 (Morey and Helin, 2010). The PRC1 complex consists of a large number of subunits with different biochemical proprieties (Ring, Chromo and Zinc finger domains; (Morey and Helin, 2010)) The minimal components of PRC1 complex than ensure *in vitro* PRC1 activities are Polyhomeotic (Ph), Polycomb (Pc), Posterior Sex Comb (PSC) - which include the proto-oncogene BMI1 - and RING1 (Francis et al., 2001; King et al., 2002; Shao et al., 1999).

The essential components of PRC2 complex are the three PcG proteins EZH2, EED and SUZ12 and the histone binding proteins RbAp46/48 (Cao and Zhang, 2004; Czermin et al.,

2002; Kuzmichev et al., 2002; Muller et al., 2002). KO mice for *EZH2*, *EED* and *SUZ12* show embryonic lethality during gastrulation (Faust et al., 1998; O'Carroll et al., 2001; Pasini et al., 2004), further supporting the fundamental role of PRC2 complex in development.

The catalytic subunit of PRC2 complex, namely EZH2, mediates the di- and tri-methylation (me2/me3) of lysine (K) 27 of histone H3 (Cao et al., 2002; Czermin et al., 2002; Kuzmichev et al., 2002; Muller et al., 2002) with the help of EED and SUZ12 (Cao and Zhang, 2004; Pasini et al., 2004). This epigenetic mark - H3K27me3 - is essential for PRC1 binding to the same target sites (Cao et al., 2005). Indeed, the chromo-domain proteins of the PRC1 complex (CBX4, CBX6, CBX7 and CBX8) mediate PRC1 recruitment to the target sites by binding H3K27me3 (Bernstein et al., 2006; Cao et al., 2002; Kuzmichev et al., 2002). Once at the target sites, PRC1 mediates ubiquitylation (ubq) of histone H2A K119 through the ubiquitin ligase activity of RING1B (Wang et al., 2004). This results in a stable transcriptional repression possibly through chromatin compaction and inhibition of SWI/SNF chromatin remodelling activity (Francis et al., 2004; Francis et al., 2001).

4.2 Polycomb and cancer

The identification of BMI1 as a proto-oncogene that cooperates with MYC to promote B- and T-cell lymphomas (Haupt et al., 1991; van Lohuizen et al., 1991), gave the first evidence for the involvement of PcG gene family in cancer development. Together with BMI1, EZH2, the catalytic subunit of the PRC2 complex, is the best-characterized PcG protein in human cancer. EZH2 has been identified as a direct downstream target of the pRB/E2F pathway and one of the most frequent over-expressed genes in malignant prostate cancer (Bracken et al., 2003; Varambally et al., 2002).

Also other PcG proteins, like BMI1, RING1B and CBX7 are highly overexpressed in malignant prostate cancers (Bernard et al., 2005; van Leenders et al., 2007). The overexpression of PcG proteins has been ascribed to deregulation of pRB/E2F pathway, as

well as specific amplification of *BMI1* and *EZH2* loci. EZH2 overexpression promotes prostate cancer development by silencing ADRB2, a ß-adrenergic receptor. Indeed loss ADRB2 expression induces cell invasion in benign prostate cells, whereas its constitutive expression counteracts the metastatic and proliferative effects induced by EZH2 overexpression. This regulatory pathway is common also to a model for mammary epithelial cellular transformation (Yu et al., 2007).

Indeed PcG proteins were also found highly overexpressed in breast cancers (Bracken et al., 2003; Collett et al., 2006; Kleer et al., 2003). High EZH2 expression in preneoplastic mammary lesions suggests deregulation of PRC2 activity as an early event in breast cancer development (Ding et al., 2006). EZH2 overexpression in breast cancer is associated with bad prognosis and correlates with metastatic sporadic and familial breast tumours (Ding et al., 2006; Kleer et al., 2003). BMI1 is also found overexpressed in breast cancers and it correlates with MYC expression. EZH2 resulted to be essential for the proliferation of BRCA1 -/- cells (Puppe et al., 2009), and BMI1 overexpression, in cooperation with H-Ras, caused MCF10A breast epithelial cells transformation (Hoenerhoff et al., 2009).

EZH2 and BMI1 are also highly expressed in glioblastoma (Abdouh et al., 2009; Godlewski et al., 2008; Korur et al., 2009; Suva et al., 2009). The proliferation of glioblastoma cells was blocked by downregulating EZH2 or BMI1 expression (Abdouh et al., 2009; Suva et al., 2009), further highlighting the role of PcG protein in cancer development.

EZH2 and BMI1 are also involved in lung tumor development. EZH2 has been found highly expressed in Squamous Lung Cell Carcinoma (SLCC) together with BMI1 and Ki67 (Breuer et al., 2004). Furthermore in Non-Small Cell Lung Cancer, BMI is required for K-RAS induced tumorigenesis *in vivo*, and plays its tumorigenic role by repressing the INK4b-ARF-INK4a locus ((Dovey et al., 2008); discussed later in paragraph *4.3 Polycomb and cellular senescence*).

Several other tumours are characterized by a significant increase in EZH2 and BMI1 expression. This suggests that deregulation of PcG proteins is a common feature of transformed cells. Other tumours that show an overexpression of EZH2 and BMI1 include Oral Squamous Cell Carcinomas (Kang et al., 2007; Kidani et al., 2009), Hepatocellular Carcinomas (Sasaki et al., 2008; Steele et al., 2006), gastrointestinal cancers (Cai et al., 2010; Mimori et al., 2005; Tateishi et al., 2006), osteosarcomas (Sasaki et al., 2010) and bladder tumours (Arisan et al., 2005; Raman et al., 2005; Shafaroudi et al., 2008; Weikert et al., 2005).

4.3 Polycomb and cellular senescence

INK4b-ARF-INK4a locus is one of the best-characterized PcG target in mammals (Bracken et al., 2007; Dietrich et al., 2007; Jacobs et al., 1999). *INK4b-ARF-INK4a* locus encodes for three fundamental tumor suppressors: $p15^{INK4b}$, $p19^{ARF}$ ($p14^{ARF}$ in humans) and $p16^{INK4a}$ (Gil and Peters, 2006). $p14^{ARF}$ binds to MDM2 blocking its ability to degrade p53. Stabilization of p53 leads to transcriptional activation of the Cyclin/CDK inhibitor p21 resulting in anti-proliferative and pro-apoptotic effects (Gil and Peters, 2006). $p16^{INK4a}$ and $p15^{INK4b}$ bind to Cyclin/CDK complexes blocking CDK mediated phosphorylation of the Retinoblastoma protein pRB, thus inhibiting cell cycle progression. Loss of function of any of these proteins prevents cells to undergo cellular senescence and promotes cellular proliferation (Gil and Peters, 2006).

PcG proteins maintain *INK4b-ARF-INK4a* locus transcriptionally repressed through the specific association of PRC1 and PRC2 to the $p16^{INK4a}$ promoter (Bracken et al., 2007; Dietrich et al., 2007).

Various studies revealed that loss of PcG functions correlates with activation of *INK4b-ARF-INK4a* expression resulting in cellular senescence (Bracken et al., 2007; Dietrich et al., 2007; Gil et al., 2004; Jacobs et al., 1999). BMI-1 deficient mouse embryonic fibroblasts (MEFs) show a dramatic proliferative block together with a strong activation of

$p15^{INK4b}$, $p19^{ARF}$ and $p16^{INK4a}$ (Jacobs et al., 1999). Also upon loss PRC2 members, like EZH2 or SUZ12, the *INK4b-ARF-INK4a* locus is actively expressed leading to premature senescence in mouse and human cells (Bracken et al., 2003; Pasini et al., 2004). Furthermore *Ink4a-Arf* inactivation can rescue Ring1B-/- mice embryonic lethality from E9.5 to E11.5 (Voncken et al., 2003), and it can partially rescue developmental defects of Bmi1-/- mice (Bruggeman et al., 2005). These results revealed the physiological relevance of PcG regulation of *Ink4a-Arf* locus. However a recent study demonstrated a role of PcG proteins in cellular proliferation that is independent of *Ink4a-Arf* expression. Indeed, loss of INK4A-ARF cannot rescue developmental defects of *Bmi1* KO mice, which are instead rescued by genetic inactivation of Chk2, independently of *Ink4a-Arf* repression (Liu et al., 2000). In agreement with these findings, no clear correlation between *INK4b-ARF-INK4a* repression and overexpression of PcG proteins has been found in human tumours. For example, no correlation between BMI1 and $p16^{INK4a}$ expression was found in different haematological malignancies (van Galen et al., 2007). Moreover, in a mouse model for lung cancer, BMI1 represses the *INK4A-ARF* locus during K-ras^{G12D} driven transformation (Young and Jacks, 2010) whereas hepatocellular carcinomas and transformation of MCF10A mammary epithelial cells by co-expression of RAS and BMI1 have no effect on INK4A-ARF expression (Hoenerhoff et al., 2009). All together these findings highlight the importance of PcG mediated *INK4A-ARF* repression in development and carcinogenesis, but they also reveal the existence of additional regulatory pathways mediated by PcG that are independent *INK4A-ARF* repression.

4.4 Polycomb and DNA replication

Growing evidence for a role of Polycomb group proteins on S phase progression and, more directly, on DNA replication has been recently shown from independent studies. Indeed, in absence of SUZ12, serum starved quiescent human fibroblasts show impairment in cell cycle re-entry as measured by BrdU incorporation (Pasini et al., 2004), suggesting an

involvement of PRC2 in G1/S progression. Furthermore, during DNA synthesis PcG proteins can stay attached to chromatin (Francis et al., 2009) and PRC2 subunits have been localized at sites of ongoing DNA replication (Hansen et al., 2008). These results support the hypothesis of a direct role of PcG on DNA replication. However the molecular mechanisms underlying the interplay between PcG proteins and DNA replication are still poorly understood.

DNA Molecular Combing: Technology set up

1. Complexity of DNA replication dissected by DNA molecular combing

DNA replication is a tightly regulated process that at each cell cycle ensures the efficient duplication of the entire genome. In metazoan, especially in mammalian cells, the elements involved in DNA replication are still poorly characterised.

The development of single molecule assays to study DNA replication dynamics has been one of the major improvements in the field. Namely DNA molecular combing has proven to be one of the most powerful technologies to address the complexity of DNA replication process at whole genome level *in vivo*.

Since the aim of my PhD project is to understand how oncogene activation alters DNA replication, I set up DNA molecular combing technology in my Institute. In this section I explain all the steps I have undertaken to make DNA molecular combing a proficient technology for my scientific purposes.

2. DNA molecular combing: physical forces to stretch the genome for High-resolution studies

DNA molecular combing exploits the physical force between air/water meniscus and the coverslips interface that occurs when the coverslips is pulled out from the DNA solution. This process allows for DNA molecules to become attached by their extremities to the silane-coated glass slide, and to be orderly stretched on the glass slide (Bensimon et al., 1994; Michalet et al., 1997) (Figure 3). This technique can be applied to different type of genomic studies (Caburet et al., 2002; Lebofsky and Bensimon, 2003). It is possible to apply FISH on combed DNA, by using specific fluorescent probe for the genomic locus of interest. This allows to physically mapping the locus of interest, as well as detecting micro and gross chromosomal rearrangements such deletion (Michalet et al., 1997) and amplifications (Gad et al., 2001a; Gad et al., 2001b).

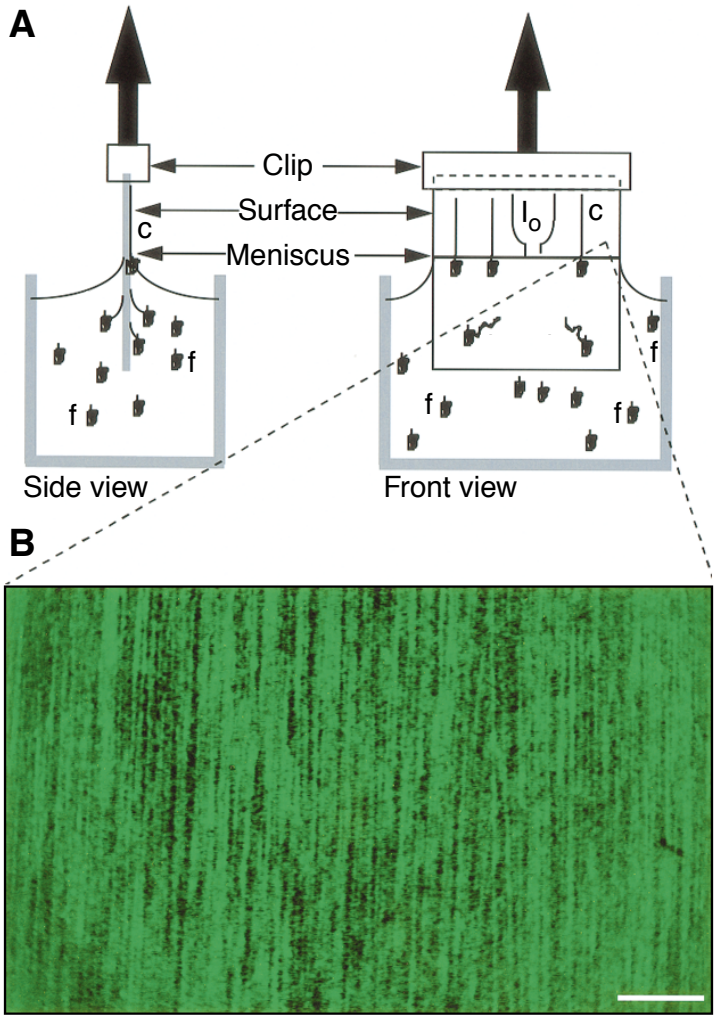

adapted from Michalet, et al 1997

Figure 3. DNA molecular combing of genomic DNA.
(A) DNA molecular combing apparatus is made of a vertically moving clip to which a silinised coverslip is attached. Coverslips are then dipped at a constant velocity of 300 μm/s into the reservoir containing the DNA solution of interest. DNA molecules (f) in the solution bind to the coverslip surface by their extremities. After 5 minutes incubation, the coverslip is pulled out of the DNA solution. In this way the DNA molecules anchored to the surface are moved upward together with the coverslip surface. The meniscus air/water exerts a localized constant and downward vertical force on the coiled DNA molecules attached to the coverslip. In this way the coiled molecules are gradually unwound and stretched on the dry part of the surface, irreversibly binding to it (c). (B) Representative image of combed human genomic DNA observed at epifluorescence microscope. Adapted from (Michalet et al., 1997).

DNA replication can be studied by fluorescent detection of thymidine analogues incorporated on combed DNA molecules. Moreover, by coupling FISH and detection of incorporated nucleotide analogues, it is possible to monitor the DNA replication at a specific locus of interest (Caburet et al., 2002; Lebofsky and Bensimon, 2003).

As for the study of DNA replication dynamics, the technique involves various steps:

1. Preparation of coverslips coated with thrichlorosilane;

2. Pulse labelling the cells with thymidine analogues and embed them in low-melting agarose plugs;

3. Preparation of a DNA solution deriving from pulse labelled cells.

4. Performing DNA molecular combing of the DNA solution prepared with the use of a specific combing apparatus produced by Genomic Vision.

5. Whole genome studies: immunofluorescence against the incorporated thymidine analogues.

6. Site specific studies: coupling FISH to the staining for thymidine analogues.

7. Image acquisition.

8. Image analysis: measurement of replication signals.

9. Image analysis: interpretation of replication signals.

To properly set up this technology I went through each one of these steps and I optimized the state of art of the protocols that are used at each phase of DNA molecular combing in different laboratories to optimize them in my hands.

2.1 Preparation of coverslips coated with thrichlorosilane

DNA molecules bind irreversibly to the glass slide only when the glass is chemically modified to obtain a hydrophobic surface onto which DNA extremities binds during the DNA molecular combing process.

Thus the production of the high quality coated glass slides becomes of primary importance. Given the fact that at the beginning of my PhD the coated glass slides for DNA combing experiments were not yet commercially available, I try to produced them in collaboration with Marcella Chiari, at the University of Milan following an adapted version of the protocol described in (Labit et al., 2008).

They used an optimized liquid-phase silanization method that utilizes a novel combination of silane/solvent. The chemicals used in the silanization process must be of the highest quality to ensure a good quality of silanized glass slides. We used ethanol and chlorophorme purchased from Carlo ERBA. As silane compound we used 7-octen-1-yl-Trimethoxysilane (Catalog no. 452815), purchased from Sigma-Aldrich. We used 22×22mm glass slides purchased from Esco (Portsmouth, VA, USA).

The steps involved in the silanization consist in:

1. Cleaning the coverslips prior to silanization;

2. Overnight silanization;

3. Post-silanization cleaning.

Before proceeding for silanization, coverslips needs to be cleaned and free from organic residues to ensure homogeneous silane coating over the surface. There are mainly three different cleaning procedures, one involves piranha solution, which contains hazardous organic solvents; the other two are safer and are based on the use of plasma cleaner or UV-ozone cleaner. In our case we used UV-ozone cleaner. Briefly coverslips were washed three times in ethanol and dried with Argon. Then coverslips cleaning was performed by incubation in the UV-ozone cleaner for 10 min. Then the coverslips were incubated with silane overnight. Briefly, (7-octen-1-yl) trimethoxysilane was diluted 1:1000 in n-heptane. Dried coverslips were rapidly transferred into the silane solution without rehydration and kept overnight in a desiccator, under a chemical hood. After silanization, coverslips were transferred into n-heptane and sonicated for 5 min. Coverslips were moved one by one into distilled water and sonicated for another 5 min in distilled water. Coverslips were recovered and dried before a 5-min final sonication in chloroform. To test the hydrophobicity of the silanized coverslips, a drop of water on a silanized coverslip will form a characteristic round drop, unlike on an untreated surface.

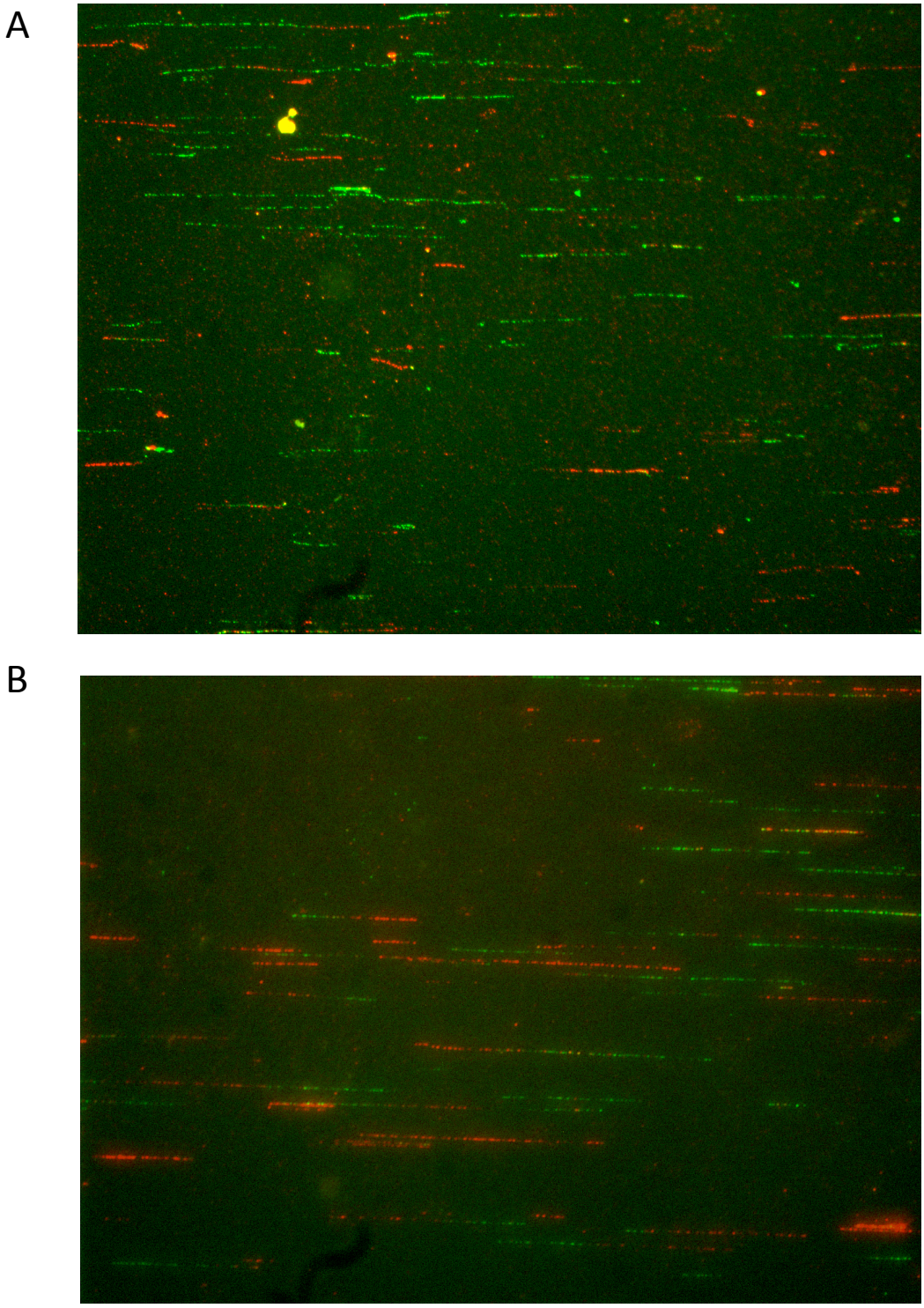

Figure 4. DNA fibers are better stretched on commercially-available silanized coverslips compared with home made ones.
DNA molecular combing was performed using a DNA solution coming from cells pulsed labeled with thymidine analogues. After immunodetection (IdU green, and CldU red), I assessed the level of DNA stretching, fiber length and fiber density on coverslips silanized by us (A) or made commercially available by Genomic Vision (B).

We tested the quality of these silanized coverslips by performing DNA molecular combing. The DNA attached to the glass slide even tough it was a bit waved (Figure 4A).

So as this coated glass slides became commercially available we tested then. As show in Figure 4, DNA is better stretched on coverslips produced by Genomic Vision (Figure 4B) as respect to the coverslips we produced (Figure 4A). Thus we stop producing them ourselves and we started purchasing them from Genomic Vision for the rest of the project.

2.2 Pulse labelling the cells with thymidine analogues and embed them in low-melting agarose plugs

DNA molecular combing allows for the visualization and the study of DNA replication dynamics occurring *in vivo* at the single DNA molecule level. To accomplish this, cells needs to be pulse labelled with analogues of thymidine, such as BrdU (Bromodeoxyuridine), IdU (Iododeoxyuridine) and CldU, (Clorodeoxyuridine). According to the specific need, one can decide whether to label the cells with a single pulse, BrdU, or to label them with two successive pulses, IdU and CldU. Pulse labelling cells with two analogues allows for the analysis of more replication parameters than in the case of labelling with a single analogue. Indeed, double labelling allows for the precise evaluation of for the symmetry of fork progression, interorigin distances, which can only be inferred in case of single labelling. Therefore in all of my combing experiments I decided to perform double labelling with thymidine analogues.

Another important aspect of the labelling is the time of incubation with the thymidine analogues, which depends on the doubling time of the cells. Usually the incubation time with thymidine analogues ranges from 15 to 30 minutes, but it can also reach 1 hour in case of slow replicating cells. It is very important to remember that the incubation time with modified nucleotides has to be really precise in order to have accurate measurements.

When studying DNA replication at specific genomic loci it is crucial to optimize the labelling protocol in order to maximize the probability to have the locus of interested replicated during the pulses. To this regard I set up a protocol of pulse and chase for the study of DNA replication dynamics at telomeres, by adapting the protocol used in (Sfeir et al., 2009). Briefly, I performed 3 rounds of pulse and chase, with 1 hour pulse labelling and 3 hours of chase. More precisely, 1 hour incubation with IdU, 1 hour incubation with CldU followed by 3 hours of chase, repeated for 3 times. The total duration of the three rounds of pulse/chase was 12 hours, which is less than the cell doubling time. Since this labelling procedure last less than a cell cycle, I am confident that cells already labelled at the beginning of the procedure will not be re-labelled at the same genomic loci.

Another key point in the labelling is the concentration at which thymidine analogues are used. In some protocols they are used at the same concentration, while in others the thymidine analogue of the second pulse is used at a higher concentration than the first analogue (1^{st} 25um vs 2^{nd} 200um). In the case of equal concentration, cells are extensively washed – 3 fast washes with PBS - between 1^{st} and 2^{nd} pulse, to ensure that the first analogue is washed away and so to proceed with the second pulse. However this procedure can more easily introduce errors in the incubation time, and it does not ensure a complete wash out of the analogue, also because the analogue is usually transported into the nucleus and the washing with PBS is not enough to wash away the nuclear thymidine analogues. Therefore other protocols optimized the washing step reducing it to a single fast wash with PBS. After this fast wash, the second labelling is performed using the thymidine analogue at a much higher concentration (8 times higher) than the analogue used in the first pulse, putting the two analogues in competition for the incorporation in the DNA. In this way, due to the higher concentration, the second analogue is winning the competition over the first analogue, reducing the probability of the first analogue that was not washed away, to be incorporated in the DNA during the second pulse.

A

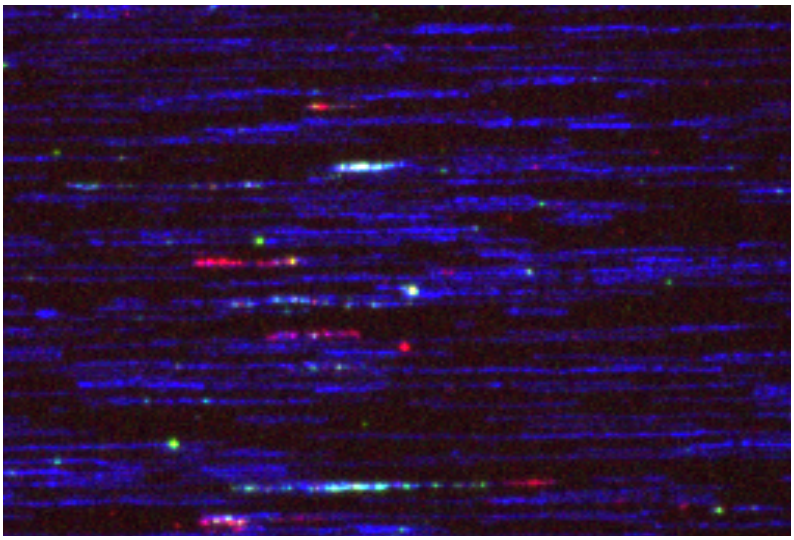

B

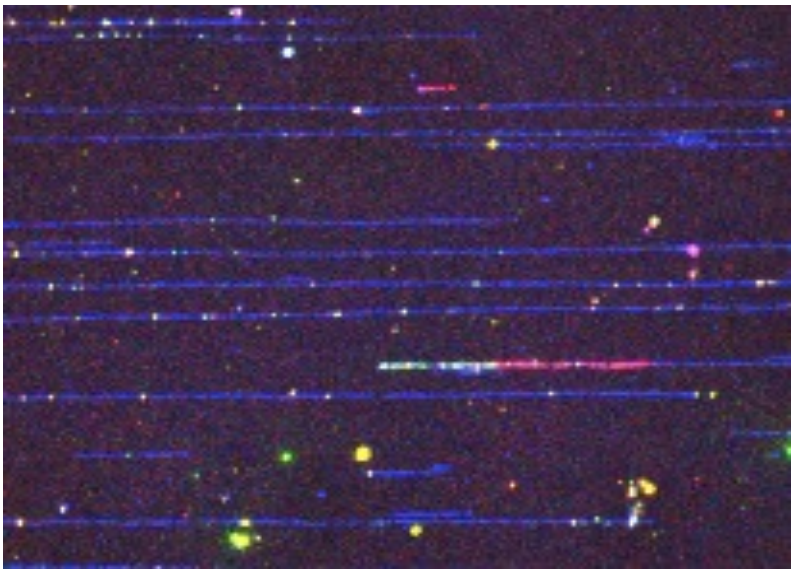

Figure 5. Optimal DNA fiber density derives from ~ 45*103 cells/plug.
DNA molecular combing was performed using a DNA solution coming from cells pulsed labeled with thymidine analogues. After immunodetection (IdU green, CldU red and ssDNA blue), I assessed the level of DNA fiber density of DNA solution derived from $250*10^3$ cells/plug (A) or $45*10^3$ cells/plug (B).

Once the cells are labelled, they need to be embedded in low-melting agarose plugs. The amount of cells per plugs is critical to obtain an optimal DNA fiber density on the slide. Thus it is very important to find the proper range of cells per plug, in order to obtain the ideal fiber density. According to various protocols the number of cells per plug can range from $45 \cdot 10^3$ to $250 \cdot 10^3$ (Bianco et al., 2012; Schurra and Bensimon, 2009). Thus I tested the two concentrations for the density of DNA fibers. As shown in Figure 5 the optimal concentration is the lowest one ($45 \cdot 10^3$ cells/plug). Indeed with 250 thousands cells the

number of fibers is so high that most of they often overlap, thus rendering the analysis unfeasible. With the lowest concentration of cells, DNA fibers on the coverslip are at a proper density that allows for the analysis of DNA replication signals.

The step involved in agarose plugs preparation is crucial and everything must be handled with care. After the labelling, cells are trypsinized and resuspended in cold PBS to slow down DNA replication. Cells are then centrifuged 5 minutes at 1200 rpm, while counting cells (from 10µl of cell culture) and calculating the amount of plugs you can obtain. Supernatant should be removed as much as possible (decantation and pipetting). To avoid clusterization of the cells, a cold PBS/trypsin mixture is added to the tube (corresponding to 45µl for one plug). The cell pellet is resuspended very gently by pipetting 10 times with P100 or 200-micropipette (with yellow cone). Then 1.2% low-melting point agarose solution (equal volume to PBS/trypsin) is added to the cell suspension while the tube of agarose is also immersed in 50°C water bath to avoid agarose solidification. Before mixing cell suspension to agarose you should leave the cell suspension at 37°C also to avoid agarose solidification before pouring it in the plug molds. The cell/agarose mixture is again mixed gently by pipetting 10 times with P100 or 200-micropipette (with yellow cone). The mixture is then poured immediately into gel plug mold (about 90 µl for each well). The poured gel plug mold is cool down immediately in a fridge for 30 min. This passage is important to avoid that the cells fall down in the plug due their higher density respect to agarose. Before storing the agarose plugs, they need to be incubated with Proteinase K to degrade all the proteins and leave just DNA inside the plugs. This deproteinization step occurs with an overnight incubation of the plugs into pre-warmed ESP solution - 2mg/ml Proteinase K, 1% sarcosyl in EDTA (0.5M, pH 8.0), 250µl for one DNA plug - at 50°C. The next day plugs are cooled down at room temperature and then washed 3 times in TE. Plugs are then ready to be processed to produce DNA solution to be combed. At this stage they can also be stored at 4°C in 0.5M EDTA.

2.3. Preparation of a DNA solution deriving from pulse labelled cells.

To obtain a DNA solution form the DNA agarose plugs produced, these plugs need to be processed through various steps. Plugs are first stained for 1 hour with the intercalating agent YOYO-1. This intercalation is an important step because it allows the DNA to be better stretched over the silanized coverslip. Moreover, since it emits light at green wavelengths, it can also be used to check for the fiber density at a fluorescent microscope, before proceeding with the immunofluorescence.

After YOYO-1 staining, plugs need to be melted in a proper buffer, since the attachment of the DNA to the silanized coverslips is highly dependent on the pH of the buffer solution in which DNA is dissolved (Allemand et al., 1997). In all my experiment I used the buffer solution proposed in (Caburet et al., 2002), that is MES 0.5 M, pH 5.5. Agarose plugs are then melted in 3ml MES buffer with 20 minutes incubation at 68°C. Longer incubation can break the DNA so this incubation time must be precise. At the end of the incubation agarose plugs should be melted. The solution is then cooled down for 10 minutes at 42°C and then 4.5 µl of β-agarase I is added to the solution and left overnight at 42°C to digest the agarose. The next day the DNA solution is ready to be combed.

2.4. Performing DNA molecular combing of the DNA solution prepared with Molecular Combing System, a specific combing apparatus produced by Genomic Vision.

DNA solution is gently poured in Teflon reservoirs. In this step the DNA solution must be handle with extreme care since minimal mechanical stress can induce the DNA to break. Silanized glass slides are then incubated for 5 minutes in the buffered DNA solution. During incubation, the extremities of DNA molecules bind naturally to the glass slides. The coverslips are then pulled out of the solution at a constant vertical velocity of 300

um/s by the Molecular Combing System, a specific combing apparatus produced by Genomic Vision (Figure 3). During this process the meniscus air/solution and coverslip interface applies a constant force on the immersed part of each attached molecule, while their emerged part comes out with the coverslip surface. Due to their hydrophobicity, the silanized coverslips dry immediately as they are pulled out of the solution. This results in permanently fixed, parallel DNA fibers, stretched in a single direction on the slide (Michalet et al., 1997). Alternative methods that do not require combing apparatus have been described (Norio and Schildkraut, 2001).

Importantly, under these conditions, the stretching of the DNA molecules results to be constant (Bensimon et al., 1994). This was proved by systematic measurements of phage λ DNA molecules (48.5 kb) combed on silanised coverslip. The stretching factor obtained by this analysis is 2 kb per 1 μm: this indicates that for any DNA molecules stretched on the class slide 1 micrometre of DNA corresponds to 2 kilobases (1μm=2kb) (Michalet et al., 1997).

After combing the DNA solution, the DNA molecules are crosslinked to the coverslips surface by incubation at 60°C for 4 hours in the oven. After crosslinking, combed DNA can be processed for immunofluorescence.

2.5. Whole genome studies: immunofluorescence against the incorporated thymidine analogues

There are different protocols to perform immunofluorescence against thymidine analogues. (Conti et al., 2001) (Bianco et al., 2012) (Schurra and Bensimon, 2009), which have in common some steps: a. dehydration step, where DNA is dehydrated by successive ethanol baths (70%, 90%, 100%); b. denaturation step, where DNA is denatured with an alkaline solution containing NaOH. After these steps slides can be hybridized with antibodies

against thymidine analogues. The difference between the two a due soli lies in the chronological sequence of the dehydration and denaturation steps and the solutions used for the DNA denaturation.

In the protocol proposed by Schurra C. and Bensimon A. (Schurra and Bensimon, 2009), the DNA is first denatured with a solution of 0.5 M NaOH and 1M NaCl and then it is dehydrated with successive ethanol bath. Differently, in the protocol proposed by Bianco, J.N. (Methods, 2012, Pasero's laboratory), slides are first dehydrated and then denatured with a solution of NaOH 1M. I tested both of these protocols and in my hands it appeared that the protocol from Bensimon's lab is perfectly suitable for the staining of the thymidine analogues (IdU and CldU). However, when one needs to stain also for the ssDNA, the protocol from Pasero's lab resulted to be the only one giving nice triple staining (IdU, CldU, ssDNA). The staining for ssDNA is fundamental to perform proper analysis of DNA replication dynamics and limits mistakes in the assessment of replication patterns. Staining of ssDNA ensures that the replication signals analysed are on the same DNA molecule, thus avoiding misinterpretation of the replication patterns. Moreover the DNA fibers length can influence the interpretation of some replication parameters (Bianco et al., 2012; Techer et al., 2013), hence knowing the distribution of the DNA fiber length ensures accurate estimation of replication parameters.

Therefore in my combing experiments, when studying DNA replication dynamics at whole genome level, I stained also for ssDNA applying the protocol from Pasero's lab. In this triple staining, the primary antibodies against IdU and ssDNA are both rose in mouse, but they are isotype-specific. For IdU I used the mouse IgG1 anti BrdU clone B44 (Becton Dickinson 347580), while for ssDNA I used Mouse IgG2a anti-ssDNA (polydt, Chemicon MAB3034). So to avoid any cross reactivity of secondary antibody recognition, the protocol includes two rounds of primary/secondary antibodies hybridization. First thymidine analogues are immunodetected with primary and secondary antibodies

hybridization. This step is then followed by immunodetection of ssDNA with primary and secondary antibodies hybridization.

Briefly, after dehydration steps by successive ethanol baths (70%, 90%, 100%, three minutes each), slides are incubated 25 min in 1M NaOH to open up the DNA double-helix, allowing for thymidine analogues immunodetection. It's very important to be precise with the time of incubation, since more than 25 minutes incubation can induced the DNA fibers to detach from the slide. After denaturation, slides are then extensively washed with PBS to neutralize NaOH. At this point immunodetection can start. Slides are incubated with blocking solution (Blockaid blocking solution, B-10710) for 15 minutes. After this blocking step, the first round of immunodetection takes place: 45 minutes incubation at 37°C in a humid chamber with primary antibodies (IdU: mouse antiBrdU clone B44 IgG1 1:20 (Becton Dickinson 347580); CldU: rat antiBrdU clone BU1/75 1:20 (ab6326 abcam)). After washing - 5 times in PBST on agitation - slides are incubated 30 minutes at 37°C in a humid chamber with secondary antibodies (IdU: Isotype specific Goat Alexa 546 anti-Mouse IgG1 1:50 (molecular probes A21123); CldU: Goat Alexa 488 anti Rat 1:50 (molecular probes A11030)). Slides are then washed 5 times in PBST on agitation. The slides then undergo the second round of immunodetection, where ssDNA is stained. Slides are incubated 30 minutes at 37°C in a humid chamber with primary antibody (ssDNA: Mouse anti-ssDNA (polydt) IgG2a 1:100 (Chemicon MAB3034)). After washing, slides are incubated 30 minutes at 37°C in a humid chamber with secondary antibody (ssDNA: Isotype specific ab Goat Alexa 647 anti- Mouse IgG2a 1:50 (molecular probes A21241)). After immunodetection slides are washed and then mounted on the coverslips. As for the mounting step I tested different kind of mounting medium (Vectashield, Prolong Gold antifade reagent) but with none of them I was satisfied. Serendipitously, I discovered that the best way of mounting combing slides is the dry mounting, with no mounting medium at all. As shown in Figure 6, bright fluorescent signals are detected only on the air bubble, while mounting medium reduces signal intensity. Since mounting medium are supposed to

stabilize the fluorescent signals and act as antifade system, I checked for the stability of the fluorescent signals over time in condition of dry mounting. Unexpectedly, the fluorescent signal was stable over months in dry medium. Therefore I always used dry mounting.

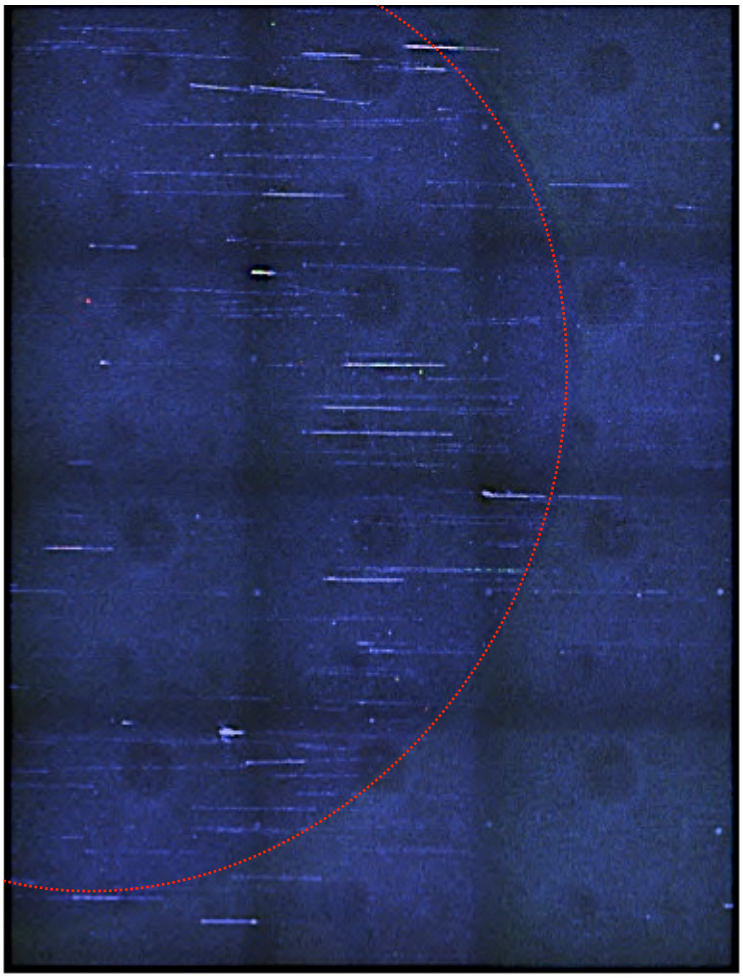

Figure 6. Dry mounting results in brighter DNA replication signals than vectashield mounting.
DNA molecular combing was performed using a DNA solution coming from cells pulsed labeled with thymidine analogues. After immunodetection (IdU green, CldU red and ssDNA blue), I mounted the coverslips with vectashield, but the replication signals were very faint and it was very difficult to properly distinguish them. Only the absence of mounting medium due to air bubble (dotted red lines) inside the coverslips allowed the visualization of nice bright signals.

2.6 Site specific studies: coupling FISH to the staining for thymidine analogues

Given my interest in the study of DNA replication dynamics at telomeres, I tried to set up a proper protocol that couples the staining of thymidine analogues with fluorescence in situ hybridization (FISH) using a Peptide Nucleic Acid (PNA) telomeric probe conjugated with Cy3. To this end I applied the protocol used in (Hande et al., 1999) for the telomere

detection in q-FISH experiment. The hybridization step with the PNA telomeric probe in the q-FISH protocol occurs after dehydration step, while the denaturation occurs directly during the hybridization, where the hybridization mix is placed on the coverslip and denatured by incubation at 80°C for 3 minutes. After these denaturation steps the coverslips are left at room temperature for 2 hours to allow probe hybridization. Since in molecular combing the denaturation of the DNA occurs by treatment with alkali solutions, which in some protocol is followed by dehydration step (Schurra and Bensimon, 2009), I decided to perform the hybridization with PNA telomeric probe after this dehydration step, on DNA previously denatured.

Briefly, combed DNA is denatured with incubation in 0.5 M NaOH, 1M NaCl for 8 minutes. Then it is washed 3 times in PBS. Then the DNA is dehydrated by successive ethanol baths (70%, 90%, 100% ethanol). The sample is then hybridized with the hybridization mix containing the PNA telomeric probe (hybridization mix: formamide 70%, Blocking reagent in maleic acid 0.25%, TRIS 10 mM, PNA-Telo-Cy3 500 nM) for 2 hours in a humid chamber at room temperature. The sample is then washed twice in *wash solution I* (formamide 70%, TRIS 10 mM, BSA 0.1%), 15 minute each wash; after this first round of wash, the slide is washed three times in *wash solution II* (TRIS 0.1 M, NaCl 0.15 M, Tween 20 0.08%), 5 minutes for each wash. At this point DNA is dehydrated again and the immunodetection of thymine analogues can start.

In this case it is not possible to stain also for ssDNA since the fluorophores needed would be four (Telomeres, IdU, CldU, ssDNA). Indeed so far I was not able to find a proper combination of fluorescent secondary antibody for all the conditions stated above. Since telomeres are probed with a Cy3-conjugated PNA probe, I used Alexa 647 donkey anti-mouse, to detect IdU and Alexa 488 goat anti-rat for CldU detection. The Thymidine immunodetection step is performed as explained above, with the exception of lighter washing (performed in PBS instead of PBST) and the secondary antibody used.

Before proceeding to perform combing staining coupled with telomeric FISH, I decided to check whether telomeric repeats could be stretched and visualised by combing with this protocol. Moreover I wanted to check which was the resolution limit of combing in terms of kb of telomeres that could be detected with this technique. To this end, I made use of two plasmids: pSX_270, which contains telomeric repeats (800 bp + 800 bp), and pSX_I-SceI, which does not contain telomeric repeats (Figure 7 A-B).

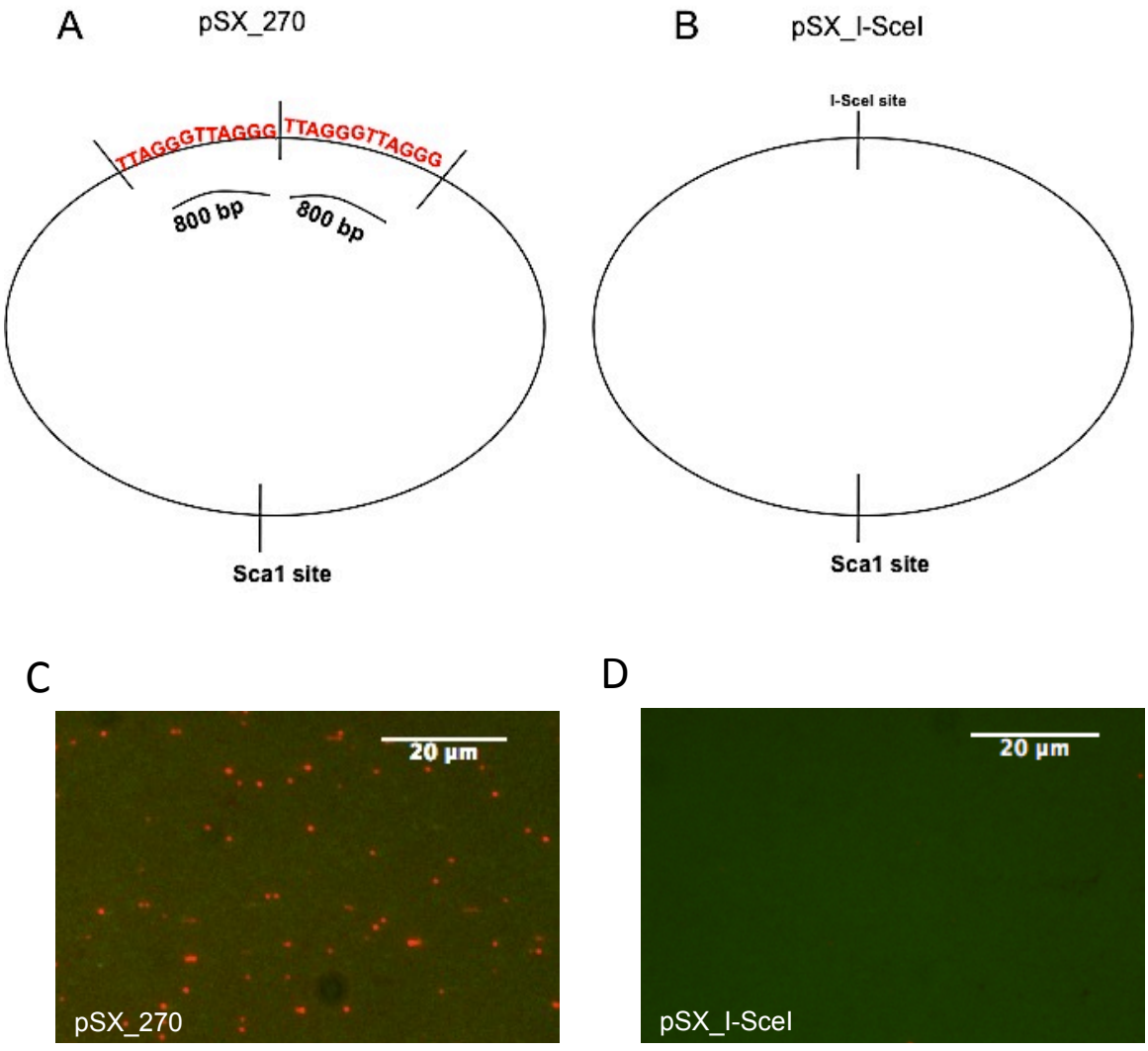

Figure 7. ImmunoFISH applied to DNA molecular combing allows to detect telomeric DNA with a resolution of around 2 kb.
(A-B) Maps of the plasmids used to test the telomeric probe with immunoFISH protocol on combed DNA. (A) pSX_270 presents two adjacent telomeric repeats of 800 bp each, for a total of 1600 bp. (B) pSX_I-SceI does not detect any telomeric repeats. (C-D) ImmunoFISH with Cy3-conjugated PNA-telomeric probe applied to the combed linearized plasmid DNA from A and B. pSX_270 (C) but not pSX_I-SceI (D) detect small red signals of around 1.6 kb length, corresponding to the length of the telomeric signal present in the plasmid.

Since molecular combing allows the DNA molecules to attach to the silanized coverslip by their extremities, plasmids were linearized through digestion with Sca1 restriction enzyme. Based on calculation made in (Michalet et al., 1997), I then combed 1.5 µg/ml of each of the two linearized plasmid. Then I performed FISH with a Cy3-conjugated-telomeric PNA probe following the protocol described above. I could see red short signals only in case of the presence of pSX_270 plasmids, which contained telomeric repeats corresponding to 1600 bp, while no signal at all in case of the empty plasmid. Thus these results indicate that telomeres are detectable with combing with the protocol adapted from (Hande et al., 1999).

We then performed FISH coupled with immunofluorescence for thymidine analogues and could appreciate nice telomeric signals and some of them were overlapping with DNA replication signal (Figure 8).

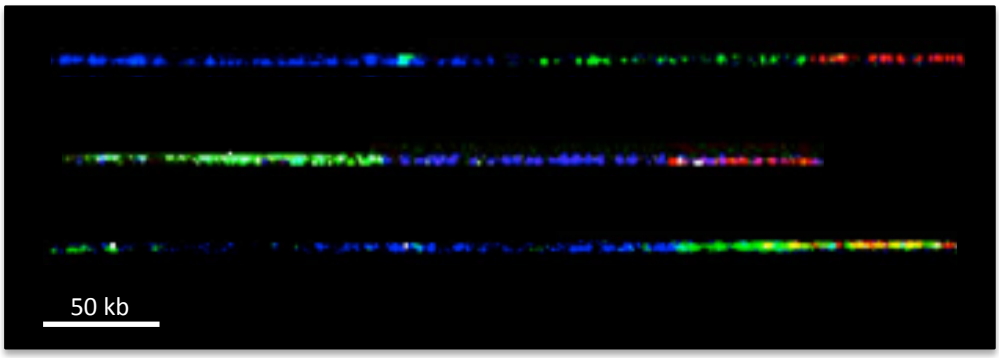

Figure 8. Representative images of DNA replication and telomeric signals.
The images result from immunoFISH on combed DNA derived from mouse embrionic fibroblast. Blue signal: IdU; Green signal: CldU; Red signal: telomere. Scale bar: 40 kb.

2.7. Image acquisition

One limiting step of this technique is the image acquisition. Indeed to obtain nice combing results enormous amounts of images need to be analysed and thus properly acquired. At the beginning of my PhD, I used to manually acquire around 500 images per condition. Moreover, since DNA fibers are often longer than a single field of view, the manual

acquisition became even more inefficient in term of time spent at the microscope because I had to carefully try to acquire partially overlapping fields of view to keep the information of the DNA fibers longer than a single field of view. So beyond being time consuming it was also not so much precise.

Thus, with the help of Dario Parazzoli and Amanda Oldani, from imaging facility IFOM, I tried to set up a system that could allow for automated image acquisition as well as for the acquisition of adjacent images with a certain overlap between each other to be then able to properly reconstruct the real mosaic image and so have the chance to see the DNA fibers in their full length.

I tried to apply different microscope systems that could perform this kind of automated acquisition. I first tried with Scan R Olympus system: it consists in a wide field microscope equipped with a motorized stage. Once the grid of points is set and the focus is reached, the acquisition is run and thus the microscope acquires sequential fields of view in the fluorescence emission channels of interest. This automated system applied to DNA molecular combing images has been a great improvement since it allowed for a fully automated acquisition of the entire coverslips. However the software running the Scan R Olympus system did not allow for the acquisition of partially overlapping fields of view, rendering impossible to recapitulate the length of DNA fibers longer than a single fields of view.

The next system we tried is the Spinning Confocal Microscope from PerkinElmer. This system, beyond automated image acquisition, allows for the acquisition of adjacent fields of view with a partial overlap. At the end of the acquisition, Volocity, the software running on this microscope, reconstructs a mosaic image by precisely stitching the images by their overlapping regions. Thus this system appeared to be the most suitable for my purposes.

Briefly, before proceeding with the automated acquisition, various parameters need first to be set: the points one wants to acquire on the grid, the dimension of the mosaic image that will be reconstructed at each point of the grid and the percentage of overlap between

adjacent images. I set the dimension of the mosaic image as 10 images in length and 5 in height, ensuring for the presence of long DNA fibers in an entire image. Longer mosaic images are possible, but they are difficult to handle computationally due to their big memory size. Then I set the points on the grid to be distant enough between each other in order to avoid mosaic images overlap (Red cross Figure 9).

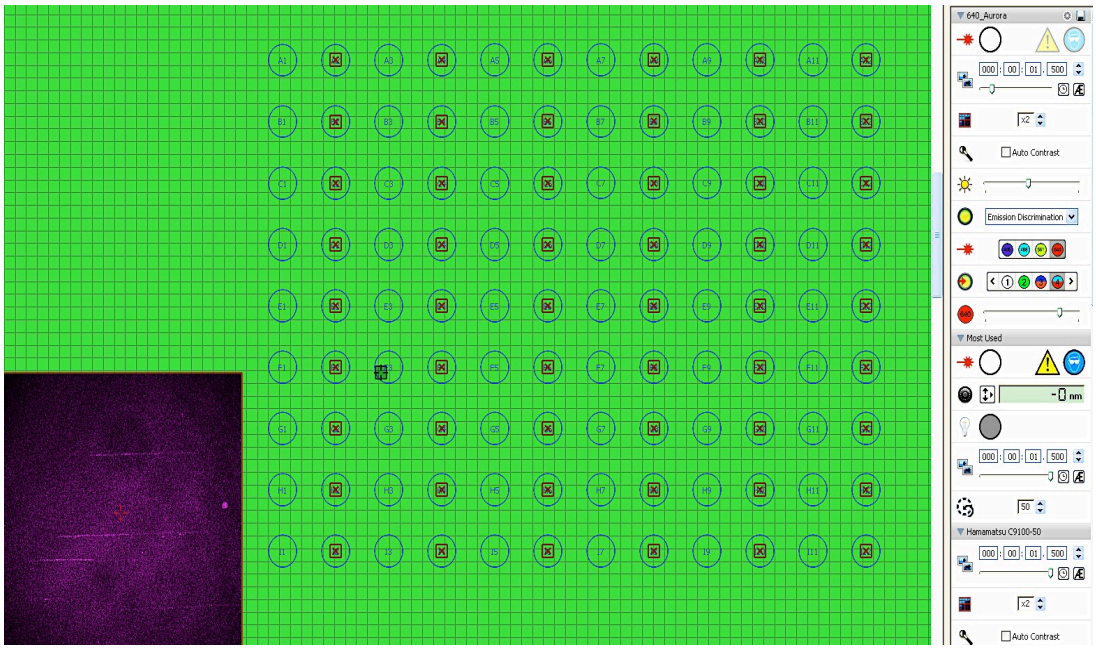

Figure 9. Screenshot of Volocity Software during image acquisition.
The grid from which the software recapitulates the fields of view to be acquired is shown. Red crosses represent the central point of each mosaic image of 10x5 fields of view. The bottom left window allows the visualization of the emitted fluorescence signal while the acquisition is ongoing.

After different trials, we concluded that the minimal % of overlap between adjacent fields of view to gain the best mosaic stitching is 10 %. Once the emission light intensity and exposure time for the three lasers (488nm, 561nm, 647nm) are set, the automated acquisition can start. Each coverslips results then in 54 mosaic images, one of them is shown in Figure 10.

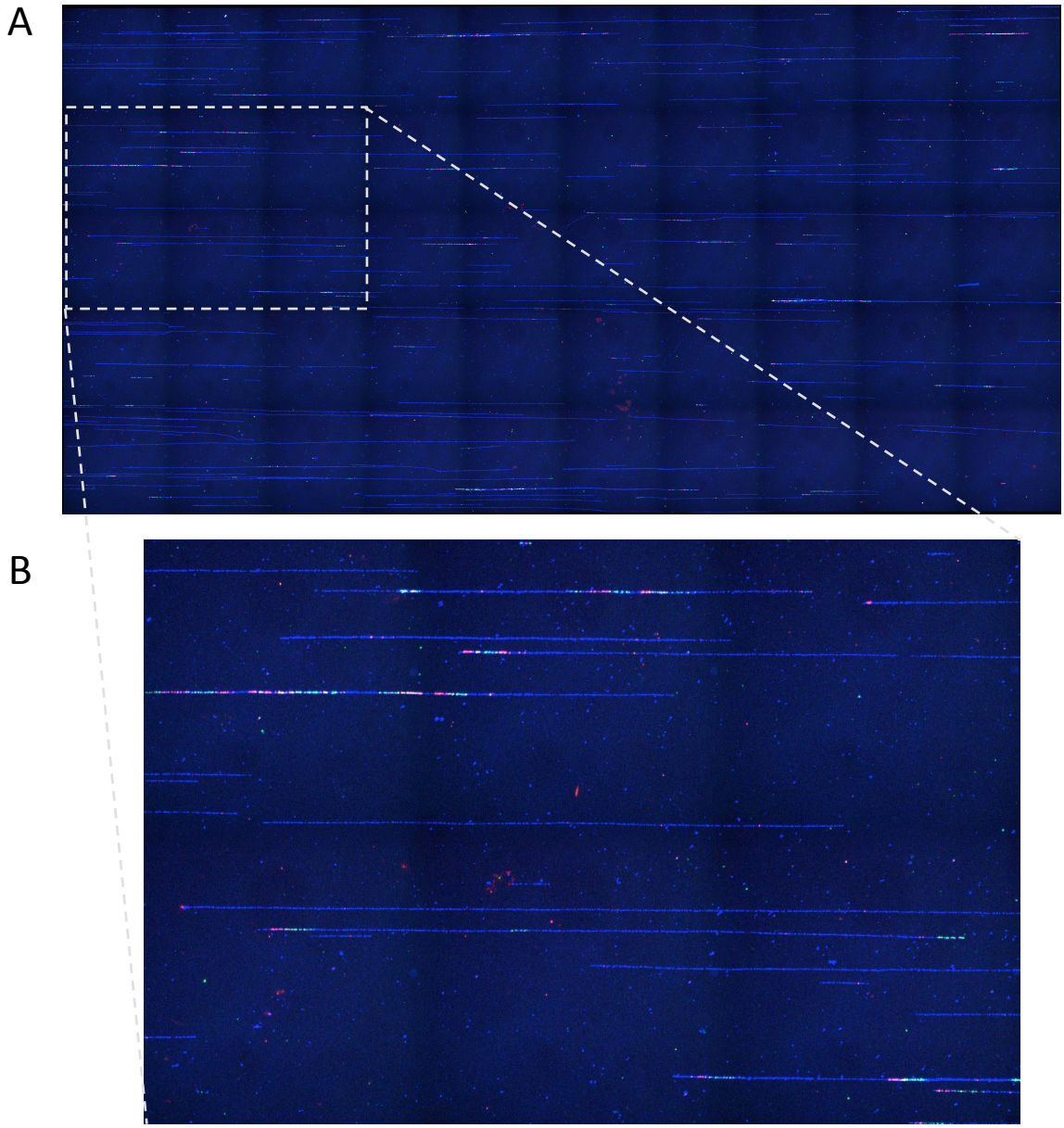

Figure 10. Representative mosaic image derived from Volocity acquisition and stitching of partially overlapping fields of view.
DNA molecular combing was performed using a DNA solution from cells pulsed-labeled with thymidine analogues. After immunodetection of DNA replication signals, the coverslips were acquired at the spinning disk confocal microscope with Volocity software. In (A) an example of a mosaic image of 10x5 fields of view derived from the stitching of adjacent acquired images is shown. An enlargement of the same mosaic image corresponding to 3x2 fields of view is shown in (B). (Green signal: CldU; Red signal: IdU; Blue signal: ssDNA).

2.8. Image analysis: measurement of replication signals

Once images are acquired, they need to be processed before proceeding with the analyses. First I need to merge the three fluorescent channels in order to obtain a composite image containing all the three signals (ssDNA, IdU, CldU). Then **I** have to convert the pixel dimension of **my** image in length units (μm). This occurs by applying a mathematical

formula that takes into account all the features of the microscope used and the conditions at which the acquisition was performed. In the acquisition performed with Spinning Confocal Microscope the software calculates directly the pixel dimension on the bases of the objective used (40X, dry). The formula used is the standard one used for cameras with also a correction coefficient of 0.89, which depends on the insertion of a projection lens in the fluorescence emission pathway. Here is the formula:

$$\mu m = 0.89 \frac{\text{Camera pixel dimension X binning factor}}{\text{Total magnification}}$$

Given the huge amount of images I needed to acquire for my experiments, Amanda Oldani helped me by generating a macro for Image software that was performing these two image processing – merge channels and conversion from pixel to μm dimension. This speeded up the images processing before the analyses.

Another limiting step of this technique is the imaging analysis. I need to analyse around 500 to 1000 DNA molecules to gain a statistical significance on the results, and sometimes it is not even enough. This analysis consists in the manual measurement of the length of each replication signal with the ruler of ImageJ software. The values of this measurement are then pasted in an excel file to be subsequently interpreted. Therefore, after having set up an automated acquisition, the images analysis became the time consuming step of this technique. Thus for an automatic analysis of spread DNA fibers I tried to apply IDeFIx software, a software developed by Thierry Gostan from Institut de Genetique Moleculaire de Montpellier.

This software is first recognizing the fluorescence signal for ssDNA and then the fluorescence signals of the thymidine analogues – IdU and CldU - that are lying on the recognized DNA fiber. However since it was first developed on images with only two

fluorescent signals, - ssDNA and BrdU - I found various bugs when applying it to my images. Given all the problems encountered while trying to apply the IDEfix software to my combing images, I decided to go back to manual analysis.

2.9. Image analysis: interpretation of replication signals

After the measurements of replication signals it is possible to evaluate various DNA replication patterns that allow to unveiling the ongoing DNA replication dynamics. We can assess fork speed, the frequency of initiation rate, and the symmetry of fork progression. In any of these patterns we excluded the ones that were lying at the extremities of DNA fibers, since it was not possible to ensure that distal end of the replication signal was not in fact the result of the breakage of the DNA fiber.

2.9.1 Fork speed

The fork speed is obtained by dividing the length of the replication signal over the incubation time of the pulse with thymidine analogue (Figure 11). The replication pattern shown in Figure 11 represents a replication origin (ORI) that fired before the first pulse of thymidine analogue. Two bidirectional forks started replicating DNA in opposite direction of the ORI. As I gave the first pulse with IdU, the DNA incorporates the thymidine analogue and red signals are detectable. After 30 minutes I gave the second pulse with CldU, DNA keeps incorporating thymidine analogue and I can see this incorporation as green signal on combed DNA. Given the incubation time interval of the pulses, I can calculate the fork speed by dividing the length of the replication signal over the incubation time of the pulse with thymidine analogue.

In Figure 11 I can assess 2 fork speeds, the ones corresponding to the first pulse (red lines) since they are the only one of which I can be sure that their lengths correspond to the entire time interval of the pulse.

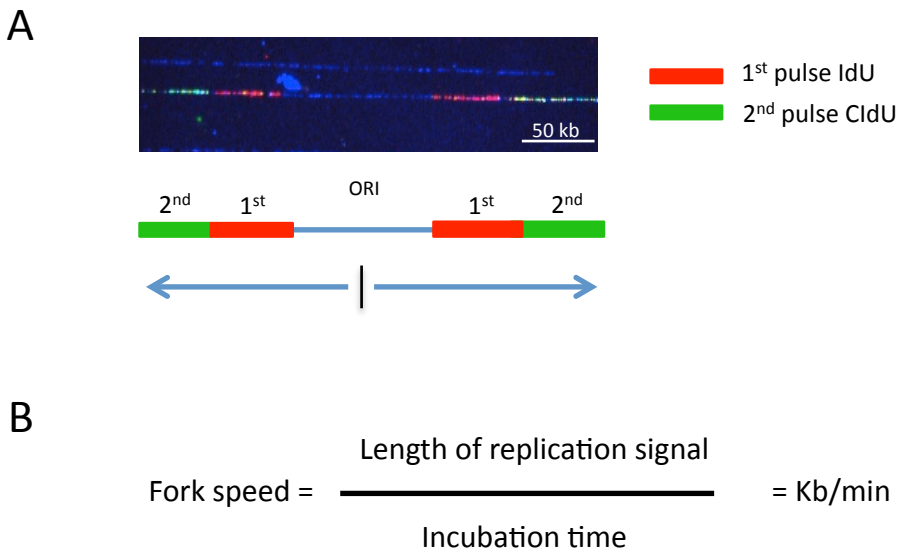

Figure 11. DNA replication pattern consistent with a replicon.
(A) Representative image of a replication bubble centred at the ORI, that started DNA replication before pulse labelling. As the labelling begins replication forks incorporate the thymidine analogues that are then visualized by immunofluorescence on combed DNA with specific antibodies against the thymidine analogues used. 1st pulse, IdU: Red signal. 2nd pulse, CldU: Green signal. ssDNA: Blue signal. ORI: DNA replication origin. From this DNA replication pattern I can calculate two fork speeds. (B) Formula used to calculate fork speed.

Indeed in all the analyses for fork speed I considered only the replication signals that were flanked on one side by the replication signal of the other thymidine analogue, and on the other side by ssDNA. Only under these conditions, I could be confident that the distal end of the replication signal was not caused by the fiber break. Thus I excluded from these analyses all replication signals in which their extremities were not flanked by ssDNA. For example, following this criteria, in case of Figure 12A I could calculate 3 fork speeds, while in Figure 12B I could consider 6 fork speeds.

This parameter can be slightly affected by fiber length, so to ensure proper estimation of fork speed it is important to guarantee that the median fiber length of the DNA used for fork speed analysis is at least equal to 200 kb (Techer et al., 2013).

2.9.2 The frequency of initiation

To assess the frequency of origin initiation it is possible to consider two different parameters: the inter-origin distances (IODs) or the number of active origin per Megabases (ORI/Mb). The IOD is the most widely used parameter to assess the frequency of initiation, while the ORI/Mb is a rather new parameter, recently proposed by (Bianco et al., 2012), and so far there are no studies in literature that include this parameter. However I decided to apply it to my analyses as a further support to what I observed by analysing the IODs. Another parameter that can be considered and that should reflect the trend of IODs, is the inter-termini distance (ITD). It consists in the distance between termini (TER) of DNA replication (Techer et al., 2013). However this parameter was not considered in my analysis.

The inter-origin distance consists in the distance between adjacent active origins and accounts for the evaluation of DNA replication initiation events: smaller IOD indicates higher number of simultaneously active origins, while higher IOD corresponds to lower number of simultaneously active origins. To properly assess the distance between replication origins (ORI) it is necessary to have replication patterns that allow precise positioning of the ORI. One ORI is defined as the central point on the ssDNA signals that is flanked on both sides from replication signal generated by the 1st pulse. Thus, I had to exclude from this analysis all the origins for which the position could not be precisely determined due to the lack of replication signal on one of the extremities of the DNA fiber, or in case of unidirectional fork, that occurs when ssDNA signal is flanked one side from red signal while on the other side is flanked on green signal. Example of unidirectional fork is shown in Figure 12B and in Figure 13C. (For further details on the unidirectional fork see the paragraph about symmetry of fork progression). IODs estimation can also be influenced by DNA fiber length. Short DNA fibers would imply an underestimation of IODs, since longer interorigin distances would be excluded due to DNA fiber

fragmentation. Thus as suggested in (Techer et al., 2013), it is necessary to have the median size of fiber length at least of 350 kb to ensure accurate IODs estimation. Moreover, to further avoid bias in IODs assessment due to fiber fragmentation, it is possible to recalculate IODs by considering only fibers at least three times longer the average of all IODs, as suggested in (Bianco et al., 2012).

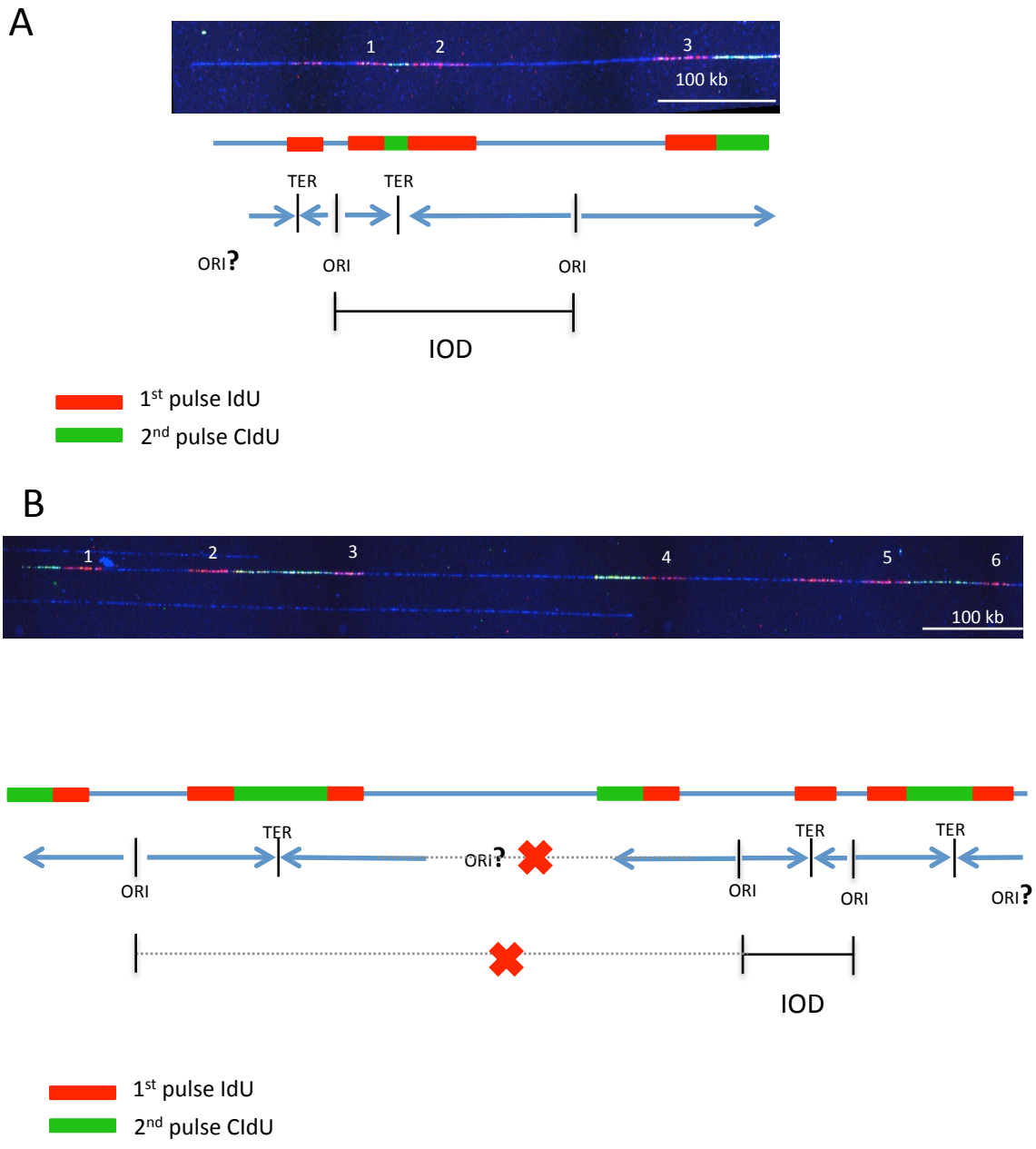

Figure 12. Examples inter-origin distances and ORI/Mb quantitation of DNA replication patterns. Representative images used to assess IODs and ORI/Mb. (A) The replication signals of this image derive from 3 ORI, of which only two can be properly positioned, thus only 1 IOD can be evaluated. (B) The replication signals of this image derive from 5 different ORIs. Since one of the ORI cannot be positioned due to the presence of unidirectional fork, only IOD can be assessed. 1st pulse, IdU: Red signal. 2nd pulse, CldU: Green signal. ssDNA: Blue signal. ORI: DNA replication origin. TER: termination of DNA replication.

The number of active ORI/Mb is obtained by evaluating the replication patterns lying on the same DNA fiber. It is less sensitive to fiber fragmentation, since it has less stringent rules to be assessed. For example, as shown in Figure 12A, the replication pattern we see depends on at least 3 replication ORIs, of which only two can be precisely positioned. This implies that if I consider IODs in this case, I can precisely evaluate the distance between two ORIs, while I am losing some information, regarding the third ORI that cannot be precisely positioned. On the other hand, evaluating the number of active ORI/Mb takes into consideration all the three ORIs from which the replication patterns derive. However ORI/Mb is less precise because the ORIs that cannot be exactly positioned due to fiber breakage can introduce some bias, some overestimation or underestimation that I cannot recapitulate since I do not have the information for this, due to fiber breakage. However these biases are limited by big sample size analysis, because one can argue that some overestimations would more easily balanced by some underestimations in big sample size. The major limitation of this parameter is that it can take into consideration molecules containing just one ORI. However one origin on a very short fiber - likely due to fiber breakage during the combing process - would result in a high level of ORI/Mb, which might not reflect the real value of ORI/Mb. One way to avoid this bias is the to exclude short DNA fibers.

Another example to compare IODs and ORI/Mb is shown in Figure 12B. By analysing these replication patterns I obtain 5 ORIs of which only three can be precisely placed. The ones that cannot be position are either at the edge of the DNA fiber or of unidirectional fork. Thus with ORI/Mb I do not lose any information. As for the IODs, even though there are 5 active ORIs I am able to assess just 1 interorigin distance. Again IODs estimation is more precise but implies the loss of some useful information that ORI/Mb can pick up.

2.9.3 The symmetry of fork progression

When DNA replication proceeds normally, the two replication forks deriving from the same ORI should proceed at the same speed. So from one ORI, normally two bidirectional forks are departing, replicating DNA in opposite directions. As a result by combing experiments, you will see symmetric replication signals (Figure 13A). On the contrary as one of the two forks encounters an obstacle, it starts to replicate DNA in a slower fashion than the other fork. Combing experiment allow you to see this difference as the appearance of asymmetric replication pattern of this bidirectional forks (Figure 13B). In case one of the two forks encounter an obstacle that is not even allowing the fork to proceed this results in fork collapse or fork breakage. This situation is the most dangerous for a cell and it can be visualized by combing as a unidirectional fork, corresponding to ssDNA signal flanked one side from red signal while on the other side is flanked on green signal (Figure 13C and also 12B).

Beyond visual interpretation of symmetry of fork progression I performed quantitative analyses by calculating the left to right fork speed correlation (Figure 13D). This parameter allows evaluating the level of symmetry of two replication forks generating from the same DNA replication origin. It consists in making the ratio between left and right fork speed deriving from the same ORI and then plotting this value in a correlation plot (Figure 13D). I defined 3 different groups of symmetry: a. symmetric, in which the difference between left and right fork speed is between 0 to 30% of the highest fork speed (blue dots lying in the cone); b. asymmetric, in which the difference between left and right fork speed is between 30 to 99 % (green dots, lying outside the cone); c. Unidirectional in which the difference between left and right fork speed is 100 %, meaning that one of the two forks did not start during the first pulse (red dots, on x and y axis) (Figure 13D).

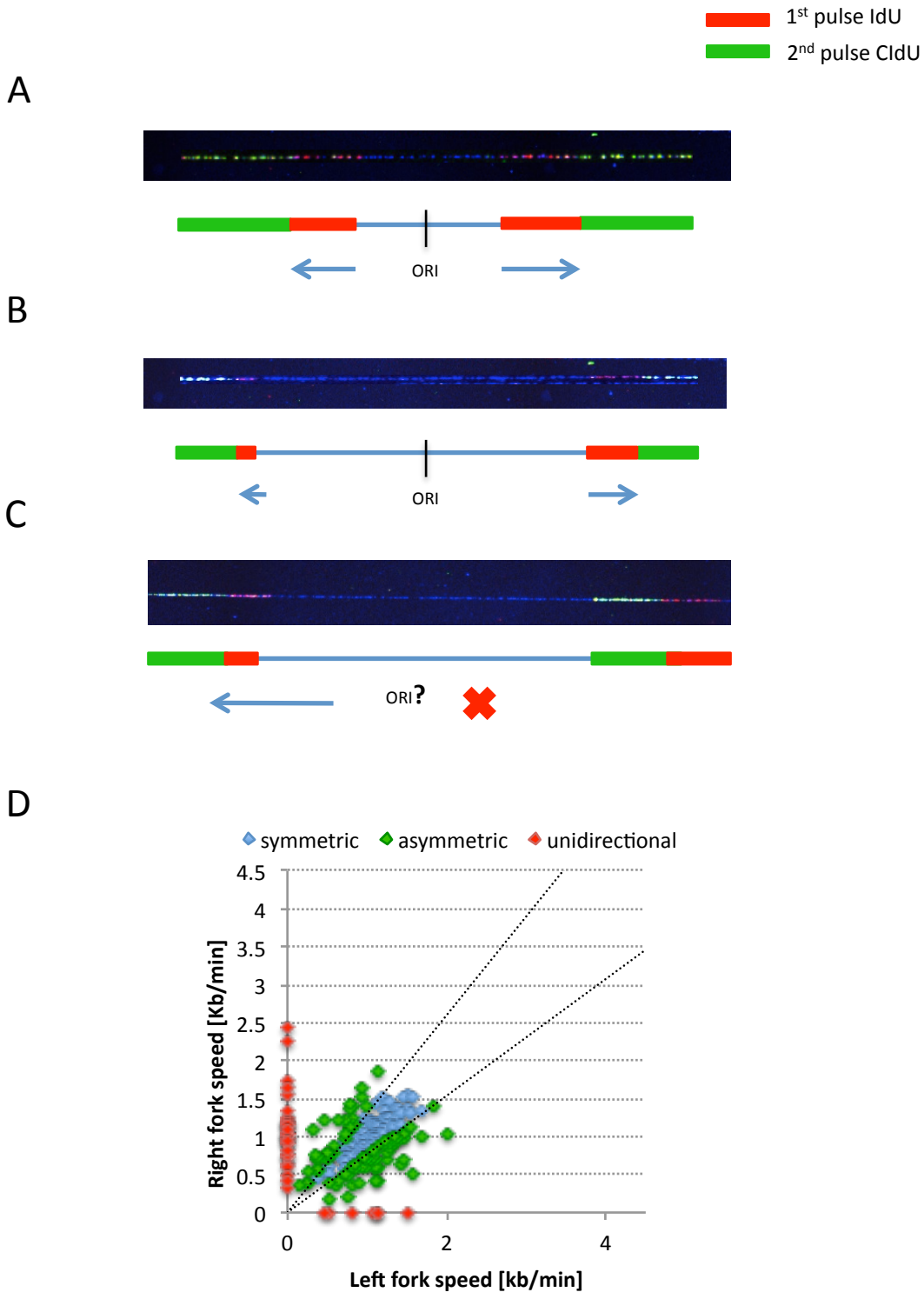

Figure 13. Representative images for DNA replication patterns used to assess the symmetry of fork progression.
(A) Symmetric replication fork progression: the difference between left and right fork speed is between 0 to 30% of the highest fork speed. (B) Asymmetric replication fork progression: the difference between left and right fork speed is between 30 to 99 %. (C) Unidirectional forks: the difference between left and right fork speed is 100 %, meaning that one of the two forks did not start during the first pulse. It represented by ssDNA that one side id flanked by red signal, while on the other side is flanked by green signal. 1st pulse, IdU: Red signal. 2nd pulse, CldU: Green signal. ssDNA: Blue signal. ORI: DNA replication origin. (D) Example of a Left to Right fork speed correlation plot. The cone on the plot separates the symmetric fork - inside the cone - from the asymmetric and unidirectional forks - outside the cone till x and y axes. Blue dots: Symmetric fork progression; Green dots: Asymmetric fork progression; Red dots: Unidirectional forks.

Another way to assess symmetry of fork progression is the evaluation of how the single fork is proceeding during 1st and 2nd pulse. It consists in the ration between the fork speed of the first pulse over the fork speed of the second pulse. The closer the ratio is to 1 the more symmetric the replication fork progression was. Instead the closer the ratio is to 0 the more asymmetric the replication fork progression was. However this kind of parameter was not taken into account in my analyses.

MATERIALS AND METHODS

Cell Culture

BJhTERT (Clontech) and BJELR (a kind gift of William C. Hahn,Harvard Medical School, Dana-Farber Cancer Institute, Boston, USA) were grown under standard tissue-culture conditions in DMEM:M199 (4:1) supplemented with 10% foetal bovine serum, 1% Na Pyruvate, 25mM Hepes pH 7.5, 1% L-glutamine, 1% penicillin/streptomycin. Phoenix amphotropic cell line HEK293-T in DMEM, supplemented with 10% foetal bovine serum, 1% L-glutamine, 1% penicillin/streptomycin. All cells were grown in 20% oxygen.

For growth curves, after retroviral infection (see the section Retroviral infection), cells were plated in triplicated at $5x10^4$ per well in six-well plates and cells were counted every day.

NIH 3T3 cells were grown in DMEM supplemented with 10% TET system approved foetal bovine serum, 1% L-glutamine, hygromicin (400 μg/ml).

Human Cancer Tissue Samples

Archival and paraffin-embedded tumor tissue was obtained from the tumor tissue bank at NJMS-University Hospital with the approval of the local IRB committee.

MEFs generation and growth conditions

The Rosa26 CRE-ERT2 *EZH2 fx/fx* MEFs used in this thesis have been derived from 13.5 dpc embryos. Rosa26 CRE-ERT2 mice and EZH2 *fx/fx* mice used have been described elsewhere (Ventura, a. Nature 2007;Su, iH, nat immunol, 2003). Low passages MEFs have been grown in DMEM medium supplemented with 10% foetal bovine serum (Euroclone), non-essential amino acids (Gibco), sodium pyruvate (Gibco) and 1% penicillin/streptomycin (Gibco), in a CO2 incubator (5% CO2) with reduced oxygen tension (3% oxygen) if not differently specified. MEFs were passaged every 3-4 days. The Rosa26 CRE-ERT2 *EZH2 fx/fx* MEFs were then immortalized by the expression of SV40

ER and HRas-V12. To induce CRE-ERT2 nuclear translocation, cells were treated for 7 days with 500 nM of 4-hydroxytamoxifen (4-OHT, Sigma) dissolved in absolute ethanol (Panreac).

For G1/S synchronization using a double thymidine block, sub-confluent asynchronous MEFs were treated with 2mM thymidine (Sigma) for 12 hours, release with normal medium for 8 hours and treated again with 2mM thymidine for additional 12 hours.

Cells Treatments

The Nox4 inhibitor used VCC444973:02 (Borbely et al., 2010), was produced by Vichem Chemie Ltd, Budapest, Hungary and was freshly resuspended in DMSO and added every 48 hours at 5 μM final concentrations. DMSO was used as control treatment.

Retroviral Infection

Human diploid fibroblasts and mouse embryonic fibroblasts are very poorly transfectable with commonly used transfection methods. I therefore took advantage of a retroviral-mediated infection method to express genes in these cells. Recombinant retroviruses have the ability to stably integrate into the host genome. They contain a reverse transcriptase, which allows integration into the host genome and are replication-defective, failing in this way to produce infective particles and to induce cell lysis and death. The primary drawback to use of retroviruses is the requirement for cells to be actively dividing for transduction. Phoenix is a second- generation retrovirus producer cell line, based on the HEK293T cell line (a human embryonic kidney line transformed with adenovirus E1a and carrying a temperature sensitive SV40 T antigen co-selected with neomycin), which is highly transfectable using calcium phosphate method. This retrovirus producer cell line was created by placing into HEK293T cells stably integrated constructs capable of producing gag-pol and envelope protein for amphotropic (able to infect more than one

species, such as human and murine cells) viruses (Pear et al., 1993). The retroviral expression vectors provide the viral packaging signal (Ψ), the gene of interest under LTR promoter and an antibiotic resistance marker. 48h prior transfection packaging cells were plated at 1.8x106 cells per 10 cm dish in producer cell growth medium. Phoenix amphotropic packaging cells were transfected by the calcium phosphate method. Calcium phosphate transfection is based on the formation of a precipitate containing calcium phosphate and DNA, which adheres to the cell surface and is internalized by endocytic process. Chloroquine, added to the medium at a final concentration of 40μM for not more than 12 hours, increases retroviral titer by approximately two fold, by inhibiting lysosomal DNases by neutralizing vescicles pH. The precipitate is prepared by slowly mixing, by bubbling, a HEPES-buffered saline solution containing sodium phosphate with a solution containing calcium chloride and high quality DNA. It is important that the pH of the Hepes is adjusted to 7.05. The HBS/DNA/CaCl2 solution should be added to the cells within 1-2 minutes of preparation. 10μg of DNA were used to transfect a 10cm dish. The day after transfection the growth medium was replaced with 5ml of fresh medium to concentrate viral supernatants and the target adherent cells were plated at 50% of confluence. At 48h post-transfection, viral supernatants were collected, filtered with 0.45μm filter, to remove cells accidentally dead or detached from the plate, and supplemented with 4μg/ml polybrene (this is a small, positively charged molecule that binds to cell surfaces and neutralizes surface charge, allowing the viral glycoproteins to bind more efficiently to their receptors). Supernatants were used to infect human primary fibroblasts. Four rounds of infections, of four hours each, distributed in two days, were carried out to have higher infection efficiency. After infection, cells were selected with puromycin (2μg/ml) or hygromycin (100μg/ml) and/or neomycin (250ng/ml). However in case of growth curve experiments cells were not selected to allow the study of DNA replication dynamics occurring immediately after oncogenic Ras expression.

Lentiviral Infection

Lentiviruses are a subclass of retroviruses, with the ability to integrate into the genome of non-dividing as well as dividing cells. Thus lentiviral infection is amenable for contact inhibited or non-cycling senescent cells. The viral genome in the form of RNA is reverse-transcribed when the virus enters the cell to produce DNA, which is then inserted into the genome at a random position by the viral integrase enzyme. The vector, now called provirus, integrated in the genome is transmitted to the progeny through cell divisions. Lentiviruses were produced by transfecting HEK293T by calcium phosphate method with pMDL g/p RRE (gag-pol elements), pVSVG (envelope elements), pRSV-REV (reverse transcriptase) plasmids and the transfer vector expressing GFP or H-RasV12. 48h after transfection, supernatants were collected, filtered and ultracentrifuged. 30µl of concentrated virus were used to infect a 35mm plate of BJhTERT. Virus efficiency was evaluated by infecting the target cells with decreasing volumes of the final viral preparation of LentiGFP to find the minimal amount of virus able to infect more than 80% of target cells.

Plasmids

pSX_270, pSX_I-SceI telo were a kind gift of Titia de Lange. pBABE-Puro H-RasV12, pBABE-Hygro H-RasV12 and corresponding empty vectors were used to infect BJ hTERT (a kind gift from Pier Giuseppe Pelicci group, IFOM). pRETROSUPER shp53 (a kind gift from Salvatore Pece, IFOM-IEO-CAMPUS). pMDL g/p RRE (gag-pol elements), pVSVG (envelope elements), pRSV-REV (reverse transcriptase) (a kind gifts from Judith Campisi, Life Sciences Division, Lawrence Berkeley National Laboratory, California, USA) were used together with the lentiviral vectors to assemble the lentivirus (see Lentiviral infection section).pRRL.SIN-18 Lenti GFP, pRRL.SIN-18 lenti H-RasV12 plasmids (kind gifts from Judith Campisi, Life Sciences Division, Lawrence Berkeley National Laboratory,

California, USA). pWZL SV40 ER neomycin (a kind gift of Diego Pasini, IFOM-IEO-CAMPUS).

Immunofluorescence

The study of the activation of DDR factors (checkpoint and DNA repair proteins) at the single cell level relies on the observation of their accumulation (or the accumulation of their activated forms) in nuclear foci that can be detected within the nucleus using specific antibodies by immunofluorescence techniques. Cells were grown on poly-D-lysinated coverslips (poly-D-lysine was used at 50μg/ml final concentration) and plated (15-20x103 cells/cover) one day before staining. Cells were gently washed 2x5 minutes with PBS and fixed and permeabilized with 1:1 methanol/acetone solution for 2 minutes at room temperature in case of DDR markers staining.

Cells were incubated for 1 hour in blocking solution (PBG, 0.5% BSA, 0.2% gelatin from cold water fish skin) and then stained with primary antibodies for 1h at room temperature in a humidified chamber. Cells were washed 3x5 minutes with PBG and incubated with secondary antibodies for 1h at RT in a dark humidified chamber; I used donkey anti-mouse or anti-rabbit Alexa488 IgG, donkey anti-mouse or anti-rabbit Alexa 546 IgG donkey anti-goat 647 Alexa IgG (Molecular Probes). 4'-6-Diamidino-2- phenylindole (DAPI, SIGMA) (excitation wavelength 358nm, emission wavelength 461nm) is known to form fluorescent complexes with natural double-stranded DNA. DAPI binds to preferentially to AT clusters of DNA minor groove. DAPI staining was used at concentration of 1μg/ml for 5 min to visualize nuclei; Coverslips were then mounted with Mowiol mounting medium (Calbiochem), which is a brand-name polyvinyl alcohol solution not only optically appropriate (non-absorbing, containing no autofluorescence, or light scattering) but also with an "anti fade" agent which is capable of reducing light-induced fading (photobleaching) of the fluorophore. Coverslips were air dried before microscope analysis.

Irradiated cells and empty-vector cells were used as a positive and negative control for DDR activation, respectively. Comparative immunofluorescence analyses were performed in parallel with identical acquisition parameters; 100-300 cells were screened for each antigen.

Brdu Incorporation Assay

Traditionally, the study of cell proliferation has involved the use of 3H thymidine to allow monitoring of DNA synthesis in individual cells by autoradiography, and hence identify proliferating cells or cell populations. More recently, alternative rapid non-radioactive techniques have been developed in which a thymidine analogue, 5-bromo-2'-deoxyuridine (BrdU), is incorporated into replicating DNA and subsequently detected using a specific antibody (Gratzner, H.G., Science, 1982). This technique requires the denaturation of cellular DNA to allow access to BrdU. This is usually achieved by treatment with acids or alkali, which may adversely affect cell and tissue morphology. To avoid this problem, I used a mild treatment with a nuclease to digest DNA to allow antibody access. This process is achieved under mild conditions, simultaneously with antibody incubation. Cells, plated on coverslips, were incubated with 10μg/ml BrdU (SIGMA) for a 6 h labelling period (for 6 hours in Figure 26 and Figure 56B; for 1 hour and 12 hours Fig.19). Cells were fixed with 4% paraformaldehyde for 10 minutes and permeabilized with 0.2% TritonX-100 for 10 minutes at room temperature. After 1 hour incubation with PBG blocking solution, cells were incubated with a mixture containing primary antibody (anti-BrdU 1:20), DNase (1:10, Stock concentration: 1U/μl, Promega), DNase buffer and MgCl2 at 3mM final concentration for 45 minutes at room temperature. Coverslips were then washed 3x with PBG and incubated with secondary antibody. DAPI staining was used to detect nuclei and Mowiol solution to mount coverslips. Proliferating cells were used as a control. At least 100-300 cells were screened for a statistically significant analysis.

Immunofluorescence and Fluorescence In Situ Hybridization (ImmunoFISH)

ImmunoFISH technique combines the immunofluorescence with an antibody that recognizes a cellular antigene and FISH with a probe that detects the presence of specific DNA sequences on chromosomes in metaphase or interphase cells. The binding to its target can be identified by a distinct fluorescence signal. A Peptide Nucleic Acid (PNA) probe is a synthetic DNA/RNA analogue capable of binding to DNA/RNA in a sequence-specific manner obeying the Watson-Crick base paring rules. In PNA molecules, a neutral peptide/polyamide backbone keeps the distances between the bases exactly the same as in DNA and gives PNA excellent properties for hybridizing to DNA or RNA. In addition, PNAs are highly resistant to degradation by DNases, RNases, proteinases and peptidases and are superior to DNA probes in terms of sensitivity and specificity. The fluorescence intensity of the spots is directly correlated to the length of the telomeres, thus it allows an exact measurement of the telomere length (Lansdorp Hum Mol Genet 1996).

Cells were fixed and probed as described in the corresponding immunofluorescence sections. Subsequently, after secondary antibodies incubation and washes, samples were fixed with 4% PFA and 0.1% Triton X-100 for 10 minutes at RT and reaction was then blocked with 100 mM Glycin, for 30 minutes at RT. Samples were washed 3 times with PBS and DNA was denaturated at 80°C for 5 minutes under a glass coverslip in the presence of the Cy3-conjugated telomeric PNA probe (Panagene, excitation wavelength 550 nm, emission wavelength 570 nm) in hybridization solution (70% formamide, 0.25% blocking reagent Roche, 10 mM Tris HCl pH 7.4, 0.5 μM telomeric PNA probe). The hybridization process took place in the dark at RT for 2 hours. Samples were washed twice for 15 minutes in wash solution I (70% formamide, 0.1% BSA, 10 mM Tris HCl pH 7.4) and twice for 5 minutes in wash solution II (100 mM Tris HCl pH 7.4, 150 mM NaCl, 0.08% Tween 20). They were stained with DAPI for 2 minutes, briefly washed with PBS and water and mounted with mowiol.

To detect TIF in tissue section, tissue sections were deparaffinized and heat treated in sodium citrate buffer (10mM Na–citrate, 0.05% Tween 20, pH.6) at 95°C for 45 min to retrieve antigens. Sections were then dehydrated by incubating them in 95% ethanol for 3 min. After air-drying, nuclear DNA was denatured for 5 min at 80°C in hybridization buffer containing Cy3-conjugated telomere-specific PNA (Cy3- (C3TA2)3; Panagene, Korea) at 0.5 **m**g/ml, 70% formamide, 12mM Tris–HCl pH.8.0, 5mM KCl, 1mM MgCl2, 0.08% Triton X-100 and 0.25% acetylated BSA (Sigma-Aldrich, St Louis, MO), followed by incubation in the same buffer for 2 h at room temperature. Slides were washed 3 times for 15 minutes with 70% formamide, 0.6 x SSC (90mM NaCl, 9mM Na–citrate (pH.7)). Afterwards slides were washed for 15 minutes in 2 **x** SSC. These washes were followed by 5 minutes wash in PBS and one 5 minutes wash in PBST (PBS.0.1% Tween 20; 5 min). Afterwards tissue sections were incubated with block buffer (4% BSA in PBST) for 30 min. It followed an overnight incubation with primary polyclonal anti-53BP1 in block buffer at 4°C. Tissue sections were then washed twice for 5 minutes in PBST. Afterwards they were incubated with secondary Alexa Fluor 488-conjugated goat anti rabbit antibody (Invitrogen, Carlsbad, CA) 1:1000 in block buffer for 1 h at room temperature. Slides were washed 3 times 5 minutes each with PBST, rinsed with water and mounted using DAPI containing mounting medium (Vector Laboratories, Burilngame, CA).

Telomere Length Measurements by Quantitative Fluorescence *In Situ* Hybridization (Qfish) and Flow Cytometry *In Situ* Hybridization (Flow-FISH)

Contact inhibited BJ cells were infected with -GFP or -H-RasV12 lentiviral vectors (see the section Lentiviral infection). To induce mitotic arrest cells were released in colcemid-containing medium (0.1mg/ml) immediately after lentiviral infection. In this way cells underwent a single DNA replication round in the presence (or not) of oncogenic Ras. Cells

were then incubated with a hypotonic solution of potassium chloride at 37°C for 15 min followed by fixation in Carnoy's fixative to then be processed for telomere fluorescence analysis by q-FISH and Flow FISH.

q-FISH consists in a software-based quantitative analysis of telomere fluorescence intensities after hybridization of denatured telomeres with a Cy3-conjugated telomere-specific PNA probe $(CCCTAA)_3$ on metaphase spreads (Hande et al., 1999). q-FISH provides estimation of telomeres length in each individual chromosome with the resolution of 200 base pairs. q-FISH was performed on metaphase spreads on a glass slide by hybridization with a Cy3 conjugated-Peptide Nucleic Acid (PNA) probe with a telomeric sequence. DAPI staining of DNA is used in q-FISH to measure the amount of DNA per each chromosome and normalize the telomeric PNA probe. Images were acquired on the same day (within 3 h) for all the samples using the Zeiss Axioplan 2 imaging fluorescence microscope. Fluorescence intensity of telomere signals was measured using the *in situ* imaging software (Metasystems, Germany).

The total amount of telomere DNA was also measured at the single-cell level by flow-FISH as described in (d'Adda di Fagagna et al., 1999; Poonepalli et al., 2005). Flow-FISH is a cytogenetic technique that couples flow cytometry with fluorescence in situ hybridization for the analysis of telomere fluorescence intensities at single-cell level. We measured the average telomere fluorescence at chromosome ends by fluorescence in situ hybridization combined with flow cytometry (flow-FISH) with minor modifications. Cells were hybridized with a fluorescein isothiocyanate (FITC)-conjugated telomere-specific (CCCTAA)X3 PNA probe (0.3 ug/ml) (Perceptive Biosystems) in hybridization buffer (70% formamide, 20 mM Tris, 0.1% BSA). After denaturation at 86°C for 10 min, hybridization was performed for 2 h at RT in the dark. The unbound telomere PNA probe was removed by post hybridization washes. Afterwards cells were counterstained with propidium iodide. Cells were then analysed on a flowcytometer (FACSCalibur Becton-Dickinson, San Jose, CA,USA) using argon ion laser (488 nm) to excite FITC. We used

FITC-labelled fluorescent calibration beads (QuantumTM-24 Premixed; Flow Cytometry Standards corporation) to correct for daily shifts in the linearity of the flow cytometer and fluctuations in the laser intensity and alignment and to express the results in standard fluorescence units. The resulting calibration curve was then used to convert telomere fluorescence data to molecules of equivalent soluble fluorochrome units (MESF), allowing comparison of results between experiments. Studies were carried out blind.

Imaging

Immunofluorescence and immunoFISH images were acquired using a wide field Olympus Biosystems Microscope BX61 or a Leica TCS SP2 AOBS confocal laser microscope. To allow a more accurate signals discrimination and detection of co-localization events, confocal sections were obtained by acquisition of optical z-sections at different levels along the optical axis. Co-localization between DDR and telomeres was assessed by ImageJ software with co-localization ImageJ plug-in on confocal 3D stacks. Two points were considered co-localizing if their respective intensities were higher than the threshold of their channels, and if the ratio of their intensity was higher than the ratio setting value. Comparative immunofluorescence analyses were performed in parallel with identical acquisition parameters.

Fluorescence microscopy for DNA Molecular Combing was performed on an UltraVIEW VoX (Perkin Elmer) spinning disk confocal unit, equipped an EclipseTi inverted microscope (Nikon), a C9100-50 emCCD camera (Hamamatsu) and driven by Volocity software (Improvision, Perkin Elmer). Images were acquired using a 40x/0.95 NA dry objective. The right focal plane was maintained using the Nikon Perfect Focus system.

Immunoblotting

Cells were lysed in Laemmli sample buffer (2% SDS, 10% glycerol, 60mM Tris pH 6.8) and 50 micrograms of whole cell extracts were resolved by sodium dodecyl sulphate-

polyacrylamide gel electrophoresis (SDS-PAGE), transferred to nitrocellulose and probed with the antibody of interest. The amount of proteins in the samples was measured by the biochemical Lowry protein assay, or Lowry method. Copper (II) ions in alkaline solution react with protein to form complexes, which react with the Folin-phenol reagent, a mixture of phosphotungstic acid and phosphomolybdic acid in phenol. The product becomes reduced to molybdenum/tungsten blue and can be detected colorimetrically by absorbance at 750nm. SDS is an anionic detergent, which denatures secondary and non-disulfide linked tertiary structures, that unfolds the protein, giving a near uniform negative charge along the length of the polypeptide, allowing separation only by molecular weight.

A tracking dye, bromophenol blue, is added to the protein solution to allow the tracking of the progress of the protein solution through the gel during the electrophoretic run. Proteins were further denatured by heating at 95°C for 5 minutes and disulfide linkages were reduced by β-mercaptoethanol. Protein solution run is performed in two layers of gel, namely stacking or spacer gel and resolving or separating gel. The stacking gel is a large pore polyacrylamide gel (4%) in which proteins are concentrated, prepared with Tris buffer pH 6.8 of about 2 pH units lower than that of electrophoresis buffer. This gel is cast over the resolving gel, which is a small pore polyacrylamide gel. The Tris buffer used is of pH 8.8. Resolving gel is used for separating different range of proteins: I commonly used 6% gel for > 100 kDa proteins, 10% gel for 40-100 kDa proteins and 15% gel for < 40 kDa proteins, in running buffer (Running Buffer 10X: 250mM Tris base, 2M glycine, 50ml SDS 20%; pH 8.3). After running, proteins were transferred to nitrocellulose membrane by a wet electroblotting transfer method with transfer buffer (transfer buffer 10X: 250mM Tris base, 2M Glycine) plus 20% methanol. Following protein transfer, membrane can be temporarily stained with Ponceau to assess the transfer efficiency. Ponceau is a negative stain, which binds to the positively charged amino groups of the protein and it also binds non-covalently to non-polar regions in the protein. Blocking of aspecific sites and primary and secondary antibody incubations are carried out in 5% milk in T-TBS (Tween 0.1% in

Tris-Buffered Saline); all the washes between incubations are performed in T-TBS. The primary antibody is specific to the protein of interest, whereas the secondary antibody is a modified antibody, which is linked to an enzyme (HRP – horse radish peroxidase) that, in the presence of the acridan-based substrate, produces localized light in the region where the antibody is bound to the membrane. The localized light, which is emitted from the bands, is detected by photosensitive photographic film. This method of detection is called chemiluminescence.

ROS measurements

Several fluorescent probes and new methods have been developed to monitor ROS generation in intact living cells. Fluorescent probes used for determining intracellular ROS in intact living cells must fulfil specific requirements: effective cell loading with the cell-permeant fluorogenic probe; oxidation of the fluorogenic probe by cellular ROS (but not by spontaneous auto-oxidation); stability and retention (low leakage) of the fluorescent probe inside the cell; easy detection of the fluorescent probe with commonly used fluorescent microscopes and lack of self-toxicity. The commonly used fluorescent probes, derived from fluorescein, rhodamine, ethidium, or other fluorescent dyes, are dehydrogenated into colourless and non-fluorescent dehydro derivatives. Hydroethidine (dihydroethidium, DHE) is a dehydro derivative of ethidium, which has blue fluorescence in the cytoplasm and does not intercalate into DNA, and can undergo a two-electron oxidation to form the DNA-binding fluorophore ethidium bromide, in a reaction relatively specific for superoxide, with minimal oxidation induced by other ROS (Amir, 2008). Ethidium then binds DNA and stains the nucleus with a bright fluorescent red, since it has an excitation wavelength at 518nm and an emission one at 605nm. Thus, for ROS measurement, cells were incubated for 30 min with 5μM DHE (Molecular Probes, Invitrogen) in complete culture medium at 37°C; cells were washed with PBS before live

imaging either by widefield or confocal microscopes without fixation. All images were obtained within 30 minutes post-treatment.

Fluorescence Activated Cell Sorting (FACS) analysis

FACS is a specialized type of flow cytometry. It provides a method for analyzing and sorting a heterogeneous mixture of biological cells, based upon the specific light scattering and fluorescent characteristics of each cell. It gives fast, objective and quantitative recording of fluorescent signals from individual cells as well as physical separation of cells of particular interest. Analyzable features range from physical cell properties, such as cell size and morphology, to expression of proteins of interest, by immunodetection via fluorochrome conjugated antibodies and quantification of cell DNA content to evaluate cell cycle progression or apoptosis. For cell cycle analysis, after double thymidine block cells were released in BrdU containing medium (33μM BrdU) for 30 minutes. Cells were then fixed with 75% ethanol (Panreac), permeabilized with 2N HCl (Panreac) for 30 minutes at RT and the pH equilibrated using 0,1M BORAX (Sigma) for 2 minutes. Afterwards cells were incubated for 1h at room temperature with a mouse anti-BrdU antibody (BD) in 1% BSA/1X PBS, washed and stained with a donkey anti- mouse FITC-conjugated antibody (Jackson). Stained cells were treated with RNAse A (Sigma) followed by DNA staining with 2,5 ug/ul propidium iodide (Sigma) O/N at 4°C. BrdU intensities have been acquired on FACS Calibur and analyzed using the FLOW JO software.

Quantitative Real Time PCR

RNeasy Mini Kit (Qiagen) was used for total RNA extraction from cultured cells, according to manufacturer's instructions. Total RNA was quantified with NanoDrop spectrophotometer (Thermo Scientific). 1 μg of RNA was retrotranscribed using

SuperScript VILO cDNA Synthesis Kit, following manufacturer's instructions. For each qPCR reaction was used a volume corresponding to 10 ng of initial RNA.

The Real Time PCR Instrument permits real time detection of PCR products as they accumulate during PCR cycles. The low fluorescence level, characteristic of the initial PCR cycles, defines the reference for the plot of fluorescence signal *vs* cycle number. A fixed fluorescence threshold can be set above the baseline. The parameter Ct (threshold cycle) is defined as the cycle number at which the fluorescence becomes higher than the fixed threshold. So, the higher the initial amount of the sample, the sooner accumulated product is detected in the PCR process as a significant increase in fluorescence, and the lower the Ct value. Ct values are very reproducible in replicates because the threshold is picked to be in the exponential phase of the PCR, where there is a linear relation between log of the change in fluorescence and cycle number. When the Ct values were higher than 35, PCR result was classified as undetermined.

The Sybr Green-based qPCR experiments were performed on a Roche LightCycler 480 sequence detection system in triplicate. Sybr Green binds to all double-stranded DNA species present in the sample, thus during the reaction the fluorescence intensity increases proportionally to the amount of PCR product produced. Ribosomal protein large P0 (Rplp0) was used as a control gene for normalization.

Primer sequences for qRT–PCR:

RPPO-fwd,5′-TTCATTGTGGGAGCAGAC-3′;

RPPO-rev, 5′-CAGCAGTTTCTCCAGAGC-3′;

Nox1-fwd,5′-AAGGATCCTCCGGTTTTACC-3′;

Nox1-rev, 5′-TTTGGATGGGTGCATAACAA-3′;

Nox2- fwd, 5′-GGTTTTGGCGATCTCAACAG- 3′;

Nox2- rev, 5′- CGATGGTTTTGAAAGGGTGA- 3′;

Nox3- fwd, 5′- AGTTCAAGCAGATTGCCTACAA- 3′;

Nox3- rev, 5′- CGAGAGAGCTTTAGGTCCACA- 3′;

Nox4- fwd, 5′- GCTGACGTTGCATGTTTCAG- 3′;

Nox4- rev, 5′- CGGGAGGGTGGGTATCTAA- 3′;

Nox5- fwd, 5′- CGTCTGTGCCGGCTTATC- 3′;

Nox5- rev, 5′- CCAATTCCAGATACAACATGACTG- 3′;

DNA Molecular combing see the section ***DNA Molecular Combing: Technology set up***

Fluorescence in situ hybridization (FISH) coupled with DNA Molecular combing see the section ***DNA Molecular Combing: Technology set up***

Antibodies

I used anti-γH2AX, (Millipore); anti-BrdU BU 1/75, anti-H2AX and anti-H3 (Abcam); anti-BrdU (Becton Dickinson); anti-ssDNA (Chemicon); anti-ATM, anti-vinculin clone hVIN-1 and anti-ERK1/2 (SIGMA); anti-pS/TQ, anti-CHK2 pT68, anti- phospho-ERK1/2, anti-p53 pS15 and anti-H3K27me3 (Cell Signalling Technology); anti-ATM pS1981 (Rockland); anti-p53 (DO1); anti-Ras, (BD Transduction Laboratories); (SIGMA); anti-53BP1 (Novus Biologicals), anti-CDC6 (Santa Cruz); anti-Ezh2 (home made, hybridoma BD 43).

For triple labeling of DNA molecular combing I used isotype specific secondary antibodies: Goat Alexa 546 anti-mouse IgG1, Goat 647 anti- Mouse IgG2a and Goat 488 anti Rat and (Invitrogen, Molecular Probes).

Statistical analyses

Results are shown as means plus minus standard deviation (s.d.) or standard error of the mean (s.e.m.) as indicated. For means measurements p-value were calculated by Student's

two-tailed t-test or in case of a non parametric distribution, by Wilcoxon test. For qualitative data p-value were calculated by chi-square test with 1 degree of freedom.

RESULTS

CHAPTER 1. Telomeres are hypersensitive to oncogene-induced replication stress.

1.1. Oncogenic H-RasV12 expression causes fragile telomeres and stochastic telomere shortening.

Since fragile sites are particularly sensitive to oncogene induced DNA replication stress (Di Micco et al., 2006), and telomeres resemble fragile sites (Sfeir et al., 2009), we asked whether oncogenic Ras could enhance telomeres fragility, thereby altering telomere structure and function. To this end, contact-inhibited human normal skin fibroblasts (BJ) were transduced with -GFP or -H-RasV12 lentiviral vectors. Cells were then replated into colcemid containing medium and metaphase chromosome spreads were prepared and analysed for their telomeric structures.

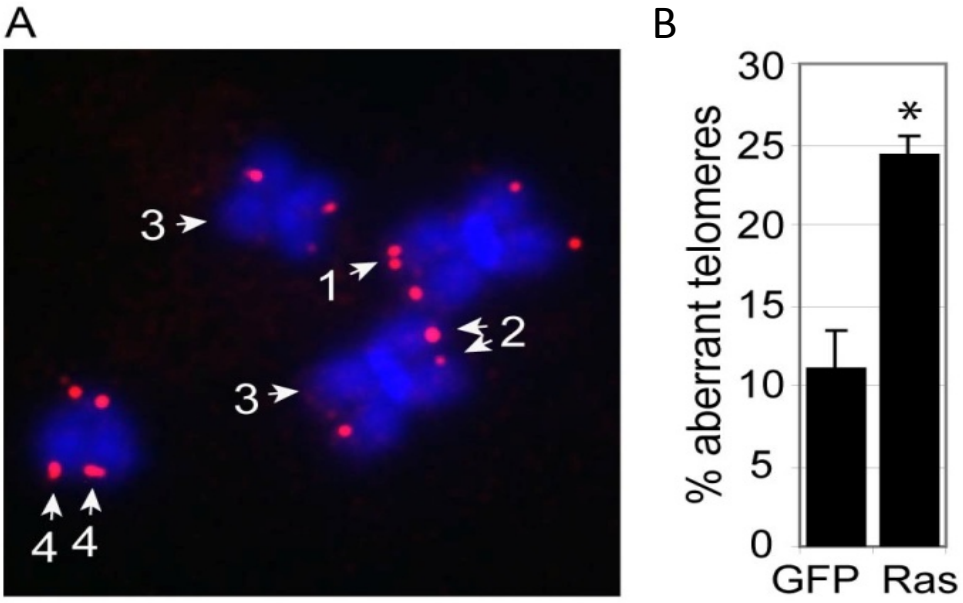

Figure 14. Oncogenic signalling causes fragile telomeres.
(A) Metaphase spreads from contact inhibited BJ cells, transduced with lentivirus encoding oncogenic Ras, and subsequently released into colcemid-containing medium to arrest them in mitosis. Chromosome ends, labelled using a telomeric Cy3-conjugated-Peptide Nucleic Acid (PNA) probe $(CCCTAA)_3$ (red), either displayed telomeric doublets (physiological condition; 1), different signal intensities on sister chromatids (2), absence of signal (3), or diffuse telomeric staining patterns (4). (B) Bar graph: percentage of aberrant telomeric structures (± s.d.) in GFP (69 metaphases) and Ras (98 metaphases) expressing cells (n.3); *P<0.001. Statistical significance was calculated by unpaired t-test. Performed by Haihe Ruan. Adapted from (Suram et al., 2012).

Upon oncogenic Ras expression, 25% of all chromosome ends analysed displayed aberrant and fragile telomeres (Figure 14A-B generated by U. Herbig group, New Jersey Medical

School), while this was not the case in the GFP-transduced cells. Furthermore the fluorescence signal intensities of sister telomeres were noticeably different, or undetectable. These data suggest that oncogene-induced DNA replication stress is also responsible for stochastic telomere attrition (Figure 14A-B). To confirm this hypothesis we asked our collaborator Prakash Hande (University of Singapore) to analyse the telomere fluorescence by Flow-FISH (Fluorescence In Situ Hybridization) (Figure 15A) or q-FISH (Figure 15B), in BJ cells expressing oncogenic Ras, or -GFP, generated in our laboratory. Briefly, contact inhibited BJ cells were infected with -GFP or -H-RasV12 lentiviral vectors. They were then released in colcemid-containing medium to induce mitotic arrest to then be processed for telomere fluorescence analysis by Flow FISH and q-FISH. In this way cells underwent a single DNA replication round in the presence (or not) of oncogenic Ras.

Flow-FISH is a cytogenetic technique developed by Peter M. Lansdorp and Prakash Hande that couples flow cytometry with fluorescence in situ hybridization for the analysis of telomere fluorescence intensities at single-cell level. After hybridization with fluorescein isothiocyanate (FITC)-labelled telomere-specific peptide nucleic acid (PNA) probe, telomere fluorescence was measured by flow cytometry (d'Adda di Fagagna et al., 1999; Poonepalli et al., 2005). Results are shown in Figure 15A.

q-FISH consists in a software-based quantitative analysis of telomere fluorescence intensities after hybridization of denatured telomeres with a Cy3-conjugated telomere-specific PNA probe $(CCCTAA)_3$ on metaphase spreads (Hande et al., 1999). Results are shown in Figure 15B.

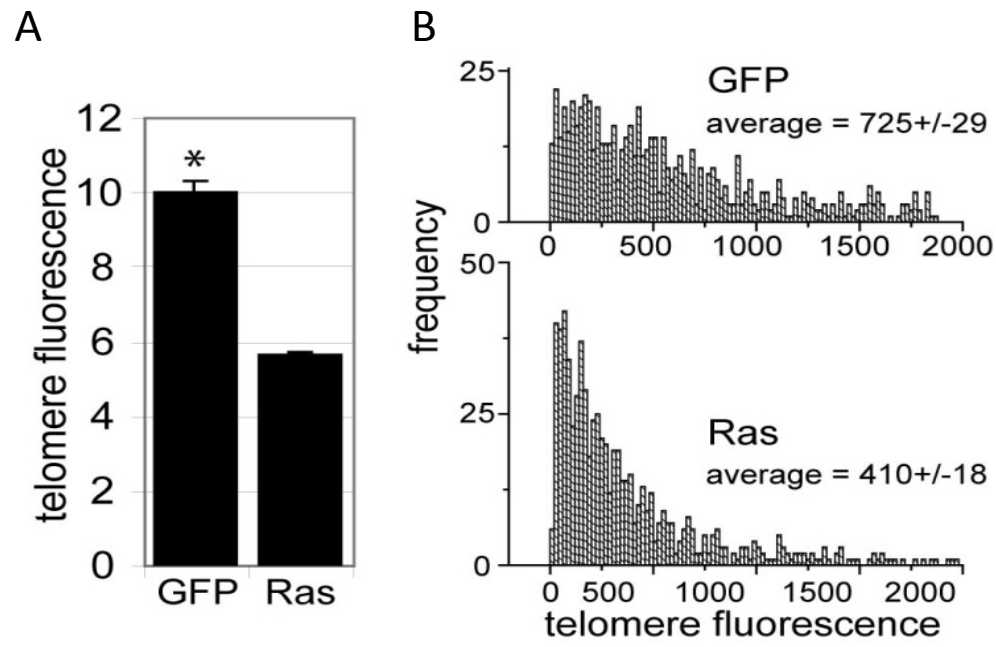

Figure 15. Oncogenic signaling causes stochastic telomere attrition.
Contact inhibited BJ cells were transduced with lentivirus encoding GFP (control) or oncogenic Ras followed by release into colcemid-containing medium. Telomere fluorescence (arbitrary units, mean±s.d.) as measured by flow-FISH (A) or q-FISH (B) in Ras- and GFP-transduced cells; *P<0.001. Statistical significance was calculated by unpaired **t**-test. Performed by Haihe Ruan, Marzia Fumagalli, Resham Lal Gurung, Manoor Prakash Hande. Adapted from (Suram et al., 2012).

Oncogenic Ras expression induced dramatic telomere shortening with a 40% reduction in telomeric repeats, as compared to the control, detectable by both techniques (Figure 15). This reduction in telomeric lengths seems to occur at all telomeres equally, with no preference for shorter or longer telomeres as demonstrated by qFISH that detects individual telomere lengths (Figure 15B).

Overall these results indicate that oncogenic Ras expression causes fragile telomeres and it is responsible for a stochastic telomere shortening.

1.2. Dysfunctional telomeres increase in vitro and in vivo upon oncogenic activation

Given the observed dramatic and rapid telomeric shortening in oncogene-expressing cells, we asked whether this could account for dysfunctional telomeres. To test this, our collaborator Utz Herbig monitored and quantified DDR activation, as detected by 53BP1 focus formation, at telomeric sequences by immunoFISH experiments, in normal human

fibroblast transduced with H-Ras V12 or empty vector (EV) (Figure 16A-B).

Oncogenic Ras expression caused a high degree of both non-telomeric and telomeric DDR foci. Interestingly, most of non-telomeric DDR foci were resolved within weeks, in contrast to telomeric DDR foci, which persisted over time (Figure 16B).

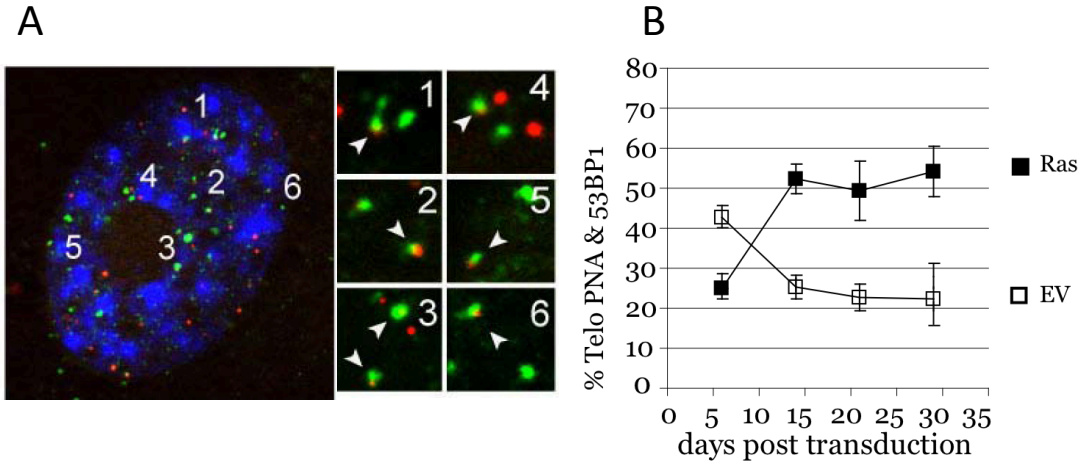

Figure 16. Dysfunctional telomeres increase in vitro upon oncogenic activation.
(A) Micrographs: dysfunctional telomeres in Ras expressing cells at days 29 following retroviral transduction. TIF were visualized by immunoFISH to simultaneously detect 53BP1 (green) and telomeres using a Cy3-labeled telomeric PNA probe (red). Enlarged versions of the numbered areas are shown on the right. White arrows indicate 53BP1-telomere co-localizations. (B) Percentages of 53BP1 foci co-localizing with telomeres in DDR positive cells (left y-axis; solid squares) vs. the average number of 53BP1 foci per cell in DDR positive cells (right y-axis; open circles) in Ras expressing cells vs control cells. Performed by Anitha Suram. Adapted from (Suram et al., 2012).

Our analyses were next extended for the presence of dysfunctional telomeres also *in vivo.* Human nevi are a well-characterized example of oncogene-induced senescent cells occurring *in vivo*. As demonstrated in (Michaloglou et al., 2005), most of human nevi are melanocytes that display classical features of senescence, due to the presence of the oncogenic form of BRAF ($BRAF^{V600E}$), a protein kinase down stream of Ras. Nevi normally remain in this growth arrest state for decades. They rarely progress into malignancy, but when they do, they inactivate other tumour suppressor genes, such as p53. Thus, we decided to use human nevi as an in vivo system for the study of the impact of oncogene activation on telomere dysfunctions in vivo. Specifically, we analysed *human* benign nevi, dysplastic nevi and melanoma for the presence of dysfunctional telomeres (Figure 17A-B).

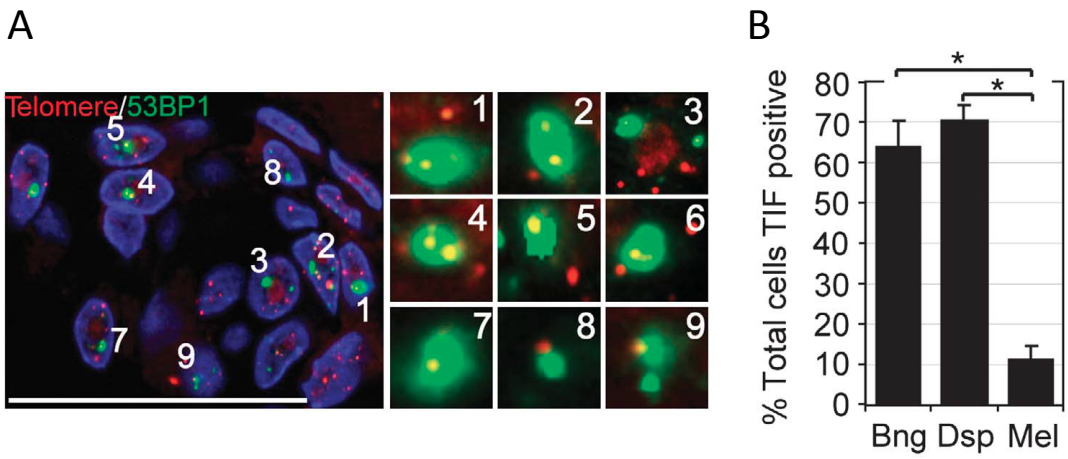

Figure 17. Dysfunctional telomeres increase in vivo upon oncogenic activation.
(A) Dysfunctional telomeres in human nevi. Tissue sections from benign nevi were processed by immunoFISH to simultaneously detect 53BP1 (green) and telomeres (red). Enlarged versions of the numbered DNA damage foci showing co-localization with telomeres are shown in the right micrographs. Note that only one optical slice is displayed. (B) Quantitation of co-localization between 53BP1 and telomeres in indicated lesions (mean±s.d.). A total of 13 benign nevi (1355 53BP1 foci), 13 dysplastic nevi (2968 53BP1 foci), and 7 melanoma (891 53BP1 foci) were counted; *P<0.001. Performed by Anitha Suram. Adapted from (Suram et al., 2012).

Our collaborator Utz Herbig observed that the majority of all DDR foci analysed in cells of benign and dysplastic nevi specifically co-localized with telomeric repeats, demonstrating that DDR signalling was primarily originating within telomeric DNA (Figure 17A). Samples were analysed for the presence of telomere dysfunction induced DNA damage foci (TIF), with cells scored as TIF positive, when at least 50% of 53BP1 foci colocalized with telomeric repeats. We discovered that most of melanocytic cells in benign (64%) and dysplastic nevi (70%) were TIF positive, while this was not the case for cells in malignant melanoma that were rarely scored as TIF positive (11%, Figure 17B).

These results indicate that oncogene activation induce dysfunctional telomeres both *in vitro* and *in vivo.*

1.3 Oncogenic Ras expression impairs telomere replication

The results described so far indicate that oncogene expression causes telomere fragility, telomere attrition and subsequent appearance of dysfunctional telomeres. Since our group had previously demonstrated that oncogenic Ras induces global DNA replication stress

that preferentially impacts on fragile loci, I then asked whether dysfunctional telomeres could be a result of oncogene-induced DNA replication alterations occurring at telomeres.

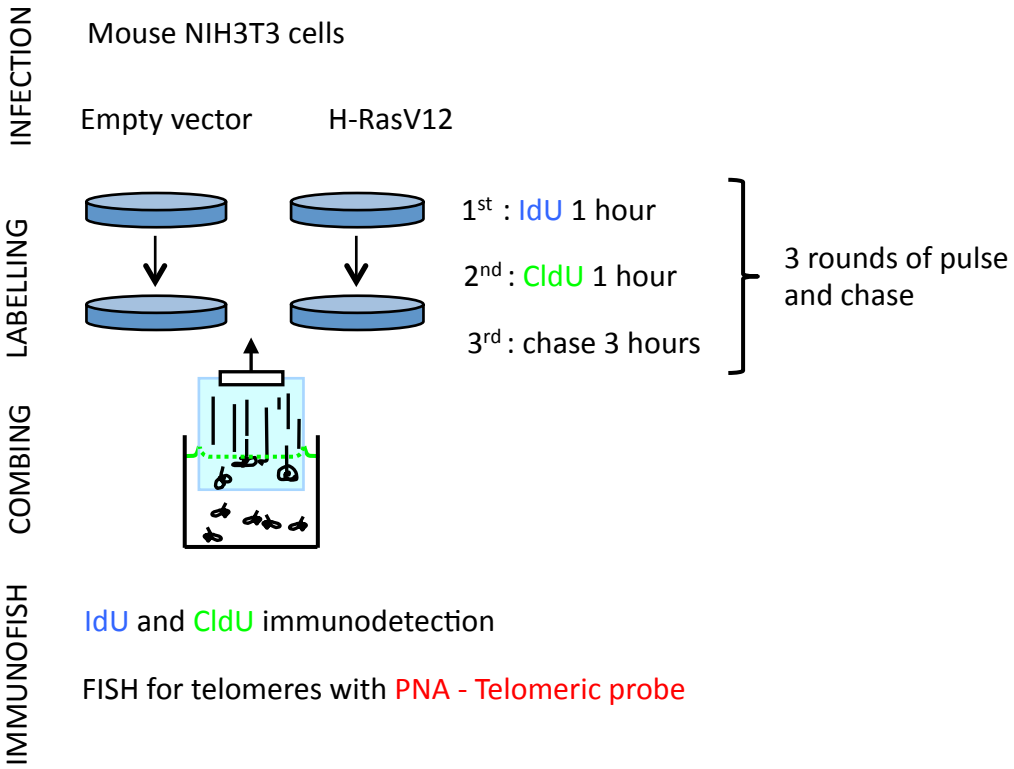

Figure 18. Experimental plan.
Three days after retroviral transduction with H-RasV12 or empty vector (EV) mouse fibroblasts were pulse labelled with halogenated nucleotides. Subsequently the DNA was extracted, combed, and processed by immunoFISH (for a detailed description of DNA combing see the section *DNA molecular combing*).

To test this hypothesis I applied DNA molecular combing technique together with FISH. These techniques allowed me to study DNA replication dynamics at specific genomic sites, the telomeres. In Figure 18 the experimental plan is shown. I used mouse fibroblast cells because mouse cells have telomeres sufficiently long - raging from 40 to 150 kb - to be studied within the resolution limits of DNA molecular combing technique and imaging setups commonly used in association with it. I infected mouse fibroblasts cells with H-RasV12, or with an empty vector (EV). 4 days after infection, cells were pulse-labelled with thymidine analogues, following a pulse and chase protocol adapted from (Sfeir et al., 2009). Since I aimed at studying replication at specific genomic loci – the telomeres - I needed to optimize the procedure in order to maximize the probability of telomere replicating while giving the pulses with the thymidine analogues. So I performed 3 rounds

of pulse and chase: 1 hour pulse with Iododeoxyuridine (IdU), 1 hour pulse with Clorodeoxyuridine (CldU) followed by 3 hours of chase, repeated for 3 times. The total duration of the three rounds of pulse/chase was 12 hours, which is less than the cell doubling time, thus ensuring that cells will be labelled once per cell cycle.

In parallel to the pulse and chase procedure, cells were incubated with BrdU to check that the proliferation rates during labelling were not changing between oncogenic Ras-expressing cells and control cells. We tested BrdU incorporation rates at the beginning of the procedure, after 1 hour of BrdU incubation, as well as at the end of the procedure, after 12 hours of BrdU incubation. As shown in Figure 19 the proliferation rates of EV- and HRasV12-transduced cells do not differ throughout the pulse labelling procedure.

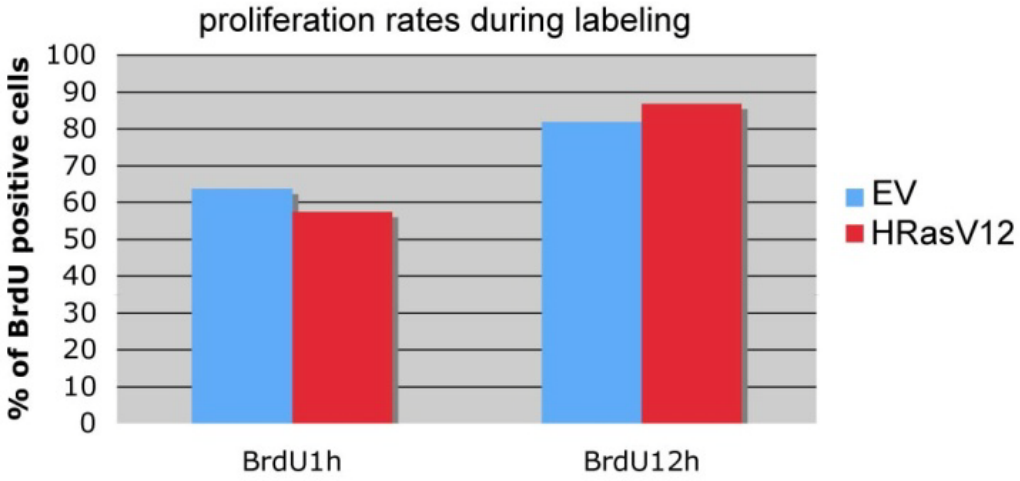

Figure 19. The proliferation rates of EV- and HRasV12-transduced cells do not differ during pulse labelling.
Percentage of control- (EV) and H-RasV12-transduced mouse cells that stained positive for BrdU. BrdU was added to the culture medium for the indicated time intervals.

I then performed DNA molecular combing coupled with immunoFISH. A scheme illustrating replication fork progression at the telomeric locus is shown in Figure 20.

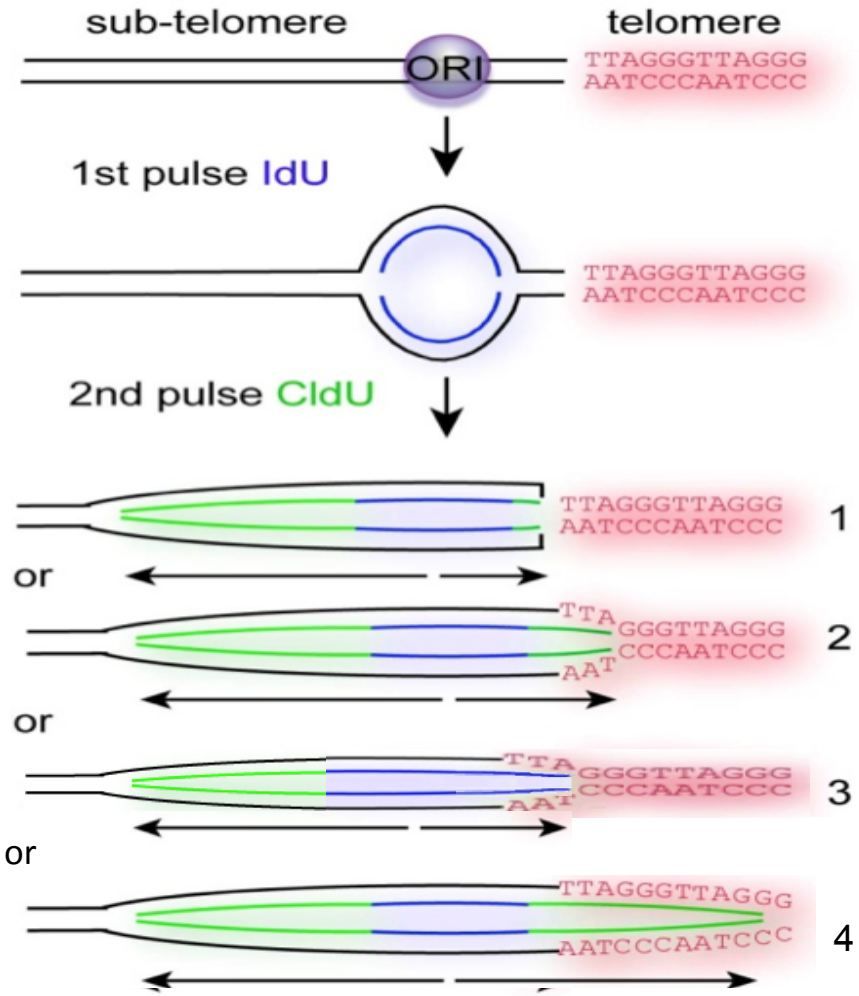

Figure 20. Scheme illustrating replication fork progression at the telomeric locus.
As an example, a newly fired DNA replication origin (ORI) that incorporates IdU during the first pulse (blue) is shown. CldU (green) is then incorporated during the second pulse. Telomeric repeats were detected using a Cy3-conjugated telomeric PNA (red). We interpret symmetric replication signals as normal replication fork progression (#4). Asymmetric DNA replication bubbles bordering, or extending into-telomeric repeats, as inferred by asymmetric replication signals were considered as telomeric fork stalling events (#1, 2 and 3).

By performing immunoFISH on combed DNA I could identify three different replication patterns occurring at telomeres: replication fork fully replicating the telomeres; replication fork partially replicating the telomere; replication fork arresting at the subtelomeric-telomeric border (within 2 kb) (Figure 21A).

I scored 140 telomeres for control cells and 171 for oncogenic Ras-expressing cells. By quantifying these telomere for the replication patterns shown in Figure 21A, I discovered that in oncogenic Ras-expressing cells, replication fork arresting at the subtelomeric-telomeric border increased (2.8% in EV vs 8.2% in Ras) as well as the replication fork partially replicating the telomere (6.3% in EV vs 14.6% in Ras). Instead the replication

forks that successfully replicate the telomere in its full length are decreased compared to control (22% in EV vs 7% in Ras) (Figure 21B). These results indicate that oncogenic Ras expression impairs telomeric DNA replication.

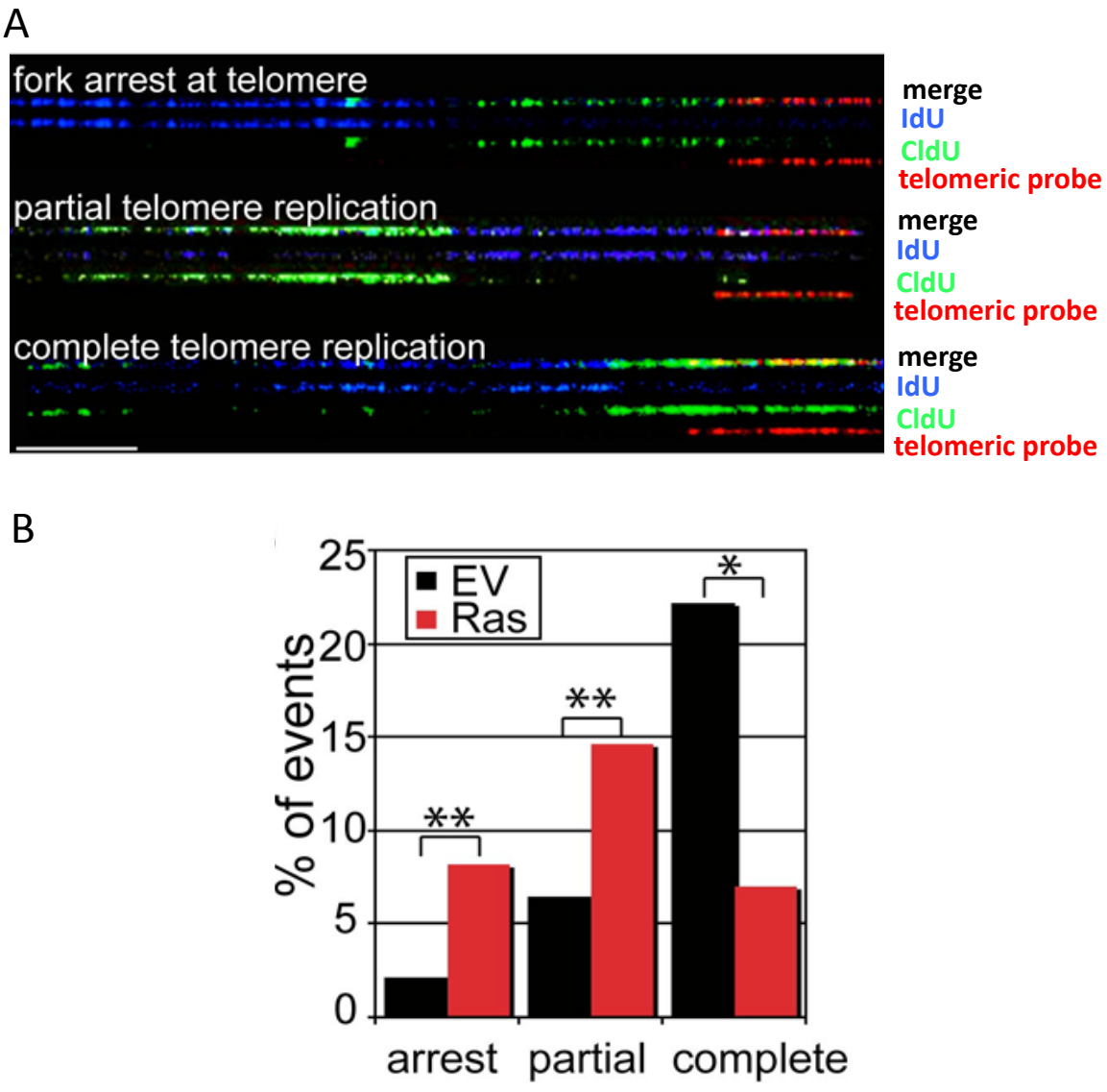

Figure 21. Oncogenic signals impair DNA replication at telomeres.
(A) Representative images of analysed DNA replication patterns. IdU: blue signal; CldU: green signal; telomere: red signal. Scale bar: 40 kb. (B) Quantitation of the percentage of DNA combing signals revealing DNA replication forks arrest at the start of a telomeric tract (within 2 kb), partial and complete telomere replication in empty vector- (EV; black bars; n=140) and H-RasV12-expressing (Ras; red bars; **n.**171) cells. ***P**<0.001, ****P**<0.02.

This first analysis was based only on the quantification of the replication patterns shown in Figure 21A, regardless the level of symmetry of fork progression. To assess the symmetry of fork progression the ratio between the replication signal of the 1st pulse over the replication signal of the 2nd pulse is calculated. Before proceeding with this analysis, it is

crucial to assess that the end of each replication signal is not due to DNA fiber breakage, since this prevents the assessment of the correct length of the replication signal. Since it was not possible to stain for DNA because 3 wavelengths were already used for IdU, CldU and PNA telomeric probe stainings, - the only case in which I could be sure about the length of replication signal, was the presence of another replication signal after the gap. Indeed this pattern indicates that in the observed gap a replication origin has fired during the first pulse and then the forks proceeded their replication in the two directions, one subtelomeric, toward the centromere, and the other end towards the telomere. Thus in this first analysis it was not always possible to assess the symmetry of fork progression at telomeres, due to the lack of enough replication signals. However I performed this first simpler analysis to have an initial idea of the effect of oncogenic Ras expression on the telomere replication. Given these preliminary encouraging results I proceeded with the analysis of symmetry of fork progression.

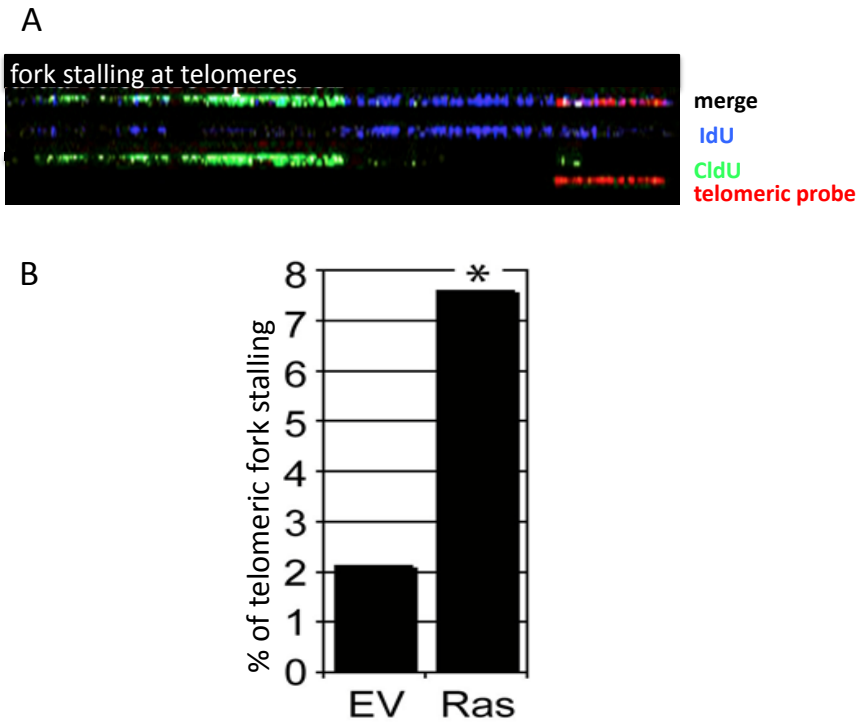

Figure 22. Oncogenic signals cause stalling of telomeric DNA replication forks.
(A) Representative image of replication fork stalling. Rows 1: merged image; 2: IdU (blue); 3: CldU (green); 4: telomere (red). Scale bar: 40 kb. (B) Quantitation of fork stalling events at telomeres in empty vector- (EV; **n.**140) and H-RasV12-expressing (Ras; **n.**171) cells. ***P**<0.03.

Thus to make a more consistent analysis, where possible, I also scored replication patterns for replication fork stalling events - inferred by asymmetric replication signals inside or at telomeres (Figure 20, patterns 1, 2 and 3). An example of fork stalling is shown in Figure 9A. Strikingly the percentage of fork stalling at telomeres is increased upon Ras activation (2.1% in EV vs 8.8% in H-RasV12; p=0.03 Figure 22B). These results clearly show the hypersensitivity of telomeres to oncogene-induced replication stress. To further support this result, I analysed the level of fork stalling in the rest of the genome – whole genome excluding telomeric loci. To this end I performed this whole genome analysis by assessing the symmetry of DNA replication fork progression as the ratio between left and right fork speed derived from the same DNA replication origin. A ratio of 0 indicates a completely asymmetric fork; as the ratio increases, the level of asymmetry decreases; a ratio of 1 indicates completely symmetric DNA replication fork progression. All the ratios (n=41) were sorted from the lowest to the highest values and plotted in the graph shown in Figure 23.

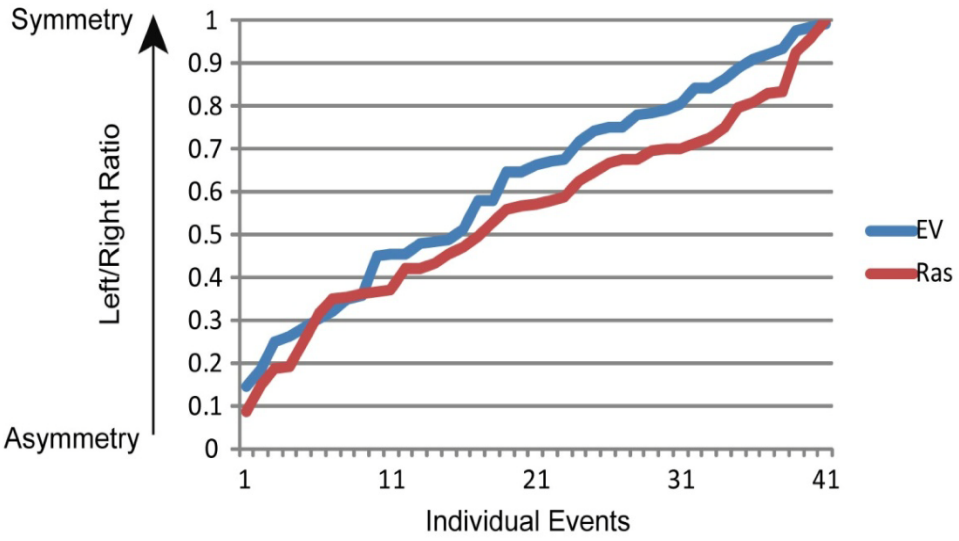

Figure 23. Oncogenic signals have a modest impact when analysed at the whole genome level.
Whole genome analysis of fork stalling was performed by assessing the symmetry of DNA replication fork progression and by generating a ratio between left and right fork speed derived from the same DNA replication origin. A ratio of 0 indicates a completely asymmetric fork; as the ratio increases, the level of asymmetry decreases; a ratio of 1 indicates completely symmetric DNA replication fork progression. All the ratios (n=41) were sorted from the lowest to the highest values and plotted in this graph. Telomeric loci were excluded from this analysis. EV, control cells; Ras, H-RasV12 expressing cells. (Wilcoxon test, p <= 0.9963).

This graph shows that in oncogenic Ras-expressing cells there is a slight decrease in the symmetry of fork progression at whole genome level as respect to the control, and this decrease is not statistically significant. These results revealed a more modest impact in response to oncogene activation at whole genome level than at telomeric loci further supporting the idea that telomere are hypersensitive to oncogene-induce replication stress.

These whole genome results are not in contrast with the previous data about the impact of oncogenic Ras on DNA replication dynamics, rather, they indicate the extreme sensitivity of telomeres to oncogene-induced DNA replication stress compared to the bulk of the genome.

While making comparison between the data about the impact of oncogenic Ras on DNA replication dynamics described in (Di Micco et al., 2006) and the data shown here, it is important to keep in mind that this two data sets derive from different experimental set up, that were properly designed to assess specific but different scientific questions. First of all, here I used mouse fibroblast cell line to have telomeres long enough to be detected with molecular combing technique and I used a pulse and chase labelling protocol. Differently, in the work of (Di Micco et al., 2006) DDR deficient (shChk2) BJ human fibroblasts were used applying standard pulse labelling protocol. Moreover, given the differences in labelling protocol and experimental conditions, I could not assess all the parameter they assessed, and the outcomes of these analyses are comparable just to a certain extent.

CHAPTER 2. Characterization of oncogene-induced altered DNA replication and DNA damage response activation.

Oncogene-induced DNA hyper-proliferation is commonly thought to be the trigger for DNA damage generation that is then responsible for DDR activation and consequent establishment and maintenance of OIS (Bartkova et al., 2006; Di Micco et al., 2006; Halazonetis et al., 2008). However, recent studies demonstrated that DNA damage itself can alter DNA replication kinetics (Doksani et al., 2009; Ge et al., 2007; Petrini, 2009). When single strand DNA is exposed (Ge et al., 2007), or when a DNA double strand break occurs (Doksani et al., 2009), the dormant replication origins in the immediate vicinity, are fired. Even though the signal that produced the effect of origin firing is still elusive (Petrini, 2009), the discovery further highlights the complex interplay between oncogene activation, DNA replication, and DNA damage (Doksani et al., 2009).

Previous studies demonstrated that oncogene activation alters DNA replication dynamics - resulting in increased origin firing together with increased fork stalling and premature termination of replication - leading to DNA damage accumulation that is then responsible for a robust DDR activation. However these studies were performed on DDR-deficient (shCHK2) fibroblasts (Di Micco et al., 2006) or in tumor cell line (U2OS) (Bartkova et al., 2006). In addition, more recent studies tried to further dissect the mechanism underlying the oncogene-induced replication stress by analysing DNA replication dynamics only at a single time point after oncogene activation (Jones et al., 2013; Neelsen et al., 2013). The results obtained shed new light on the complexity of oncogene-induced DNA replication stress, linking it to increased replication initiation that results in forks colliding with transcription machinery (Jones et al., 2013), or to the accumulation of unusual replication intermediates that entering mitosis lead to genomic instability (Neelsen et al., 2013).

However given the complexity of the molecular mechanisms exploited by oncogene activation to induce replication stress and subsequent DDR activation, more detailed

studies to dissect the kinetics of oncogene-induced altered DNA replication dynamics are needed.

Thus, I performed a time course analysis to assess the effects that oncogenic Ras expression has on DDR activation, DNA replication dynamics, from the initial hyperproliferative burst till the establishment of oncogene-induced cellular senescence (OIS). Such an approach has never been reported in the literature so far.

Therefore I transduced BJ hTERT human fibroblasts with the oncogenic form of Ras (H-RasV12) or the empty vector Babe and I monitored their growth over time, every day after transduction till OIS establishment.

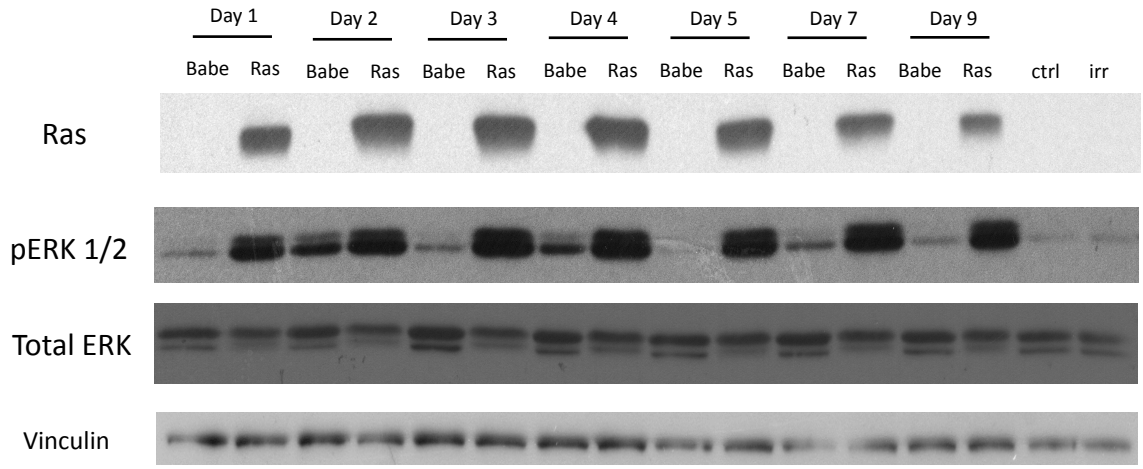

Figure 24. H-RasV12 expression and activation of Ras downstream pathway were studied by immunoblotting.
Immunoblotting analysis shows equal level of RAS expression and ERK1/2 activation - as detected by phospho ERK1/2 - a downstream factor of the RAS-signalling cascade, in H-RasV12 transduced BJ hTERT cells throughout the time course analysis. Vinculin serves as loading control.

Before proceeding for any further analysis I checked the oncogenic-Ras overexpression and the activation of the Ras downstream pathway by western blot analysis. As shown in Figure 24 Ras is overexpressed in H-RasV12 infected cells, while it is not the case for the cells infected with the empty vector. Furthermore, the level of H-RasV12 overexpression is constant overtime. Ras downstream pathway activation can be studied by detecting the presence of the phosphorylated form of ERK1/2. Thus to check for the activation of Ras downstream pathways, I probed the membrane with an antibody against phosphoERK1/2.

As shown in Figure 24 Ras-overexpression corresponds to high level of phosphoERK1/2, indicating that Ras downstream pathway is active.

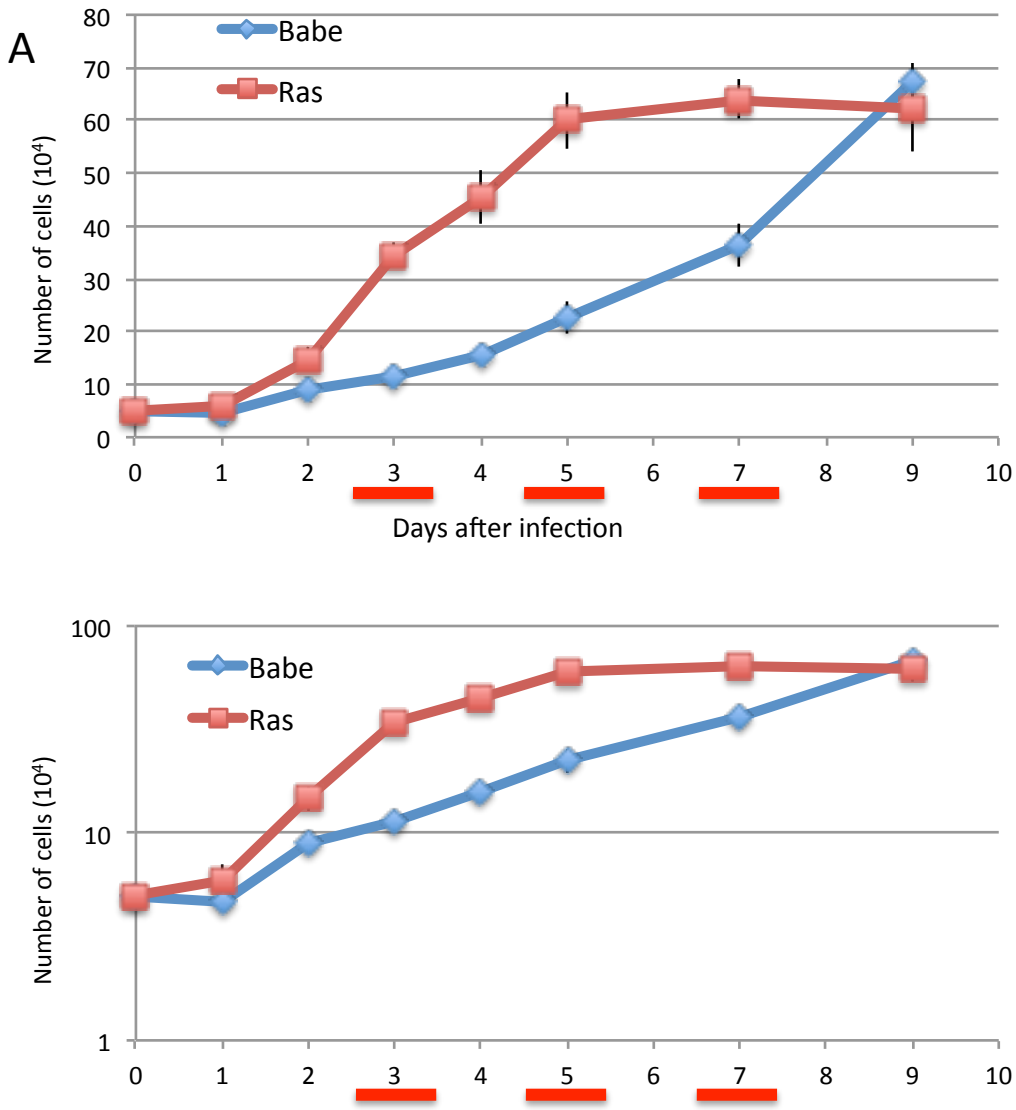

Figure 25. Growth curve experiment of empty vector (Babe)- or H-RasV12-transduced human normal fibroblast.
BJ hTERT cells were retrovirally infected with empty vector (Babe) or the oncogenic form of Ras (H-RasV12) and their proliferation was followed by cells counting every day after infection till the onset of senescence. (A) Growth curve graph with decimal scale on the vertical axis. (B) Growth curve graph with logarithmic scale on the vertical axis. Red lines indicate the time points when cells were split.

The results obtained are consistent with previous data from the lab (Di Micco et al., 2006). Indeed upon H-RasV12 expression cells start to hyperproliferate (between day 2 and day 3 after infection, Figure 25). This hyperproliferative burst is then followed by a slow down in growth, starting from day 5 after infection, that then turns into a permanent proliferative arrest also known as oncogene-induced senescence (day 9 after infection, Ras curve

crossing and Babe curve). These results are supported by a very similar pattern observed in BrdU incorporation experiment (Figure 26).

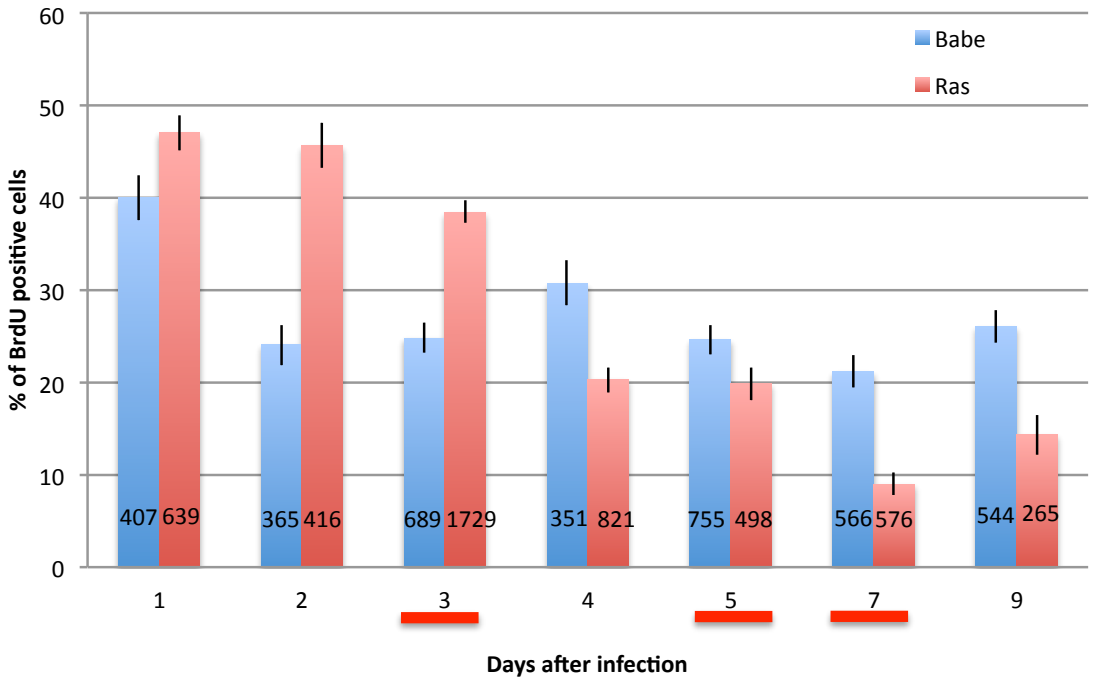

Figure 26. Proliferation rates of the growth curve experiments assessed by quantification of BrdU incorporation.
At every time point of the growth curve, cells were incubated with BrdU for 6 hours. The red lines indicate the time points when cells were split. Numbers on the graph indicate the sample size. The error bars indicate the Standard Error of the Mean (SEM). Red lines indicate days when cells were split.

Here, oncogenic Ras-expressing cells show an initial high rate of BrdU incorporation (Ras day 2) that then progressively decreases to lower BrdU incorporation rates (Ras day 7-9). Unexpectedly, on day 1 after retroviral infection, BrdU incorporation rates were high also in the control (Babe) cells, similar to oncogenic Ras-expressing cells. This may be due to the effect that infection itself has on cells independently of the gene transduced. Indeed retroviral integration in addition to DDR activation (Lau et al., 2005), may alter cell-cycle progression. Thus I decided not take into further consideration the time point of day 1 for subsequent analyses. BrdU incorporation rates of control cells (Babe) stayed quite constant over time, except from day 4, which shows a slight increase. This might be due to the effect of cell splitting which was performed on the day before. Trypsinization, pipetting and reseeding to a lower confluency are all events that may alter cellular physiology and

cell proliferation (Huang et al., 2010) to which normal and oncogene-expressing cells may be differently sensitive – importantly splitting were performed always in parallel for control and oncogene-expressing cells. This should to be kept in mind when drawing conclusions from analyses of events at day 4.

2.1 Kinetics of oncogene-induced damage response activation.

I then assessed the kinetics of oncogene-induced DNA damage response activation, by the use of two independent methods: immunofluorescence against upstream DDR markers (γH2AX, 53PB1, ATM (pSer1981), pS/TQ, Figure 27 and Figure 28), and analyses of DDR activation markers (p53 (pSer15), γH2AX, pATM (pSer1981), Chk2 (pThr68) by western blot Figure 29, 30 and 31).

Immunofluorescence analyses showed that the level of γH2AX, evaluated by the mean number of foci per cell and percentage of γH2AX-positive cells, is low and constant over time in control cells. Differently, in oncogenic Ras-expressing cells the level of γH2AX is overall higher than control cells. (Figure 27 B-C). Western blot analyses confirmed a robust induction of γH2AX throughout the time course of the experiment, with differences between control and oncogene-expressing cells becoming more dramatic at later time points (Figure 29).

I then monitored and quantified the level of another DDR marker: 53BP1 (Figure 27 D-E). Immunofluorescence analyses of 53BP1, assessed by mean number of foci per cell and percentage of 53BP1-positive cells, showed a low and fairly constant level of 53BP1 activation in control cells, while it progressively increased with time in oncogenic Ras-expressing cells. As for γH2AX, also 53BP1 levels were very high in oncogenic Ras-expressing cells at day 2, in association (possibly a causative one) with the hyperproliferative phase that starts at that time point.

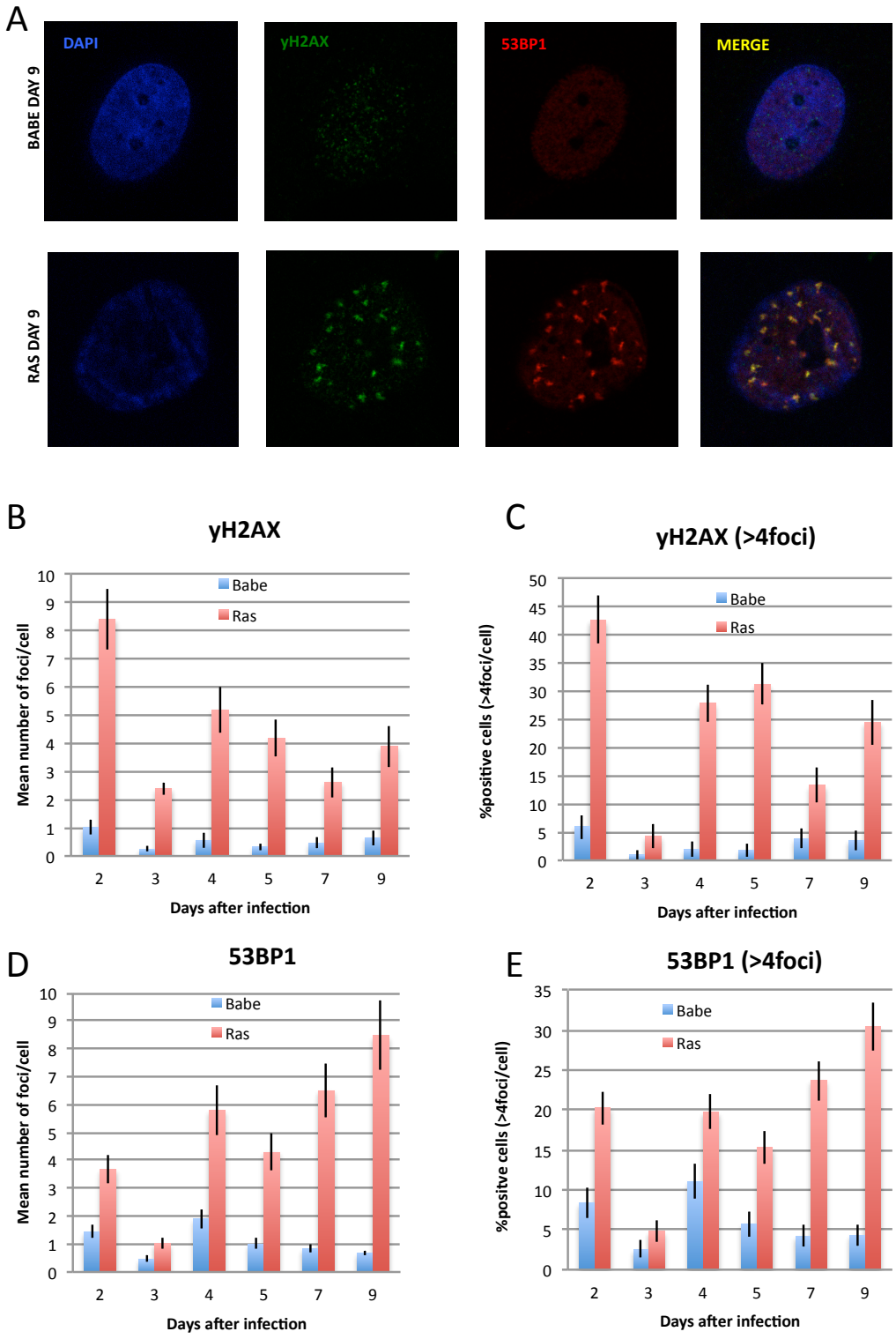

Figure 27. Quantification of DDR activation by immunofluorescence for γH2AX and 53BP1.
(A) Confocal images of empty vector (Babe) and oncogenic Ras at day 9 after infection, showing DAPI in blue, γH2AX in green and 53BP1 in red. (B) Quantification of mean number of γH2AX foci per cell. (C) Quantification of % of γH2AX-positive cells (a cells is considered as positive when it has more than 4 foci). (D) Quantification of mean number of 53BP1 foci per cell. (E) Quantification of % of 53BP1 positive cells (a cell is considered as positive when it has more than 4 foci). The error bars indicate the Standard Error of the Mean (SEM).

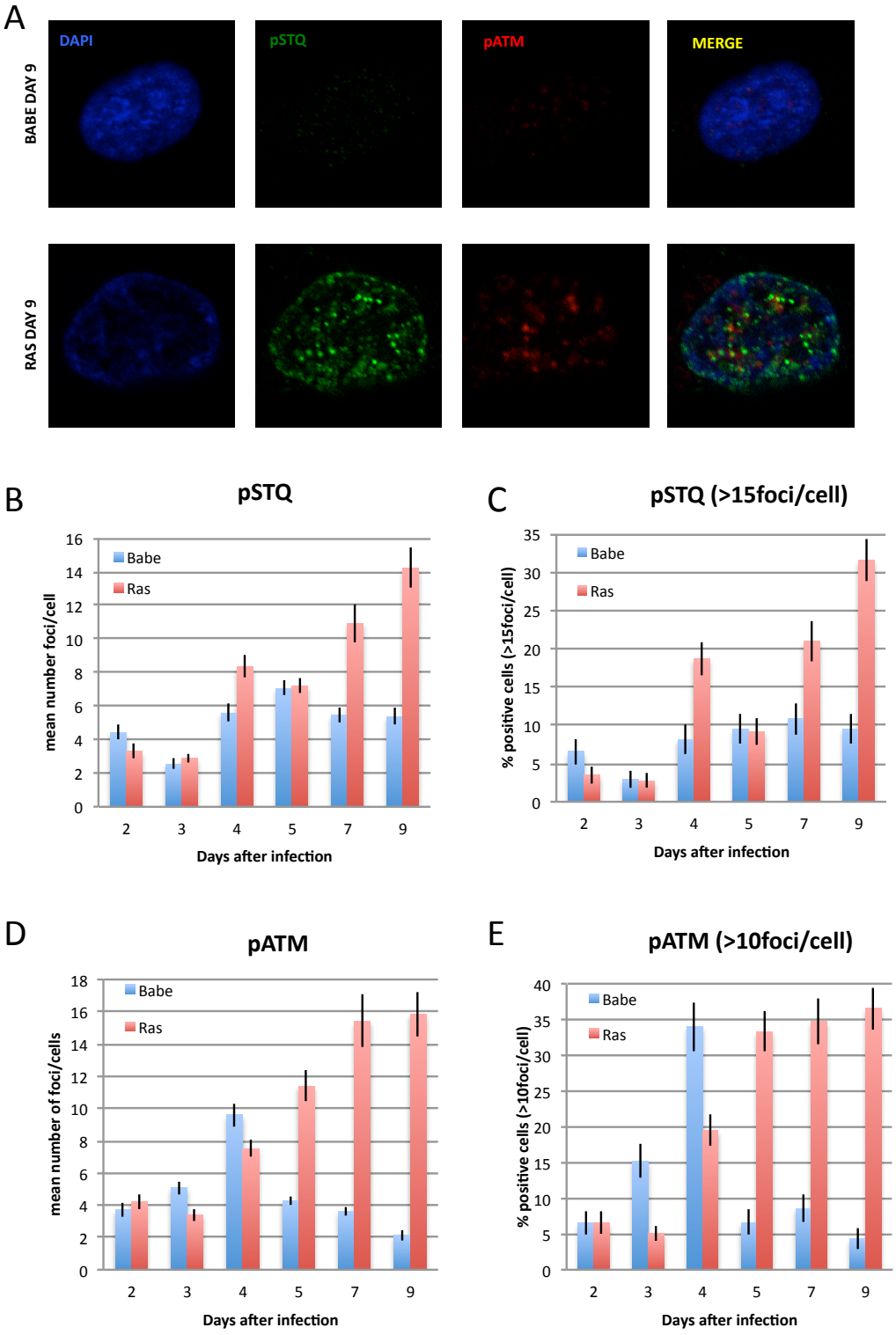

Figure 28. Quantification of DDR activation by immunofluorescence for pATM and pS/TQ.
(A) Confocal images of empty vector (Babe) and oncogenic Ras at day 9 after infection, showing DAPI in blue, pS/TQ in green and pATM in red. (B) Quantification of mean number of pS/TQ foci per cell. (C) Quantification of % of positive pSTQ cells (a cells is considered as positive when it has more than 15 foci). (D) Quantification of mean number of pATM foci per cell. (E) Quantification of % of pATM positive cells (a cell is considered as positive when it has more than 10 foci). The error bars indicate the Standard Error of the Mean (SEM).

To assess the global activation of the three members of the PI-3 like kinases ATM, ATR and DNA-PK, I quantified the signals generated by an antibody raised against the pS/TQ epitope, a phosphorylated epitope characteristic of protein substrates phosphorylated by these activated protein kinases. pS/TQ levels, assessed by mean number of pS/TQ foci per cell and percentage of pS/TQ positive cells, remain lower in control compared with oncogene-expressing cells which show a trend toward progressively higher levels in time (Figure 28 B-C).

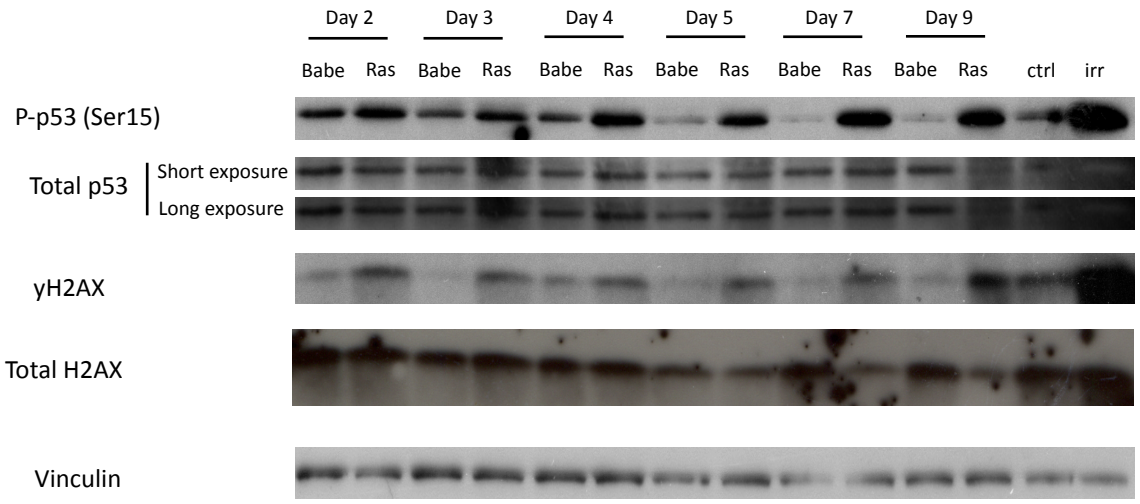

Figure 29. Quantification of DDR activation by western blot for p53 (pSer15) and γH2AX.
Immunoblot analysis of γH2AX and p53 (pSer15) reveals that DDR starts to be activated from the first days after Ras infection, and it gradually increases, reaching its maximum levels at the onset of senescence (day9). Vinculin serves as loading control

I then checked for the activation of one of the PI-3 like kinases, ATM, by quantifying the phospho(Ser1981)-ATM levels, by immunofluorescence and western blot analysis (Figure 28 and 30). ATM gets activated upon DNA damage by autophosphorylation on serine 1981. pATM levels in oncogenic Ras cells, assessed by mean number of pATM foci per cell and percentage of pATM positive cells, increased gradually from the basal level of the first days after infection, till it reached its maximum level on day 9 after infection, which corresponds to the establishment of cellular senescence (Figure 28). This trend is confirmed by pATM western blot analysis (Figure 30).

Chk2, a checkpoint kinase activated by ATM by phosphorylation on Threonin 68, is generally activated in oncogenic Ras-expressing cells since the first days after infection, while this is not in control cells (Figure 31).

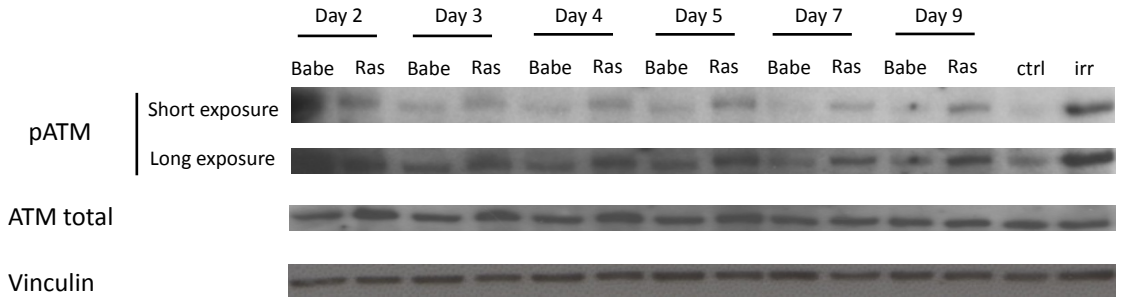

Figure 30. Quantification of DDR activation by western blot for pATM.
Immunoblot analysis of pATM (pSer1981) reveals that DDR starts to be activated from the first days after Ras infection, and it gradually increases, reaching its maximum levels at the onset of senescence (day9). Vinculin serves as loading control.

To check for the activation of downstream effectors in the DDR pathway I quantified the levels of phospho-p53 by western blot. p53 is a target of the PIKK family (ATM, ATR and DNA-PK) that upon DNA damage gets activate by phosphorylation on serine 15. Phospho(Ser15)-p53 levels increase over time in oncogenic Ras cells, while it is almost not present in control cells, except from the first days after infection, and on day 4 (Figure 29).

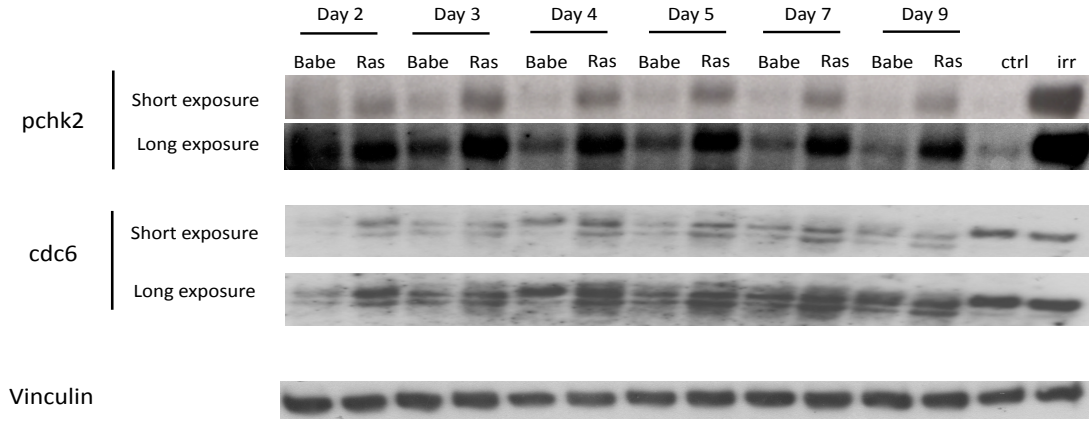

Figure 31. Quantification of DDR activation by western blot for pChk2 and quantification of DNA replication up regulation by western blot for Cdc6.
Immunoblot analysis of phospho-Chk2 (pThr68) reveals that DDR is activated from the first days after Ras infection, and it gradually increases, reaching its maximum levels at the onset of senescence (day9). Immunoblot analysis of Cdc6 reveals that upon Ras overexpression Cdc6 is promptly upregulated, while as cells are entering senescence, Cdc6 is downregulated to control levels. Vinculin serves as loading control.

Taken together this data show that, upon oncogenic Ras expression, DDR is gradually activated till it reaches its maximum level of activation at the moment of OIS establishment.

2.2 Kinetics of oncogene-induced DNA replication stress

Oncogenic Ras acts on a plethora of molecular pathways to promote uncontrolled cellular proliferation. Indeed oncogene activation acts directly on DNA replication by upregulating Cdc6, a crucial positive regulator of DNA replication origin licencing (Bartkova et al., 2006; Di Micco et al., 2006). This upregulation results in an alteration of DNA replication dynamics and it is often associated with replication origins firing more than once per cell cycle - re-replication - a mechanism of genomic instability (Takeda et al., 2005).

Also in the experiments I performed, oncogenic Ras upregulated Cdc6 during the hyperproliferative phase, before becoming downregulated upon entry into cellular senescence (Figure 31).

This result confirms data shown in previous studies (Bartkova et al., 2006; Di Micco et al., 2006) giving a more precise kinetic of the impact that Ras activation has on DNA replication dynamics through the upregulation of an important replication factor as Cdc6.

2.2.1 Oncogene activation and DNA replication dynamics

To dissect the replication dynamics at whole genome level, I used the DNA molecular combing technique (Lebofsky and Bensimon, 2003; Michalet et al., 1997). Cells were labelled with thymidine analogues for a precise time interval (1^{st} pulse IdU: 30 min; 2^{nd} pulse CldU: 30 min), at each time point after Ras-infection or empty vector infection, from day 2 till day 7. As cells replicate, they incorporate the thymidine analogues in their DNA. Cells are then embedded in agarose plugs. After deproteinization with proteinase K, DNA is extracted by melting the agarose, which is degraded by β agarase I digestion. The DNA

solution is then combed on silane-coated glass slides. This procedure allows for the stretching of single DNA molecules on the slide. By performing immunostainings with primary antibodies specific for individual thymidine analogues and total DNA and secondary fluorescent antibodies, I can visualize and measure replication patterns. (For further details see the section *DNA Molecular Combing*).

2.2.2 Oncogene activation and DNA replication fork speed

The first replication parameter I checked is the DNA replication fork speed, obtained by dividing the length of the replication signal by the incubation time (30 min).

For each time point I analysed around 600 fork speeds for control cells, and around 1000 for oncogenic Ras-expressing cells. In these analyses, I considered only the replication signals that were flanked on one side by the replication signal of the other thymidine analogue, and on the other side by detectable ssDNA. Only under these conditions, I could be confident that the distal end of the replication signal was not caused by the fiber break. Thus I excluded from these analyses all replication signals in which their extremities were not flanked by ssDNA (for further details the section *DNA Molecular Combing*).

Upon oncogenic Ras expression, fork speed is increased during the first day studied after infection (day 2). Starting from day 3 after infection, fork speed gradually decreased till it reached levels that are lower than the control (day 5-7 after infection). On the contrary, fork speed of control cells stay quite constant throughout the growth curve experiment (Figure 32A). The differences in fork speed between Ras and control at each time point are statistically significant. For more detailed statistics, I checked for the statistical significance of each condition against all the other conditions, and plotted the resulting p values in the table of Figure 32B.

A

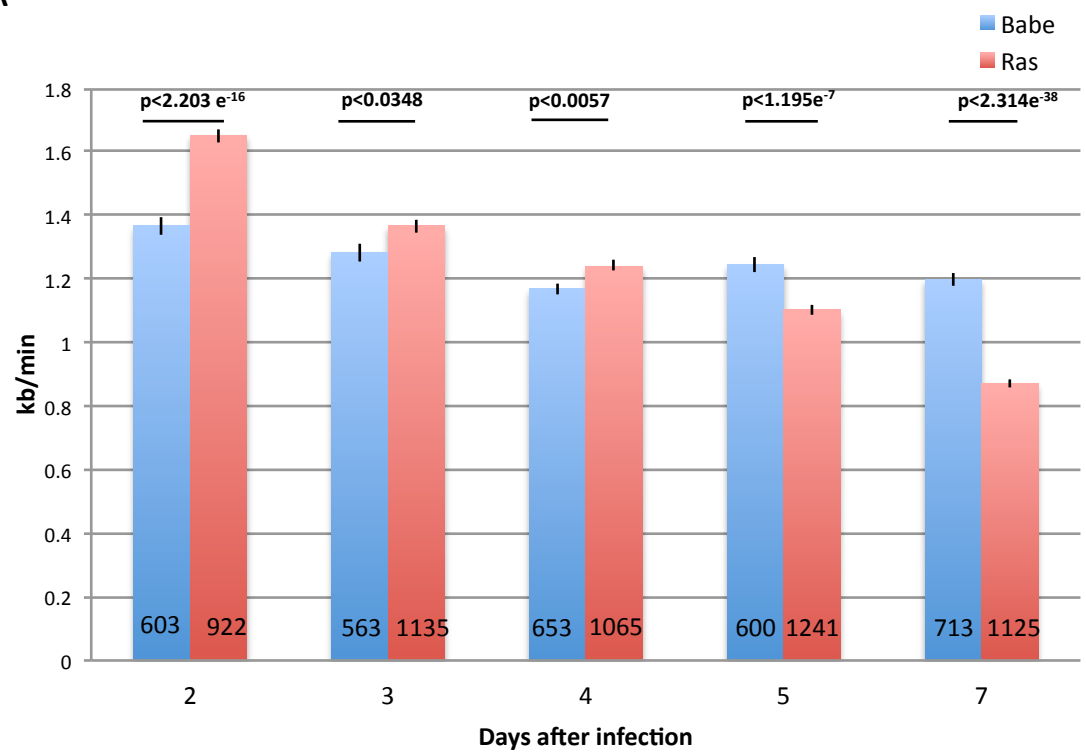

B

	R2	B2	R3	B3	R4	B4	R5	B5	R7	B7
R2		p<2.203e-16	p<2.611e-25	p<2.45e-23	p<7.813e-54	p<1.201e-56	p<3.468e-87	p<2.167e-33	p<7.08e-152	p<2.808e-53
B2	p<2.203e-16		p<0.8171	p<0.03561	p<4.135e-05	p<9.454e-09	p<9.601e-17	p<0.002672	p<2.547e-53	p<2.355e-07
R3	p<2.611e-25	p<0.8171		p<0.0348	p<1.378e-05	p<1.155e-09	p<7.633e-22	p<0.00166	p<2.004e-74	p<3.417e-08
B3	p<2.45e-23	p<0.03561	p<0.0348		p<0.1269	p<0.0006318	p<9.853e-09	p<0.4398	p<2.314e-38	p<0.0348
R4	p<7.813e-54	p<4.135e-05	p<1.378e-05	p<0.1269		p<0.005729	p<1.106e-09	p<0.5189	p<1.598e-66	p<0.03233
B4	p<1.201e-56	p<9.454e-09	p<1.155e-09	p<0.0006318	p<0.005729		p<0.006261	p<0.004681	p<9.465e-39	p<0.0006318
R5	p<3.468e-87	p<9.601e-17	p<7.633e-22	p<9.853e-09	p<1.106e-09	p<0.006261		p<1.195e-07	p<4.584e-29	p<9.853e-09
B5	p<2.167e-33	p<0.002672	p<0.00166	p<0.4398	p<0.5189	p<0.004681	p<1.195e-07		p<4.666e-41	p<4.927e-43
R7	p<7.08e-152	p<2.547e-53	p<2.004e-74	p<2.314e-38	p<1.598e-66	p<9.465e-39	p<4.584e-29	p<4.666e-41		p<2.314e-38
B7	p<2.808e-53	p<2.355e-07	p<3.417e-08	p<0.0348	p<0.03233	p<0.0006318	p<9.853e-09	p<4.927e-43	p<2.314e-38	

Figure 32. Quantification of DNA replication fork speed.
Fork speed was calculated as the ratio between the length of the replication signal and the time interval of the incubation with thymidine analogues (30 min). (A) Graph showing the average fork speeds of the growth curve experiment. Numbers on the graph indicate the sample size. (B) Table showing the p-value for the graph shown in A. The error bars indicate the Standard Error of the Mean (SEM). p-values were calculated applying Wilcoxon test.

In order to better visualize these results, I plotted fork speed distribution of each time point (Figure 33A-E). At day 2 after infection, the distribution of fork speeds in oncogenic Ras-expressing cells is clearly centred to the right (higher values) of control cells (Figure 33A). As oncogenic Ras-expressing cells approach their entry into cellular senescence, fork speeds then shift towards lower values, actually lower than the control (day 5-7; Figure 33D-E). Days in between (day 3 and 4) show similar fork speeds, likely as the outcome of the transition from faster to slower forks in oncogenic Ras-expressing cells (Figure 33B-C).

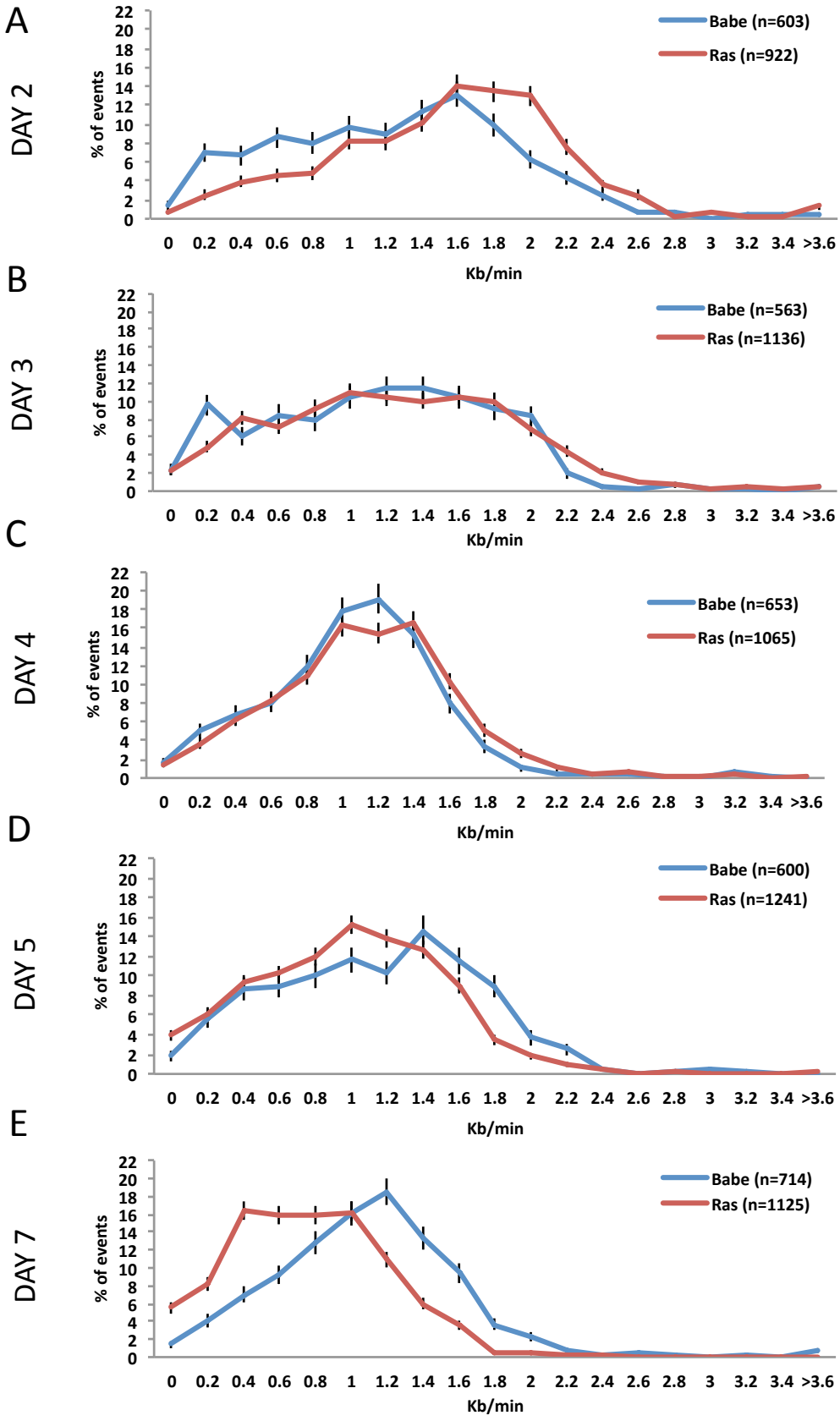

Figure 33. Fork speed distributions.
(A) Fork speed distribution of empty vector and Ras cells at day 2 after infection. (B) Fork speed distribution of empty vector and Ras cells at day 3 after infection. (C) Fork speed distribution of empty vector and Ras cells at day 4 after infection. (D) Fork speed distribution of empty vector and Ras cells at day 5 after infection. (E) Fork speed distribution of empty vector and Ras cells at day 7 after infection. The error bars indicate the Standard Error of the Mean (SEM).

It has been suggested that DNA fiber integrity is an important parameter in fork speed studies and that to ensure accurate fork speed estimation, the median size of fiber length should be at least of 200 kb (Techer et al., 2013). I therefore checked the fiber length distribution to make sure that it did not bias my fork spee

d analyses (Figure 34-35).

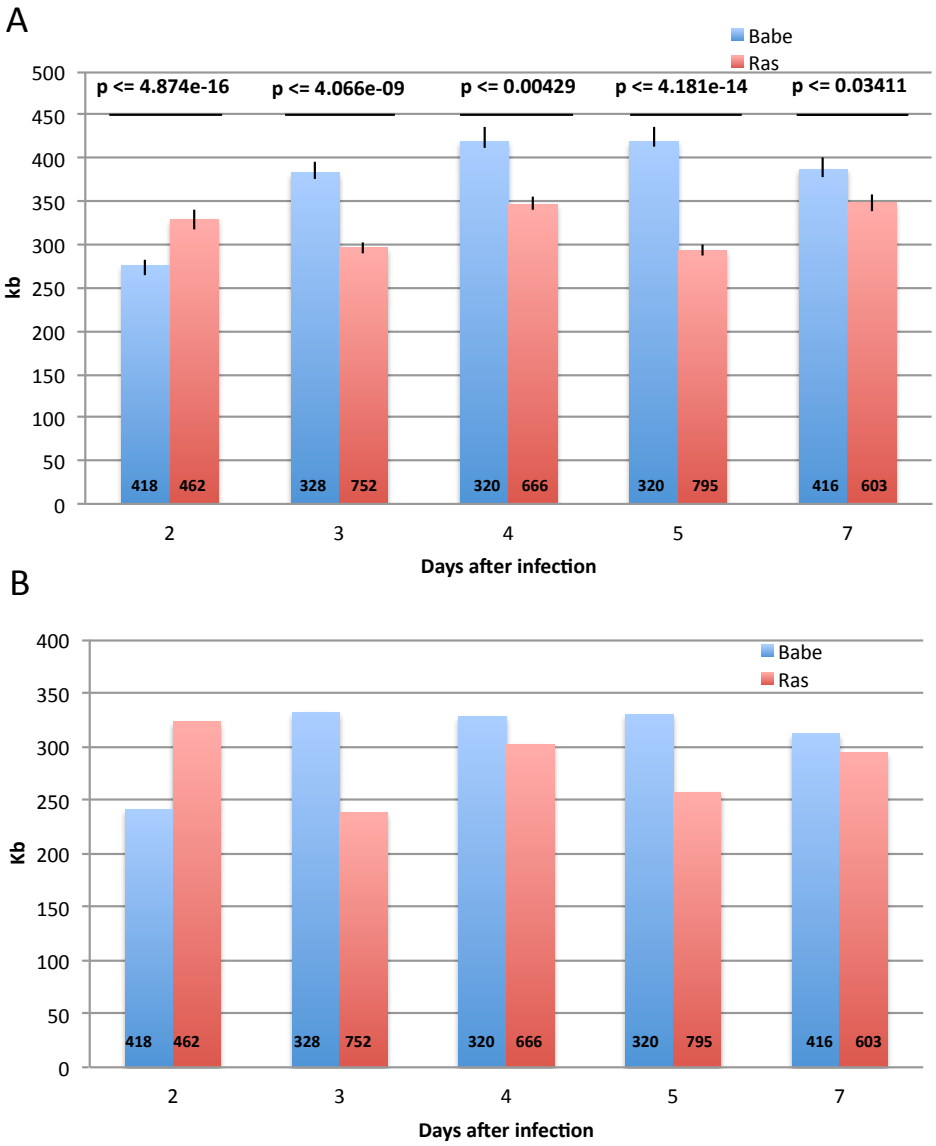

Figure 34. DNA Fiber length analysis.
(A) Average length of the DNA fibers analysed to obtain fork speed. (B) Median length of the DNA fibers analysed to obtain fork speed. The error bars indicate the Standard Error of the Mean (SEM).

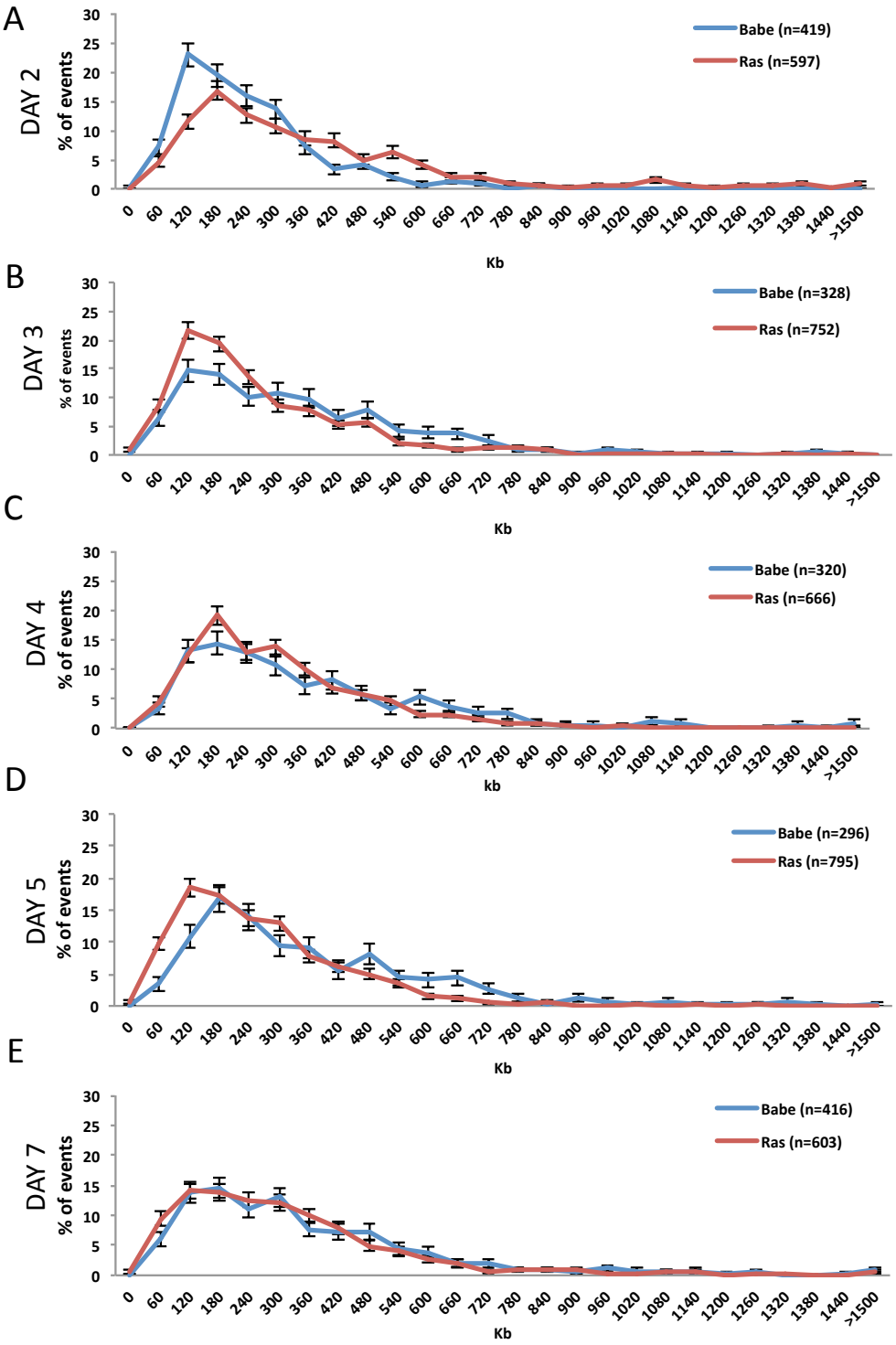

Figure 35. DNA Fiber length distribution.
(A) DNA fiber length distribution of empty vector and Ras cells at day 2 after infection. (B) DNA fiber length distribution of empty vector and Ras cells at day 3 after infection. (C) DNA fiber length distribution of empty vector and Ras cells at day 4 after infection. (D) DNA fiber length distribution of empty vector and Ras cells at day 5 after infection. (E) DNA fiber length distribution of empty vector and Ras cells at day 7 after infection. The error bars indicate the Standard Error of the Mean (SEM).

Reassuringly, the medians of fiber length of all our samples are higher than 200 kb (Figure B). Intriguingly, all oncogenic Ras samples, except from day 2, have shorter DNA fibers as compared to the control (Figure 34-35). This is consistent with the intriguing possibility

that oncogenic Ras introduces DNA discontinuities (including DNA nicks and aberrant DNA replication structures) that may be prone to breakage during sample preparation resulting in shorter DNA fibers and that DNA combing is a technique that may allow to visualize this – similar to comet assays, but more sensitive.

In summary, these analyses indicate that oncogenic Ras expression induces an initial increase in fork speed, which then gradually decreases over time as cells enter into senescence to levels lower than control cells.

2.2.3 The impact of oncogene activation on DNA replication origins firing as measured by inter-origin distances

The next parameter I assessed is the Inter-Origin-Distance (IOD), which consists in the measure of the distance between two adjacent origins and accounts for the evaluation of DNA replication initiation events: smaller IOD indicates higher number of simultaneously active origins, while higher IOD corresponds to lower number of simultaneously active origins. For each time point I analysed around 100 IODs both for control and for oncogenic Ras-expressing cells. To assess the distance between replication origins (ORI) it is necessary to have replication patterns that allow precise positioning of the ORI. One ORI is defined as the central point on the ssDNA signals that is flanked on both sides from replication signal generated by the 1st pulse. Thus, I had to exclude from this analysis all the origins for which the position could not be precisely determined due to the lack of replication signal on one of the extremities of the DNA fiber or in case of unidirectional forks (for further details the section *DNA Molecular Combing*).

A

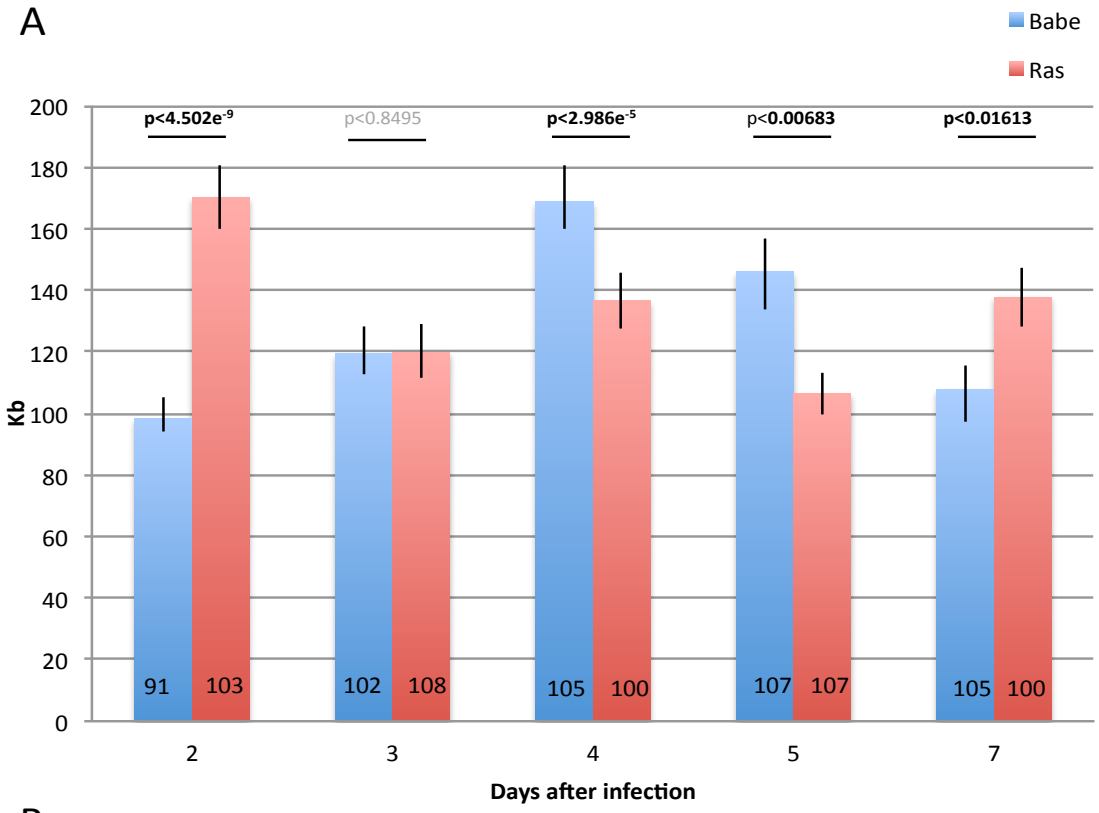

B

	R2	B2	R3	B3	R4	B4	R5	B5	R7	B7
R2		**p<4.502e-09**	**p<1.228e-05**	**p<2.847e-05**	**p<0.0074**	**p<0.4468**	**p<7.015e-07**	**p<0.011**	**p<0.0042**	**p<1.87e-07**
B2	**p<4.502e-09**		p<0.08799	p<0.2139	**p<0.0034**	**p<5.468e-07**	p< 0.6686	**p<0.0012**	**p<0.0021**	p<0.497
R3	**p<1.228e-05**	p<0.08799		p<0.8495	p<0.1227	**p<0.0005**	p<0.2822	p<0.0937	p<0.1606	p<0.322
B3	**p<2.847e-05**	p<0.2139	p<0.8495		p<0.0969	**p<0.0006**	p<0.4536	p<0.07411	p<0.1196	p<0.5256
R4	**p<0.0074**	**p<0.0034**	p<0.1227	p<0.0969		**p<2.986e-05**	**p<0.0152**	p<0.8191	p<0.9057	**p<0.0192**
B4	**p<0.4468**	**p<5.468e-07**	**p<0.0005**	**p<0.0006**	**p<2.986e-05**		p<0.06417	p<0.0938	**p<0.04801**	**p<1.024e-05**
R5	**p<7.015e-07**	p< 0.6686	p<0.2822	p<0.4536	**p<0.0152**	p<0.06417		**p<0.0068**	**p,0.02067**	p<0.783
B5	**p<0.011**	**p<0.0012**	p<0.0937	p<0.07411	p<0.8191	p<0.0938	**p<0.0068**		p<0.769	**p<0.01**
R7	**p<0.0042**	**p<0.0021**	p<0.1606	p<0.1196	p<0.9057	**p<0.04801**	**p,0.02067**	p<0.769		**p<0.0161**
B7	**p<1.87e-07**	p<0.497	p<0.322	p<0.5256	**p<0.0192**	**p<1.024e-05**	p<0.783	**p<0.01**	**p<0.0161**	

Figure 36. Quantification of Inter-Origin Distances.
Inter-Origin-Distances (IODs) were calculated as the distance between two adjacent DNA replication origins. (A) Graph showing average IODs of the growth curve experiment. Numbers on the graph indicate the sample size. (B) Table showing the p-value for the graph shown in A. The error bars indicate the Standard Error of the Mean (SEM). p-values were calculated applying Wilcoxon test.

The first days after infection (day 2), oncogenic Ras-expressing cells show a dramatic increase in IODs as compared to the control (Babe vs Ras, 98.33 kb vs 170.19 kb; Figure 36 and 37), indicating that Ras activation induces a reduction of simultaneously active origins. This result is consistent with my previous observation (Figure 32) that oncogenic Ras increases DNA replication fork speed at this time point. Indeed fork speed and the number of simultaneously active origins is often inversely correlated: faster forks usually correspond to fewer active origins (Zhong et al., 2013).

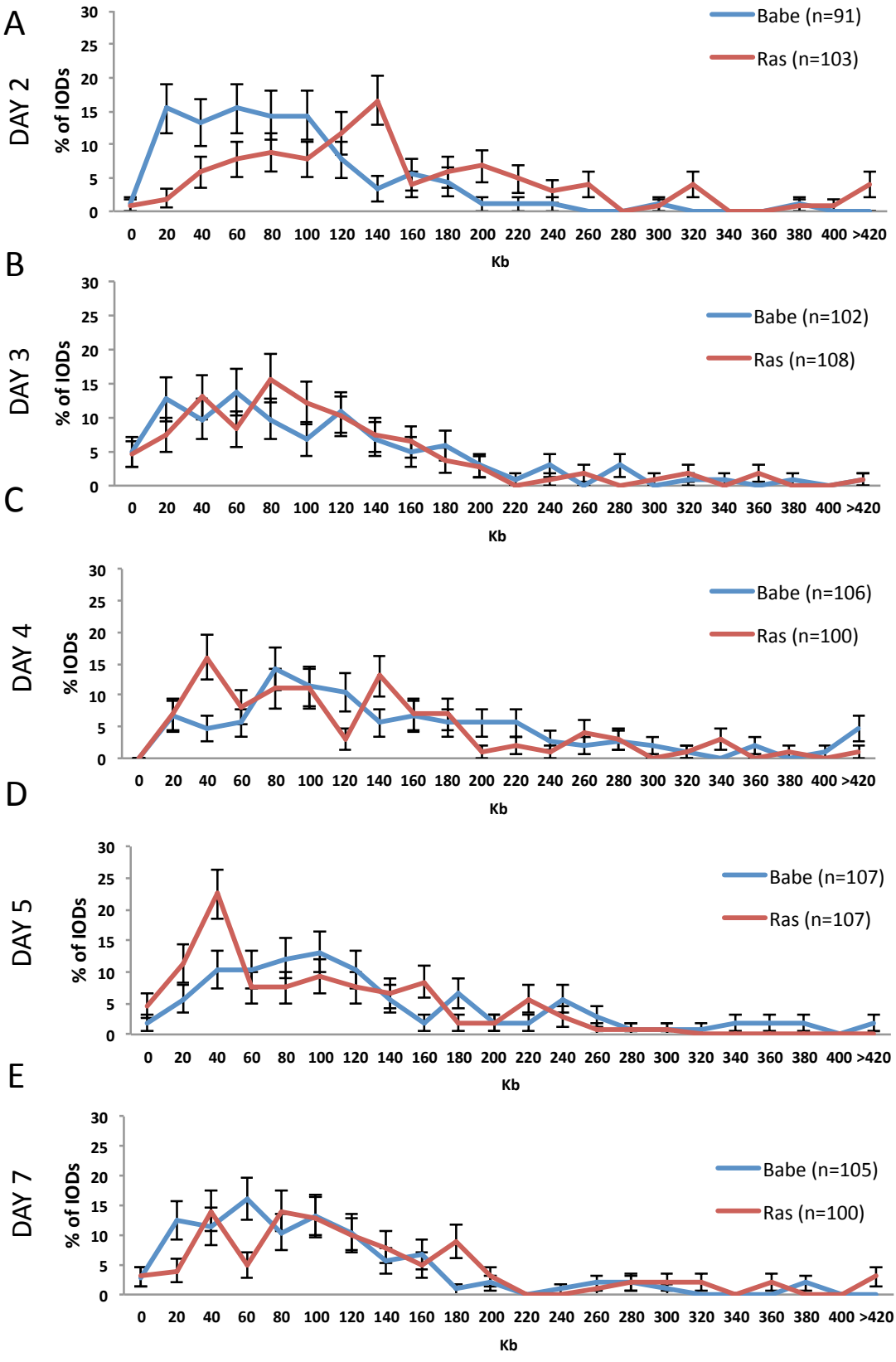

Figure 37. Inter-Origin-Distances distributions.
(A) IODs distribution of empty vector and Ras cells at day 2 after infection. (B) IODs distribution of empty vector and Ras cells at day 3 after infection. (C) IODs distribution of empty vector and Ras cells at day 4 after infection. (D) IODs distribution of empty vector and Ras cells at day 5 after infection. (E) IODs distribution of empty vector and Ras cells at day 7 after infection. The error bars indicate the Standard Error of the Mean (SEM).

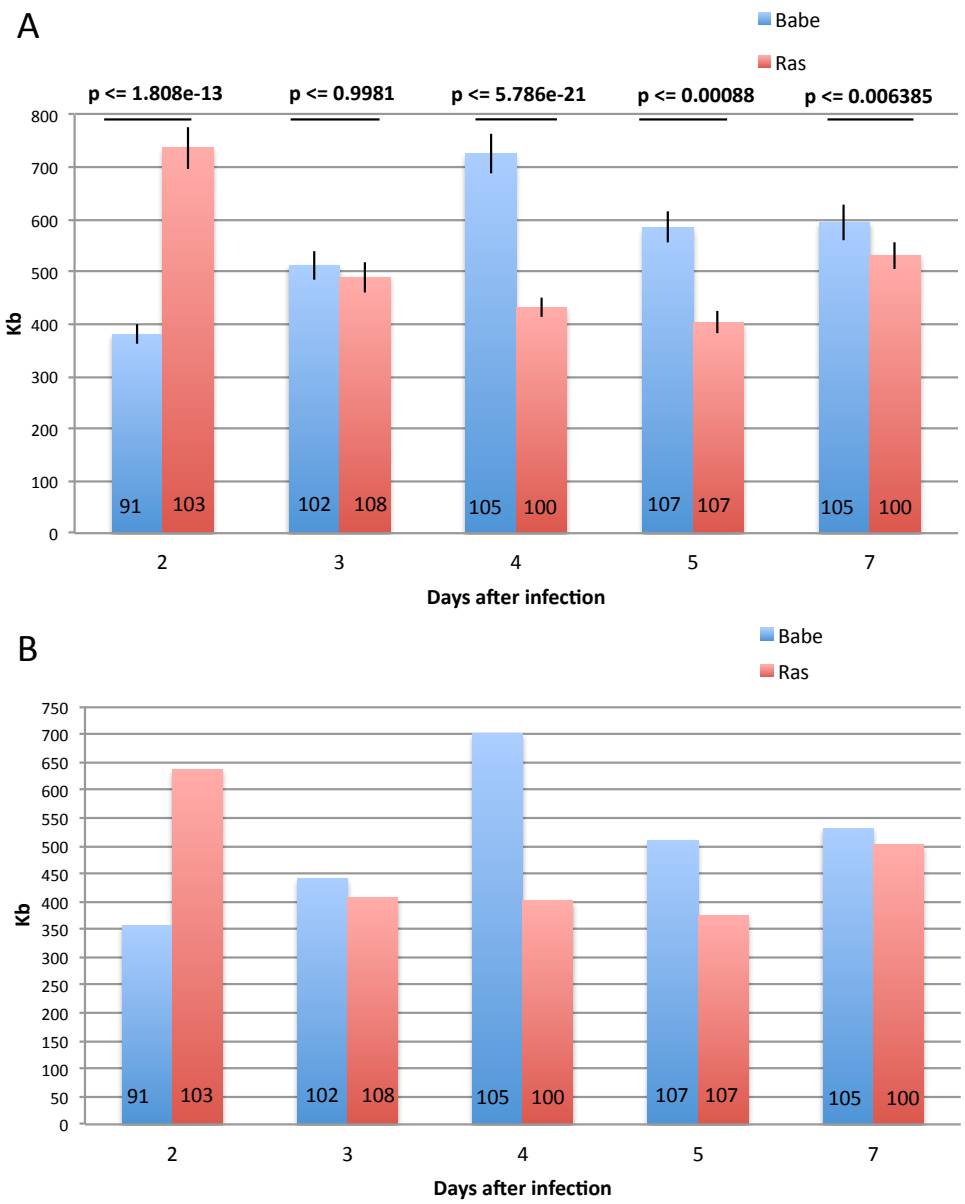

Figure 38. Average and median DNA fibers lengths of the DNA fibers containing IODs.
(A) Average length of the DNA fibers analysed to obtain IODs. (B) Median length of the DNA fibers analysed to obtain IODs. The error bars indicate the Standard Error of the Mean (SEM). Numbers on the graph indicate the sample size.

With time, comparisons within the same day show that IODs of oncogenic Ras-expressing cells become progressively shorter than control cells with day 3 being the transition point in which they are identical (Figure 36-37). Admittedly, the last day studied (day 7) shows an inversion of this trend, although the p-values suggest that this difference is the least robust of all studied. It is also worth noticing that at day 7, most cells are actually senescent and thus the little ongoing DNA replication detected (day 7 Ras is the lowest BrdU incorporating time point in Figure 26) may be occurring in that subset of cells

actually not expressing H-RasV12 (in our cellular system, cells are not selected for drug resistance, to avoid the confounding effect of cell death due to drug selection, thus a small fraction of uninfected cells may exist).

As suggested in literature (Techer et al., 2013), the median size of fiber length should be at least of 350 kb to ensure accurate IODs estimation. Therefore I measured the fiber length distribution to make sure that it did not influence the IODs analyses (Figure 38). Indeed the median fiber length of our samples is higher than 350 kb in all samples studied. Thus the fiber length of our samples is unlikely to influence IODs assessment.

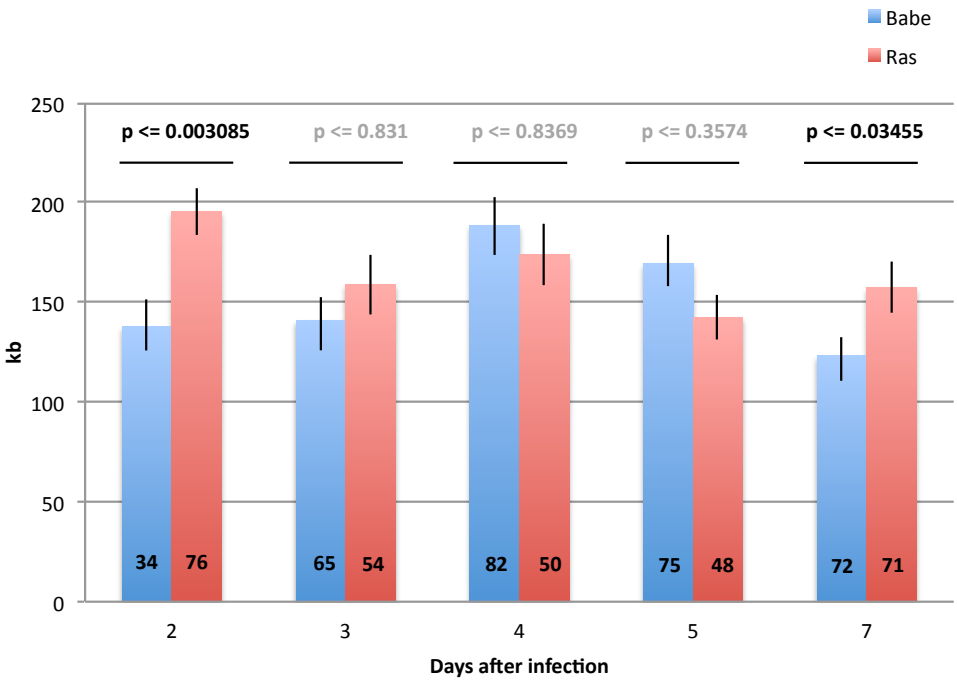

Figure 39. Quantification of Inter-Origin-Distances on long fibers.
The graph shows the average of IODs on long DNA fibers (longer than 3 times the average IODs) to avoid possible bias introduced by fiber length (Bianco et al., 2012). The error bars indicate the Standard Error of the Mean (SEM). Numbers on the graph indicate the sample size.

In any case, to further exclude any bias caused by fiber fragmentation in IODs estimation, I recalculated IODs by studying only fibers at least three times longer the average of IODs – in this case equal to 394.3 kb -, as suggested in (Bianco et al., 2012). Also under these more stringent conditions in which only signals in very long fibers are studied, I could confirm the trend (Figure 39-40) previously observed in the bulk of fibers (Figure 36-37).

Taken together these results suggest that oncogenic Ras expression initially downregulates the number of simultaneously active ORI - as inferred by higher IOD -, while as the time passes it upregulates their number. To further confirm this trend we analysed also another parameter to estimate the frequency of initiation: the active ORI/Mb.

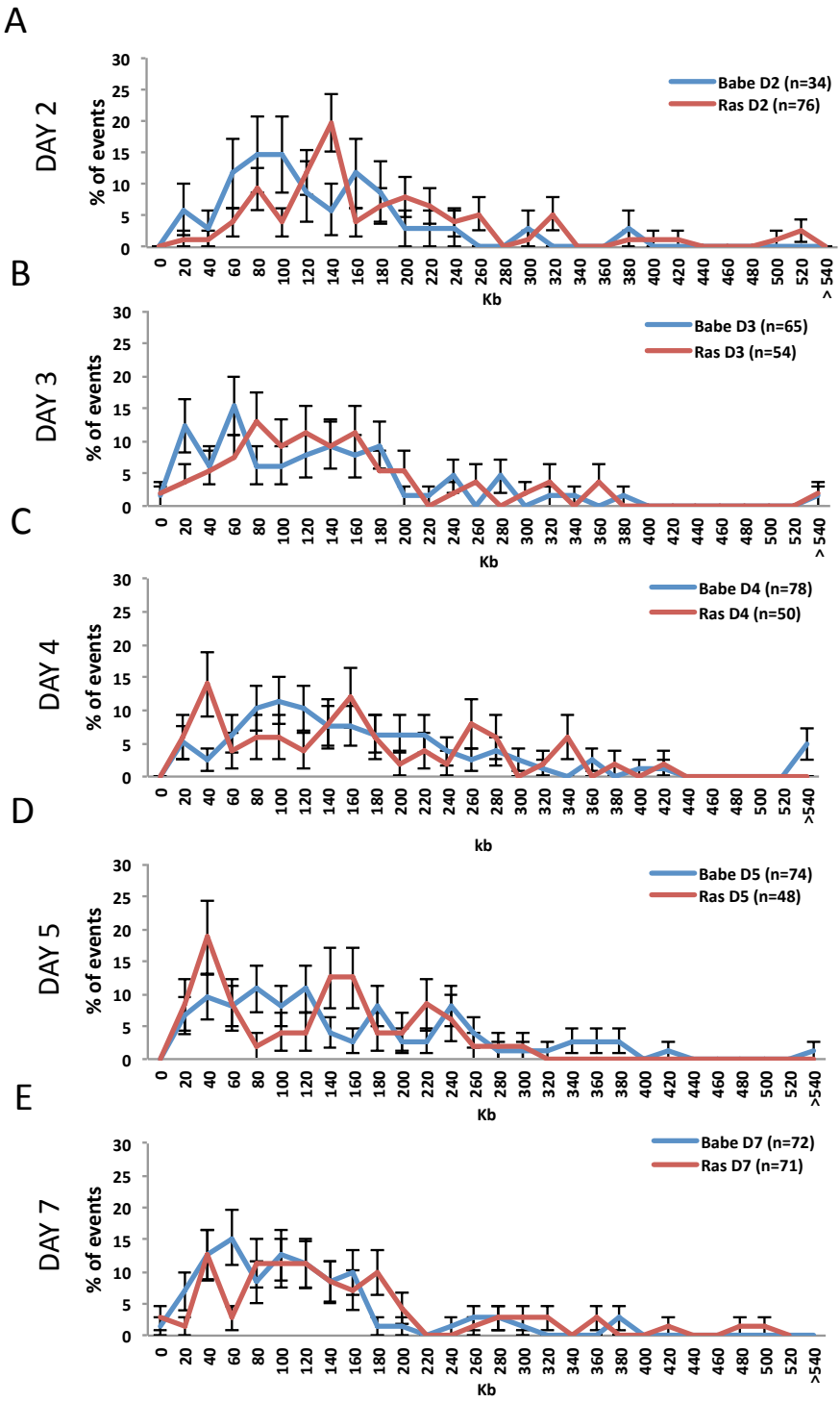

Figure 40. Distributions of Inter-Origin-Distances on long DNA fibers.
(A) IODs distribution of empty vector and Ras cells at day 2 after infection. (B) IODs distribution of empty vector and Ras cells at day 3 after infection. (C) IODs distribution of empty vector and Ras cells at day 4 after infection. (D) IODs distribution of empty vector and Ras cells at day 5 after infection. (E) IODs distribution of empty vector and Ras cells at day 7 after infection. The error bars indicate the Standard Error of the Mean (SEM).

2.2.4 The impact of oncogene activation on DNA replication origins firing as measured by active origins per Mb

It has been proposed that another manner to account for the frequency of initiation events is the measure of active replication origin per Megabases of DNA (ORI/Mb). This approach is less sensitive to variations in fibers length and takes into account also fibers containing a single active origin (Bianco et al., 2012). This may be qualitative, not just quantitatively different, as these individual ORIs may lie in ORI deserts or away from ORI clusters. Even though this approach is less sensitive to fiber length, it has a major limitation when considering DNA molecules containing a single origin. Indeed the fibers length of DNA molecules containing just one ORI can bias the analysis. One origin on a very short fiber - likely due to fiber breakage during the combing process - would result in a high level of ORI/Mb, which might not reflect the real value of ORI/Mb. One way to avoid this bias is the to exclude short DNA fibers (for further details the section *DNA Molecular Combing*). I nevertheless analysed my combing data according to this approach. Also in this way, on day 2 oncogenic Ras-expressing cells showed a dramatic reduction in the number of active origins (Figure 41-42A). Likely due to the above-mentioned sensitivity to fiber lengths, the values of the later days showed a fuzzier trend although not in contrast with a general increase in origins activation in oncogenic Ras-expressing cells (Figure 41-42).

A

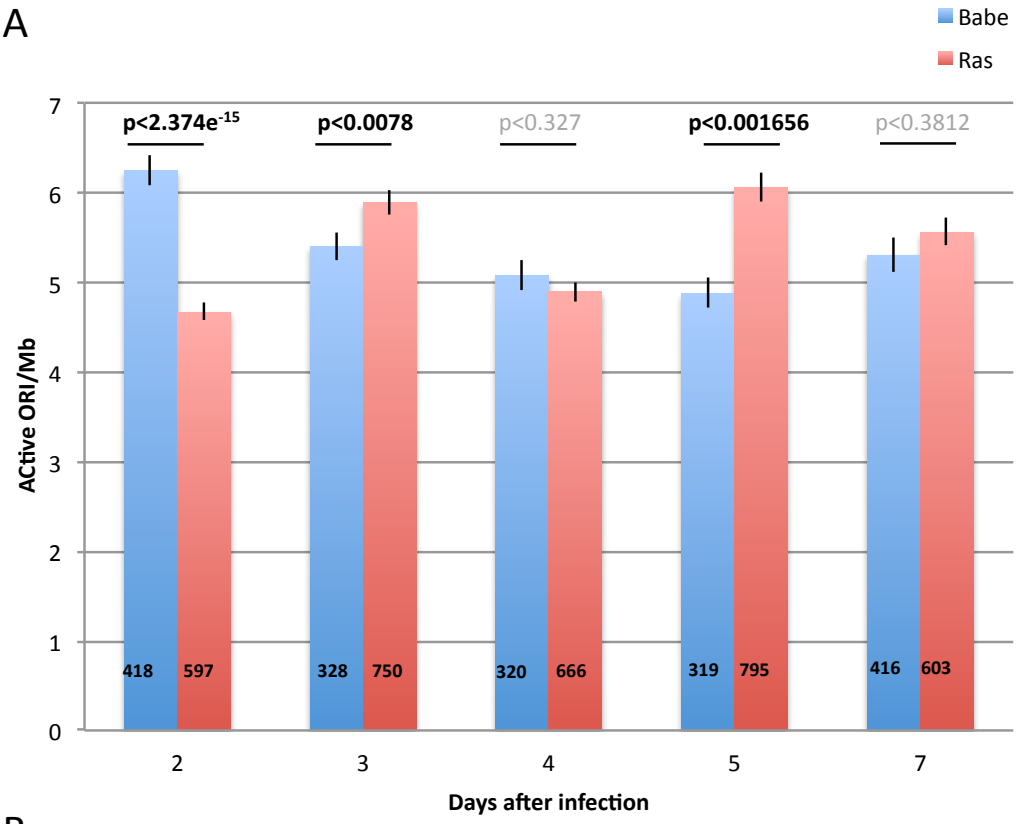

B

	R2	B2	R3	B3	R4	B4	R5	B5	R7	B7
R2		p<2.374e-15	p<8.561e-11	p<0.01823	p<0.146	p<0.0324	p<9.437e-11	p<0.3568	p<0.0012	p<0.0386
B2	p<2.374e-15		p<0.0192	p<2.073e-05	p<8.813e-12	p<1.028e-06	p<0.0163	p<5.685e-09	p<6.604e-06	p<5.775e-07
R3	p<8.561e-11	p<0.0192		p<0.0078	p<2.224e-07	p<0.0014	p<0.9418	p<1.781e-05	p<0.0074	p<0.0008
B3	p<0.01823	p<2.073e-05	p<0.0078		p<0.2296	p<0.7855	p<0.0076	p<0.2172	p<0.6352	p<0.7604
R4	p<0.146	p<8.813e-12	p<2.224e-07	p<0.2296		p<0.3207	p<2.171e-07	p<0.8311	p<0.0507	p<0.3881
B4	p<0.0324	p<1.028e-06	p<0.0014	p<0.7855	p<0.3207		p<0.0017	p<0.2946	p<0.4892	p<0.9055
R5	p<9.437e-11	p<0.0163	p<0.9418	p<0.0076	p<2.171e-07	p<0.0017		p<1.897e-05	p<0.0066	p<0.0008
B5	p<0.3568	p<5.685e-09	p<1.781e-05	p<0.2172	p<0.8311	p<0.2946	p<1.897e-05		p<0.07704	p<0.3772
R7	p<0.0012	p<6.604e-06	p<0.0074	p<0.6352	p<0.0507	p<0.4892	p<0.0066	p<0.07704		<0.3812
B7	p<0.0386	p<5.775e-07	p<0.0008	p<0.7604	p<0.3881	p<0.9055	p<0.0008	p<0.3772	<0.3812	

Figure 41. Quantification of the number of active Origin per Megabases (ORI/Mb).
The number of active origins per megabases (ORI/Mb) was calculated by the ratio between the number active origins present in the DNA fiber analyzed and the length of the fiber (Bianco et al., 2012). (A) Graph showing average number of active ORI/Mb. Numbers on the graph indicate the sample size. (B) Table showing the p-value for the graph shown in A. The error bars indicate the Standard Error of the Mean (SEM). p-values were calculated applying Wilcoxon test.

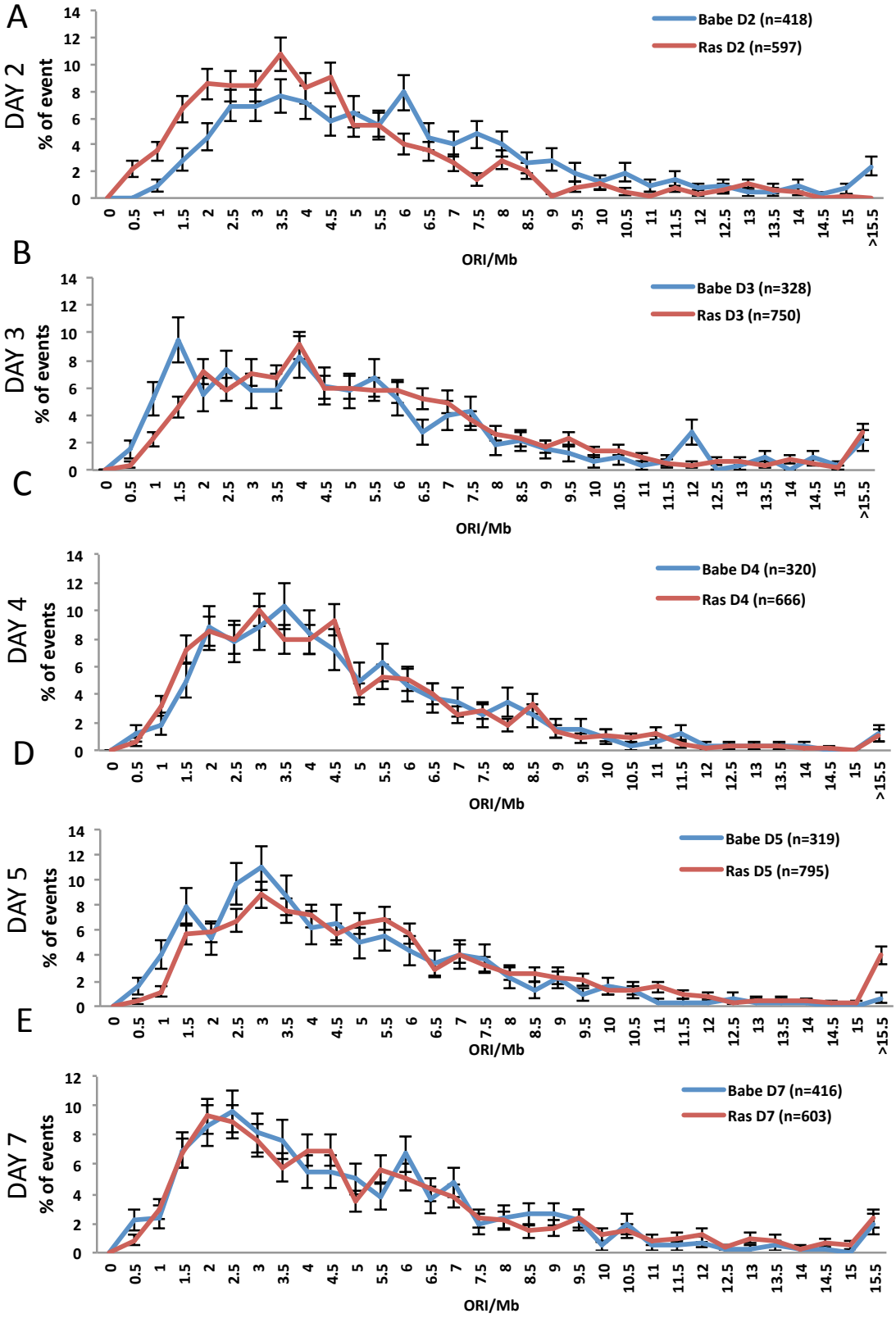

Figure 42. ORI/Mb distributions.
(A) ORI/Mb distribution of empty vector and Ras cells at day 2 after infection. (B) ORI/Mb distribution of empty vector and Ras cells at day 3 after infection. (C) ORI/Mb distribution of empty vector and Ras cells at day 4 after infection. (D) ORI/Mb distribution of empty vector and Ras cells at day 5 after infection. (E) ORI/Mb distribution of empty vector and Ras cells at day 7 after infection. The error bars indicate the Standard Error of the Mean (SEM).

In order to decrease the variability due to fiber lengths, I decided to consider only the ORI/Mb deriving from fibers longer than 300 kb. This further analysis reduced variability and showed a fairly stable difference between control and oncogenic Ras-expressing cells with a mild increase in origins firing at later time point in oncogene-expressing cells (Figure 43-44).

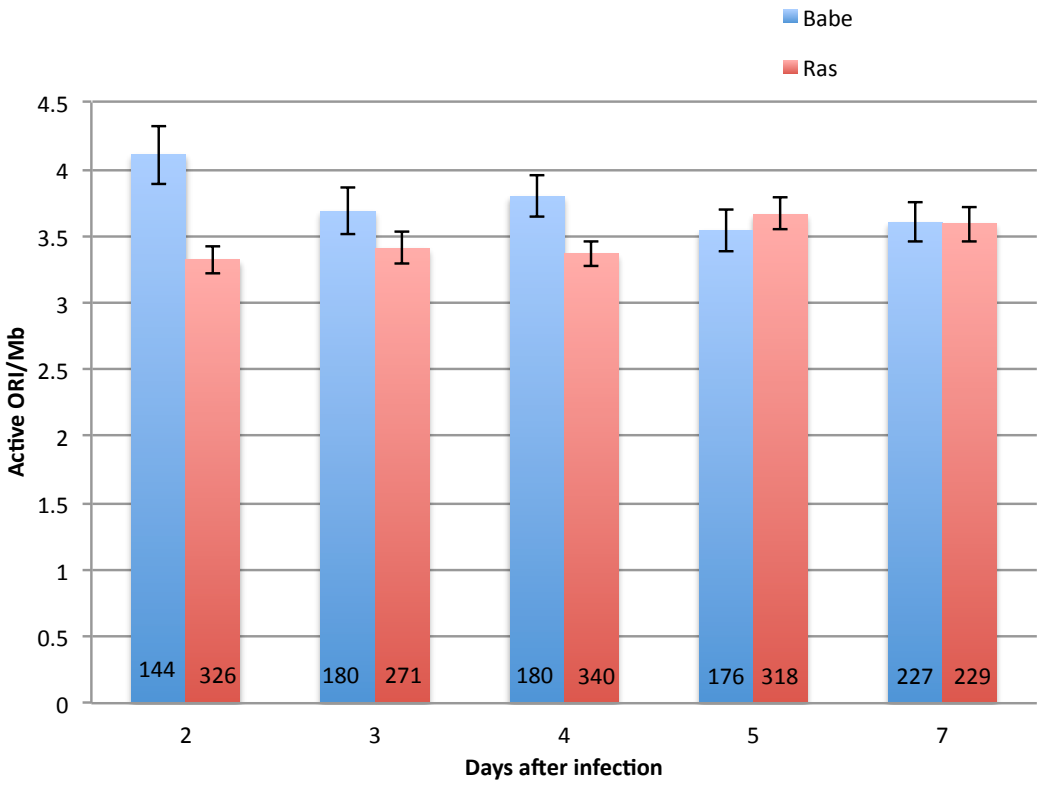

Figure 43. Quantification of the number of active Origin per Megabases (ORI/Mb) on long fibers.
(A) Number of active origin per Megabases (ORI/Mb) on fibers longer than 300 kb. The graph shows the average of ORI/Mb for each condition analysed. The error bars indicate the Standard Error of the Mean (SEM). Numbers on the graph indicate the sample size. p-values were calculated applying Wilcoxon test.

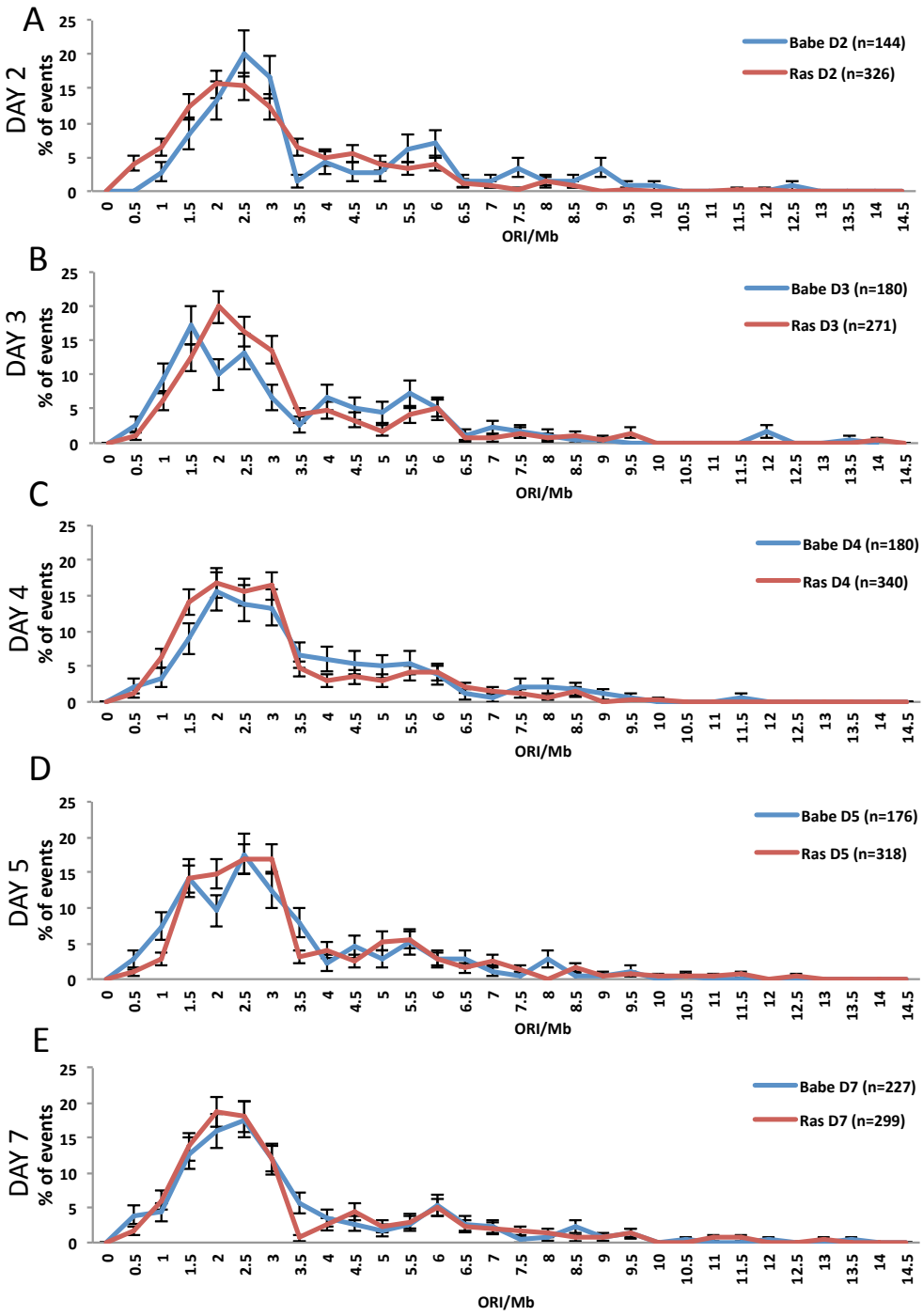

Figure 44. Distribution of ORI/Mb lying on long DNA fibers.
(A) ORI/Mb distribution of empty vector and Ras cells at day 2 after infection. (B) ORI/Mb distribution of empty vector and Ras cells at day 3 after infection. (C) ORI/Mb distribution of empty vector and Ras cells at day 4 after infection. (D) ORI/Mb distribution of empty vector and Ras cells at day 5 after infection. (E) ORI/Mb distribution of empty vector and Ras cells at day 7 after infection. The error bars indicate the Standard Error of the Mean (SEM).

Taken together these results, even though the differences are relatively small, confirm the presence of a trend where upon oncogenic Ras expression the frequency of initiation events increases over time, both in the bulk of fibers and, though to a lesser extent, also in the long fibers.

2.2.5 Oncogene activation and the symmetry of fork progression

I then tested the effect of oncogene activation on the symmetry of fork progression by analysing the left to right fork speed correlation (Figure 45-50). This parameter allows the evaluation of the level of symmetry of two replication forks generated at the same DNA replication origin. I could define 3 different groups of symmetry: a. symmetric (blue dots), in which the difference between left and right fork speed is between 0 to 30% of the highest fork speed; b. asymmetric (green dots), in which the difference between left and right fork speed is between 30 to 99 %; c. Unidirectional (red dots) in which the difference between left and right fork speed is 100 %, meaning that one of the two forks did not start during the first pulse (for further details the section *DNA Molecular Combing*). During the first day after infection (day 2) the level of symmetry (blue bar, Figure 45) of fork progression is similar between oncogenic Ras-expressing cells and control cells. The main difference between oncogenic Ras-expressing cells and control cells lies in the unidirectional forks (the highest level of fork stalling, red bar, Figure 45). Indeed they are almost doubled in oncogenic Ras-expressing cells as respect to control cells (Figure 45). This high level of unidirectional fork holds true also in the following day (day3, Figure 46). Moreover on day 3 the overall level of symmetry of fork progression is around 15% lower in oncogenic Ras-expressing cells as respect to control cells (Figure 46).

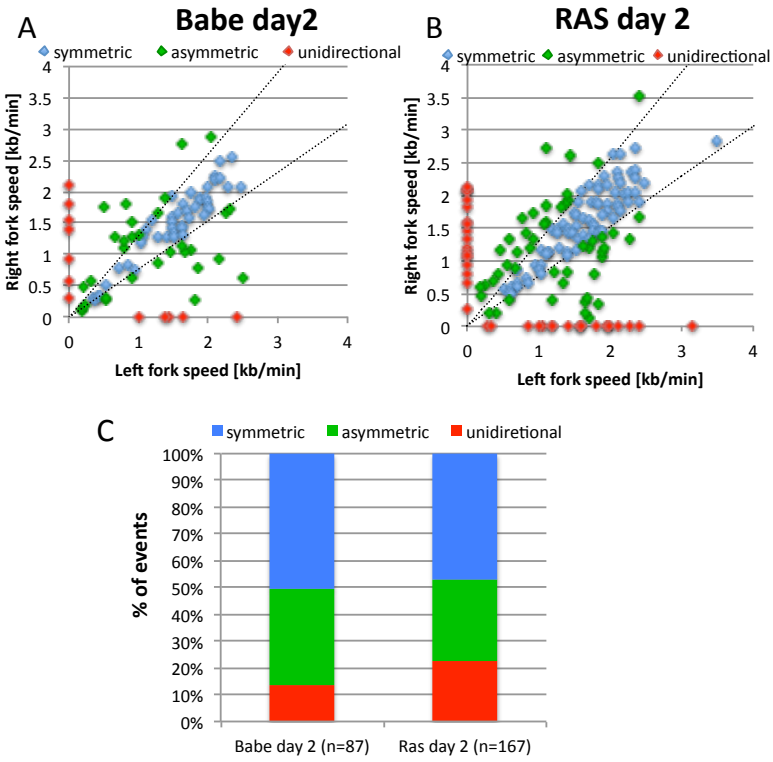

Figure 45. Symmetry of fork progression on day 2 after infection.
Symmetry of fork progression was calculated as the Left to Right fork speed correlation: right (y axis) and left (x axis) fork speed coming from the same replication origin are plotted in A and B. Three groups of fork progression were considered: symmetric (blue dots), in which the difference between Left and Right fork speed is between 0 to 30%; Asymmetric (green dots), in which the difference between Left and Right fork speed is between 30 to 99 %; Unidirectional (red dots) in which the difference between Left and Right fork speed is 100 %, where one of the two forks did not even start during the first pulse. (A-B) Left to right fork speed correlation at day 2 after infection with the empty vector (Babe) (A), and oncogenic form of Ras (B). (C) Percentage of symmetric, asymmetric and unidirectional fork progression on day 2 after infection.

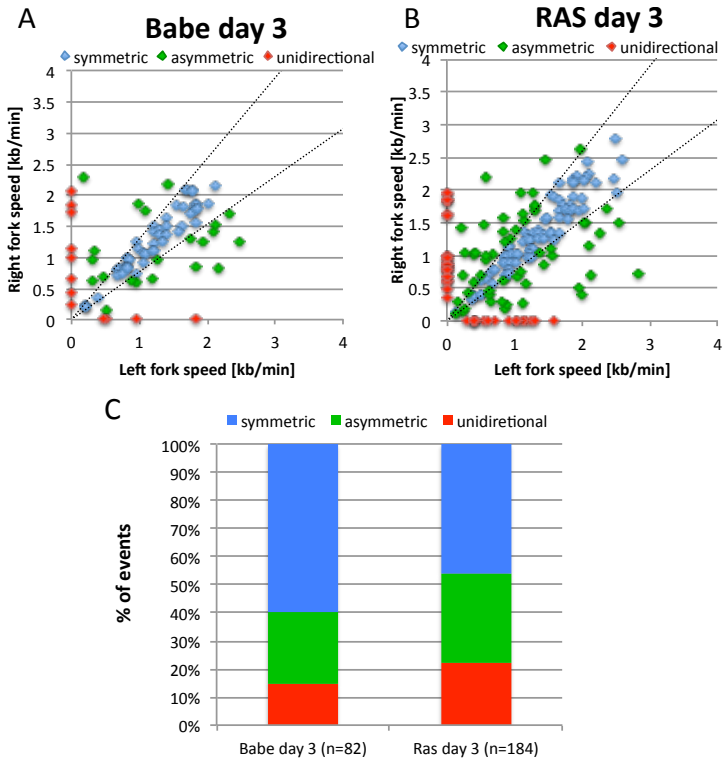

Figure 46. Symmetry of fork progression on day 3 after infection.
(A-B) Left to right fork speed correlation at day 3 after infection with the empty vector (Babe) (A), and oncogenic form of Ras (B). (C) Percentage of symmetric, asymmetric and unidirectional fork progression on day 3 after infection.

At later time points, with day 4 being the transition point (Figure 47), the level of symmetry of fork progression in oncogenic Ras-expressing cells reaches the level of control cells (day 4-5, Figure 47-48), with unidirectional forks becoming even lower than the control (day 7, Figure 49).

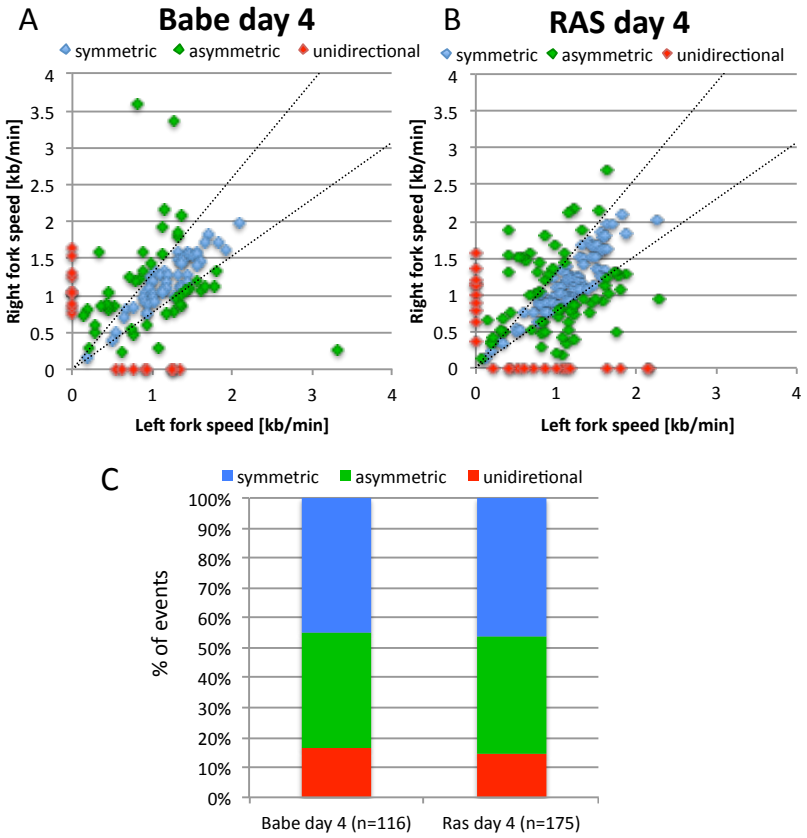

Figure 47. Symmetry of fork progression on day 4 after infection.
(A-B) Left to right fork speed correlation at day 4 after infection with the empty vector (Babe) (A), and oncogenic form of Ras (B). (C) Percentage of symmetric, asymmetric and unidirectional fork progression on day 4 after infection.

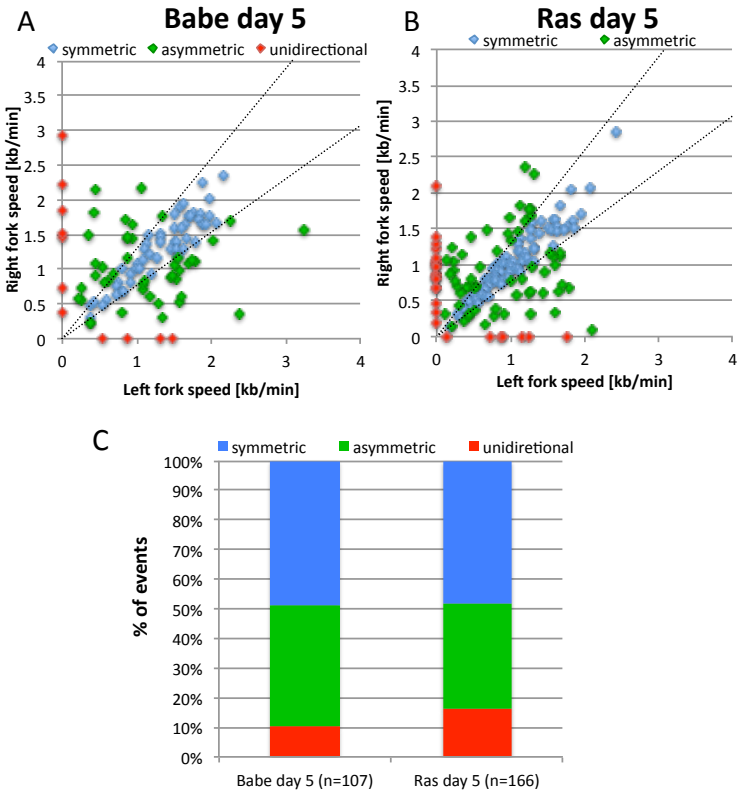

Figure 48. Symmetry of fork progression on day 5 after infection.
(A-B) Left to right fork speed correlation at day 5 after infection with the empty vector (Babe) (A), and oncogenic form of Ras (B). (C) Percentage of symmetric, asymmetric and unidirectional fork progression on day 5 after infection.

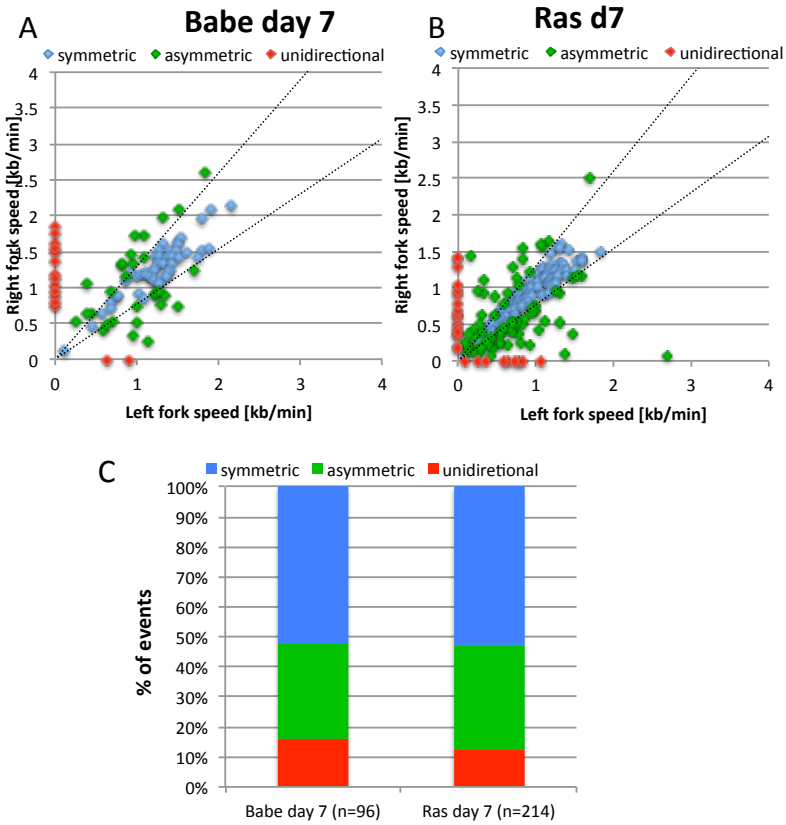

Figure 49. Symmetry of fork progression on day 7 after infection.
(A-B) Left to right fork speed correlation at day 7 after infection with the empty vector (Babe) (A), and oncogenic form of Ras (B). (C) Percentage of symmetric, asymmetric and unidirectional fork progression on day 7 after infection.

To check how the symmetry of fork progression is changing over time, I plotted the data of symmetry time point by time point in Figure 50. As for the control, the level of symmetry and asymmetry is fairly constant. As for oncogenic Ras-expressing cells, the overall level of symmetry is rather constant over time, while the level of unidirectional forks shows an apparent decrease over time.

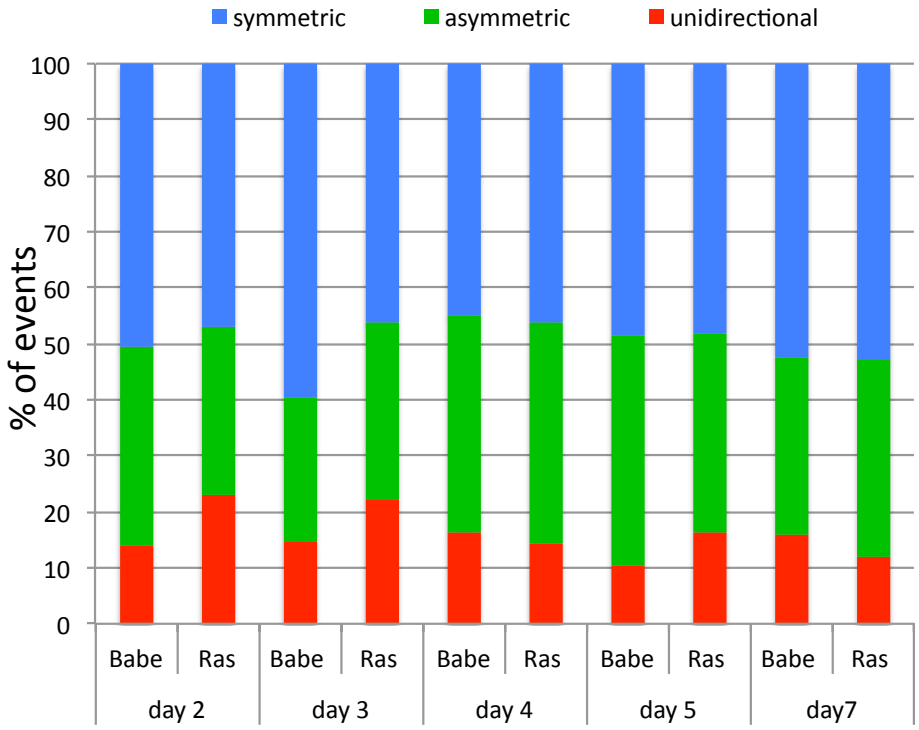

Figure 50. Symmetry of fork progression occurring during the growth curve experiments.
Percentage of symmetric, asymmetric and unidirectional fork progression during growth curve experiment in –Babe (empty vector) and H-RasV12 infected cells.

I then quantified the percentage of fork stalling occurrence. I considered fork stalling as all the forks that show an asymmetric behaviour as respect to the sister fork (sister fork = fork coming from the same DNA replication origin). Thus fork stalling consists in the sum of asymmetric and unidirectional forks. As shown in Figure 51, oncogene activation does not seem to induce massive fork stalling. Indeed the levels of fork stalling are similar between oncogenic Ras-expressing cells and control cells in all time points, except from day 3, where oncogenic Ras has a more than 10% increase in fork

stalling as compared to the control and this difference is statistically significant.

A

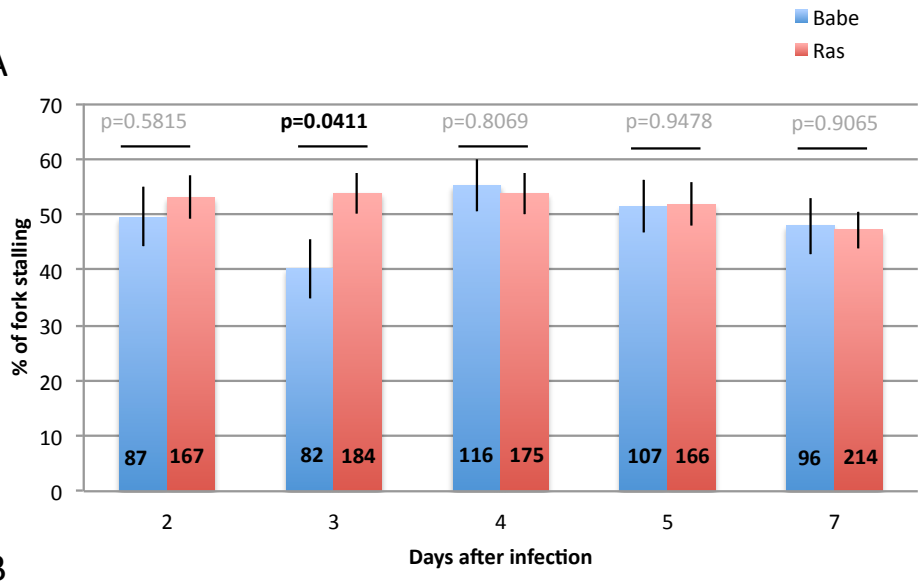

B

	B2	R2	B3	R3	B4	R4	B5	R5	B7	R7
B2		0.5815	0.2305	0.5004	0.417	0.5127	0.7842	0.7188	0.8384	0.7256
R2	0.5815		0.058	0.8937	0.7308	0.9081	0.7866	0.8166	0.422	0.258
B3	0.2305	0.058		**0.0411**	**0.0385**	**0.0441**	0.1275	0.0864	0.3044	0.2822
R3	0.5004	0.8937	**0.0411**		0.8168	0.9864	0.6922	0.7086	0.3493	0.1887
B4	0.417	0.7308	**0.0385**	0.8168		0.8069	0.5728	0.5773	0.2926	0.1665
R4	0.5127	0.9081	**0.0441**	0.9864	0.8069		0.7058	0.7244	0.361	0.2009
B5	0.7842	0.7866	0.1275	0.6922	0.5728	0.7058		0.9478	0.5545	0.4773
R5	0.7188	0.8166	0.0864	0.7086	0.5773	0.7244	0.9478		0.5439	0.3725
B7	0.8384	0.422	0.3044	0.3493	0.2926	0.361	0.5545	0.5439		0.9065
R7	0.7256	0.258	0.2822	0.1887	0.1665	0.2009	0.4773	0.3725	0.9065	

Figure 51. Effect of oncogene activation on fork stalling and unidirectional forks.
(A) Percentage of fork stalling. We intend fork stalling as the sum of the asymmetric and the unidirectional forks. (B) Table showing the p-value for the graph shown in A. The error bars indicate the Standard Error of the Mean (SEM). p-values were calculated applying Chi-squared test.

So I further checked for the impact of oncogene activation on the unidirectional forks (Figure 52). As for the control, the level of unidirectional forks seems to be constant over time. As for Ras samples, it seems that there is a trend: right after oncogenic activation (day 2 and 3) high levels of unidirectional forks are detected, these then decrease gradually to levels even lower than controls (day 7). Even though the statistical significance of these data is not completely proven (see Figure 52B for p values), a trend is clearly appreciable.

A

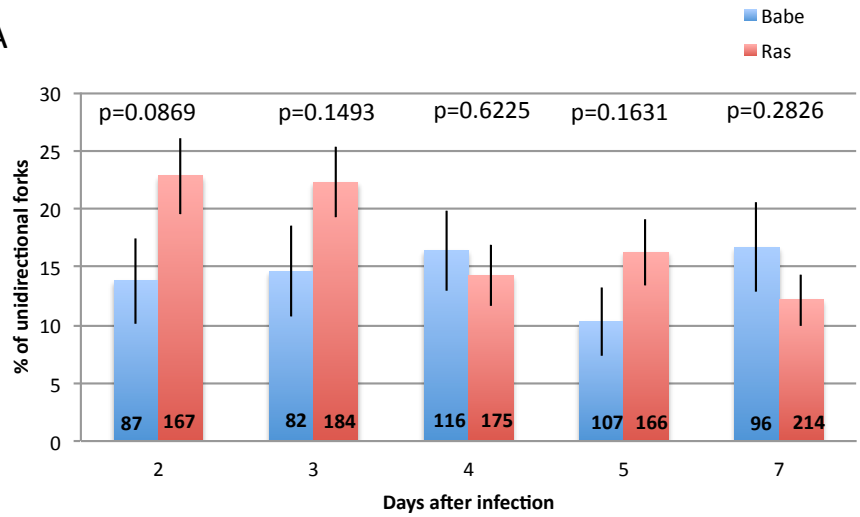

B

	B2	R2	B3	R3	B4	R4	B5	R5	B7	R7
B2		0.0869	0.8756	0.1000	0.6122	0.9141	0.4516	0.6050	0.5897	0.6971
R2	0.0869		0.1307	0.9016	0.1854	**0.0429**	**0.0085**	0.1331	0.2355	**0.0060**
B3	0.8756	0.1307		0.1493	0.7392	0.9409	0.3642	0.7400	0.7105	0.5674
R3	0.1000	0.9016	0.1493		0.2132	0.0506	**0.0100**	0.1554	0.2680	**0.0071**
B4	0.6122	0.1854	0.7392	0.2132		0.6255	0.1824	0.9796	0.9553	0.2851
R4	0.9141	**0.0429**	0.9409	0.0506	0.6255		0.3281	0.6113	0.6009	0.5346
B5	0.4516	**0.0085**	0.3642	**0.0100**	0.1824	0.3281		0.1631	0.1810	0.6211
R5	0.6050	0.1331	0.7400	0.1554	0.9796	0.6113	0.1631		0.9326	0.2507
B7	0.5897	0.2355	0.7105	0.268	0.9553	0.6009	0.1810	0.9326		0.2826
R7	0.6971	**0.0060**	0.5674	**0.0071**	0.2851	0.5346	0.6211	0.2507	0.2826	

Figure 52. Effect of oncogene activation on fork stalling and unidirectional forks.
(A) Percentage of unidirectional forks. (B) Table showing the p-value for the graph shown in A. The error bars indicate the Standard Error of the Mean (SEM). p-values were calculated applying Chi-squared test.

Taken together these data about the symmetry of fork progression reveal an overarching trend in which at early time points oncogenic Ras-expressing cells show high levels of unidirectional forks, with the differences with control cells reduced at minimal level at the latest time point.

2.2.6 Effect of Oncogene activation on DNA replication dynamics

To gain a synthetic picture of the impact of oncogene activation on DNA replication dynamics I compiled the observation of all the replication parameters that I assessed (fork speed, IODs, ORI/Mb, Fork stalling, Unidirectional forks) in one figure (Figure 53) and I tried to extrapolate possible trends for each factor over time. To achieve this, I added trend lines for each parameter. These trend lines are directly built over the graph by an Excel

function. For all the parameters I choose polynomial regression of order 3. R^2 is the coefficient of determination and it estimates how the regression line is close to the real data point. R^2 varies from 0 to 1. The closest this coefficient is to 1 the most reliable the trend line is.

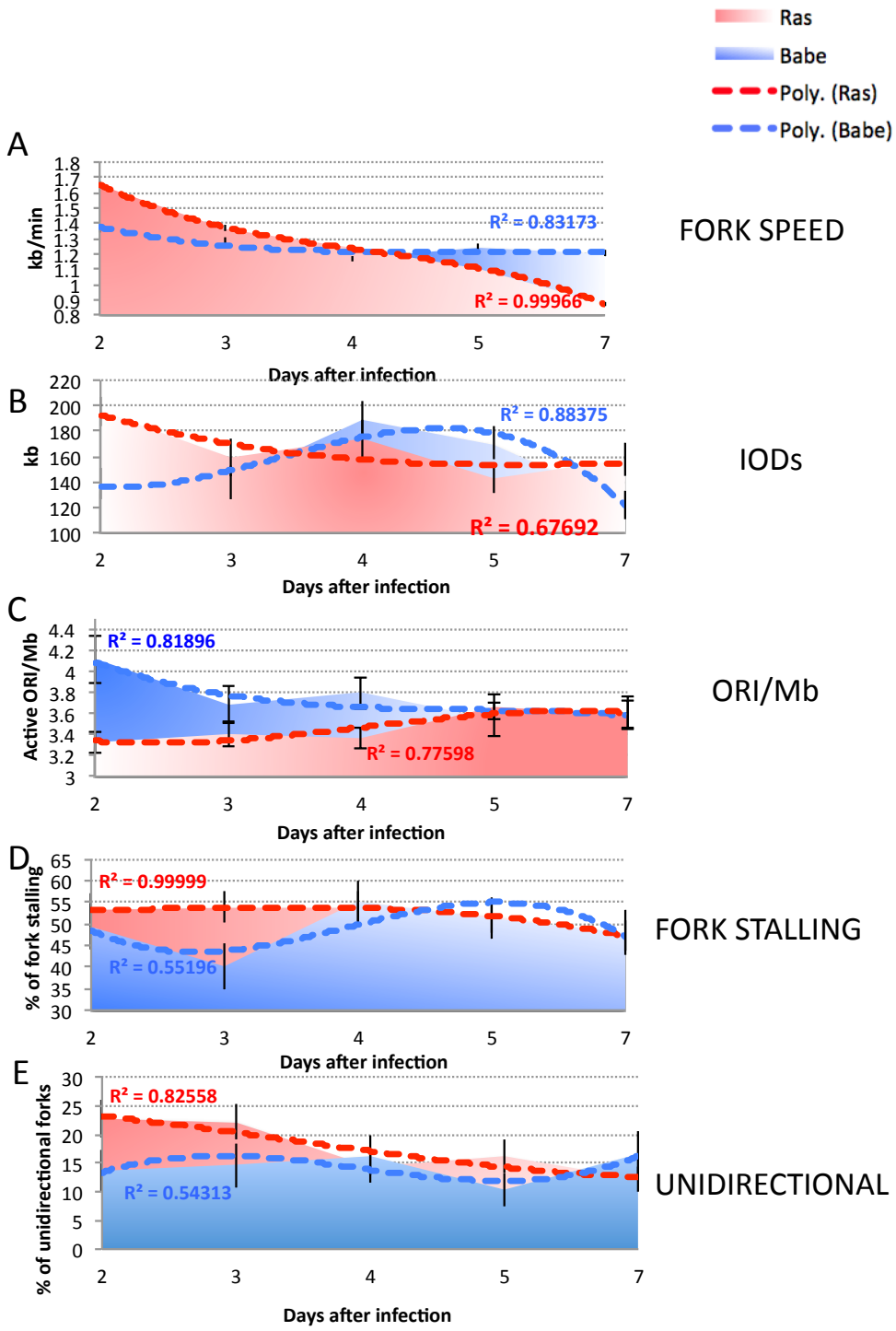

Figure 53. Trend plots for each DNA replication parameter.
Trend lines (dashed lines, blue for control, red for H-RasV12 are directly built over the graphs by an excel function. All trend lines derive from polynomial regression curves of order 3 directly calculated by an Excel function. R^2 is the coefficient of determination, and it estimates how the regression line is close to the real data point. R^2 varies from 0 to 1. The closest it is to 1 the most reliable the trend line is. (A) Fork speed. (B) IODs from long fibers. (C) ORI/Mb from long fibers. (D) Fork stalling. (E) Unidirectional forks.

From this analysis I do not intend to infer any statistical correlation. This analysis is made to better appreciate possible trends of the replication changes over time at a glance.

With this approach, is appreciated that at early time points after oncogene activation, fork speed is very high, being the highest amongst all the conditions analysed. Consequently, the frequency of initiation events is low, as inferred both by high IODs and low ORI/Mb. Only at later time points, as the fork speed decreases the frequencies of initiation are slightly increasing, reaching control levels as cells are entering OIS. Moreover, together with the high fork speed of the early time points, oncogenic Ras cells have higher levels of fork stalling, in particular of unidirectional forks, which represent forks undergoing the highest level of fork stalling. The unidirectional forks are gradually reduced to control levels at later time points.

CHAPTER 3. Nox4 plays an essential role in Ras-induced ROS production

Oncogenic Ras expression is responsible for increased production of Reactive Oxygen Species (ROS). Beyond their toxic effects, ROS are essential intracellular second messengers for several cytokines and growth factors (Lee et al., 1999) mediating mitogenic signalling (Irani et al., 1997). Unpublished data from our lab (Muege Ogrunc et al. under revision) indicate that ROS are essential for the onset of OIS: ROS depletion by treatment with ROS scavengers - such as N-Acetyl-Cystein (NAC) - prevents cells to undergo senescence by suppressing oncogene-induced hyperproliferation and DNA damage response (DDR) activation. Thus ROS are the "fuel" that drives the aberrant cell proliferation intrinsically associated with DNA damage generation and DDR activation.

Given the fundamental role of ROS in the establishment of OIS, our lab searched for the enzymes that could account for oncogene-induced ROS production. Some members of NADPH oxidases (NOX) family have been previously implicated in cell proliferation and cancer (Block and Gorin, 2012; Burdon, 1995; Suh et al., 1999). We observed that, among the NOX1-5 genes tested, NOX4 is most strongly expressed in human fibroblasts, and it was further induced upon oncogene activation (Figure 54).

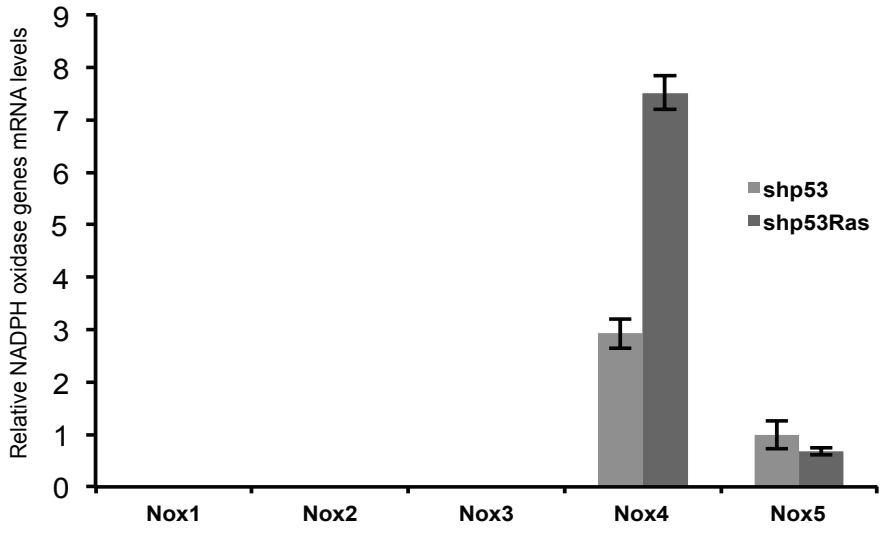

Figure 54. NOX4 is upregulated upon oncogenic Ras expression.
qRT-PCR analysis of human NOX genes in shp53 or shp53 Ras Human Normal Fibroblasts. (Performed by Muge Ogrunc. Adapted from Ogrunc et al 2013 under revision).

3.1 Pharmacological inhibition of NOX4 prevents oncogene-induced hyperproliferation, DDR activation and OIS establishment

Our data indicate that Nox4 is the candidate enzyme to be the responsible for oncogene-induced ROS production. Therefore we tested the effects that Nox4 inhibition has on ROS production as well as on oncogene-induced hyperproliferation, DDR activation and OIS. For this purpose we used a specific Nox4 small-molecule inhibitor (Nox4i). We chose this Nox4 inhibitor, since it was the most potent among the compounds identified and characterized in a cell-based assay for the ability to inhibit ROS production by Nox4 (Borbely et al., 2010). Figure 55 shows the chemical structure of the compound.

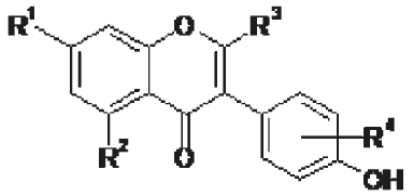

7c: R^1= OH, R^2= H, R^3= OH, R^4= 3-OH

Figure 55. Chemical structure of small-molecule inhibitors of NOX4 enzymatic activity.
Nox4 inhibitor, a derivative of flavonoids (Borbely et al., 2010).

Normal human fibroblasts were transduced with H-RasV12 or EV retroviral vectors and treated with NOX4i or DMSO as a control. Their growth was followed for 9 days, till OIS was established in H-Ras untreated cells (Figure 56A).

Treatment with the Nox4 inhibitor efficiently prevents ROS accumulation upon oncogenic Ras expression, as detected by the Dihydroethidium (DHE) probe. DHE after entering the cells, interacts with O•− to form oxyethidium, and emits a bright red colour detectable by fluorescence microscopy ((Amir, 2008), see Materials and Methods for further details; Figure 57).

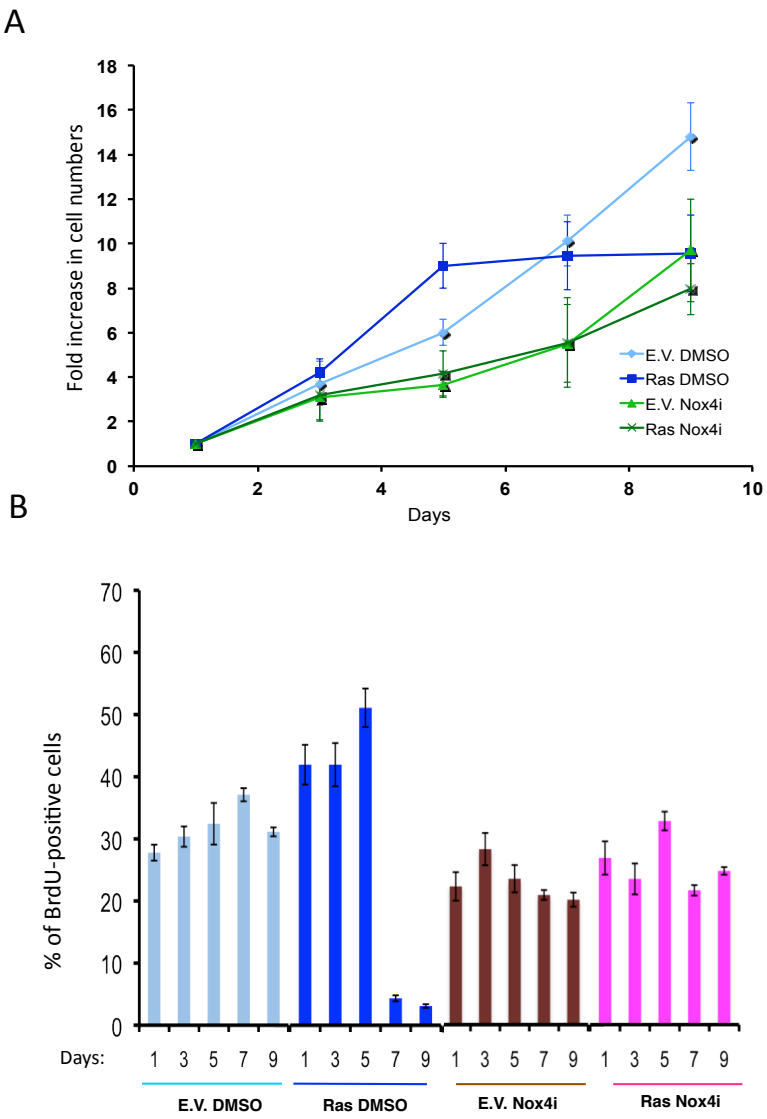

Figure 56. Pharmacological inhibition of Nox4 enzymatic activity prevents OIS establishment.
Pharmacological inhibition of Nox4 enzymatic activity prevents hyperproliferation by H-RasV12. (A) NOX4 inhibitor, but not its vehicle (DMSO) prevents H-RasV12-induced hyperproliferation and OIS establishment. (B) BrdU incorporation rates measured at the indicated time points of the growth curve displayed in panel 3A show that both hyperproliferation and cellular senescence are abolished by Nox4i treatment. (Performed by Muge Ogrunc. Adapted from Ogrunc et al 2013 under revision).

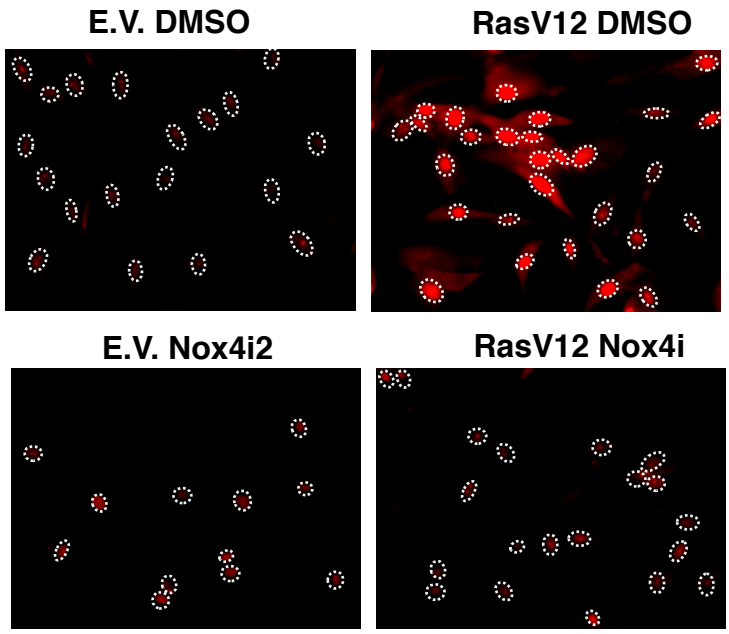

Figure 57. Upon pharmacological inhibition of Nox4 enzymatic activity ROS quantities are reduced to control levels.
Nox4i treatment reduces ROS accumulation in H-RasV12 cells as detected by the DHE probe. (Performed by Muge Ogrunc. Adapted from Ogrunc et al 2013 under revision).

In addition to inhibiting ROS production, this treatment fully suppresses oncogene-induced cell hyperproliferation, while empty vector-transduced cells are not significantly affected by NOX4i treatment. This effect is apparent both on cell proliferation and DNA replication rates as measured by BrdU incorporation (Figure 56 A-B). In agreement with our model, the suppression of hyperproliferation by the use of a NOX4 inhibitor also prevents oncogene-induced DDR activation (Figure 58).

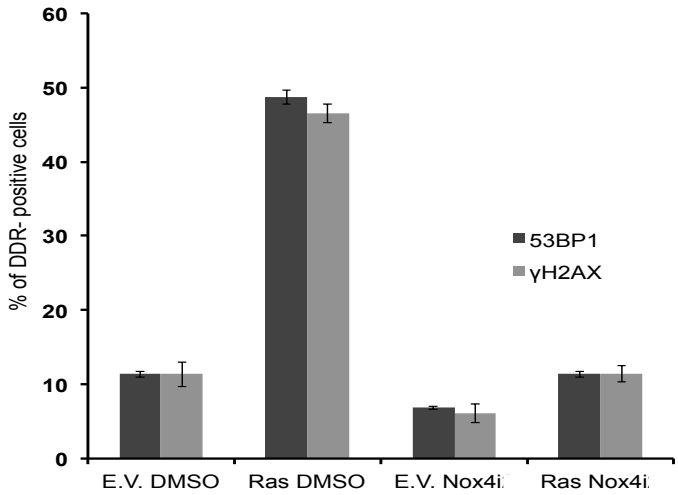

Figure 58. Pharmacological inhibition of Nox4 enzymatic activity strongly reduces DDR activation.
Immunostaining of cells at the last time point of the growth curves shown in Figure 56, indicates that DDR activation is strongly reduced by Nox4i treatment. (Performed by Muge Ogrunc. Adapted from Ogrunc et al

2013 under revision).

3.2 Inhibition of ROS production by NOX4 inhibitors treatment reduces proliferation rates specifically in cells expressing oncogenic Ras.

The results of NOX4 inhibitor are consistent with the model previously discussed, in which ROS reduction is an efficient mechanism to suppress hyperproliferation, prevent DDR activation and OIS establishment. Nonetheless, cancer cells avoid OIS by DDR inactivation and are characterized by rampant proliferation and high levels of ROS (Grek and Tew, 2010) (Szatrowski and Nathan, 1991). To better understand the role of ROS in the context of DDR-deficiency, we therefore tested fully transformed HNF (BJELR; expressing oncogenic Ras, hTERT and the SV40 early region (Hahn et al., 1999) and the respective control cell line (BJhTERT) for their response to NOX4i. Cells were treated for 6 days with NOX4i or with DMSO as a control and proliferation rates were checked by BrdU incorporation. We observed that NOX4 inhibition, and subsequent ROS levels reduction, dramatically decreases BrdU incorporation rates only in cells expressing oncogenic Ras (Figure 59). These data further support the hypothesis of ROS as the fuel of oncogene-induced hyperproliferation and highlight the dependency of oncogene-expressing cells on ROS.

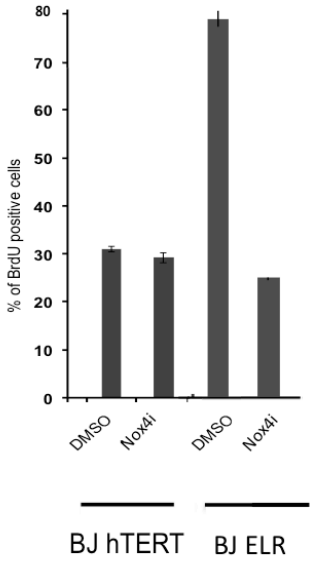

Figure 59. ROS scavenging with NOX4 inhibitor treatment reduced proliferation rates only in cells expressing oncogenic Ras.
Both BJ hTERT and BJ ELR cells were cultured in the presence of NOX4i or DMSO for six consecutive days. BrdU incorporation rates for day 6 are shown. (Performed by Muge Ogrunc. Adapted from Ogrunc et

al 2013 under revision).

3.4 Effect of NOX4 inhibition on DNA replication dynamics.

Given the fundamental role of ROS in oncogene-induced proliferation, I tested the effect that ROS suppression by NOX4 inhibition has on DNA replication dynamics. To address this question I used the DNA molecular combing technique (Lebofsky and Bensimon, 2003; Michalet et al., 1997). Briefly, after 6 days of treatment with the NOX4i or with DMSO as a control, BJELR cells were pulse labelled with thymidine analogues for a precise time interval (1^{st} pulse IdU, 20 min: 2^{nd} pulse CldU 20 min). DNA was then purified, combed on glass slides and IdU and CIdU were detected by fluorescent staining, together with anti single-strand DNA antibodies. Before proceeding with the analysis of DNA replication parameters, I checked for the effect of NOX4 inhibition on the proliferation rates on the cells used for combing experiments. As shown in Figure 59 NOX4 inhibitor induces a 55% reduction in BrdU incorporation rates as compared to control cells.

3.4.1 Nox4 inhibitor reduces fork speed upon oncogene activation

I checked the effect that NOX4 inhibition has on replication fork speed. Fork speed is calculated dividing the length of the replication signal by the incubation time. For each condition I analysed around 1200 fork speeds. I excluded from these analyses all replication signals in which their extremities were not flanked by ssDNA, since I could not be confident that the distal end of the replication signal was not caused by the fiber break. (for further details the section *DNA Molecular Combing*).

I observed that Nox4i treatment induces a ~ 20% decrease in fork speed as respect to the control, where Nox4i is 0.824 kb/min (n=1156) and DMSO is 1.01 kb/min (n=1185). These differences are highly statistically significant ($p< 1.114e^{-40}$) and can be better appreciated as a shift of the fork speed distribution towards smaller values (Figure 60).

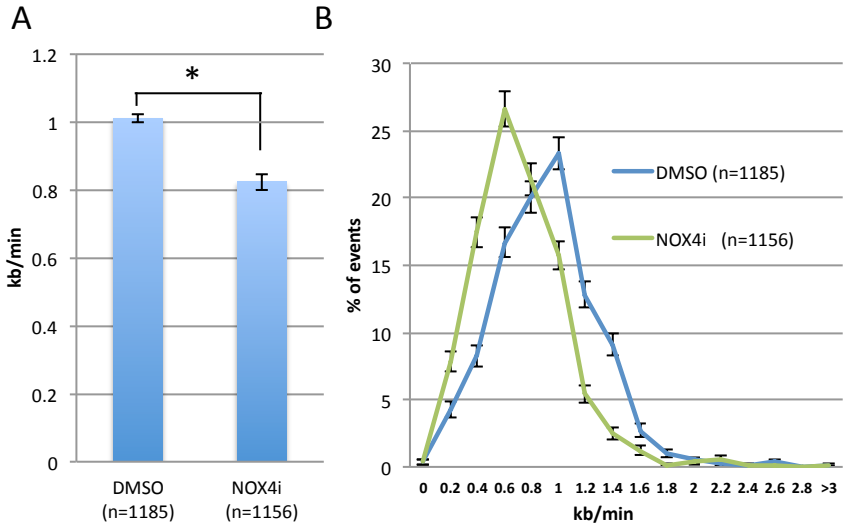

Figure 60. NOX4 inhibitor treatment reduces for speed.
(A) The graph shows the average of fork speed for each condition analysed. Fork speeds were calculated by dividing the length of replication signal over the time of incubation with the thymidine analogues (20 min). (B) Fork speed distribution. The error bars indicate the Standard Error of the Mean (SEM). p values were obtained applying Wilcoxon test. * ***P***<1.114e-40.

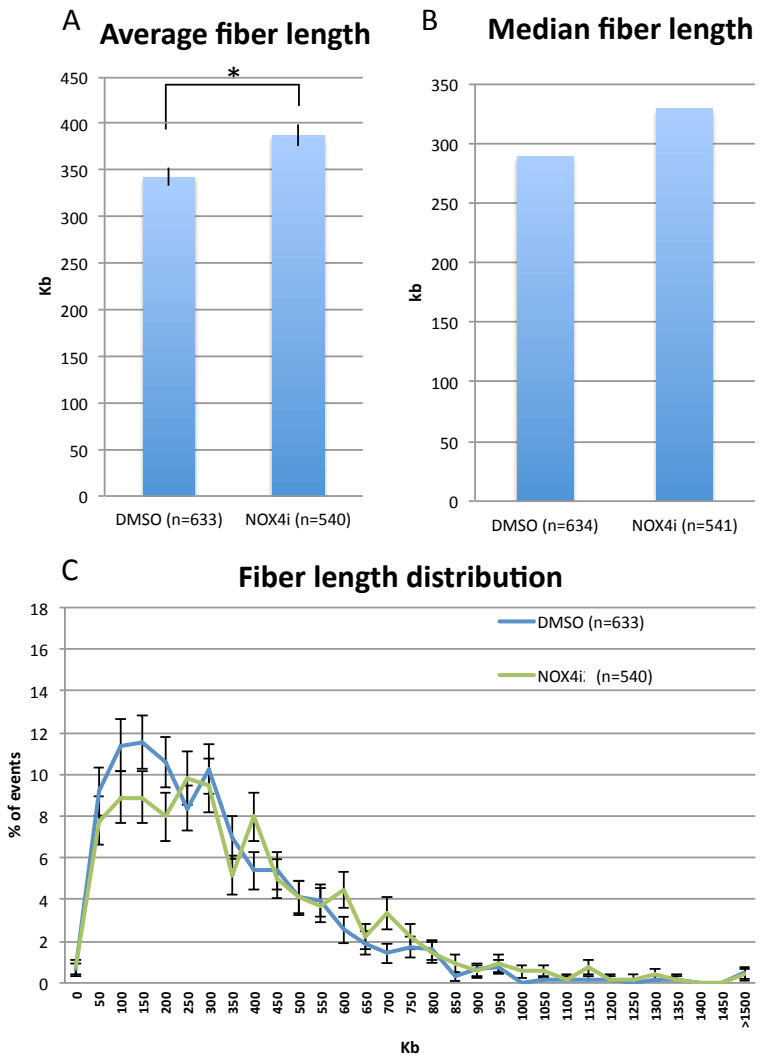

Figure 61. DNA Fiber length analysis.
(A) Average length of the DNA fibers analysed to obtain fork speed. (B) Median length of the DNA fibers analysed to obtain fork speed. (C) DNA Fiber length distribution. The error bars indicate the Standard Error of the Mean (SEM). p values were calculated applying Wilcoxon test. *P<0.004966.

To ensure accurate fork speed estimation, the median size of fiber length should be at least 200 kb, as suggested in (Techer et al., 2013). Therefore I checked the fiber length distribution to make sure that it did not influence my fork speed analysis (Figure 61).

Indeed the median size of fiber length is always higher than 200 kb in my samples (NOX4i: 288.714 kb; DMSO: 328.926 kb). Thus the fork speed estimation is not affected by fiber length in our samples.

Taken together these data indicate that treatment with Nox4-generated ROS impact on DNA replication by increasing fork speed.

3.4.2 Nox4 inhibition does not affect Inter-Origin-Distances

The next parameter I assessed is the Inter-Origin-Distance (IOD), that is the measure of the distance between two adjacent origins and account for the evaluation of DNA replication initiation events: a smaller IOD indicates higher number of simultaneously active origins, while higher IOD corresponds to lower number of simultaneously active origins. For each condition I analysed around 100 IODs both for control and for oncogenic Ras-expressing cells. The proper estimation of the distance between replication origins (ORI) requires replication patterns that allow precise positioning of the ORI. One ORI is defined as the central point on the ssDNA signals that is flanked on both sides from replication signal generated by the 1st pulse. Thus, all the origins for which the position could not be precisely determined - due to the lack of replication signal on one of the extremities of the DNA fiber or in case of unidirectional forks - were excluded from the analysis (for further details the section *DNA Molecular Combing*).

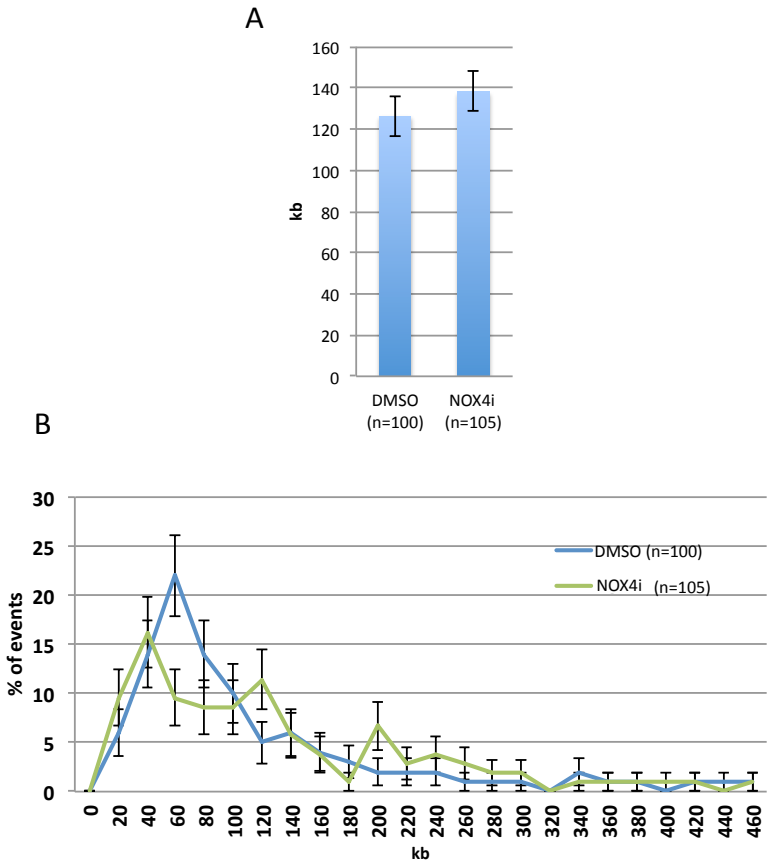

Figure 62. Effect of pharmacological inhibition of Nox4 enzymatic activity on Inter-Origin-Distances (IODs).
Inter-Origin-Distances (IODs) were calculated as the distance between two adjacent origins laying on the same DNA fiber. (A) Average of IODs for each condition analysed. (B) IODs distribution for each condition analysed. The error bars indicate the Standard Error of the Mean (SEM).

IODs are larger in Nox4i-treated cells, 138.123 kb (n=105), compared with DMSO, 126.23 kb (n=100), but these differences are not statistically significant ($p<0.4$) (Figure 62A). However by analysing the distributions of IODs (Figure 62B) it becomes apparent that Nox4 inhibition impacts differently on different sets of origins causing the appearance of two or possibly three peaks of IOD lengths, centred on IODs smaller or larger than controls. This may be interpreted as different kinds of DNA replication origins may respond differently to ROS modulation. Consequently, when all IODs are pooled and compared to control (DMSO) cells, the differences lose statistical significance. To ensure IODs analysis was not influenced by DNA fibers length I checked the median size of fibers length, as suggested in (Techer et al., 2013). To accurately estimate IODs, the median size of fibers length should be at least of 350 kb (Techer et al., 2013), which was always the

case in our sample (NOX4i: 525.95 kb; DMSO: 652.70 kb), indicating that IODs evaluation was not influenced by fibers length (Figure 63).

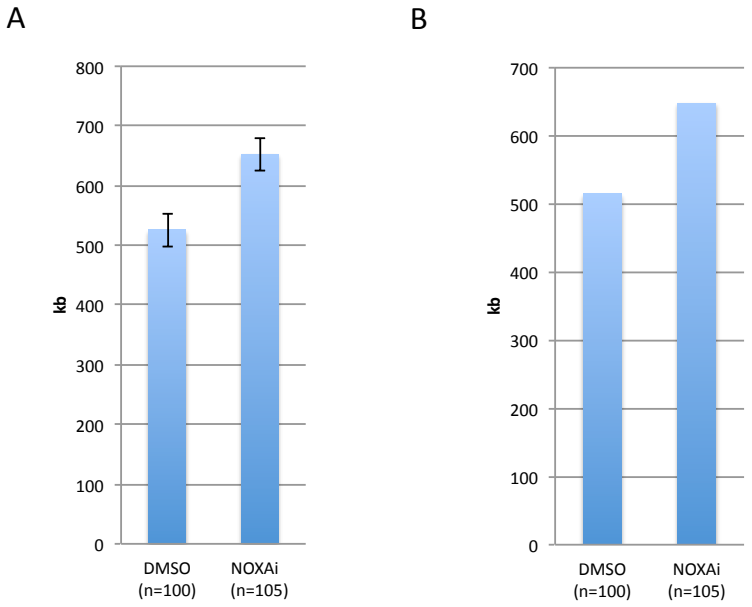

Figure 63. Average and Median DNA fibers lengths of the DNA fibers containing IODs.
(A) Average length of the DNA fibers analysed to obtain IODs. (B) Median length of the DNA fibers analysed to obtain IODs. The error bars indicate the Standard Error of the Mean (SEM).

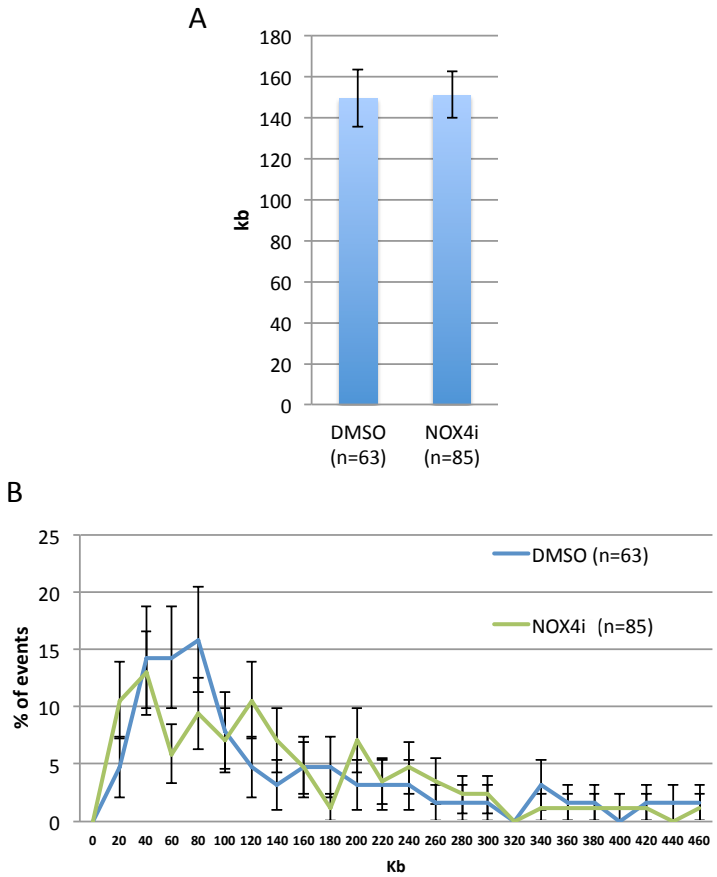

Figure 64. Quantification of Inter-Origin-Distances on long fibers.
(A) Inter-Origin-Distances (IODs) lying on DNA fibers that are at least 3 times longer than the average of each condition analysed. This procedure allows you to avoid bias due to DNA fibers fragmentation in different sample (Bianco et al., 2012). (B) Distribution of the IODs lying on DNA fibers at least 3 times longer than the IODs average. The error bars indicate the Standard Error of the Mean (SEM).

In any case, to further exclude any bias caused by fibers fragmentation in IODs estimation, I recalculated IODs by studying only fibers at least three times longer the average of IODs, as suggested in (Bianco et al., 2012). Under these conditions the two samples reach similar levels: 150.84 kb in Nox4i treated cells versus 149.5 kb in control cells, confirming the absence of a statistically and biological significant difference in IODs between Nox4i and DMSO (Figure 64A). Nevertheless also in this case by checking the distributions of IODs (Figure 64B) Nox4 inhibition shows two peaks of IOD lengths, while the control cells present a single peak, further supporting the possibility that Nox4 inhibition impacts differently on different set of origins. To further confirm this trend I analysed also another parameter to estimate the frequency of initiation: the active ORI/Mb.

3.4.3 NOX4 inhibition does not affect the number of active ORI/Mb

Another parameter that accounts for the frequency of initiation events that is less sensitive to variations in fiber length (Bianco et al., 2012), is the measure of ORI/Mb that corresponds to the number of active replication origin per Megabase of DNA.

NOX4i treatment does not affect the number of active ORI/Mb as compared to control (DMSO vs NOX4i, 6.07 ORI/Mb vs 5.85 ORI/Mb, p<=0.03603) (Figure 65). To further avoid bias due to fiber length I considered only the ORI/Mb deriving from fibers longer than 300 kb. Also in this case, NOX4i treatment does not affect the number of active ORI/Mb as compared to control (DMSO vs NOX4i1, 3.59 ORI/Mb vs 3.47 ORI/Mb; p <= 0.6607; Figure 66). Moreover, the observation of multiple peaks found in the IODs distributions of cells treated with the NOX4 inhibitor is different from the absence of peaks in the distributions of ORI/Mb in the same cells. Although these differences may account to the different sensitivity of the two parameters analysed, an intriguing interpretation is that IODs are more sensitive to (or measure only) the simultaneously active origins in clusters, whereas the number of active ORI/Mb incorporates also isolated origins.

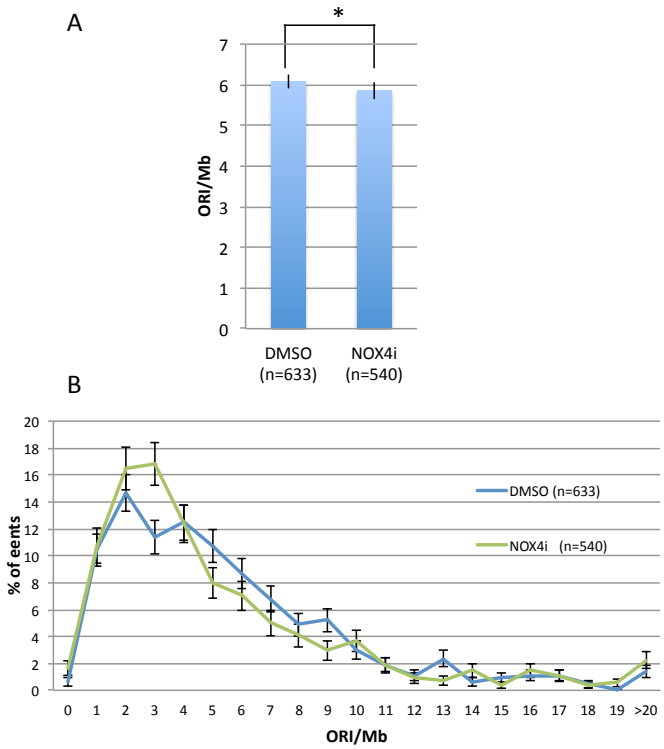

Figure 65. Quantification of the number of active Origin per Megabases (ORI/Mb).
The number of active origins per Megabases (ORI/Mb) was calculated by making the ratio between the number active origins present in the DNA fiber analyzed and the length of the fiber (Bianco et al., 2012). (A) Number of active origin per Mega base (ORI/Mb). The graph shows the average of ORI/Mb for each condition analysed. (B) ORI/Mb distribution for each condition analysed. The error bars indicate the Standard Error of the Mean (SEM). p values were calculated applying Wilcoxon test. *p <0.03603.

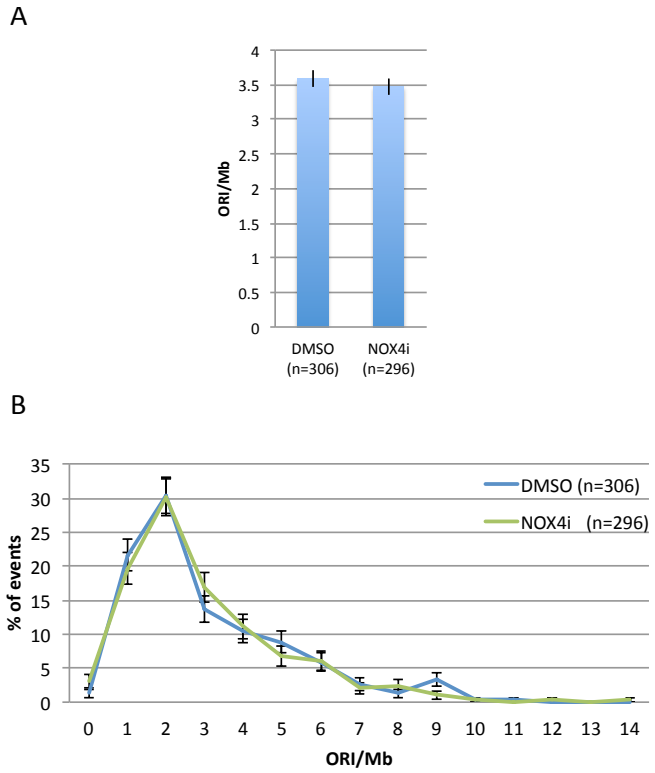

Figure 66. Quantification of the number of active Origin per Megabases (ORI/Mb) on long fibers.
(A) Number of active origin per Megabases (ORI/Mb) on fibers longer than 300 kb. The graph shows the average of ORI/Mb for each condition analysed. (B) ORI/Mb distribution for each condition analysed. The error bars indicate the Standard Error of the Mean (SEM).

Taken together, the results about the frequency of initiation events, - assessed by IODs and the number of active ORI/Mb - indicate that even though the general frequency of initiation does not seem to be affected by NOX4 inhibition, when looking at IODs distribution, which account for clustered simultaneously active origins, the presence of multiple peaks might indicate a differential regulation of local origin initiation upon NOX4 inhibition.

3.4.4 NOX4 inhibition does not influence the symmetry of fork progression

I then tested the effect of NOX4 inhibition on the symmetry of fork progression by analysing the Left to Right fork speed correlation (Figure 67). This parameter allows evaluating the level of symmetry of two replication forks generating from the same DNA replication origin. I could define 3 different groups of symmetry: a. Symmetric (blue dots), in which the difference between Left and Right fork speed is between 0 to 30% of the highest fork speed between the left and the right; b. Asymmetric (green dots), in which the difference between Left and Right fork speed is between 30 to 99 %; c. Unidirectional (red dots) in which the difference between Left and Right fork speed is 100 %, where one of the two fork did not even start during the first pulse (for further details the section *DNA Molecular Combing*).

By looking at the correlation plots it seems there are no differences in terms of replication fork progression upon NOX4 inhibition compared with the control (Figure 67).

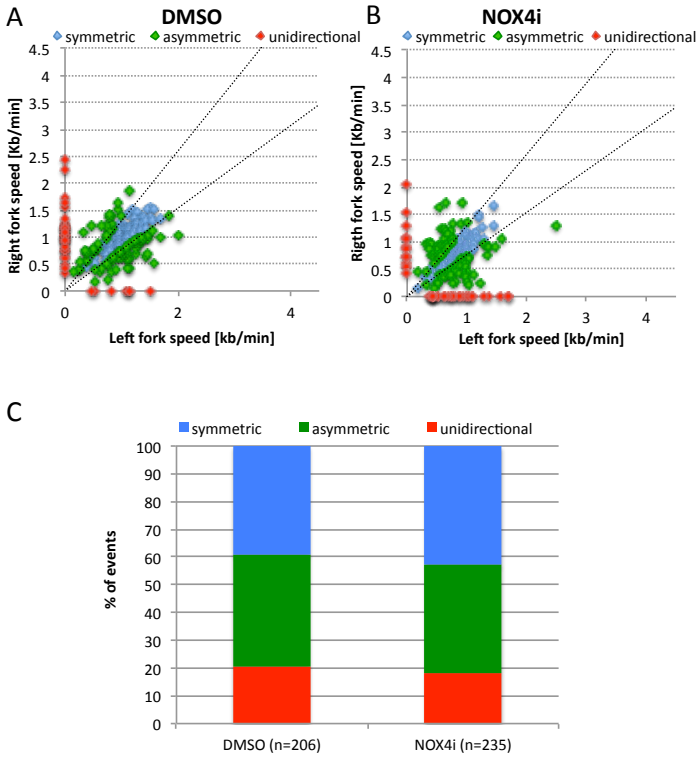

Figure 67. Left to Right fork speed correlation upon treatment with NOX4 inhibitors.
Right (y axis) and left (x axis) fork speed coming from the same replication origin, are plotted. To asses symmetry of for progression we distinguished 3 different groups of Left/Right fork speed: symmetric (blue dots), in which in which the difference between Left and Right fork speed is between 0 to 30%; Asymmetric (green dots), in which the difference between Left and Right fork speed is between 30 to 99 %; Unidirectional (red dots) in which the difference between Left and Right fork speed is 100 %, where one of the two fork did not even start during the first pulse. (see introduction/ M&M for details). (A) Left to Right fork speed correlation upon DMSO treatment. (B) Left to Right fork speed correlation upon NOX4i1 treatment. (C) Left to Right fork speed correlation upon NOX4i2 treatment. (D) Histogram showing the percentage of symmetric, asymmetric and unidirectional forks, in each condition analysed.

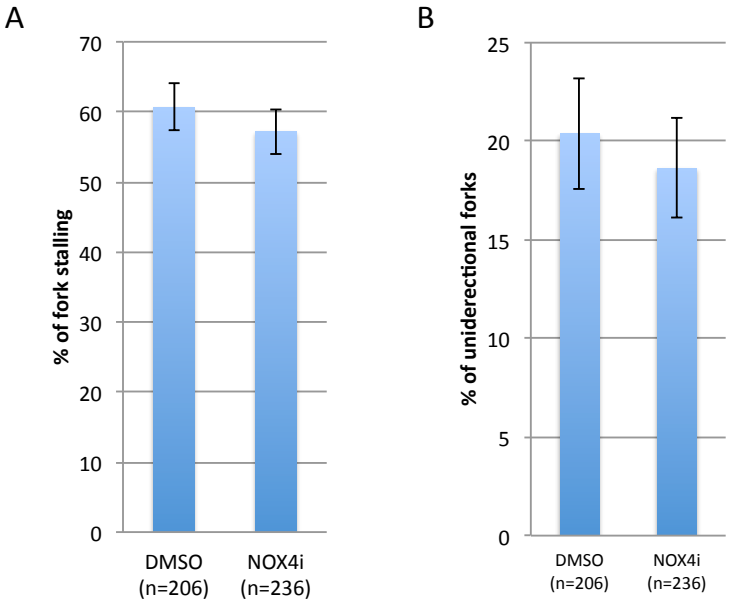

Figure 68. Pharmacological inhibition of Nox4 enzymatic activity does not affect the symmetry of fork progression.
(A) Percentage of fork stalling. We intend fork stalling as the sum of the asymmetric and the unidirectional forks. (B) Percentage of unidirectional forks. The error bars indicate the Standard Error of the Mean (SEM).

I then focused my attention on the effect of NOX4 inhibition on fork stalling events. I considered fork stalling as the sum of asymmetric and unidirectional forks. NOX4i treatment slightly decreases the level of fork stalling (DMSO, 60.68%, NOX4i vs 57.2%; Figure 68B) and the level of unidirectional forks (DMSO, 20.39%, NOX4i vs 18.64%; Figure 68B). However these differences are so small that they do not reach statistical significance.

CHAPTER 4. Polycomb role in the regulation of DNA replication dynamics

4.1 Absence of PRC2 activity achieved by knock out of EZH2 reduces the number of cells that are in S phase

Polycomb group (PcG) proteins are mainly known for their role in establishing and maintaining cell identity during development as well as in adult organisms. The Polycomb repressive complexes exert these functions by repression of a large set of genes involved in proliferation, development and differentiation via trimethylation of H3K27, catalysed mainly by EZH2. Recent independent studies revealed a role of Polycomb group proteins on S phase progression and, more directly, on DNA replication (Francis et al., 2009; Hansen et al., 2008; Pasini et al., 2004). Absence of SUZ12 leads to impairment in cell cycle re-entry (Pasini et al., 2004). Furthermore, during DNA synthesis PcG proteins can stay attached to chromatin (Francis et al., 2009), and EZH2, the catalytic subunit of PRC2, has been localized at sites of ongoing DNA replication (Hansen et al., 2008).

To better understand the function of PRC2 on cell cycle progression and DNA replication we used SV40 H-RasV12 *Ezh2 fx/fx* and *Ezh2-/-* MEFs. EZH2 KO was obtained by 7-days treatment of SV40 H-RasV12 *Ezh2 fx/fx* MEFs containing the Rosa26 CRE-ERT2 construct, with 4-hydroxy-tamoxifen. In this way Cre recombinase was induced, leading to EZH2 KO. Before proceeding with further analyses we tested for the absence of EZH2 in EZH2 KO MEFs by western blot. Indeed in *Ezh2-/-* MEFs EZH2 protein is absent; similarly EZH2 activity is lost, as determined by lack of H3K27me3 (Figure 69).

Figure 69. Immunoblot analysis reveals that Ezh2 -/- MEFs lack of EZH2 protein and activity.
Immunoblots shows that H-RASV12 SV40ER *Ezh2 -/-* MEFs have no EZH2 protein and the lack of EZH2 leads to absence of EZH2 activity, as detected by lack of H3K27me3 signal. β-tubulin and total Histone H3 served as loading control. (Performed by Andrea Piunti; Adapted from Piunti A. et al under revision 2013)

We then tested the impact of EZH2 KO on cell cycle progression, with flow cytometric analyses (FACS). Briefly, *Ezh2 fx/fx* and *Ezh2-/-* MEFs were synchronized at the G1/S boundary with a double-thymidine block. Cells were then allowed to re-enter S-phase for 30 minutes in the presence of BrdU, and DNA synthesis was measured by flow cytometric analyses (FACS) using a specific antibody against BdrU. Since the MEFs used stably-express SV40 and RasV12, their level of polyploidy is high ((Duhamel et al., 2012); Figure 70), thus BrdU measurements were restricted to the 2C population to prevent cross-contaminations of G1/S boundaries.

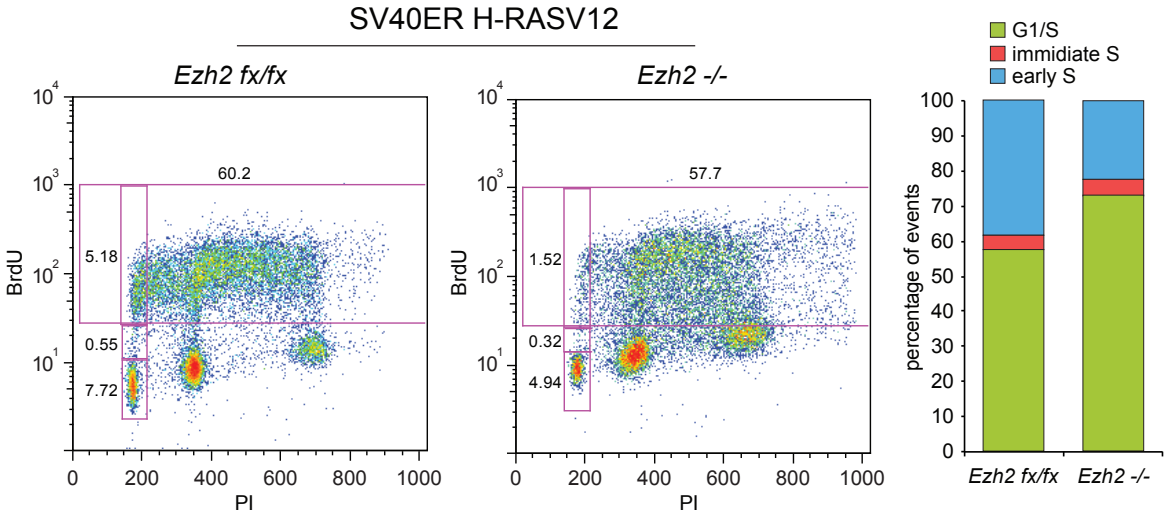

Figure 70. Absence of EZH2 results in an impairment in G1/S transition of cell cycle progression.
FACS analyses of H-RASV12 SV40ER immortalized *Ezh2 fx/fx* or *Ezh2 -/-*. 7 days after OHT (*Ezh2 -/-*) and EtOH (*Ezh2 fx/fx*) treatment; cells were incubated 30 minutes in the presence of BrdU after release from a double-thymidine G1/S block. The bar plots show the relative percentage of cells with 2C DNA content that are present in the highlighted gates (BrdU negative, intermediate and BrdU positive). (Performed by Andrea Piunti; Adapted from Piunti A. et al under revision 2013)

This analysis revealed that EZH2 KO results in a 20 % reduction of cells that are in S phase compared with control cells. This may indicate a more direct effect of PRC2 deficiency on DNA replication dynamics.

4.2 Effects of EZH2 knock out on DNA replication dynamics

To test the effect of PcG deficiency on DNA replication dynamics, I performed DNA molecular combing experiments (Lebofsky and Bensimon, 2003; Michalet et al., 1997) on EZH2 KO MEFs. Briefly, after knocking out EZH2 by 7-days treatment with 4-hydroxy-tamoxifen in SV40ER H-RASV12 mouse fibroblasts, *Ezh2 fx/fx* and *Ezh2 KO* cells were labelled with thymidine analogues for a precise time interval (1st pulse IdU: 20 min; 2nd pulse CldU: 20 min). As cells replicate they incorporate the thymidine analogues in their DNA. Cells were then embedded in agarose plugs. After deproteinization with proteinase K, DNA was extracted by melting the agarose, which is degraded by β agarase I digestion. The DNA solution was then combed on silane-coated glass slides. This procedure allows for the stretching of single DNA molecules on the slide. By performing immunostainings with primary antibodies specific for individual thymidine analogues and total DNA and secondary fluorescent antibodies, I can visualize and measure DNA replication patterns.

4.2.1 Effects of EZH2 knock out on replication fork speed

The first parameter I assessed was the fork speed, calculated by dividing the length of the replication signal by the incubation time (20 min). This analysis revealed that upon Ezh2 KO (*Ezh2 -/-*), cells display a reduction in fork speed (1.79 kb/min) as compared to the Ezh2 proficient cells (2.02 Kb/min). Interestingly, while control cells have a unimodal fork speed distribution, Ezh2 depleted cells present a bimodal fork speed distribution

underlying the existence of a sub-population of DNA replication forks significantly slower (Figure 71).

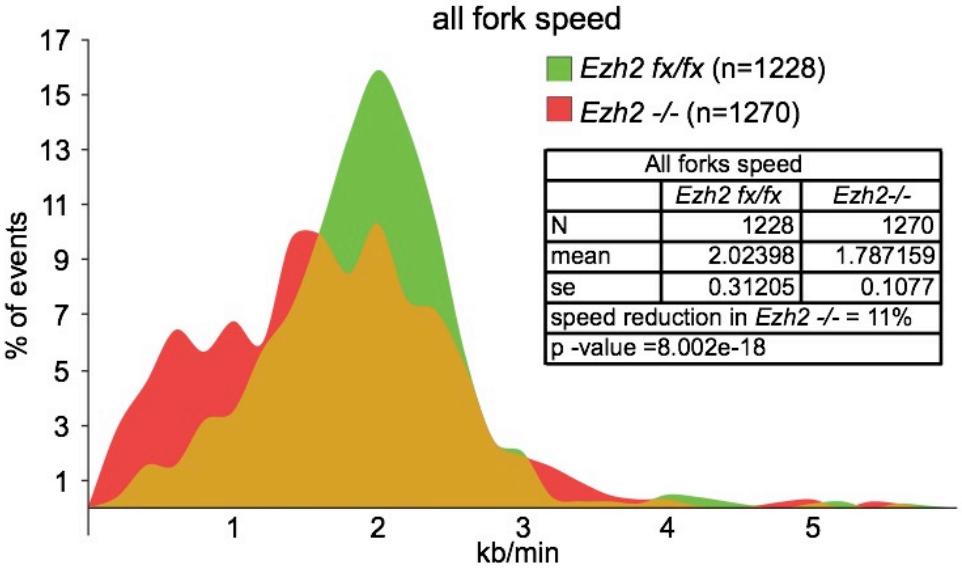

All forks speed		
	Ezh2 fx/fx	*Ezh2-/-*
N	1228	1270
mean	2.02398	1.787159
se	0.31205	0.1077
speed reduction in *Ezh2 -/-* = 11%		
p -value =8.002e-18		

Figure 71. EZH2 KO leads to reduced fork speed.
Fork speed was calculated by dividing the length of the replication signal by the time interval of the incubation with thymidine analogues (20 min). The graph shows the distribution of fork speeds in *Ezh2 fx/fx* or *Ezh2 -/-* MEFs. p-values were calculated applying Wilcoxon test.

4.2.2 Effects of EZH2 knock out on the symmetry of fork progression

Next, I assessed the symmetry of fork progression. To achieve this, I compared the speeds of left and right DNA replication forks that derive from the same DNA replication origin. I was able to distinguish three main patterns of DNA replication progression: a. symmetric fork progression, in which left and right fork speeds are comparable, differing at maximum of a 30 % between each other; b. asymmetric fork progression, in which left and right fork speeds differ between 30% - 99%, and unidirectional fork progression in which one of the two forks did not even start during the first pulse, thus showing a 100% difference between left an right fork speed (for further details the section *DNA Molecular Combing*).

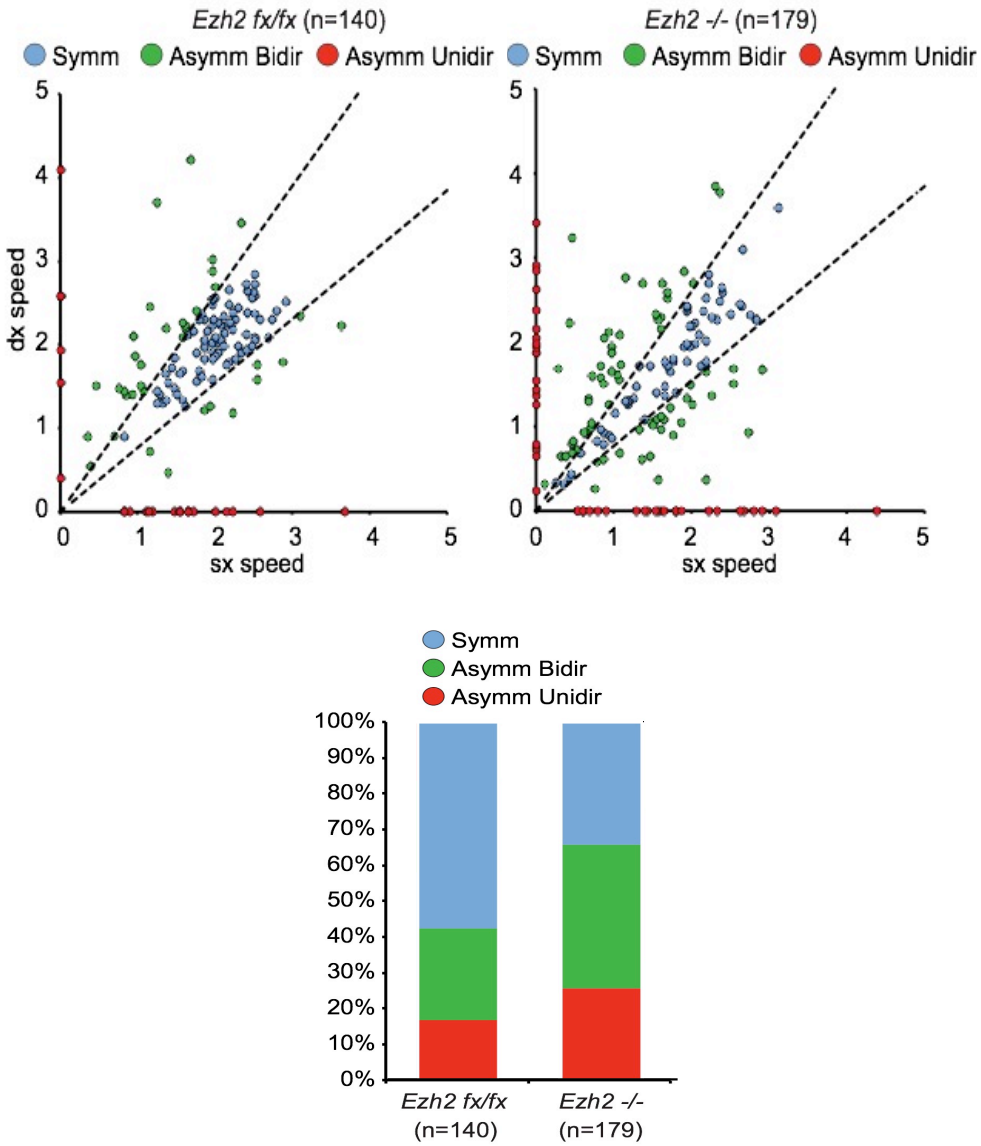

Figure 72. EZH2 KO leads to increase fork stalling.
Symmetry of fork progression was calculated as the Left to Right fork speed correlation: right (y axis) and left (x axis) fork speed coming from the same replication origin, are plotted in A and B. Three groups of fork progression were considered: symmetric (blue dots), in which the difference between Left and Right fork speed is between 0 to 30%; Asymmetric (green dots), in which the difference between Left and Right fork speed is between 30 to 99 %; Unidirectional (red dots) in which the difference between Left and Right fork speed is 100 %, where one of the two forks did not even start during the first pulse. (A-B) Left to right fork speed correlation plots of *Ezh2 fx/fx* (A) or *Ezh2* -/- MEFs (B). (C) Percentage of symmetric, asymmetric and unidirectional fork progression of *Ezh2 fx/fx* (A) or *Ezh2* -/- MEFs.

As shown in Figure 72, *Ezh2* -/- MEFs accumulate a greater number of forks stalling, as seen by increased in asymmetric (Green) and unidirectional (Red) DNA replication forks as compared to control cells.

4.2.3 Reduction in fork speed does not correlate with increased fork stalling

Given the reduction in fork speed and the increase asymmetric fork progression occurring in absence of EZH2, I was eager to test whether asymmetric fork progression within individual replicons was associated with the reduced fork speed. Thus I considered only the fork speeds deriving from replicons, in spite of their levels of symmetry (Figure 73A).

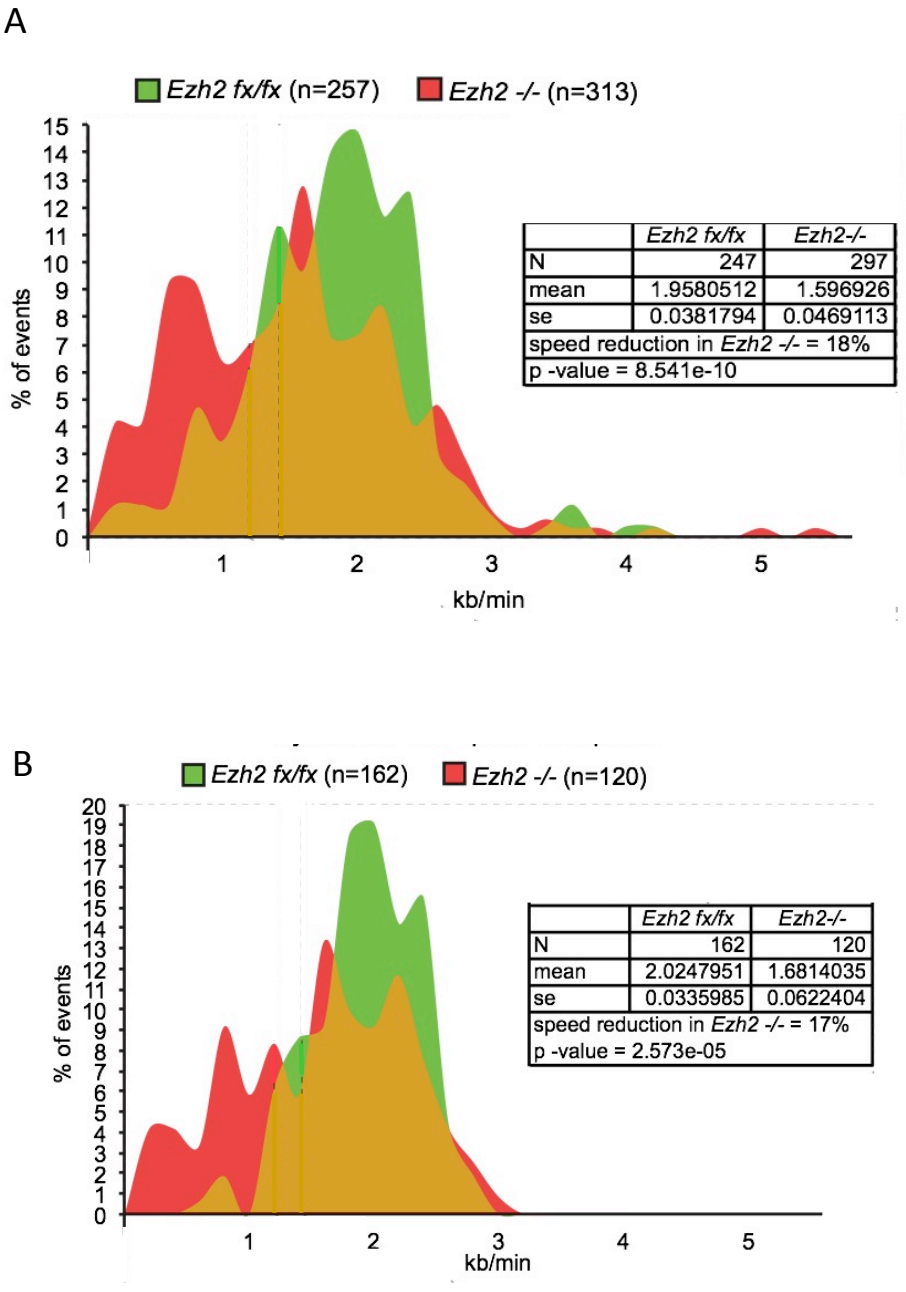

Figure 73. Increased fork stalling observed upon EZH2 KO does not correlate with slow forks.
To test whether asymmetric fork progression within individual replicons was associated with the reduced fork speed, I considered the distribution of fork speeds deriving from replicons, in spite of their levels of symmetry (A) and compared this with (B) the distribution of fork speeds deriving from symmetric replicons, excluding asymmetric ones.

Noteworthy, the replication fork speed deriving from replicons still presents a bimodal distribution in *Ezh2* -/- MEFs, consistent with the fork speed distribution previously shown (Figure 71). Next, I selected only the fork speeds deriving from symmetric replicons, thus excluding asymmetric ones. Also in case of symmetric replicons, I found a consistent reduction in fork speed in *Ezh2* -/- MEFs as compared with wild-type MEFs (Figure 73B). Taken together, these results indicate that the reduction in fork speed seen in *Ezh2* -/- MEFs is not a feature of asymmetric forks, but it affects all forks, regardless the level of symmetry of fork progression.

4.2.4 Impact of EZH2 knock out on Inter-origin distances

I then analysed the impact of loss of Ezh2 expression on the frequency of replication initiation, by evaluating the inter-origin distances (IODs). IODs consist in the distance between two adjacent origins, and from them it is possible to infer the number of active origins: the smaller the IODs are, the higher the number of active origins, and vice versa.

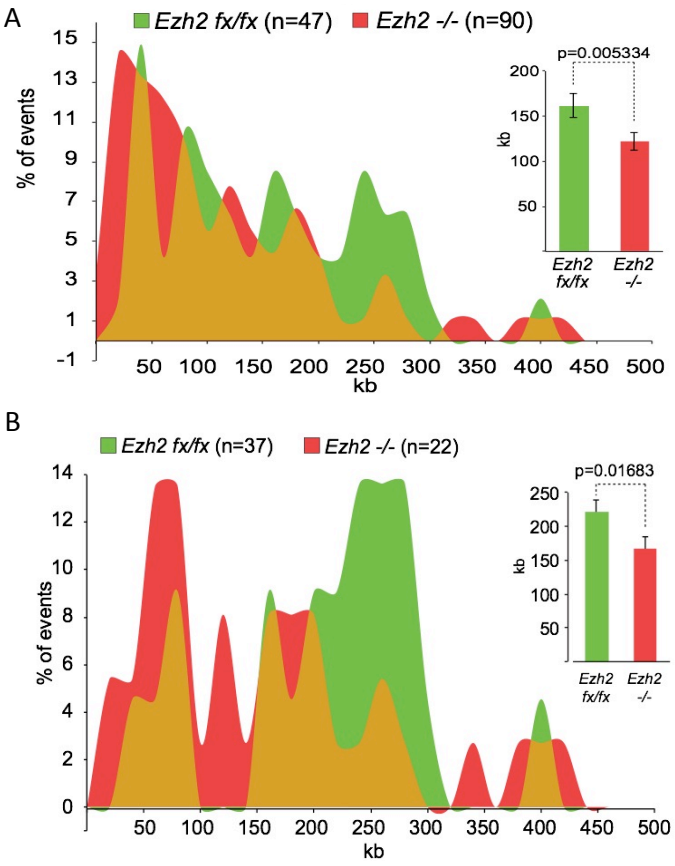

Figure 74. EZH2 KO results in a reduction in IODs.
Inter-Origin-Distances (IODs) were calculated as the distance between two adjacent DNA replication origins. (A) Graph showing the distribution of IODs in the bulk of the fibers. (B) Graph showing the distribution of IODs in fibers longer than 3 times the IODs average. p-values were calculated applying Wilcoxon test.

Ezh2 KO resulted in a reduction in IODs (122.78 kb**)** as respect to control cells (168.6 kb), thus indicating that *Ezh2 KO* leads to an increased number of simultaneously active replication origins respect to *Ezh2 fx/fx* control cells (Figure 74A).

These differences are preserved also when considering the IODs observed among DNA fibers that are longer than three times the average IODs (*Ezh2 KO vs Ezh2 fx/fx* : 166.43 kb vs 220.69 kb) ((Bianco et al., 2012); Figure 74B) suggesting that fibers breakage is not affecting these results. Moreover since the DNA preparations of the conditions analysed displayed overlapping DNA fiber lengths distribution (Figure 75) the results presented here are not influence by difference in fiber length or increased DNA fibers fragmentation of one of the conditions.

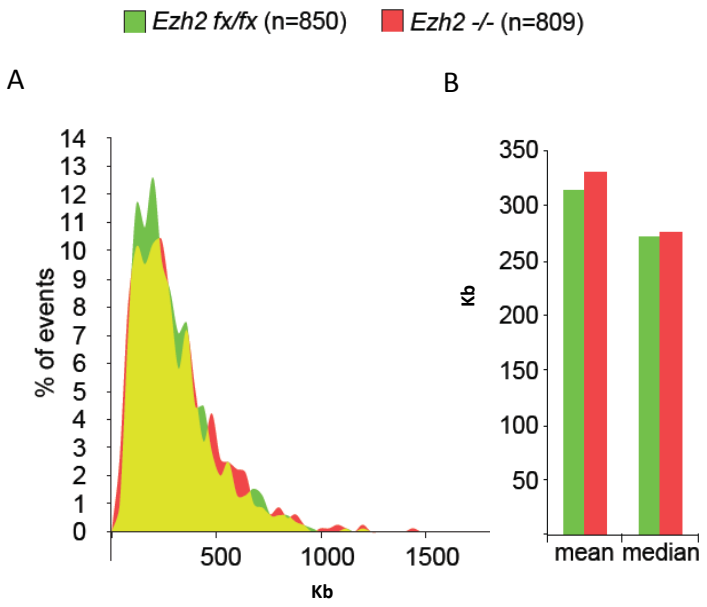

Figure 75. DNA fiber length analysis.
(A) Fiber length distribution. (B) Average fiber length and median size of fiber length are plotted.

4.3 Impact of EZH2 knock out on the DDR activation

Since altered DNA replication - mainly fork stalling events - usually triggers DNA damage response (DDR) activation, we checked for DDR activation by immunofluorescence quantification of 53BP1 foci formation (Lukas et al., 2011). Indeed Ezh2 deficient MEFs show an increased number of 53BP1 foci compared with WT cells (Figure 76).

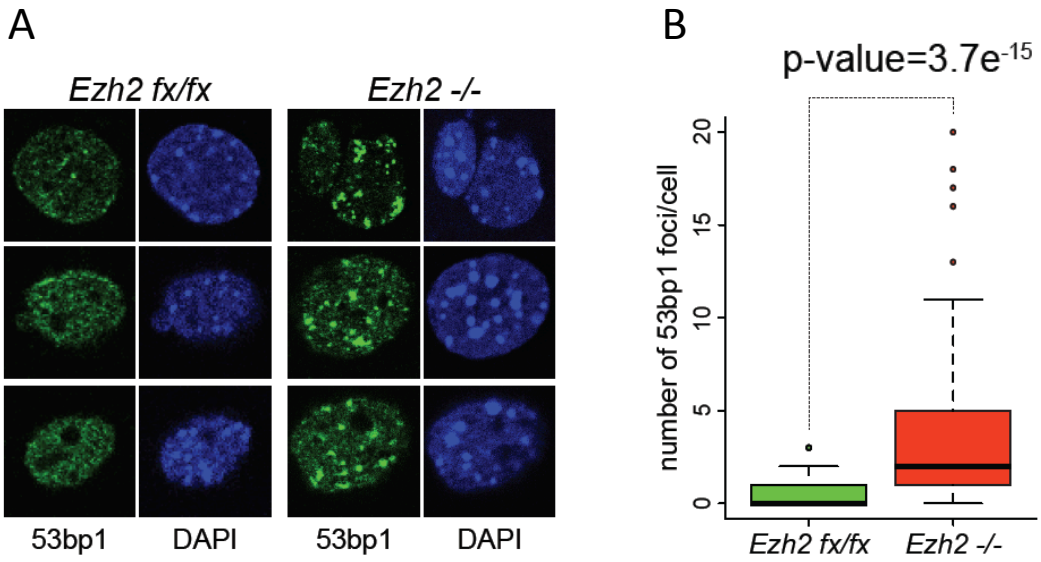

Figure 76. EZH2 KO resulted in DDR activation.
(A) Confocal immunofluorescence images of H-RASV12 SV40ER *Ezh2 fx/fx MEFs* 7 days after EtOH (*Ezh2 fx/fx*) and OHT (*Ezh2 -/-*) treatment, 30 minutes after release from a double-thymidine G1/S block, stained with 53BP1 specific antibody. (B) Box plot shows the number 53bp1 foci per cell. Quantification was obtained using ImageJ software. n is indicated in the figure. p-value was determined with paired t-test. (Performed by Andrea Piunti; Adapted from Piunti A. et al under revision 2013).

Overall, these data demonstrate that PcG deficiency leads to altered DNA replication dynamics resulting also in the activation of DDR. Thus these results revealed a novel role of PcG activity in the regulation of DNA replication dynamics.

DISCUSSION

CHAPTER 1. Oncogene activation induces telomere dysfunction by impairing telomere replication

1.1 Oncogene-induced replication stress at telomere results in telomeric fork stalling and telomeric DNA damage accumulation

In this thesis I presented a set of data that revealed a novel and unprecedented link between telomere dysfunction and oncogene activation, unveiling the molecular mechanisms underlying oncogene-induced telomere dysfunction. Oncogene activation is known to induce replication stress affecting preferentially fragile sites (Bartkova et al., 2006; Di Micco et al., 2006; Tsantoulis et al., 2008). Therefore the discovery of telomere fragility (Sfeir et al., 2009) becomes the key element that allows the connection between oncogene activation and dysfunctional telomeres.

The dramatic telomeric shortening occurring within a single cell cycle after oncogene activation, as measured by q-FISH and flow-FISH (Figure 15), together with the appearance of aberrant telomeric structures that resemble fragile sites (Figure 14), revealed a direct impact of oncogene activation on telomere structure. Moreover these structural alterations were accompanied by DDR activation at telomeres, both *in vitro* in oncogene-expressing fibroblasts, and *in vivo* in preneoplastic lesions, but not in the fully malignant counterparts. Thus the telomeric structural alterations induced by oncogene activation result also in the impairment of telomeric functions. The link between oncogene activation and the appearance of dysfunctional telomeres lies in the telomere hypersensitivity to oncogene induced replication stress. This hypersensitivity results in impaired telomeric DNA replication that leads to increased telomeric fork stalling (Figure 22). The data presented here suggests that oncogene-induced replication stress leads to a general increase in fork stalling that preferentially occurs at telomeres. Since the initial phases after

oncogene overexpression in fibroblasts result in a robust DDR activation at whole genome level, which is then resolved except from telomeric DDR that persists over time (Figure 16), it seems that the replication fork stalling at non-telomeric region can be resolved, while the stalled forks inside telomeres result in irreparable and persistent DNA damage.

These results are in line with a recent publication from our laboratory showing the accumulation of irreparable and persistent DNA damage at telomeres in response to IR-induced DNA damage and aging (Fumagalli et al., 2012).

The data presented here reveal a crucial role for dysfunctional telomeres in OIS establishment: oncogene-induced fork stalling alters telomeric structure and function inducing telomeric DDR activation that persists over time leading to establishment of senescence, that is independent of telomere shortening.

1.2 Unifying mechanisms mediating cellular senescence: oncogene activation and telomere dysfunction

The data presented in this thesis revealed a refined model for tumor suppression that unifies oncogene activation and telomere dysfunction-induced senescence (TDIS). Dysfunctional telomeres are telomeres that had lost their structure and function so that they are sensed as DSBs, inducing DDR/p53-dependent senescence pathways. They play critical role in cancer progression, most probably by inducing chromosomal instability, as observed in ductal carcinoma *in situ* (Chin et al., 2004), rand colonic adenomas with high dysplasia (Rudolph et al., 2001). However the causative role of TDIS as tumor suppressive mechanism so far has been demonstrated only in mouse model systems. (Cosme-Blanco et al., 2007; Feldser and Greider, 2007; Sharpless and DePinho, 2005). Noteworthy, the results shown here shed new light on the fundamental role of dysfunctional telomeres to limit cancer progression in preneoplastic lesions. Indeed the analysis of preneoplastic lesions (benign and dysplastic nevi) and the malignant counterpart (melanoma), revealed

that dysfunctional telomeres - detected as colocalization between DDR marker 53BP1 and telomeric DNA - are present in the preneoplastic lesions but not in the malignant counterpart (Figure 17). Beyond the relevance of telomere dysfunction in tumor suppression these data revealed also a direct link between oncogene activation and telomere dysfunction, since the preneoplastic lesions analysed are human nevi, melanocytes that display classical features of senescence, due to the presence of the oncogenic form of BRAF (*$BRAF^{V600E}$*), a protein kinase downstream of Ras (Michaloglou et al., 2005).

Thus, in line with similar analyses undertaken in other human cancer precursor lesions - breast and colon adenomas (Suram et al., 2012) - the results reported in this thesis unveil the interplay between oncogene activation and dysfunctional telomere.

CHAPTER 2. Impact of oncogene activation on DNA replication dynamics and DDR activation

2.1 Oncogene activation results in a prompt DDR activation

The results presented in this thesis derive from the study of the kinetics underlying altered DNA replication dynamics and DDR activation that occur upon oncogene activation. Previous studies in literature have shown that oncogene activation leads to an increase in DNA replication initiation events as well as an increase in fork stalling that account for the subsequent robust DDR activation responsible for OIS onset (Bartkova et al., 2006; Di Micco et al., 2006). However these studies were conducted in DDR-deficient cells (shChk2) (Di Micco et al., 2006) or in tumor cell line (U2OS) (Bartkova et al., 2006), whereas here I used fully DDR-proficient cells. Moreover so far no studies in literature tried to dissect the impact that oncogene activation has over time on DNA replication and DDR activation.

Thus to better understand the impact of oncogene activation at the various steps till OIS establishment, I performed a time course analysis to assess the effects that oncogenic Ras expression has on DDR activation, DNA replication dynamics, from the initial hyperproliferative burst till OIS establishment. The cellular growth and the proliferation rates confirmed previous data about the effect of oncogenes on proliferation and OIS establishment: a first hyerproliferation phase (day 2-3) is followed by a gradual slow down (day 4 - 7) till the entrance into senescence (day 9, Figure 25).

By looking at the kinetics of DDR activation, γH2AX show very high level starting from the initial days after oncogenic Ras expression and it is the only DDR marker studied to show such a high level of activation at the initial stages (Figure 27B-C and 29). In the following day the levels of γH2AX are a little bit reduced as compared to the initial robust γH2AX activation, but then γH2AX levels stay almost constant till the onset of senescence.

On the other hand all the other DDR markers analysed, - such as 53BP1, ATM (pSer1981), Chk2 (pThr68), pS/TQ and p53 (pSer15) - show a gradual increase over time, reaching their maximum level at the latest time point (Figure 27-31). The level of DDR activation in control cells remained almost constant throughout the time course analyses, except for high levels of p53 (pSer15) at the first day after infection that could be due to DDR activation triggered by the retroviral integration independently of the gene transduced (Lau et al., 2005).

As for the kinetics of DDR activation, here I showed that DDR is activated since the first day after oncogenic Ras infection, suggesting that oncogenic Ras may induce replication stress from the very initial stage following the infection. Indeed by looking at data of DNA replication dynamics, at day 2 after infection the replication fork speed is already very high as compared with the control (Figure 32 and 53A). This may indicate that oncogenic Ras expression has an almost immediate effect on DNA replication, inducing DNA hyper-replication that could be mediated by the upregulation of a crucial replication licencing factor such as Cdc6 (Figure 31). At the same time as forks replicate faster, they stall more easily as shown by the increase in unidirectional forks (Figure 52 and 53E). Furthermore the unidirectional forks correspond to the highest level of asymmetric fork progression, and represent both fork stalling and fork breakage, which can result in DNA damage and subsequent activation of the DDR cascade. As time passes fork breakage and the consequent DNA damage are resolved - as seen in the decrease in unidirectional forks (Figure 52 and 53E). Various DNA replication parameters may account for the accumulation or decrease in unidirectional fork: frequency of initiation is increasing, making forks more prone to stall due to collision with ongoing transcription machinery; on the other hand the fork speeds are decreasing over time, and this might indicate a lower chance to stall. Given the complexity of the DNA replication dynamics, in the next paragraphs I will discuss in details the results of each DNA parameter I analysed.

Thus the data shown in this thesis suggest that robust activation of γH2AX is the primary response to the initial oncogene induced replication stress that in the following days results in a gradual activation of downstream DDR kinases and effectors.

2.2 Oncogene-induced replication stress: increased initiation and decrease fork speed

It has been demonstrated in various studies that oncogene activation results in an increase in the replication initiation events, together with an increase in fork stalling (Bartkova et al., 2006; Di Micco et al., 2006; Jones et al., 2013). However none of these studies took into consideration an analysis of the kinetics of oncogene-induced altered DNA replication dynamics, and the conclusions they obtained derived from studies in DDR deficient cells (Di Micco et al., 2006), or in tumor cell lines (Bartkova et al., 2006; Jones et al., 2013). The set of data presented in this thesis try to dissect the impact that oncogene activation has on DNA replication over time, from the first hyerproliferative phase (day 2-3) till the entrance into senescence (day 9), giving a more complete and detailed picture of the interplay between oncogene activation, DNA replication and DDR.

Even if in some conditions of the various parameters analysed the statistical significance is not completely proven, I will discuss the possible mechanisms underlying the oncogene-induced DNA replication stress, keeping in mind the need to further confirm the results presented here. Furthermore, even in the lack of complete statistical significances, different parameters - IODs and ORI/Mb - used to estimate the same issue (frequency of DNA replication initiation) have comparable trends, achieving similar results. This further supports the idea that, beyond their statistical significance, the parameters analysed give robust and consistent results.

The first day after oncogenic Ras expression shows the highest fork speed, which then starts to gradually decrease in the following days, till becoming even smaller than control cells fork speed as oncogenic Ras-expressing cells undergo senescence. This gradual decrease in fork speed shows the same trend as the BrdU incorporation rates.

As for the frequency of initiation, I took into consideration the analysis of two independent parameters - IODs and ORI/Mb – which generated similar results: at the beginning of the time course analysis, oncogenic Ras-expressing cells show the lowest frequency of initiation both as respect to control cells and to oncogenic Ras-expressing cells in the following time points. As time passes, the frequency of initiation increases, reaching levels close to the control (Figure 39, 43 and 53B-C). However some unexpected fluctuations over time in the control cells are also observed: the IODs in control cells are slightly increasing, reaching the highest values on day 4, to then decrease again to initial values. The increase in IODs shown on day 4 is present also in oncogenic Ras-expressing cells (Figure 36 and 39). Thus these fluctuations could be ascribed to the effect on cell cycle of cells splitting performed the previous day (day 3). Indeed trypsinization, pipetting and reseeding to a lower confluency are all events that may alter cellular physiology and cell proliferation (Huang et al., 2010).

Therefore, apart day 4, the fluctuations of control cells are reduced to minimal levels, while the trend of oncogenic Ras-expressing cells is more clearly gradually going from initial high IODs (around 200 kb) to smaller IODs (around 150 kb). As the distance between origins gets smaller, it indicates that the number of simultaneously active origins increases. Similar results were obtained with the analysis of the number of active origins per Megabase (ORI/Mb): oncogenic Ras-expressing cells show a slight increase in the number of active ORI/Mb over time, both in the bulk of the fibers (from 4.5 to 6 ORI/Mb, Figure 41), and in the long fibers, even though to a lesser extent (from 3.2 to 3.6 ORI/Mb, Figure 43). To note that also in the case of ORI/Mb there is a fluctuation on day 4 (oncogenic Ras-expressing cells invert their trend), which further supports the link between cells splitting and proliferation.

The increase in initiation event upon oncogene activation is in line with previous discoveries (Di Micco et al., 2006; Jones et al., 2013). The replication stress mechanism underlying the increase in replication initiation has been ascribed to increased interference

between transcription and replication, leading to fork stalling and subsequent DNA damage accumulation that activates DDR leading to OIS (Jones et al., 2013). However in my case the increase of replication initiation does not correspond to increase in fork stalling or in unidirectional forks. Actually it seems that upon increase initiation either fork stalling is staying constant or unidirectional fork are decreasing. These differences may lie in the different experimental approach used: the data presented in Jones RM et al (2013), show an increase in initiation after 3 days post cyclin E overexpression in U2OS cell line, while I performed a time course analysis assessing DNA replication dynamics every day after oncogenic Ras expression. Thus the increase in initiation events that I observe is mainly related to an increase initiation in oncogenic Ras-expressing cells over time, rather than comparing it with control cells. Indeed at the very initial phase after oncogenic Ras expression (day2), the initiation events are at their lowest level and then start to increase in the following days. Furthermore the way used to estimate fork stalling is different than the one used in this thesis: they evaluate di symmetry of progression between first and second pulse of the same replication fork (Jones et al., 2013), whereas I consider the symmetry of fork progression between two replication forks deriving from the same replication origin. Thus I cannot exclude replication/transcription collision as a possible mechanism underlying oncogene-induced replication stress. Further experiments are needed to demonstrate a role of transcription in oncogenic Ras-induced replication stress.

Moreover considering the time course analysis, the presence of a robust γH2AX activation from the very initial phase after oncogenic Ras expression, might indicate an immediate impact of oncogenic Ras on DNA replication dynamics. Indeed the initial phase is characterized by the highest fork speed as well as by the highest level of unidirectional forks, together with the lowest level of replication initiation. Thus it seems that oncogenic Ras is altering DNA replication dynamics from the very beginning after its activation. In support to this view, a recent paper demonstrated that oncogenic Ras expression is inducing the downregulation of RRM2 - a key enzyme involved in the dNTP pool

biosynthesis - already after 24 hour from oncogenic Ras infection. This immediate downregulation of dNTP pools may account for the oncogene-induced replication stress: upon oncogene activation cells are hyper-replicating and thus the consumption of dNTPs is increasing in a manner faster than their biosynthesis, which is instead blocked (Aird et al., 2013). Hence as cells replicate they run out of dNTPs, replication fork stalls more frequently due to the lack of the right complementary dNTP to be incorporated in the DNA, leading to increased genomic instability and DDR activation. What I see, under the conditions studied here, is that indeed from the beginning of the time course analysis, already at day 2 after oncogenic Ras expression, the unidirectional forks, which represent the greatest level of asymmetric fork progression, are at their highest level. This is in line with the possible effect of dNTP pool depletion in inducing an increased fork stalling (Aird et al., 2013; Bester et al., 2011). However to prove this hypothesis, further studies need to be undertaken.

2.3 Oncogene-induced fork stalling: whole genome studies versus fragile site specific studies

The data presented in this thesis revealed that the oncogene-induced DNA replication stress results mainly in an increase in unidirectional forks, which represent the highest level of asymmetry. Indeed unidirectional fork are at their highest already from the initial stages after oncogene activation. As time passes, unidirectional forks decrease till they reach levels lower than control cells, in correspondence to OIS onset (Figure 52).

Instead general fork stalling, that includes both bidirectional asymmetric forks as well as unidirectional forks, does not seem to be affected by oncogene activation. Indeed the level of fork stalling stays almost constant over time (Figure 51). These results are unexpected, since oncogene-induced replication stress is known to result in increased fork stalling (Bartkova et al., 2006; Di Micco et al., 2006) that preferentially affects fragile sites (Tsantoulis et al., 2008). Thus, the lack of oncogene-induced fork stalling shown here

might result from the whole genome analysis performed. Indeed, if forks stall preferentially at fragile sites, the assessment of fork stalling at whole genome level may mask the fork stalling occurring at fragile sites. Hence the genomic analysis would result in an underestimation of the fork stalling itself, which occurred mainly at critical sensitive genomic loci like fragile sites. Furthermore the data about the impact of oncogene activation on telomeric DNA replication, previously described in this thesis, are in support to this idea. Indeed, even if the experimental set-ups are slightly different, I showed that upon oncogene activation there is a dramatic increase in fork stalling at telomeric DNA, whereas in the rest of the genome the impact of oncogene activation on fork stalling is much more modest.

Another possible reason that did not let me appreciate an increased fork stalling as respect to previous studies (Di Micco et al., 2006) could be ascribed to the different cell line used: in Di Micco, Nature 2006 fork stalling was assessed in DDR-deficient cells (shChk2), while the in my case in fully DDR proficient cells. In the absence of effective DDR pathway fork stalling might have not been properly resolved, leading to an accumulation of these events, whereas in my case, full proficient DDR pathway might have solved them, avoiding their accumulation.

Thus a way to better appreciate the dynamics of fork stalling would be to analyse the effect of oncogene-induce replication stress at specific fragile sites, both with DNA molecular combing as well as with Repli-Seq analysis (Hansen et al., 2010), as done in (Letessier et al., 2011). Repli-Seq would allow to map the replicating DNA and to recapitulate the ongoing replication at specific genomic sites that could be supported by the combing analysis at the same genomic sites that showed altered DNA replication upon oncogene-activation.

2.4 The complex interplay between oncogene activation, replication stress, DDR activation: a mathematical model may help?

Here I summarize the results presented and discussed in this thesis about the oncogene-induced DNA replication stress and DDR activation.

At the initial stages after oncogene activation, the frequency of initiation is at the lowest level, both as respect to control cells and to oncogenic Ras-expressing cells in the following days. This corresponds to high replication fork speed in oncogenic Ras-expressing cells, the highest of all time course analysis. These fast forks are accompanied by an increase in fork stalling, mainly unidirectional forks. This may account to higher probability of fast forks to stall, due to higher chances to encounter obstacles - proteins, DNA topological problems - while replicating in a faster manner. Indeed as forks slow down also the unidirectional forks decrease. This decrease might be due to both to a lower chance to stall together with higher probability that stalled forks might be repaired as DDR is activated.

Furthermore the initial high level of unidirectional forks together with a robust γH2AX activation may indicate an immediate role of oncogenic Ras expression in altering DNA replication dynamics. This initial high level of unidirectional forks and the robust γH2AX activation can be ascribed to the effect of dNTP pool depletion that occurs at early stage after oncogenic Ras expression (day 1-2) as shown in (Aird et al., 2013).

As for the frequency of initiation and the replication fork speed, there is a progressive increase in replication initiation together with a gradual decrease in the fork speed. These results are in line with other studies showing that cyclin E overexpression leads to an increase in replication initiation (Jones et al., 2013). Jones R.M et al (2013) demonstrated that these higher frequencies of initiation result in increased collision between replication and transcription machinery, leading to increased fork stalling and subsequent DNA damage. Even though it is tempting to speculate it as a possible mechanism occurring also

in the experimental set up used here, further analysis are needed to confirm this hypothesis. As previously explained, my experimental set up is different (time course analysis vs single time point analysis) and some parameters - fork stalling - were estimated in a different way (Left/Right fork speed correlation *vs* $1^{st}/2^{nd}$ pulse symmetry of fork progression). Indeed our increased in initiation is mainly related to an increase in oncogenic Ras-expressing cells over time, rather than comparing it with control cells, while the lack of increased fork stalling could be ascribed to the different methods used to assess it.

Given the complexity of these processes, it is difficult to extrapolate information on the various parameters and relate them both to the control as well as to the trend each of these parameters has over time. It is however possible to infer some trends within same parameter, comparing them with control conditions or/and with the results of the other parameters occurring at the same time point. However when it comes to relate all the data obtained for one parameter to all the parameters over time then it can become very challenging to get a clear picture of the relations existing between different parameters analysed. Thus following a growing line of research (Bechhoefer and Rhind, 2012; Gauthier et al., 2010; Sancar et al., 2004), the use of mathematical models designed *ad hoc* to dissect the complex interplay between oncogene activation, DNA replication and DDR activation would be very helpful.

CHAPTER 3. Ras-induced ROS production via NOX4 as the fuel for oncogene induced hyperproliferation

The data presented in this thesis describe the mechanisms underlying oncogenic Ras-induced ROS production and the central role of ROS in the oncogene-induced hyperproliferation.

It was previously proposed that oncogene activation leads to genomic instability in a DNA replication-dependent manner (Bartkova et al., 2006; d'Adda di Fagagna, 2008; Di Micco et al., 2006; Halazonetis et al., 2008). Indeed it was observed that oncogene activation is followed by an initial hyperproliferative burst that results in replication stress, DDR activation and ultimately senescence. In addition, it has been demonstrated that several oncogenes - including RAS -, when activated, induce the accumulation of ROS and experimental evidence revealed that ROS scavenging can prevent senescence establishment. However the pathways involved in Ras-induced ROS production together with the causative role of ROS in OIS establishment has remained elusive.

The data presented here demonstrated that NOX4 is the central mediator of oncogenic Ras signaling: it is upregulated upon oncogenic Ras expression and its inhibition prevents the onset of senescence in oncogenic Ras-expressing cells. The key effectors involved in this process resulted to be ROS. Indeed pharmacological inhibition of NOX4 revealed that in absence of NOX4 enzymatic activity, the Ras-induced ROS production is completely abolished. As a consequence, in absence of ROS also Ras-induced hyperproliferation is prevented, further supporting a mitogenic role of ROS compounds, as previously shown in the literature (Irani et al., 1997). Furthermore, the lack of hyperproliferation prevents also the oncogene-induced DDR activation and the subsequent OIS establishment. This set of results highlight the essential role of ROS in Ras-induced hyperproliferation. We also observed that fully transformed oncogene-expressing cells that have bypassed senescence by DDR inactivation are particularly

sensitive to ROS inhibition by specific NOX4 inhibition. Indeed upon NOX4 inhibition their proliferation is reduced to control levels. This further supports the idea of ROS as the mitogenic molecules that fuel the oncogene-induced hyperproliferation.

The results presented here revealed also possible molecular mechanisms underlying the reduced proliferation rates occurring upon NOX4 inhibition. Molecular combing experiment indicates that inhibition of ROS production by specific NOX4 inhibitor treatment, affects DNA replication by inducing a general reduction in replication fork speed, together with a different regulation of clustered origins initiation. Indeed even though the general frequency of initiation seems not affected, when analysing the distribution of IODs, which account for clusters of simultaneously active origins, the presence of multiple peaks might indicate a local regulation of origin initiation, that is not appreciable when considering the average IOD. These results shed new light on the possible mechanism underlying ROS-induced altered DNA replication. Since the analyses shown here were performed in transformed human fibroblasts (BJELR), further studies will be useful to better dissect the molecular mechanisms underlying the effect of inhibition of ROS production by specific NOX4 inhibitor treatment in fully DDR proficient human fibroblast upon oncogenic Ras activation, by following their effect on DNA replication dynamics over time, from the first hyperproliferative phase till OIS onset.

In conclusion, the results presented here demonstrate the fundamental role of NOX4 - and consequently of ROS - in mediating oncogene-induced hyperproliferation. ROS appears to be the fuel of Ras-induced hyperproliferation and it seems to act on DNA replication dynamics by altering replication fork speed and deregulating clustered origin initiation. Furthermore the reduced proliferation of fully transformed cells occurring upon NOX4 inhibition indicates possible therapeutic application of NOX4 inhibition in cancer treatment.

CHAPTER 4. Novel Polycomb functions in DNA replication dynamics

The set of data presented in this thesis revealed a novel function of Polycomb group proteins in S phase progression and in the regulation of DNA replication dynamics. The impairment of cell cycle progression occurring upon EZH2 KO is in line with previous studies showing that PRC2 deficiency leads indeed to impairment in cell cycle re-entry (Pasini et al., 2004). PRC2 deficiency led also to an impairment of the DNA replication dynamics, further supporting a direct role of PcG protein in the regulation of DNA replication. Indeed, upon PRC2 deficiency I observed a reduction of fork speed, accompanied by an increase in simultaneously active origins, together with increased fork stalling, demonstrating that PcG deficiency results in DNA replication stress. The presence of replication stress upon PRC2 deficiency is highlighted by increased 53BP1 foci, a known DDR maker activated upon DNA replication stress (Lukas et al., 2011).

PcG proteins may act on the progression of DNA replication by regulating origin firing, as shown here by the reduced inter-origin distance of Ezh2 -/- MEFs. Given the fact that PRC2 subunits have been localized at sites of ongoing DNA replication (Hansen et al., 2008) another mechanism through which PcGs could act on DNA replication dynamics is by PcGs control on chromatin dynamics during the progression of the replication forks. PcGs could also play a role in preventing the collision between DNA replication and RNA transcription machineries, thanks to PcGs ability to bind and disassemble the RNA polymerase II complex (Lehmann et al., 2012). However further studies to better understand the molecular mechanisms underlying the function of PcG on DNA replication are needed.

Taken together, the data presented in this thesis unveil a novel and unprecedented function of PcG proteins in the regulation of cellular proliferation through a direct role in DNA replication dynamics. This PcG novel function further support the essential role of PcG activity for the growth of normal and cancer cells, underlying novel mechanisms of proliferation control that opens new perspective in the field.

REFERENCES

Aaltonen, L., Johns, L., Jarvinen, H., Mecklin, J.P., and Houlston, R. (2007). Explaining the familial colorectal cancer risk associated with mismatch repair (MMR)-deficient and MMR-stable tumors. Clin Cancer Res *13*, 356-361.

Abdouh, M., Facchino, S., Chatoo, W., Balasingam, V., Ferreira, J., and Bernier, G. (2009). BMI1 sustains human glioblastoma multiforme stem cell renewal. J Neurosci *29*, 8884-8896.

Acosta, J.C., O'Loghlen, A., Banito, A., Guijarro, M.V., Augert, A., Raguz, S., Fumagalli, M., Da Costa, M., Brown, C., Popov, N.*, et al.* (2008). Chemokine signaling via the CXCR2 receptor reinforces senescence. Cell *133*, 1006-1018.

Ahnesorg, P., Smith, P., and Jackson, S.P. (2006). XLF interacts with the XRCC4-DNA ligase IV complex to promote DNA nonhomologous end-joining. Cell *124*, 301-313.

Aird, K.M., Zhang, G., Li, H., Tu, Z., Bitler, B.G., Garipov, A., Wu, H., Wei, Z., Wagner, S.N., Herlyn, M.*, et al.* (2013). Suppression of nucleotide metabolism underlies the establishment and maintenance of oncogene-induced senescence. Cell Rep *3*, 1252-1265.

Allemand, J.F., Bensimon, D., Jullien, L., Bensimon, A., and Croquette, V. (1997). pH-dependent specific binding and combing of DNA. Biophys J *73*, 2064-2070.

Altieri, F., Grillo, C., Maceroni, M., and Chichiarelli, S. (2008). DNA damage and repair: from molecular mechanisms to health implications. Antioxid Redox Signal *10*, 891-937.

Alzu, A., Bermejo, R., Begnis, M., Lucca, C., Piccini, D., Carotenuto, W., Saponaro, M., Brambati, A., Cocito, A., Foiani, M.*, et al.* (2012). Senataxin associates with replication forks to protect fork integrity across RNA-polymerase-II-transcribed genes. Cell *151*, 835-846.

Amir, Y., Edward, O.-A., and Utpal, B. (2008). A protocol for _in vivo_ detection of reactive oxygen species. Protocol Exchange.

Arisan, S., Buyuktuncer, E.D., Palavan-Unsal, N., Caskurlu, T., Cakir, O.O., and Ergenekon, E. (2005). Increased expression of EZH2, a polycomb group protein, in bladder carcinoma. Urol Int *75*, 252-257.

Barlow, J.H., Faryabi, R.B., Callen, E., Wong, N., Malhowski, A., Chen, H.T., Gutierrez-Cruz, G., Sun, H.W., McKinnon, P., Wright, G.*, et al.* (2013). Identification of early replicating fragile sites that contribute to genome instability. Cell *152*, 620-632.

Bartek, J., Lukas, C., and Lukas, J. (2004). Checking on DNA damage in S phase. Nat Rev Mol Cell Biol *5*, 792-804.

Bartek, J., and Lukas, J. (2003). Chk1 and Chk2 kinases in checkpoint control and cancer. Cancer Cell *3*, 421-429.

Bartkova, J., Horejsi, Z., Koed, K., Kramer, A., Tort, F., Zieger, K., Guldberg, P., Sehested, M., Nesland, J.M., Lukas, C.*, et al.* (2005). DNA damage response as a candidate anti-cancer barrier in early human tumorigenesis. Nature *434*, 864-870.

Bartkova, J., Rezaei, N., Liontos, M., Karakaidos, P., Kletsas, D., Issaeva, N., Vassiliou, L.V., Kolettas, E., Niforou, K., Zoumpourlis, V.C.*, et al.* (2006). Oncogene-induced senescence is part of the tumorigenesis barrier imposed by DNA damage checkpoints. Nature *444*, 633-637.

Bassing, C.H., Suh, H., Ferguson, D.O., Chua, K.F., Manis, J., Eckersdorff, M., Gleason, M., Bronson, R., Lee, C., and Alt, F.W. (2003). Histone H2AX: a dosage-dependent suppressor of oncogenic translocations and tumors. Cell *114*, 359-370.

Batty, D.P., and Wood, R.D. (2000). Damage recognition in nucleotide excision repair of DNA. Gene *241*, 193-204.

Beausejour, C.M., Krtolica, A., Galimi, F., Narita, M., Lowe, S.W., Yaswen, P., and Campisi, J. (2003). Reversal of human cellular senescence: roles of the p53 and p16 pathways. Embo J *22*, 4212-4222.

Bechhoefer, J., and Rhind, N. (2012). Replication timing and its emergence from stochastic processes. Trends Genet *28*, 374-381.

Behrend, L., Henderson, G., and Zwacka, R.M. (2003). Reactive oxygen species in oncogenic transformation. Biochem Soc Trans *31*, 1441-1444.

Bennett, D.C. (2003). Human melanocyte senescence and melanoma susceptibility genes. Oncogene *22*, 3063-3069.

Bensimon, A., Simon, A., Chiffaudel, A., Croquette, V., Heslot, F., and Bensimon, D. (1994). Alignment and sensitive detection of DNA by a moving interface. Science *265*, 2096-2098.

Bernard, D., Martinez-Leal, J.F., Rizzo, S., Martinez, D., Hudson, D., Visakorpi, T., Peters, G., Carnero, A., Beach, D., and Gil, J. (2005). CBX7 controls the growth of normal and tumor-derived prostate cells by repressing the Ink4a/Arf locus. Oncogene *24*, 5543-5551.

Bernstein, E., Duncan, E.M., Masui, O., Gil, J., Heard, E., and Allis, C.D. (2006). Mouse polycomb proteins bind differentially to methylated histone H3 and RNA and are enriched in facultative heterochromatin. Mol Cell Biol *26*, 2560-2569.

Bester, A.C., Roniger, M., Oren, Y.S., Im, M.M., Sarni, D., Chaoat, M., Bensimon, A., Zamir, G., Shewach, D.S., and Kerem, B. (2011). Nucleotide deficiency promotes genomic instability in early stages of cancer development. Cell *145*, 435-446.

Bianco, J.N., Poli, J., Saksouk, J., Bacal, J., Silva, M.J., Yoshida, K., Lin, Y.L., Tourriere, H., Lengronne, A., and Pasero, P. (2012). Analysis of DNA replication profiles in budding yeast and mammalian cells using DNA combing. Methods *57*, 149-157.

Block, K., and Gorin, Y. (2012). Aiding and abetting roles of NOX oxidases in cellular transformation. Nat Rev Cancer *12*, 627-637.

Bodnar, A.G., Ouellette, M., Frolkis, M., Holt, S.E., Chiu, C.P., Morin, G.B., Harley, C.B., Shay, J.W., Lichtsteiner, S., and Wright, W.E. (1998). Extension of life-span by introduction of telomerase into normal human cells. Science *279*, 349-352.

Bond, J.A., Wyllie, F.S., and Wynford-Thomas, D. (1994). Escape from senescence in human diploid fibroblasts induced directly by mutant p53. Oncogene *9*, 1885-1889.

Borbely, G., Szabadkai, I., Horvath, Z., Marko, P., Varga, Z., Breza, N., Baska, F., Vantus, T., Huszar, M., Geiszt, M., *et al.* (2010). Small-molecule inhibitors of NADPH oxidase 4. J Med Chem *53*, 6758-6762.

Bracken, A.P., Kleine-Kohlbrecher, D., Dietrich, N., Pasini, D., Gargiulo, G., Beekman, C., Theilgaard-Monch, K., Minucci, S., Porse, B.T., Marine, J.C., *et al.* (2007). The Polycomb group proteins bind throughout the INK4A-ARF locus and are disassociated in senescent cells. Genes Dev *21*, 525-530.

Bracken, A.P., Pasini, D., Capra, M., Prosperini, E., Colli, E., and Helin, K. (2003). EZH2 is downstream of the pRB-E2F pathway, essential for proliferation and amplified in cancer. Embo J *22*, 5323-5335.

Branzei, D., and Foiani, M. (2007). Interplay of replication checkpoints and repair proteins at stalled replication forks. DNA Repair (Amst) *6*, 994-1003.

Breuer, R.H., Snijders, P.J., Smit, E.F., Sutedja, T.G., Sewalt, R.G., Otte, A.P., van Kemenade, F.J., Postmus, P.E., Meijer, C.J., and Raaphorst, F.M. (2004). Increased expression of the EZH2 polycomb group gene in BMI-1-positive neoplastic cells during bronchial carcinogenesis. Neoplasia *6*, 736-743.

Brown, E.J., and Baltimore, D. (2003). Essential and dispensable roles of ATR in cell cycle arrest and genome maintenance. Genes Dev *17*, 615-628.

Brown, J.P., Wei, W., and Sedivy, J.M. (1997). Bypass of senescence after disruption of p21CIP1/WAF1 gene in normal diploid human fibroblasts. Science *277*, 831-834.

Bruggeman, S.W., Valk-Lingbeek, M.E., van der Stoop, P.P., Jacobs, J.J., Kieboom, K., Tanger, E., Hulsman, D., Leung, C., Arsenijevic, Y., Marino, S., *et al.* (2005). Ink4a and Arf differentially affect cell proliferation and neural stem cell self-renewal in Bmi1-deficient mice. Genes Dev *19*, 1438-1443.

Bulavin, D.V., Higashimoto, Y., Popoff, I.J., Gaarde, W.A., Basrur, V., Potapova, O., Appella, E., and Fornace, A.J., Jr. (2001). Initiation of a G2/M checkpoint after ultraviolet radiation requires p38 kinase. Nature *411*, 102-107.

Burdon, R.H. (1995). Superoxide and hydrogen peroxide in relation to mammalian cell proliferation. Free Radic Biol Med *18*, 775-794.

Buscemi, G., Perego, P., Carenini, N., Nakanishi, M., Chessa, L., Chen, J., Khanna, K., and Delia, D. (2004). Activation of ATM and Chk2 kinases in relation to the amount of DNA strand breaks. Oncogene *23*, 7691-7700.

Caburet, S., Conti, C., and Bensimon, A. (2002). Combing the genome for genomic instability. Trends Biotechnol *20*, 344-350.

Cadet, J., Douki, T., Gasparutto, D., and Ravanat, J.L. (2003). Oxidative damage to DNA: formation, measurement and biochemical features. Mutat Res *531*, 5-23.

Cai, G.H., Wang, K., Miao, Q., Peng, Y.S., and Chen, X.Y. (2010). Expression of polycomb protein EZH2 in multi-stage tissues of gastric carcinogenesis. J Dig Dis *11*, 88-93.

Cao, R., Tsukada, Y., and Zhang, Y. (2005). Role of Bmi-1 and Ring1A in H2A ubiquitylation and Hox gene silencing. Mol Cell *20*, 845-854.

Cao, R., Wang, L., Wang, H., Xia, L., Erdjument-Bromage, H., Tempst, P., Jones, R.S., and Zhang, Y. (2002). Role of histone H3 lysine 27 methylation in Polycomb-group silencing. Science *298*, 1039-1043.

Cao, R., and Zhang, Y. (2004). SUZ12 is required for both the histone methyltransferase activity and the silencing function of the EED-EZH2 complex. Mol Cell *15*, 57-67.

Casper, A.M., Nghiem, P., Arlt, M.F., and Glover, T.W. (2002). ATR regulates fragile site stability. Cell *111*, 779-789.

Celeste, A., Difilippantonio, S., Difilippantonio, M.J., Fernandez-Capetillo, O., Pilch, D.R., Sedelnikova, O.A., Eckhaus, M., Ried, T., Bonner, W.M., and Nussenzweig, A. (2003a). H2AX haploinsufficiency modifies genomic stability and tumor susceptibility. Cell *114*, 371-383.

Celeste, A., Fernandez-Capetillo, O., Kruhlak, M.J., Pilch, D.R., Staudt, D.W., Lee, A., Bonner, R.F., Bonner, W.M., and Nussenzweig, A. (2003b). Histone H2AX

phosphorylation is dispensable for the initial recognition of DNA breaks. Nat Cell Biol *5*, 675-679.

Celeste, A., Petersen, S., Romanienko, P.J., Fernandez-Capetillo, O., Chen, H.T., Sedelnikova, O.A., Reina-San-Martin, B., Coppola, V., Meffre, E., Difilippantonio, M.J., *et al.* (2002). Genomic instability in mice lacking histone H2AX. Science *296*, 922-927.

Chang, B.D., Broude, E.V., Dokmanovic, M., Zhu, H., Ruth, A., Xuan, Y., Kandel, E.S., Lausch, E., Christov, K., and Roninson, I.B. (1999). A senescence-like phenotype distinguishes tumor cells that undergo terminal proliferation arrest after exposure to anticancer agents. Cancer Res *59*, 3761-3767.

Chen, Z., Trotman, L.C., Shaffer, D., Lin, H.K., Dotan, Z.A., Niki, M., Koutcher, J.A., Scher, H.I., Ludwig, T., Gerald, W., *et al.* (2005). Crucial role of p53-dependent cellular senescence in suppression of Pten-deficient tumorigenesis. Nature *436*, 725-730.

Chiarugi, P., and Cirri, P. (2003). Redox regulation of protein tyrosine phosphatases during receptor tyrosine kinase signal transduction. Trends Biochem Sci *28*, 509-514.

Chin, K., de Solorzano, C.O., Knowles, D., Jones, A., Chou, W., Rodriguez, E.G., Kuo, W.L., Ljung, B.M., Chew, K., Myambo, K., *et al.* (2004). In situ analyses of genome instability in breast cancer. Nat Genet *36*, 984-988.

Chin, L., Merlino, G., and DePinho, R.A. (1998). Malignant melanoma: modern black plague and genetic black box. Genes Dev *12*, 3467-3481.

Cho, H.J., Jeong, H.G., Lee, J.S., Woo, E.R., Hyun, J.W., Chung, M.H., and You, H.J. (2002). Oncogenic H-Ras enhances DNA repair through the Ras/phosphatidylinositol 3-kinase/Rac1 pathway in NIH3T3 cells. Evidence for association with reactive oxygen species. J Biol Chem *277*, 19358-19366.

Cimprich, K.A., and Cortez, D. (2008). ATR: an essential regulator of genome integrity. Nat Rev Mol Cell Biol *9*, 616-627.

Collado, M., Blasco, M.A., and Serrano, M. (2007). Cellular senescence in cancer and aging. Cell *130*, 223-233.

Collado, M., Gil, J., Efeyan, A., Guerra, C., Schuhmacher, A.J., Barradas, M., Benguria, A., Zaballos, A., Flores, J.M., Barbacid, M.*, et al.* (2005). Tumour biology: senescence in premalignant tumours. Nature *436*, 642.

Collado, M., and Serrano, M. (2010). Senescence in tumours: evidence from mice and humans. Nat Rev Cancer *10*, 51-57.

Collett, K., Eide, G.E., Arnes, J., Stefansson, I.M., Eide, J., Braaten, A., Aas, T., Otte, A.P., and Akslen, L.A. (2006). Expression of enhancer of zeste homologue 2 is significantly associated with increased tumor cell proliferation and is a marker of aggressive breast cancer. Clin Cancer Res *12*, 1168-1174.

Conti, C., Caburet, S., Schurra, C., and Bensimon, A. (2001). Molecular combing. Curr Protoc Cytom *Chapter 8*, Unit 8 10.

Cortez, D., Guntuku, S., Qin, J., and Elledge, S.J. (2001). ATR and ATRIP: partners in checkpoint signaling. Science *294*, 1713-1716.

Cosme-Blanco, W., Shen, M.F., Lazar, A.J., Pathak, S., Lozano, G., Multani, A.S., and Chang, S. (2007). Telomere dysfunction suppresses spontaneous tumorigenesis in vivo by initiating p53-dependent cellular senescence. EMBO Rep *8*, 497-503.

Craig, A., Scott, M., Burch, L., Smith, G., Ball, K., and Hupp, T. (2003). Allosteric effects mediate CHK2 phosphorylation of the p53 transactivation domain. EMBO Rep *4*, 787-792.

Cuadrado, M., Martinez-Pastor, B., Murga, M., Toledo, L.I., Gutierrez-Martinez, P., Lopez, E., and Fernandez-Capetillo, O. (2006). ATM regulates ATR chromatin loading in response to DNA double-strand breaks. J Exp Med *203*, 297-303.

Czermin, B., Melfi, R., McCabe, D., Seitz, V., Imhof, A., and Pirrotta, V. (2002). Drosophila enhancer of Zeste/ESC complexes have a histone H3 methyltransferase activity that marks chromosomal Polycomb sites. Cell *111*, 185-196.

d'Adda di Fagagna, F. (2008). Living on a break: cellular senescence as a DNA-damage response. Nat Rev Cancer *8*, 512-522.

d'Adda di Fagagna, F., Hande, M.P., Tong, W.M., Lansdorp, P.M., Wang, Z.Q., and Jackson, S.P. (1999). Functions of poly(ADP-ribose) polymerase in controlling telomere length and chromosomal stability. Nat Genet *23*, 76-80.

d'Adda di Fagagna, F., Reaper, P.M., Clay-Farrace, L., Fiegler, H., Carr, P., Von Zglinicki, T., Saretzki, G., Carter, N.P., and Jackson, S.P. (2003). A DNA damage checkpoint response in telomere-initiated senescence. Nature *426*, 194-198.

D'Autreaux, B., and Toledano, M.B. (2007). ROS as signalling molecules: mechanisms that generate specificity in ROS homeostasis. Nat Rev Mol Cell Biol *8*, 813-824.

de Boer, J., and Hoeijmakers, J.H. (2000). Nucleotide excision repair and human syndromes. Carcinogenesis *21*, 453-460.

Debidda, M., Williams, D.A., and Zheng, Y. (2006). Rac1 GTPase regulates cell genomic stability and senescence. J Biol Chem *281*, 38519-38528.

Deng, C., Zhang, P., Harper, J.W., Elledge, S.J., and Leder, P. (1995). Mice lacking p21CIP1/WAF1 undergo normal development, but are defective in G1 checkpoint control. Cell *82*, 675-684.

Di Micco, R., Cicalese, A., Fumagalli, M., Dobreva, M., Verrecchia, A., Pelicci, P.G., and di Fagagna, F. (2008). DNA damage response activation in mouse embryonic fibroblasts undergoing replicative senescence and following spontaneous immortalization. Cell Cycle *7*, 3601-3606.

Di Micco, R., Fumagalli, M., Cicalese, A., Piccinin, S., Gasparini, P., Luise, C., Schurra, C., Garre, M., Nuciforo, P.G., Bensimon, A.*, et al.* (2006). Oncogene-induced senescence is a DNA damage response triggered by DNA hyper-replication. Nature *444*, 638-642.

Di Micco, R., Sulli, G., Dobreva, M., Liontos, M., Botrugno, O.A., Gargiulo, G., dal Zuffo, R., Matti, V., d'Ario, G., Montani, E.*, et al.* (2011). Interplay between oncogene-induced DNA damage response and heterochromatin in senescence and cancer. Nat Cell Biol *13*, 292-302.

Dietrich, N., Bracken, A.P., Trinh, E., Schjerling, C.K., Koseki, H., Rappsilber, J., Helin, K., and Hansen, K.H. (2007). Bypass of senescence by the polycomb group protein CBX8 through direct binding to the INK4A-ARF locus. Embo J *26*, 1637-1648.

Dimri, G.P., Lee, X., Basile, G., Acosta, M., Scott, G., Roskelley, C., Medrano, E.E., Linskens, M., Rubelj, I., Pereira-Smith, O.*, et al.* (1995). A biomarker that identifies senescent human cells in culture and in aging skin in vivo. Proc Natl Acad Sci U S A *92*, 9363-9367.

Ding, L., Erdmann, C., Chinnaiyan, A.M., Merajver, S.D., and Kleer, C.G. (2006). Identification of EZH2 as a molecular marker for a precancerous state in morphologically normal breast tissues. Cancer Res *66*, 4095-4099.

DiTullio, R.A., Jr., Mochan, T.A., Venere, M., Bartkova, J., Sehested, M., Bartek, J., and Halazonetis, T.D. (2002). 53BP1 functions in an ATM-dependent checkpoint pathway that is constitutively activated in human cancer. Nat Cell Biol *4*, 998-1002.

Doksani, Y., Bermejo, R., Fiorani, S., Haber, J.E., and Foiani, M. (2009). Replicon dynamics, dormant origin firing, and terminal fork integrity after double-strand break formation. Cell *137*, 247-258.

Dominguez-Sola, D., Ying, C.Y., Grandori, C., Ruggiero, L., Chen, B., Li, M., Galloway, D.A., Gu, W., Gautier, J., and Dalla-Favera, R. (2007). Non-transcriptional control of DNA replication by c-Myc. Nature *448*, 445-451.

Donzelli, M., and Draetta, G.F. (2003). Regulating mammalian checkpoints through Cdc25 inactivation. EMBO Rep *4*, 671-677.

Dovey, J.S., Zacharek, S.J., Kim, C.F., and Lees, J.A. (2008). Bmi1 is critical for lung tumorigenesis and bronchioalveolar stem cell expansion. Proc Natl Acad Sci U S A *105*, 11857-11862.

Downey, M., and Durocher, D. (2006). gammaH2AX as a checkpoint maintenance signal. Cell Cycle *5*, 1376-1381.

Duhamel, S., Hebert, J., Gaboury, L., Bouchard, A., Simon, R., Sauter, G., Basik, M., and Meloche, S. (2012). Sef downregulation by Ras causes MEK1/2 to become aberrantly nuclear localized leading to polyploidy and neoplastic transformation. Cancer Res *72*, 626-635.

Durkin, S.G., and Glover, T.W. (2007). Chromosome fragile sites. Annu Rev Genet *41*, 169-192.

Evan, G.I., and d'Adda di Fagagna, F. (2009). Cellular senescence: hot or what? Curr Opin Genet Dev *19*, 25-31.

Eymin, B., Claverie, P., Salon, C., Leduc, C., Col, E., Brambilla, E., Khochbin, S., and Gazzeri, S. (2006). p14ARF activates a Tip60-dependent and p53-independent ATM/ATR/CHK pathway in response to genotoxic stress. Mol Cell Biol *26*, 4339-4350.

Faust, C., Lawson, K.A., Schork, N.J., Thiel, B., and Magnuson, T. (1998). The Polycomb-group gene eed is required for normal morphogenetic movements during gastrulation in the mouse embryo. Development *125*, 4495-4506.

Feldser, D.M., and Greider, C.W. (2007). Short telomeres limit tumor progression in vivo by inducing senescence. Cancer Cell *11*, 461-469.

Fortini, P., and Dogliotti, E. (2007). Base damage and single-strand break repair: mechanisms and functional significance of short- and long-patch repair subpathways. DNA Repair (Amst) *6*, 398-409.

Francis, N.J., Follmer, N.E., Simon, M.D., Aghia, G., and Butler, J.D. (2009). Polycomb proteins remain bound to chromatin and DNA during DNA replication in vitro. Cell *137*, 110-122.

Francis, N.J., Kingston, R.E., and Woodcock, C.L. (2004). Chromatin compaction by a polycomb group protein complex. Science *306*, 1574-1577.

Francis, N.J., Saurin, A.J., Shao, Z., and Kingston, R.E. (2001). Reconstitution of a functional core polycomb repressive complex. Mol Cell *8*, 545-556.

Fumagalli, M., Rossiello, F., Clerici, M., Barozzi, S., Cittaro, D., Kaplunov, J.M., Bucci, G., Dobreva, M., Matti, V., Beausejour, C.M., *et al.* (2012). Telomeric DNA damage is irreparable and causes persistent DNA-damage-response activation. Nat Cell Biol *14*, 355-365.

Gad, S., Aurias, A., Puget, N., Mairal, A., Schurra, C., Montagna, M., Pages, S., Caux, V., Mazoyer, S., Bensimon, A., *et al.* (2001a). Color bar coding the BRCA1 gene on combed DNA: a useful strategy for detecting large gene rearrangements. Genes Chromosomes Cancer *31*, 75-84.

Gad, S., Scheuner, M.T., Pages-Berhouet, S., Caux-Moncoutier, V., Bensimon, A., Aurias, A., Pinto, M., and Stoppa-Lyonnet, D. (2001b). Identification of a large rearrangement of the BRCA1 gene using colour bar code on combed DNA in an American breast/ovarian cancer family previously studied by direct sequencing. J Med Genet *38*, 388-392.

Gamou, S., and Shimizu, N. (1995). Hydrogen peroxide preferentially enhances the tyrosine phosphorylation of epidermal growth factor receptor. FEBS Lett *357*, 161-164.

Gauthier, M.G., Herrick, J., and Bechhoefer, J. (2010). Defects and DNA replication. Phys Rev Lett *104*, 218104.

Ge, X.Q., Jackson, D.A., and Blow, J.J. (2007). Dormant origins licensed by excess Mcm2-7 are required for human cells to survive replicative stress. Genes Dev *21*, 3331-3341.

Gil, J., Bernard, D., Martinez, D., and Beach, D. (2004). Polycomb CBX7 has a unifying role in cellular lifespan. Nat Cell Biol *6*, 67-72.

Gil, J., and Peters, G. (2006). Regulation of the INK4b-ARF-INK4a tumour suppressor locus: all for one or one for all. Nat Rev Mol Cell Biol *7*, 667-677.

Gire, V., Roux, P., Wynford-Thomas, D., Brondello, J.M., and Dulic, V. (2004). DNA damage checkpoint kinase Chk2 triggers replicative senescence. Embo J *23*, 2554-2563.

Godlewski, J., Nowicki, M.O., Bronisz, A., Williams, S., Otsuki, A., Nuovo, G., Raychaudhury, A., Newton, H.B., Chiocca, E.A., and Lawler, S. (2008). Targeting of the

Bmi-1 oncogene/stem cell renewal factor by microRNA-128 inhibits glioma proliferation and self-renewal. Cancer Res *68*, 9125-9130.

Gorbunova, V., Seluanov, A., and Pereira-Smith, O.M. (2002). Expression of human telomerase (hTERT) does not prevent stress-induced senescence in normal human fibroblasts but protects the cells from stress-induced apoptosis and necrosis. J Biol Chem *277*, 38540-38549.

Grek, C.L., and Tew, K.D. (2010). Redox metabolism and malignancy. Curr Opin Pharmacol *10*, 362-368.

Guo, Z., Kozlov, S., Lavin, M.F., Person, M.D., and Paull, T.T. (2010). ATM activation by oxidative stress. Science *330*, 517-521.

Hahn, W.C., Counter, C.M., Lundberg, A.S., Beijersbergen, R.L., Brooks, M.W., and Weinberg, R.A. (1999). Creation of human tumour cells with defined genetic elements. Nature *400*, 464-468.

Halazonetis, T.D., Gorgoulis, V.G., and Bartek, J. (2008). An oncogene-induced DNA damage model for cancer development. Science *319*, 1352-1355.

Hande, P., Slijepcevic, P., Silver, A., Bouffler, S., van Buul, P., Bryant, P., and Lansdorp, P. (1999). Elongated telomeres in scid mice. Genomics *56*, 221-223.

Hansen, K.H., Bracken, A.P., Pasini, D., Dietrich, N., Gehani, S.S., Monrad, A., Rappsilber, J., Lerdrup, M., and Helin, K. (2008). A model for transmission of the H3K27me3 epigenetic mark. Nat Cell Biol *10*, 1291-1300.

Hansen, R.S., Thomas, S., Sandstrom, R., Canfield, T.K., Thurman, R.E., Weaver, M., Dorschner, M.O., Gartler, S.M., and Stamatoyannopoulos, J.A. (2010). Sequencing newly replicated DNA reveals widespread plasticity in human replication timing. Proc Natl Acad Sci U S A *107*, 139-144.

Harley, C.B., Futcher, A.B., and Greider, C.W. (1990). Telomeres shorten during ageing of human fibroblasts. Nature *345*, 458-460.

Haupt, Y., Alexander, W.S., Barri, G., Klinken, S.P., and Adams, J.M. (1991). Novel zinc finger gene implicated as myc collaborator by retrovirally accelerated lymphomagenesis in E mu-myc transgenic mice. Cell *65*, 753-763.

Hayflick, L., and Moorhead, P.S. (1961). The serial cultivation of human diploid cell strains. Exp Cell Res *25*, 585-621.

Hemann, M.T., Strong, M.A., Hao, L.Y., and Greider, C.W. (2001). The shortest telomere, not average telomere length, is critical for cell viability and chromosome stability. Cell *107*, 67-77.

Herbig, U., Jobling, W.A., Chen, B.P., Chen, D.J., and Sedivy, J.M. (2004). Telomere shortening triggers senescence of human cells through a pathway involving ATM, p53, and p21(CIP1), but not p16(INK4a). Mol Cell *14*, 501-513.

Hirao, A., Cheung, A., Duncan, G., Girard, P.M., Elia, A.J., Wakeham, A., Okada, H., Sarkissian, T., Wong, J.A., Sakai, T.*, et al.* (2002). Chk2 is a tumor suppressor that regulates apoptosis in both an ataxia telangiectasia mutated (ATM)-dependent and an ATM-independent manner. Mol Cell Biol *22*, 6521-6532.

Hitomi, K., Iwai, S., and Tainer, J.A. (2007). The intricate structural chemistry of base excision repair machinery: implications for DNA damage recognition, removal, and repair. DNA Repair (Amst) *6*, 410-428.

Hoenerhoff, M.J., Chu, I., Barkan, D., Liu, Z.Y., Datta, S., Dimri, G.P., and Green, J.E. (2009). BMI1 cooperates with H-RAS to induce an aggressive breast cancer phenotype with brain metastases. Oncogene *28*, 3022-3032.

Huang, H.L., Hsing, H.W., Lai, T.C., Chen, Y.W., Lee, T.R., Chan, H.T., Lyu, P.C., Wu, C.L., Lu, Y.C., Lin, S.T.*, et al.* (2010). Trypsin-induced proteome alteration during cell subculture in mammalian cells. Journal of biomedical science *17*, 36.

Irani, K., Xia, Y., Zweier, J.L., Sollott, S.J., Der, C.J., Fearon, E.R., Sundaresan, M., Finkel, T., and Goldschmidt-Clermont, P.J. (1997). Mitogenic signaling mediated by oxidants in Ras-transformed fibroblasts. Science *275*, 1649-1652.

Itahana, K., Zou, Y., Itahana, Y., Martinez, J.L., Beausejour, C., Jacobs, J.J., Van Lohuizen, M., Band, V., Campisi, J., and Dimri, G.P. (2003). Control of the replicative life span of human fibroblasts by p16 and the polycomb protein Bmi-1. Mol Cell Biol *23*, 389-401.

Jackson, J.G., and Pereira-Smith, O.M. (2006). p53 is preferentially recruited to the promoters of growth arrest genes p21 and GADD45 during replicative senescence of normal human fibroblasts. Cancer Res *66*, 8356-8360.

Jackson, S.P., and Bartek, J. (2009). The DNA-damage response in human biology and disease. Nature *461*, 1071-1078.

Jacobs, J.J., and de Lange, T. (2004). Significant role for p16INK4a in p53-independent telomere-directed senescence. Curr Biol *14*, 2302-2308.

Jacobs, J.J., Kieboom, K., Marino, S., DePinho, R.A., and van Lohuizen, M. (1999). The oncogene and Polycomb-group gene bmi-1 regulates cell proliferation and senescence through the ink4a locus. Nature *397*, 164-168.

Jazayeri, A., Falck, J., Lukas, C., Bartek, J., Smith, G.C., Lukas, J., and Jackson, S.P. (2006). ATM- and cell cycle-dependent regulation of ATR in response to DNA double-strand breaks. Nat Cell Biol *8*, 37-45.

Jiricny, J. (2006). The multifaceted mismatch-repair system. Nat Rev Mol Cell Biol *7*, 335-346.

Johnson, D.G., and Degregori, J. (2006). Putting the Oncogenic and Tumor Suppressive Activities of E2F into Context. Curr Mol Med *6*, 731-738.

Jones, R.M., Mortusewicz, O., Afzal, I., Lorvellec, M., Garcia, P., Helleday, T., and Petermann, E. (2013). Increased replication initiation and conflicts with transcription underlie Cyclin E-induced replication stress. Oncogene *32*, 3744-3753.

Kang, M.K., Kim, R.H., Kim, S.J., Yip, F.K., Shin, K.H., Dimri, G.P., Christensen, R., Han, T., and Park, N.H. (2007). Elevated Bmi-1 expression is associated with dysplastic

cell transformation during oral carcinogenesis and is required for cancer cell replication and survival. Br J Cancer *96*, 126-133.

Kastan, M.B., and Bartek, J. (2004). Cell-cycle checkpoints and cancer. Nature *432*, 316-323.

Kennison, J.A. (1995). The Polycomb and trithorax group proteins of Drosophila: trans-regulators of homeotic gene function. Annu Rev Genet *29*, 289-303.

Kidani, K., Osaki, M., Tamura, T., Yamaga, K., Shomori, K., Ryoke, K., and Ito, H. (2009). High expression of EZH2 is associated with tumor proliferation and prognosis in human oral squamous cell carcinomas. Oral Oncol *45*, 39-46.

King, I.F., Francis, N.J., and Kingston, R.E. (2002). Native and recombinant polycomb group complexes establish a selective block to template accessibility to repress transcription in vitro. Mol Cell Biol *22*, 7919-7928.

King, M.C., Marks, J.H., and Mandell, J.B. (2003). Breast and ovarian cancer risks due to inherited mutations in BRCA1 and BRCA2. Science *302*, 643-646.

Kitagawa, R., Bakkenist, C.J., McKinnon, P.J., and Kastan, M.B. (2004). Phosphorylation of SMC1 is a critical downstream event in the ATM-NBS1-BRCA1 pathway. Genes Dev *18*, 1423-1438.

Kleer, C.G., Cao, Q., Varambally, S., Shen, R., Ota, I., Tomlins, S.A., Ghosh, D., Sewalt, R.G., Otte, A.P., Hayes, D.F.*, et al.* (2003). EZH2 is a marker of aggressive breast cancer and promotes neoplastic transformation of breast epithelial cells. Proc Natl Acad Sci U S A *100*, 11606-11611.

Knapp, L.T., and Klann, E. (2000). Superoxide-induced stimulation of protein kinase C via thiol modification and modulation of zinc content. J Biol Chem *275*, 24136-24145.

Korur, S., Huber, R.M., Sivasankaran, B., Petrich, M., Morin, P., Jr., Hemmings, B.A., Merlo, A., and Lino, M.M. (2009). GSK3beta regulates differentiation and growth arrest in glioblastoma. PLoS One *4*, e7443.

Kosar, M., Bartkova, J., Hubackova, S., Hodny, Z., Lukas, J., and Bartek, J. (2011). Senescence-associated heterochromatin foci are dispensable for cellular senescence, occur in a cell type- and insult-dependent manner and follow expression of p16(ink4a). Cell Cycle *10*, 457-468.

Krishnamurthy, J., Torrice, C., Ramsey, M.R., Kovalev, G.I., Al-Regaiey, K., Su, L., and Sharpless, N.E. (2004). Ink4a/Arf expression is a biomarker of aging. J Clin Invest *114*, 1299-1307.

Kuilman, T., Michaloglou, C., Vredeveld, L.C., Douma, S., van Doorn, R., Desmet, C.J., Aarden, L.A., Mooi, W.J., and Peeper, D.S. (2008). Oncogene-induced senescence relayed by an interleukin-dependent inflammatory network. Cell *133*, 1019-1031.

Kumagai, A., Lee, J., Yoo, H.Y., and Dunphy, W.G. (2006). TopBP1 activates the ATR-ATRIP complex. Cell *124*, 943-955.

Kuzmichev, A., Nishioka, K., Erdjument-Bromage, H., Tempst, P., and Reinberg, D. (2002). Histone methyltransferase activity associated with a human multiprotein complex containing the Enhancer of Zeste protein. Genes Dev *16*, 2893-2905.

Labit, H., Goldar, A., Guilbaud, G., Douarche, C., Hyrien, O., and Marheineke, K. (2008). A simple and optimized method of producing silanized surfaces for FISH and replication mapping on combed DNA fibers. Biotechniques *45*, 649-652, 654, 656-648.

Lam, M.H., Liu, Q., Elledge, S.J., and Rosen, J.M. (2004). Chk1 is haploinsufficient for multiple functions critical to tumor suppression. Cancer Cell *6*, 45-59.

Lau, A., Swinbank, K.M., Ahmed, P.S., Taylor, D.L., Jackson, S.P., Smith, G.C., and O'Connor, M.J. (2005). Suppression of HIV-1 infection by a small molecule inhibitor of the ATM kinase. Nat Cell Biol *7*, 493-500.

Lebofsky, R., and Bensimon, A. (2003). Single DNA molecule analysis: applications of molecular combing. Brief Funct Genomic Proteomic *1*, 385-396.

Lechel, A., Satyanarayana, A., Ju, Z., Plentz, R.R., Schaetzlein, S., Rudolph, C., Wilkens, L., Wiemann, S.U., Saretzki, G., Malek, N.P.*, et al.* (2005). The cellular level of telomere

dysfunction determines induction of senescence or apoptosis in vivo. EMBO Rep *6*, 275-281.

Lee, A.C., Fenster, B.E., Ito, H., Takeda, K., Bae, N.S., Hirai, T., Yu, Z.X., Ferrans, V.J., Howard, B.H., and Finkel, T. (1999). Ras proteins induce senescence by altering the intracellular levels of reactive oxygen species. J Biol Chem *274*, 7936-7940.

Lee, B.Y., Han, J.A., Im, J.S., Morrone, A., Johung, K., Goodwin, E.C., Kleijer, W.J., DiMaio, D., and Hwang, E.S. (2006). Senescence-associated beta-galactosidase is lysosomal beta-galactosidase. Aging Cell *5*, 187-195.

Lehmann, A.R., Niimi, A., Ogi, T., Brown, S., Sabbioneda, S., Wing, J.F., Kannouche, P.L., and Green, C.M. (2007). Translesion synthesis: Y-family polymerases and the polymerase switch. DNA Repair (Amst) *6*, 891-899.

Lehmann, L., Ferrari, R., Vashisht, A.A., Wohlschlegel, J.A., Kurdistani, S.K., and Carey, M. (2012). Polycomb repressive complex 1 (PRC1) disassembles RNA polymerase II preinitiation complexes. J Biol Chem *287*, 35784-35794.

Letessier, A., Millot, G.A., Koundrioukoff, S., Lachages, A.M., Vogt, N., Hansen, R.S., Malfoy, B., Brison, O., and Debatisse, M. (2011). Cell-type-specific replication initiation programs set fragility of the FRA3B fragile site. Nature *470*, 120-123.

Lin, A.W., Barradas, M., Stone, J.C., van Aelst, L., Serrano, M., and Lowe, S.W. (1998). Premature senescence involving p53 and p16 is activated in response to constitutive MEK/MAPK mitogenic signaling. Genes Dev *12*, 3008-3019.

Liu, Q., Guntuku, S., Cui, X.S., Matsuoka, S., Cortez, D., Tamai, K., Luo, G., Carattini-Rivera, S., DeMayo, F., Bradley, A.*, et al.* (2000). Chk1 is an essential kinase that is regulated by Atr and required for the G(2)/M DNA damage checkpoint. Genes Dev *14*, 1448-1459.

Lukas, C., Falck, J., Bartkova, J., Bartek, J., and Lukas, J. (2003). Distinct spatiotemporal dynamics of mammalian checkpoint regulators induced by DNA damage. Nat Cell Biol *5*, 255-260.

Lukas, C., Savic, V., Bekker-Jensen, S., Doil, C., Neumann, B., Pedersen, R.S., Grofte, M., Chan, K.L., Hickson, I.D., Bartek, J., *et al.* (2011). 53BP1 nuclear bodies form around DNA lesions generated by mitotic transmission of chromosomes under replication stress. Nat Cell Biol *13*, 243-253.

Mailand, N., and Diffley, J.F. (2005). CDKs promote DNA replication origin licensing in human cells by protecting Cdc6 from APC/C-dependent proteolysis. Cell *122*, 915-926.

Mailand, N., Falck, J., Lukas, C., Syljuasen, R.G., Welcker, M., Bartek, J., and Lukas, J. (2000). Rapid destruction of human Cdc25A in response to DNA damage. Science *288*, 1425-1429.

Marusyk, A., Wheeler, L.J., Mathews, C.K., and DeGregori, J. (2007). p53 mediates senescence-like arrest induced by chronic replicational stress. Mol Cell Biol *27*, 5336-5351.

Mason, D.X., Jackson, T.J., and Lin, A.W. (2004). Molecular signature of oncogenic ras-induced senescence. Oncogene *23*, 9238-9246.

Maya, R., Balass, M., Kim, S.T., Shkedy, D., Leal, J.F., Shifman, O., Moas, M., Buschmann, T., Ronai, Z., Shiloh, Y., *et al.* (2001). ATM-dependent phosphorylation of Mdm2 on serine 395: role in p53 activation by DNA damage. Genes Dev *15*, 1067-1077.

Menendez, S., Khan, Z., Coomber, D.W., Lane, D.P., Higgins, M., Koufali, M.M., and Lain, S. (2003). Oligomerization of the human ARF tumor suppressor and its response to oxidative stress. J Biol Chem *278*, 18720-18729.

Menon, S.G., and Goswami, P.C. (2007). A redox cycle within the cell cycle: ring in the old with the new. Oncogene *26*, 1101-1109.

Menon, S.G., Sarsour, E.H., Spitz, D.R., Higashikubo, R., Sturm, M., Zhang, H., and Goswami, P.C. (2003). Redox regulation of the G1 to S phase transition in the mouse embryo fibroblast cell cycle. Cancer Res *63*, 2109-2117.

Michalet, X., Ekong, R., Fougerousse, F., Rousseaux, S., Schurra, C., Hornigold, N., van Slegtenhorst, M., Wolfe, J., Povey, S., Beckmann, J.S., *et al.* (1997). Dynamic molecular

combing: stretching the whole human genome for high-resolution studies. Science *277*, 1518-1523.

Michaloglou, C., Vredeveld, L.C., Soengas, M.S., Denoyelle, C., Kuilman, T., van der Horst, C.M., Majoor, D.M., Shay, J.W., Mooi, W.J., and Peeper, D.S. (2005). BRAFE600-associated senescence-like cell cycle arrest of human naevi. Nature *436*, 720-724.

Mimori, K., Ogawa, K., Okamoto, M., Sudo, T., Inoue, H., and Mori, M. (2005). Clinical significance of enhancer of zeste homolog 2 expression in colorectal cancer cases. Eur J Surg Oncol *31*, 376-380.

Morey, L., and Helin, K. (2010). Polycomb group protein-mediated repression of transcription. Trends Biochem Sci *35*, 323-332.

Mortusewicz, O., Herr, P., and Helleday, T. (2013). Early replication fragile sites: where replication-transcription collisions cause genetic instability. Embo J *32*, 493-495.

Muller, J., Hart, C.M., Francis, N.J., Vargas, M.L., Sengupta, A., Wild, B., Miller, E.L., O'Connor, M.B., Kingston, R.E., and Simon, J.A. (2002). Histone methyltransferase activity of a Drosophila Polycomb group repressor complex. Cell *111*, 197-208.

Narita, M., Nunez, S., Heard, E., Lin, A.W., Hearn, S.A., Spector, D.L., Hannon, G.J., and Lowe, S.W. (2003). Rb-mediated heterochromatin formation and silencing of E2F target genes during cellular senescence. Cell *113*, 703-716.

Neelsen, K.J., Zanini, I.M., Herrador, R., and Lopes, M. (2013). Oncogenes induce genotoxic stress by mitotic processing of unusual replication intermediates. J Cell Biol *200*, 699-708.

Norio, P., and Schildkraut, C.L. (2001). Visualization of DNA replication on individual Epstein-Barr virus episomes. Science *294*, 2361-2364.

O'Carroll, D., Erhardt, S., Pagani, M., Barton, S.C., Surani, M.A., and Jenuwein, T. (2001). The polycomb-group gene Ezh2 is required for early mouse development. Mol Cell Biol *21*, 4330-4336.

O'Driscoll, M., Ruiz-Perez, V.L., Woods, C.G., Jeggo, P.A., and Goodship, J.A. (2003). A splicing mutation affecting expression of ataxia-telangiectasia and Rad3-related protein (ATR) results in Seckel syndrome. Nat Genet *33*, 497-501.

Olsen, C.L., Gardie, B., Yaswen, P., and Stampfer, M.R. (2002). Raf-1-induced growth arrest in human mammary epithelial cells is p16-independent and is overcome in immortal cells during conversion. Oncogene *21*, 6328-6339.

Orlando, V., and Paro, R. (1995). Chromatin multiprotein complexes involved in the maintenance of transcription patterns. Curr Opin Genet Dev *5*, 174-179.

Ozeri-Galai, E., Bester, A.C., and Kerem, B. (2012). The complex basis underlying common fragile site instability in cancer. Trends Genet *28*, 295-302.

Panier, S., and Durocher, D. (2013). Push back to respond better: regulatory inhibition of the DNA double-strand break response. Nat Rev Cancer *13*, 661-672.

Pasini, D., Bracken, A.P., Jensen, M.R., Lazzerini Denchi, E., and Helin, K. (2004). Suz12 is essential for mouse development and for EZH2 histone methyltransferase activity. Embo J *23*, 4061-4071.

Pear, W.S., Nolan, G.P., Scott, M.L., and Baltimore, D. (1993). Production of high-titer helper-free retroviruses by transient transfection. Proc Natl Acad Sci U S A *90*, 8392-8396.

Petrini, J.H. (2009). DNA replication reaches the breaking point. Cell *137*, 211-212.

Pines, J. (1999). Four-dimensional control of the cell cycle. Nat Cell Biol *1*, E73-79.

Poonepalli, A., Balakrishnan, L., Khaw, A.K., Low, G.K., Jayapal, M., Bhattacharjee, R.N., Akira, S., Balajee, A.S., and Hande, M.P. (2005). Lack of poly(ADP-ribose) polymerase-1 gene product enhances cellular sensitivity to arsenite. Cancer Res *65*, 10977-10983.

Puppe, J., Drost, R., Liu, X., Joosse, S.A., Evers, B., Cornelissen-Steijger, P., Nederlof, P., Yu, Q., Jonkers, J., van Lohuizen, M.*, et al.* (2009). BRCA1-deficient mammary tumor cells are dependent on EZH2 expression and sensitive to Polycomb Repressive Complex 2-inhibitor 3-deazaneplanocin A. Breast Cancer Res *11*, R63.

Rainwater, R., Parks, D., Anderson, M.E., Tegtmeyer, P., and Mann, K. (1995). Role of cysteine residues in regulation of p53 function. Mol Cell Biol *15*, 3892-3903.

Raman, J.D., Mongan, N.P., Tickoo, S.K., Boorjian, S.A., Scherr, D.S., and Gudas, L.J. (2005). Increased expression of the polycomb group gene, EZH2, in transitional cell carcinoma of the bladder. Clin Cancer Res *11*, 8570-8576.

Robinson, W.A., Lemon, M., Elefanty, A., Harrison-Smith, M., Markham, N., and Norris, D. (1998). Human acquired naevi are clonal. Melanoma Res *8*, 499-503.

Rudolph, K.L., Millard, M., Bosenberg, M.W., and DePinho, R.A. (2001). Telomere dysfunction and evolution of intestinal carcinoma in mice and humans. Nat Genet *28*, 155-159.

Sancar, A., Lindsey-Boltz, L.A., Unsal-Kacmaz, K., and Linn, S. (2004). Molecular mechanisms of mammalian DNA repair and the DNA damage checkpoints. Annu Rev Biochem *73*, 39-85.

Sasaki, H., Setoguchi, T., Matsunoshita, Y., Gao, H., Hirotsu, M., and Komiya, S. (2010). The knock-down of overexpressed EZH2 and BMI-1 does not prevent osteosarcoma growth. Oncol Rep *23*, 677-684.

Sasaki, M., Ikeda, H., Itatsu, K., Yamaguchi, J., Sawada, S., Minato, H., Ohta, T., and Nakanuma, Y. (2008). The overexpression of polycomb group proteins Bmi1 and EZH2 is associated with the progression and aggressive biological behavior of hepatocellular carcinoma. Lab Invest *88*, 873-882.

Schurra, C., and Bensimon, A. (2009). Combing genomic DNA for structural and functional studies. Methods Mol Biol *464*, 71-90.

Schwartz, Y.B., and Pirrotta, V. (2008). Polycomb complexes and epigenetic states. Curr Opin Cell Biol *20*, 266-273.

Serrano, M., Lin, A.W., McCurrach, M.E., Beach, D., and Lowe, S.W. (1997). Oncogenic ras provokes premature cell senescence associated with accumulation of p53 and p16INK4a. Cell *88*, 593-602.

Sfeir, A., Kosiyatrakul, S.T., Hockemeyer, D., MacRae, S.L., Karlseder, J., Schildkraut, C.L., and de Lange, T. (2009). Mammalian telomeres resemble fragile sites and require TRF1 for efficient replication. Cell *138*, 90-103.

Shafaroudi, A.M., Mowla, S.J., Ziaee, S.A., Bahrami, A.R., Atlasi, Y., and Malakootian, M. (2008). Overexpression of BMI1, a polycomb group repressor protein, in bladder tumors: a preliminary report. Urol J *5*, 99-105.

Shao, Z., Raible, F., Mollaaghababa, R., Guyon, J.R., Wu, C.T., Bender, W., and Kingston, R.E. (1999). Stabilization of chromatin structure by PRC1, a Polycomb complex. Cell *98*, 37-46.

Sharpless, N.E., and DePinho, R.A. (2005). Cancer: crime and punishment. Nature *436*, 636-637.

Sherr, C.J., and McCormick, F. (2002). The RB and p53 pathways in cancer. Cancer Cell *2*, 103-112.

Sherr, C.J., and Roberts, J.M. (1999). CDK inhibitors: positive and negative regulators of G1-phase progression. Genes Dev *13*, 1501-1512.

Shiloh, Y. (1997). Ataxia-telangiectasia and the Nijmegen breakage syndrome: related disorders but genes apart. Annu Rev Genet *31*, 635-662.

Shiloh, Y. (2003). ATM and related protein kinases: safeguarding genome integrity. Nat Rev Cancer *3*, 155-168.

Shiloh, Y., and Kastan, M.B. (2001). ATM: genome stability, neuronal development, and cancer cross paths. Adv Cancer Res *83*, 209-254.

Shiloh, Y., and Ziv, Y. (2013). The ATM protein kinase: regulating the cellular response to genotoxic stress, and more. Nat Rev Mol Cell Biol *14*, 197-210.

Simon, J. (1995). Locking in stable states of gene expression: transcriptional control during Drosophila development. Curr Opin Cell Biol *7*, 376-385.

Simon, J.A., and Kingston, R.E. (2009). Mechanisms of polycomb gene silencing: knowns and unknowns. Nat Rev Mol Cell Biol *10*, 697-708.

Smogorzewska, A., and de Lange, T. (2002). Different telomere damage signaling pathways in human and mouse cells. Embo J *21*, 4338-4348.

Sparmann, A., and van Lohuizen, M. (2006). Polycomb silencers control cell fate, development and cancer. Nat Rev Cancer *6*, 846-856.

Steele, J.C., Torr, E.E., Noakes, K.L., Kalk, E., Moss, P.A., Reynolds, G.M., Hubscher, S.G., van Lohuizen, M., Adams, D.H., and Young, L.S. (2006). The polycomb group proteins, BMI-1 and EZH2, are tumour-associated antigens. Br J Cancer *95*, 1202-1211.

Stein, G.H., Drullinger, L.F., Robetorye, R.S., Pereira-Smith, O.M., and Smith, J.R. (1991). Senescent cells fail to express cdc2, cycA, and cycB in response to mitogen stimulation. Proc Natl Acad Sci U S A *88*, 11012-11016.

Stewart, G.S., Maser, R.S., Stankovic, T., Bressan, D.A., Kaplan, M.I., Jaspers, N.G., Raams, A., Byrd, P.J., Petrini, J.H., and Taylor, A.M. (1999). The DNA double-strand break repair gene hMRE11 is mutated in individuals with an ataxia-telangiectasia-like disorder. Cell *99*, 577-587.

Stewart, G.S., Stankovic, T., Byrd, P.J., Wechsler, T., Miller, E.S., Huissoon, A., Drayson, M.T., West, S.C., Elledge, S.J., and Taylor, A.M. (2007). RIDDLE immunodeficiency syndrome is linked to defects in 53BP1-mediated DNA damage signaling. Proc Natl Acad Sci U S A *104*, 16910-16915.

Stucki, M., and Jackson, S.P. (2004). MDC1/NFBD1: a key regulator of the DNA damage response in higher eukaryotes. DNA Repair (Amst) *3*, 953-957.

Suh, Y.A., Arnold, R.S., Lassegue, B., Shi, J., Xu, X., Sorescu, D., Chung, A.B., Griendling, K.K., and Lambeth, J.D. (1999). Cell transformation by the superoxide-generating oxidase Mox1. Nature *401*, 79-82.

Sulli, G., Di Micco, R., and d'Adda di Fagagna, F. (2012). Crosstalk between chromatin state and DNA damage response in cellular senescence and cancer. Nat Rev Cancer *12*, 709-720.

Sundaresan, M., Yu, Z.X., Ferrans, V.J., Sulciner, D.J., Gutkind, J.S., Irani, K., Goldschmidt-Clermont, P.J., and Finkel, T. (1996). Regulation of reactive-oxygen-species generation in fibroblasts by Rac1. Biochem J *318 (Pt 2)*, 379-382.

Sung, P., Krejci, L., Van Komen, S., and Sehorn, M.G. (2003). Rad51 recombinase and recombination mediators. J Biol Chem *278*, 42729-42732.

Suram, A., Kaplunov, J., Patel, P.L., Ruan, H., Cerutti, A., Boccardi, V., Fumagalli, M., Di Micco, R., Mirani, N., Gurung, R.L.*, et al.* (2012). Oncogene-induced telomere dysfunction enforces cellular senescence in human cancer precursor lesions. Embo J *31*, 2839-2851.

Suva, M.L., Riggi, N., Janiszewska, M., Radovanovic, I., Provero, P., Stehle, J.C., Baumer, K., Le Bitoux, M.A., Marino, D., Cironi, L.*, et al.* (2009). EZH2 is essential for glioblastoma cancer stem cell maintenance. Cancer Res *69*, 9211-9218.

Suzuki, M., Suzuki, K., Kodama, S., and Watanabe, M. (2006). Interstitial chromatin alteration causes persistent p53 activation involved in the radiation-induced senescence-like growth arrest. Biochem Biophys Res Commun *340*, 145-150.

Szatrowski, T.P., and Nathan, C.F. (1991). Production of large amounts of hydrogen peroxide by human tumor cells. Cancer Res *51*, 794-798.

Takeda, D.Y., Shibata, Y., Parvin, J.D., and Dutta, A. (2005). Recruitment of ORC or CDC6 to DNA is sufficient to create an artificial origin of replication in mammalian cells. Genes Dev *19*, 2827-2836.

Tateishi, K., Ohta, M., Kanai, F., Guleng, B., Tanaka, Y., Asaoka, Y., Tada, M., Seto, M., Jazag, A., Lianjie, L.*, et al.* (2006). Dysregulated expression of stem cell factor Bmi1 in precancerous lesions of the gastrointestinal tract. Clin Cancer Res *12*, 6960-6966.

Taylor, R.C., Cullen, S.P., and Martin, S.J. (2008). Apoptosis: controlled demolition at the cellular level. Nat Rev Mol Cell Biol *9*, 231-241.

Taylor, W.R., and Stark, G.R. (2001). Regulation of the G2/M transition by p53. Oncogene *20*, 1803-1815.

Techer, H., Koundrioukoff, S., Azar, D., Wilhelm, T., Carignon, S., Brison, O., Debatisse, M., and Le Tallec, B. (2013). Replication Dynamics: Biases and Robustness of DNA Fiber Analysis. J Mol Biol.

Thompson, L.H., and Schild, D. (2002). Recombinational DNA repair and human disease. Mutat Res *509*, 49-78.

Tsantoulis, P.K., Kotsinas, A., Sfikakis, P.P., Evangelou, K., Sideridou, M., Levy, B., Mo, L., Kittas, C., Wu, X.R., Papavassiliou, A.G.*, et al.* (2008). Oncogene-induced replication stress preferentially targets common fragile sites in preneoplastic lesions. A genome-wide study. Oncogene *27*, 3256-3264.

Tuduri, S., Crabbe, L., Conti, C., Tourriere, H., Holtgreve-Grez, H., Jauch, A., Pantesco, V., De Vos, J., Thomas, A., Theillet, C.*, et al.* (2009). Topoisomerase I suppresses genomic instability by preventing interference between replication and transcription. Nat Cell Biol *11*, 1315-1324.

Vafa, O., Wade, M., Kern, S., Beeche, M., Pandita, T.K., Hampton, G.M., and Wahl, G.M. (2002). c-Myc can induce DNA damage, increase reactive oxygen species, and mitigate p53 function: a mechanism for oncogene-induced genetic instability. Mol Cell *9*, 1031-1044.

van Galen, J.C., Muris, J.J., Oudejans, J.J., Vos, W., Giroth, C.P., Ossenkoppele, G.J., Otte, A.P., Raaphorst, F.M., and Meijer, C.J. (2007). Expression of the polycomb-group gene BMI1 is related to an unfavourable prognosis in primary nodal DLBCL. J Clin Pathol *60*, 167-172.

van Leenders, G.J., Dukers, D., Hessels, D., van den Kieboom, S.W., Hulsbergen, C.A., Witjes, J.A., Otte, A.P., Meijer, C.J., and Raaphorst, F.M. (2007). Polycomb-group oncogenes EZH2, BMI1, and RING1 are overexpressed in prostate cancer with adverse pathologic and clinical features. Eur Urol *52*, 455-463.

van Lohuizen, M., Verbeek, S., Scheijen, B., Wientjens, E., van der Gulden, H., and Berns, A. (1991). Identification of cooperating oncogenes in E mu-myc transgenic mice by provirus tagging. Cell *65*, 737-752.

Varambally, S., Dhanasekaran, S.M., Zhou, M., Barrette, T.R., Kumar-Sinha, C., Sanda, M.G., Ghosh, D., Pienta, K.J., Sewalt, R.G., Otte, A.P.*, et al.* (2002). The polycomb group protein EZH2 is involved in progression of prostate cancer. Nature *419*, 624-629.

Vaziri, C., Saxena, S., Jeon, Y., Lee, C., Murata, K., Machida, Y., Wagle, N., Hwang, D.S., and Dutta, A. (2003). A p53-dependent checkpoint pathway prevents rereplication. Mol Cell *11*, 997-1008.

Velimezi, G., Liontos, M., Vougas, K., Roumeliotis, T., Bartkova, J., Sideridou, M., Dereli-Oz, A., Kocylowski, M., Pateras, I.S., Evangelou, K.*, et al.* (2013). Functional interplay between the DNA-damage-response kinase ATM and ARF tumour suppressor protein in human cancer. Nat Cell Biol *15*, 967-977.

Venkitaraman, A.R. (2002). Cancer susceptibility and the functions of BRCA1 and BRCA2. Cell *108*, 171-182.

Voncken, J.W., Roelen, B.A., Roefs, M., de Vries, S., Verhoeven, E., Marino, S., Deschamps, J., and van Lohuizen, M. (2003). Rnf2 (Ring1b) deficiency causes gastrulation arrest and cell cycle inhibition. Proc Natl Acad Sci U S A *100*, 2468-2473.

Wahl, G.M., and Carr, A.M. (2001). The evolution of diverse biological responses to DNA damage: insights from yeast and p53. Nat Cell Biol *3*, E277-286.

Wang, H., Wang, L., Erdjument-Bromage, H., Vidal, M., Tempst, P., Jones, R.S., and Zhang, Y. (2004). Role of histone H2A ubiquitination in Polycomb silencing. Nature *431*, 873-878.

Ward, I.M., Minn, K., van Deursen, J., and Chen, J. (2003). p53 Binding protein 53BP1 is required for DNA damage responses and tumor suppression in mice. Mol Cell Biol *23*, 2556-2563.

Weikert, S., Christoph, F., Kollermann, J., Muller, M., Schrader, M., Miller, K., and Krause, H. (2005). Expression levels of the EZH2 polycomb transcriptional repressor correlate with aggressiveness and invasive potential of bladder carcinomas. Int J Mol Med *16*, 349-353.

Won, J., Kim, M., Kim, N., Ahn, J.H., Lee, W.G., Kim, S.S., Chang, K.Y., Yi, Y.W., and Kim, T.K. (2006). Small molecule-based reversible reprogramming of cellular lifespan. Nat Chem Biol *2*, 369-374.

Xu, B., Kim, S., and Kastan, M.B. (2001). Involvement of Brca1 in S-phase and G(2)-phase checkpoints after ionizing irradiation. Mol Cell Biol *21*, 3445-3450.

Young, N.P., and Jacks, T. (2010). Tissue-specific p19Arf regulation dictates the response to oncogenic K-ras. Proc Natl Acad Sci U S A *107*, 10184-10189.

Yu, J., Cao, Q., Mehra, R., Laxman, B., Tomlins, S.A., Creighton, C.J., Dhanasekaran, S.M., Shen, R., Chen, G., Morris, D.S.*, et al.* (2007). Integrative genomics analysis reveals silencing of beta-adrenergic signaling by polycomb in prostate cancer. Cancer Cell *12*, 419-431.

Zhang, W.W., Mendez, S., Ghosh, A., Myler, P., Ivens, A., Clos, J., Sacks, D.L., and Matlashewski, G. (2003). Comparison of the A2 gene locus in Leishmania donovani and Leishmania major and its control over cutaneous infection. J Biol Chem *278*, 35508-35515.

Zhong, Y., Nellimoottil, T., Peace, J.M., Knott, S.R., Villwock, S.K., Yee, J.M., Jancuska, J.M., Rege, S., Tecklenburg, M., Sclafani, R.A.*, et al.* (2013). The level of origin firing inversely affects the rate of replication fork progression. J Cell Biol *201*, 373-383.

Zhu, J., Woods, D., McMahon, M., and Bishop, J.M. (1998). Senescence of human fibroblasts induced by oncogenic Raf. Genes Dev *12*, 2997-3007.

Zou, L. (2007). Single- and double-stranded DNA: building a trigger of ATR-mediated DNA damage response. Genes Dev *21*, 879-885.

ACKNOWLEGMENTS

This research project would not have been possible without the support and help of many people.

First of all, I would like to express my gratitude to my supervisor, Dr. Fabrizio d'Adda di Fagagna, whose expertise, understanding, advices and patience were of great importance in the course of my PhD work.

I would like to thank Prof. Marco Foiani from IFOM-IEO-Campus and Dr. Philippe Pasero from Institut De Genetique Humaine (Montpellier, France), for taking time out from their busy schedules to serve as my internal and external co-supervisors, respectively.

I would like to thank to Prof. Francesco Blasi from IFOM-IEO-Campus (Milan, Italy) and Prof. Thomas Helleday from Karolinska Institutet (Stockholm, Sweden), my internal and external examiners respectively, for having found time and energy to read and criticize my thesis.

A special thank to Dr. Aaron Bensimon and Dr. Jun komatsu from Genomic Vision (Paris, France), where I spent 3 pleasant months of hard work to learn how to use the DNA molecular combing technique. Without their expertise and their patience in teaching me, this project would not have been possible.

A special thank to Prof. Utz Herbig from New Jersey Medical (Newark, USA), Dr. Diego Pasini, Andrea Piunti, Dr Muge Ogrunc from IFOM-IEO-Campus for their willing to collaborate with me, and for the interesting scientific discussion made.

I would like also to thank the IFOM-IEO-Campus facilities, in particular the Cell Culture, the Imaging, the RT-PCR and the Kitchen units, for their important help in my work. A special thank to Dr. Dario Parazzoli and Dr Amanda Oldani, from the Imaging facility of IFOM-IEO-Campus, for the precious help in setting up a suitable system for automated combing image acquisition. Without their help this work would have been not possible.

A special thank to all member of Lab F. For all the time shared in doing science, for the useful scientific discussions as well as for the break time spent together, sharing hopes, fears and dream.

To all my friends Alessandra, Francesca, Glenda, Sara, Giusy, Inaki, Stefan, Marianna, Marika, Adam, Bartek, Marta, Adonis, Alica, Domenico, Stefano, Anna, Sebastiano, Giacomo, Alberto, Massimo and Angelica. For the time and experience shared with them that helped me becoming the person I am.

To Francesca, Flavia and Valentina. For being The lab family to count on. For the great and endless support and help given during difficult moments. For all the amusing time spent together outside the lab. For us, ''le daddine'', that have shared all bad and good things of this scientific life. For rendering these years the greatest experience of my life.

To my Spanish sister Amaya, for the great support given, for all of our pseudo-philosophical and pseudo-psychological everlasting chat in front of Sushi. For all the advice, time, experience, hopes, ideas we shared. Without them I would not be able to achieve this important step in my life.

To my teacher, guide and friend Stefania. For making me discovering the theatre. That kind of theatre that is life. That kind of theatre that makes you more conscious of yourself and of the world. That kind of theatre that now I cannot live without.

To my little cousin-sisters Federica and Letizia. For their sweetness and amazing strength in dealing with the troubles life has imposed to them. Their inspiring attitude has accompanied me during these tough PhD years making me staying focused on my objective even in the hardest periods.

To my brother, for all the moments we shared in life. For all the patience and support given during these years. For his strength and courage, for his ability to always see the positive aspect of things. For his ability to simplify and solve problems. Thank you my little brother, for every little thing you did for me in these years. That little things that make the differences in life.

To my parents. For their endless support in all my choices. Thanks Mum for being my best supporter, for being optimistic when things seems to become troubles. And for always being right in approaching things in an optimistic perspective. You are the best both at 'supportarmi e sopportarmi'. Thanks Daddy for inspiring me great interest in research, both scientific and philosophical.

To my grandmother, for her strength and for all the great values she transmitted me. For believing in me.

To all the ones that, even though unluckily not anymore physically present in this world, were always present in my heart. For all the things they taught me and that made me undertake this road. You will always be like shining stars enlightening the way to take.